NONLINEAR VIBRATION ENERGY HARVESTING BY INTENTIONAL EXCITATION OF HIGH-FREQUENCY DYNAMICAL INSTABILITY

BY

KEVIN R. REMICK

DISSERTATION

Submitted in partial fulfillment of the requirements
for the degree of Doctor of Philosophy in Mechanical Engineering
in the Graduate College of the
University of Illinois at Urbana-Champaign, 2015

Urbana, Illinois

Doctoral Committee:

Professor Alexander F. Vakakis, Chair
Professor Lawrence A. Bergman
Professor D. Michael McFarland
Professor Andrew G. Alleyne
Professor D. Dane Quinn

ABSTRACT

In this thesis, a vibration-based energy harvesting system utilizing essential (nonlinearizable) nonlinearities and various electromechanical coupling elements is investigated. These elements include electromagnetic and piezoelectric methods of energy conversion. The mechanical system of interest consists of a grounded, weakly damped linear oscillator (primary system) subjected impulsive loading. This primary system is coupled to a light-weight, damped oscillating attachment (nonlinear energy sink, NES) via a thin wire, which generates an essential geometric cubic stiffness nonlinearity. Various electromechanical coupling elements are included within the oscillator coupling in various configurations depending on the system being studied. Under single or repeated impulsive input, the damped dynamics of this system exhibit transient resonance captures (TRCs) causing large-amplitude, high-frequency instabilities in the response of the NES. These TRCs result in strong energy transfer from the directly excited primary system to the light-weight attachment. The energy is harvested by the electromechanical elements in the coupling and, in this present case, dissipated across a resistive element in the electrical circuit. The primary goal of this work is to numerically, analytically, and experimentally demonstrate the efficacy of employing this type of high-frequency dynamic instability to achieve enhanced vibration energy harvesting under single or repeated impulsive excitation.

To my loving family, for their endless support, patience, drive, and inspiration.

ACKNOWLEDGMENTS

I would like to give special thanks to my advisors, Dr. Alexander Vakakis, Dr. Lawrence Bergman, and Dr. Michael McFarland, for their continuous support of my work, devoted laboratory time, professional advice, and all the laughs along the way. Working in the Linear and Nonlinear Dynamics and Vibrations Laboratory was the most rewarding experience I've had throughout my college career. The open use of equipment provided there enabled me to prove the existence of the phenomena presented in this work.

I would like to thank to Dr. Dane Quinn at the University of Akron and Dr. Themistoklis Sapsis at the Massachusetts Institute of Technology for additional support, invaluable discussion, and unique perspectives.

I would like to thank the National Science Foundation. Without the support from NSF Grant No. CMMI-1100722 the work established here would not have been possible.

I would like to thank the Mechanical Science and Engineering Department at the University of Illinois at Urbana-Champaign. Without this support, many things would not have happened. In particular thank you for the financial support during my last two semesters, in which I was able to participate in rewarding experiences being a teaching assistant and even leading the experimental stress analysis course.

TABLE OF CONTENTS

CHAPTER 1

STATE OF THE ART IN VIBRATION ENERGY HARVESTING AND TARGETED ENERGY TRANSFER

The work presented in this chapter lays the groundwork for the mechanical system and resulting phenomena upon which a novel vibration energy harvesting apparatus is designed and validated. This document seeks to expand the use of strong nonlinearities in systems for enhanced vibration energy harvesting capability using induced dynamic instabilities inherent to nonlinear systems. Advantages over traditional linear energy harvesting systems are discussed and validated. The analysis is initiated by exploring the characteristics of strongly nonlinear mechanical systems, particularly subject to impulsive excitation conditions.

It has been shown that linear damped oscillators with essentially nonlinear damped attachments provide a means for efficient broadband vibration suppression [1, 2, 3], in contrast to the linear vibration absorber whose operation is narrowband [4]. Targeted energy transfer has been observed in these strongly nonlinear systems, with the attachments being commonly referred to as *nonlinear energy sinks - NESs* [5, 6]. Targeted energy transfer describes the nearly irreversible passive transfer of a significant amount of energy initially stored in a linear structure to an appropriately designed strongly nonlinear lightweight attachment which acts, in essence, as a passive broadband adaptive boundary controller [7, 8, 9, 10]. The complex dynamics of these systems results from the capacity of the essentially nonlinear attachment to engage in resonance captures with modes of the linear structure over an extensive range of frequencies and energies. This behavior arises from dynamics of the underlying Hamiltonian systems, which possess highly degenerate eigenstructures with pairs of complex conjugate imaginary and multiple zero eigenvalues. These result in complex, high co-dimensional bifurcations, which may lead to interesting nonlinear dynamics, such as chaotic motions and dynamic instabilities. These dynamic instabilities give rise to large amplitude responses in the nonlinear attachment and will be referred

to as such throughout this work.

An additional interesting feature of this class of highly degenerate systems is the occurrence of nonlinear instabilities associated with geometric stiffness [11] and damping nonlinearities [3]. In [3] a rather unexpected result was reported, namely that a geometrically nonlinear viscous damping element can lead to dynamic instability of the linear oscillator to which it is attached. This instability appeared as a buildup of the response of a nonlinear attachment as it engaged in resonance capture with the linear oscillator, in similarity to classical self-excited systems with energy intake such as the Van der Pol oscillator or systems undergoing aeroelastic flutter. An additional interesting dynamic phenomenon was reported in [11], in which a peculiar damped nonlinear transition into a state of sustained nonlinear resonance scattering [12, 13, 14] in a system of two coupled oscillators with essential stiffness was observed. This transition was realized for sufficiently weak damping and only in the neighborhood of the low-frequency branch of the *impulsive orbit manifold IOM* of the underlying Hamiltonian dynamical system. Moreover, sustained resonance scattering was realized only in certain frequency ranges and was eliminated when the dynamics was attracted to a 1:3 resonance capture which was manifested as dynamic instability in the transient response of the system, similar to [3].

In a Hamiltonian system of coupled oscillators with strong stiffness nonlinearities, an IOM consists of a countable infinity of periodic orbits and an uncountable infinity of quasi-periodic orbits, which typically extends over broad frequency and energy ranges [15]. These orbits, which are in the form of nonlinear beats, arise when an impulsive force is applied to the linear oscillator with the system being initially at rest. A periodic impulsive orbit corresponds to a rational relationship of the dominant frequencies of the responses of the oscillators, while a quasi-periodic impulsive orbit corresponds to an irrational frequency relationship. As shown in [3] and the present work here, dynamic instability resulting in large amplitude displacements is associated with excitation of the dynamics in the neighborhood of the IOM.

1.1 Vibration Energy Harvesting

The research performed in the course of this work seeks to apply the above phenomena to a novel, nonlinear energy harvesting apparatus. Two major classes of electromechanical coupling elements exist for converting mechanical energy into usable electrical energy. Piezoelectric and electromagnetic coupling elements have distinct advantages and disadvantages, which will be discussed next by considering the relevant literature. Vibration energy harvesting systems can be employed in a variety of environments, each with unique excitation power spectra. Harvesting robustness to a variety of excitation conditions is a paramount demand for these vibration energy harvesting devices. Basic principles behind linear and nonlinear energy harvesting systems are discussed first in what follows.

Typical vibration-based energy harvesting systems are based on linear or weakly nonlinear tuned mass dampers (TMD), which consist of an oscillating primary mass coupled to a secondary light-weight absorbing mass. With the primary mass subject to harmonic excitation, these linear systems can be specifically tuned to efficiently harvest energy. This is accomplished by matching the uncoupled natural frequency of the primary and secondary systems to the external forcing frequency [16, 17]. Furthermore, proper tuning of the electrical circuit parameters optimizes the electromechanical conversion process, providing for increased harvesting efficiency [18, 19, 20, 21, 22]. Energy transfer from the primary system to the linear harvester is increased for larger primary excitation amplitude and weaker system damping [23]. Low system damping results in a sharp resonant peak, which is indicative of the narrowband operation of these linear harvesting systems. Harvesting efficiency decreases significantly from excitations with time-varying frequency or from frequencies that vary slightly from the tuned resonance frequency of the mechanical system. Optimizing strategies for the former class of excitations were formulated theoretically in [24] for a linear single-degree-of-freedom harvester.

Nonlinear energy harvesting systems have been employed in a variety of methods as a solution to frequency variation and frequency mistuning [25, 26, 27]. Mann and Sims [26] investigated magnetic restoring force spacing, which allowed for tunable resonance of an oscillator to input conditions. The authors also discovered experimentally that damping plays a vital role in

the ability of the harvester to engage in high-energy responses. Ma and Zhang [28, 29] utilized a pendulum system with a potential well to increase energy harvesting efficiency when the dynamics escape the well. Modulating forcing frequency and tunable damping was investigated as a means to tune resonance of the system for increased harvesting efficiency. The authors conclude that an active element in the system to keep the oscillator operating outside of the well would greatly benefit the harvesting efficiency. Erturk et al. [30] showed superior harvesting performance for an inverted cantilever beam under buckling conditions and broadband excitation. The authors used piezo-magneto-elastic effects to enhance harvesting compared to systems without these effects.

Incorporating nonlinear mechanical attachments into linear primary systems has been explored in the literature as a means to broaden response bandwidth and provide large amplitude solutions [31, 32]. As described above, these mechanical attachments use strong cubic stiffness nonlinearities to accomplish this behavior. The literature describes this class of strong nonlinearity, which lacks a linear part and hence cannot be linearized, as essential (nonlinearizable) nonlinearity. Kremer and Liu [31] use magnetic restoring force to provide the cubic term in the coupling; however, the authors must also use a linear term in the coupling due to the experimental configuration. Hu et al. [32] use geometric effects to provide the cubic term and minimize linear effects in the coupling. These nonlinear systems exhibit the phenomenon of targeted energy transfer (TET) when subject to proper conditions and are the basis for the proposed system in this document. The two major electromechanical coupling methods will be discussed next.

1.1.1 Electromagnetic Energy Harvesting

The principles governing electromagnetic energy harvesting extend back to 1831. Michael Faraday discovered that a potential difference is created by moving an electric conductor through a magnetic field. This eventually led to Faraday's Law, which describes how electromotive force induced in a circuit is proportional to the time rate change of the magnetic flux linkage. This will be described in further detail in Chapter 3. This was first applied to electrical energy generation in the early 1930s, in which rotational generators were me-

chanically driven to produce small-scale power output. Rotational or linear electromagnetic energy harvesters can be highly efficient in turning kinetic energy into usable electrical energy with proper design and scaling. These devices can operate in the large-scale power regime or the relatively small scale regime of μW to mW [33]. Further minimization in scaling leads to vast efficiency reduction, imposing design restrictions for micro-fabrication.

The electromechanical coupling is commonly achieved using permanent magnets and a wire-wound induction coil. The cross-sectional area of the coil as well as the number of wire turns primarily determines coupling effectiveness. The permanent magnets can be realized with several different materials, of which neodymium provides the strongest magnetic flux field density per volume. The electromechanical coupling produced from these electromagnetic elements is physically realized in the mechanical system as electromagnetically induced damping, in which performance is thus proportional to velocity. The electromagnetic elements are relatively easily tunable to produce the desired electromechanical coupling, which is described in more detail in Chapter 3 and the work in [34]. These coupling elements have been utilized in a variety of configurations in the literature for small-scale vibration energy harvesting.

Ma and Zhang [28] use a rotational electromagnetic energy harvester based on a pendulum system with nonlinearity further induced via a potential well design. The authors investigated this system for various harmonic excitation frequencies, circuit loads, and excitation magnitudes, resulting in power output on the scale of $0.5 - 3.0mW$ while operating outside of the potential well. The authors expand the work in [29] to consider modulated forcing and damping, resulting in a power increase to a maximum of $\sim 20mW$. Mann and Sims [26] use a unique energy harvesting apparatus based on magnetic levitation via permanent magnets, which induce cubic restoring force while operating inside of a wire-wound coil. The authors consider a range of harmonic excitation frequencies and magnitudes and make conjectures about improvements to harvesting perofrmance; however, the authors do not report harvesting performance. Kremer and Liu [31] use a linear electromagnetic energy harvester design based on cubic restoring force coupling in a two degree-of-freedom system similar to the one described earlier. The restoring force is induced with one set permanent magnets while electromagnetic energy harvesting is performed with an additional set of permanent

magnets and induction coils. The authors investigate the system subjected to various magnitude impulsive forces and circuit loads theoretically and experimentally, incorporating an extensive system identification procedure. The maximum reported harvesting capability for this study is on the scale of $1.5 - 6.7mJ$. Additional electromagnetic energy harvesters on this size scale report similar power output, establishing this as a baseline performance floor for the device presented in this document.

Karami and Inman [35] utilize an inverted cantilever beam for study of linear, softly nonlinear, and bistable nonlinear energy harvesting device configurations incorporating electromagnetic and piezoelectric coupling elements. The authors analyze the systems for a variety of harmonic forcing magnitudes and frequencies for the various system configurations, in which the bistable nonlinear device indicated superior relative performance. The maximum reported harvesting capability for the electromagnetic elements is $\sim 0.002mW$, while the harvesting capability for the piezoelectric elements is $\sim 2mW$. The piezoelectric harvesting elements out-perform the electromagnetic harvesting elements in this small-scale apparatus, indicating an advantage of piezoelectric harvesting over electromagnetic harvesting. These devices will be discussed next.

1.1.2 Piezoelectric Energy Harvesting

The principles governing piezoelectric energy harvesting extend back to 1880. The piezoelectric effect was discovered by Jacques and Pierre Curie, in which a linear relationship was established between mechanical and electrical states in crystalline materials [36]. Piezoelectric materials have a wide variety of uses covering high voltage sources, sensors, actuators, vibration and noise reduction, and, in this case, vibration energy harvesting, which is a more recent application. Due to size constraints imposed by cost, construction, and placement, piezoelectric elements operate on a smaller power scale relative to the capability of electromagnetic harvesting elements; however, micro-scale limitations imposed on electromagnetic systems are no longer valid for piezoelectric systems. This trade-off is an important consideration when determining the scale of the device needed in the application environment.

The electromechanical coupling is commonly achieved using a variety of

different piezoelectric crystalline materials, such as quartz, topaz, tourmaline, or, in the case considered in Chapter 4, polyvinylidene fluoride dielectrics. The achievable induced strains and properties inherent to the crystalline material primarily determines coupling effectiveness. Maximization of the product of the piezoelectric voltage constant and the piezoelectric strain constant is paramount for suitable material selection for vibration energy harvesting, which serves to maximize the electromechanical coupling. Suitable materials often come in the form of crystalline ceramics, thin films, and polymers, which have applications according to various frequency and excitation ranges. Many piezoelectric materials used for energy harvesting are commercially manufactured in a variety of sizes and shapes, such as MFC, bimorph, multilayer, or QuickPack [37]. The electromechanical coupling produced from these crystals is physically realized in the mechanical system as a stiffness term with structural-like damping behavior, in which performance is thus proportional to displacement. The piezo-constitutive law dictates how stress and strain are related to electric charge density and electric field strength, respectively, via the material parameters described above. These principles are described in more detail in Chapter 4. The piezoelectric parameters are inherent to the material selected, making them not easily tunable or designable. This makes incorporating piezoelectric materials into unique harvesting devices challenging. Custom piezoelectric materials are expensive and require calibration, which is difficult to accomplish in a typical academic research laboratory. These coupling elements have been utilized in a variety of configurations in the literature for small-scale vibration energy harvesting.

Mak et al. [38] use a traditional linear cantilever beam setup with nonlinearity induced via a vibro-impact bump stop and piezoelectric harvesting elements. The bump stop impacts the beam when it is excited at a sufficient magnitude, causing the beam to vibrate at higher frequencies. The authors investigate this system subject to various forcing frequencies and magnitudes, concluding that energy harvesting performance is increased when the high-frequency conditions are induced by the bump stop relative to lower frequency 1:1 resonance harvesting. The maximum reported energy harvesting capability for this study is on the scale of $0.2\mu W$. Garcia et al. [39] use a traditional linear cantilever beam setup with nonlinearity induced via electromagnetic means. The authors investigate this system subject to various forcing frequencies and magnitudes, concluding that energy harvesting

performance is increased again with induced high-frequency oscillations. The maximum reported energy harvesting capability for this study is on the scale of $2.6 - 13.7mW$. Liao and Sodano [39] use the traditional linear cantilever beam to study optimal electrical tuning parameters for piezoelectric elements. The authors study the system subject to various forcing frequency, magnitude, and load resistance, reporting a maximum energy harvesting capability on the scale of $2 - 9mW$. Additional piezoelectric energy harvesters on this size scale report similar power output, again establishing this as a baseline performance floor for the device presented in this document.

1.2 Targeted Energy Transfer in Strongly Nonlinear Coupled Oscillators

Discussed here is a peculiar damped nonlinear transition of a system of two coupled oscillators into a state of sustained nonlinear resonance scattering. This system consists of a grounded, weakly damped linear oscillator attached to a light, weakly damped oscillator with essential (nonlinearizable) stiffness nonlinearity of the third degree, and linear damping. Under specific forcing conditions, the damped response of this system locks into a damped, non-resonant transition resembling continuous resonance scattering, whereby the transient damped dynamics closely follows an impulsive orbit manifold of the dynamics in the frequency-energy plane. Such transitions represent an anti-resonance state, where the dynamics is farthest away from resonance. It is conjectured that such transitions are only made possible by the essential stiffness nonlinearity of the nonlinear attachment and cannot be realized in linearizable nonlinear dynamics where resonance captures prevent sustained resonance scattering. Note, of particular interest for the case of vibration energy harvesting is the response of the system upon exiting the anti-resonance state and entering into resonance capture, which causes a large-amplitude "burst" in the response [40].

1.2.1 System Modeling

A system of coupled oscillators composed of a linear oscillator coupled to an essentially nonlinear attachment is considered,

$$x'' + \lambda_1 x' + \lambda_2(x' - v') + \omega_0^2 x + C(x - v)^3 = I_0\delta(t) \tag{1.1a}$$

$$\epsilon v'' + \lambda_2(v' - x') + C(v - x)^3 = 0 \tag{1.1b}$$

In (1.1), x denotes the response of the linear oscillator, v that of the nonlinear attachment, and prime denotes differentiation with respect to the time variable t. Moreover, the nonlinear attachment is assumed to be lightweight implied by the small parameter $0 < \epsilon \ll 1$ denoting its mass and to possess a nonlinearizable cubic stiffness nonlinearity with coefficient equal to C; ω_0 and λ_1 denote the natural frequency and the linear viscous damping coefficient, respectively, of the linear oscillator, whereas λ_2 is the coefficient of the nonlinear component of the damping of the nonlinear attachment. The nonlinear terms in (1.1) can be realized by geometric and kinematic nonlinearities [15]; i.e., through suitable geometric arrangement of stiffness elements perpendicular to the direction of the oscillation. Moreover, since we are interested in studying damped transitions of (1.1) along the impulsive orbit manifold of the underlying Hamiltonian system, it is assumed that the system is initially at rest, and an impulsive force of magnitude I_0 is applied to the linear oscillator at $t = 0$. These forcing and initial conditions are equivalent to the following initial conditions at $t = 0+$,

$$\begin{aligned} x(0+) &= 0, \qquad x'(0+) = I_0, \\ v(0+) &= 0, \qquad v'(0+) = 0 \end{aligned} \tag{1.2}$$

and no external forcing. Prior to studying sustained nonlinear resonance in the damped system (1.2), the underlying Hamiltonian system dynamics will be considered.

1.2.2 Underlying Hamiltonian Dynamics

The underlying Hamiltonian system corresponding to $\lambda_1 = \lambda_2 = I_0 = 0$ is considered, and thus the concept of *frequency energy plot (FEP)*. We focus

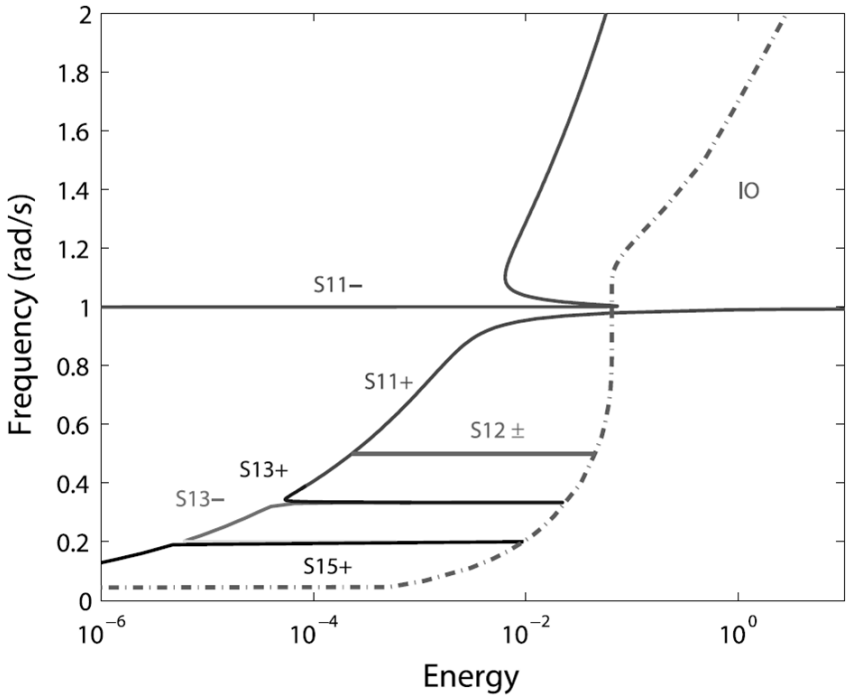

Figure 1.1: Frequency-energy plot of the underlying Hamiltonian system (1.1).

specifically on the manifold of impulsive orbits in that plot. The FEP was introduced in detail in [15] and in references therein, and depicts the branches of periodic and quasi-periodic orbits of the Hamiltonian system for varying energy. Specifically, the frequency of each periodic orbit of the Hamiltonian system is plotted against its corresponding (conserved) energy; by varying the energy level, branches (families) of periodic orbits are computed and depicted in the FEP.

Fig.1.1 depicts the FEP of the system with $C = 4\epsilon/3$, $\omega_0 = 1$, and $\epsilon = 0.01$ (these parameters will be used later in our analytical study). Three global branches of solutions are presented in that plot (i.e., defined over extended frequency and energy ranges); namely, the backbone branches $S11$ of in-phase and out-of-phase 1:1 periodic orbits (that is, periodic orbits where the linear and nonlinear oscillator execute in-phase or out-of-phase oscillations with identical frequencies, respectively) and the manifold of impulsive orbits composed of a countable infinity of periodic orbits and an uncountable infinity of quasi-periodic orbits, corresponding to impulsive excitation of the linear oscillator and all initial conditions zero. As discussed in [15]

the countable infinity of periodic orbits lie on pairs of in-phase/out-of-phase local subharmonic tongues defined over definitive energy ranges and connecting the backbone branches $S11$ with the manifold of impulsive orbits. Each point on a subharmonic branch corresponds to an in-phase or out-of-phase subharmonic periodic orbit with the frequencies of the linear and nonlinear oscillators being rationally related. In Fig.1.1, only the three pairs of subharmonic tongues $S12\pm$, $S13\pm$ and $S15+$ are shown, corresponding to periodic orbits with ratios of frequencies of the nonlinear and linear oscillators being equal to $1:m$ where $m = 1, 3, 5$. Moreover, some of the branches of periodic orbits are unstable [15], but this is not indicated in Fig.1.1.

The Hamiltonian FEP will be the basis of the analysis of the weakly damped system (1.1), since depending on the applied initial energy (impulse) the damped dynamics "visit" different branches of the FEP and make transitions (jumps) between them. This is best shown by computing the wavelet transforms of the damped responses and superimposing the resulting wavelet spectra on the Hamiltonian FEP. Then, it can be shown [15] that the duration of visits on different branches of the FEP depends on the strength of the damping terms, and as energy decreases the system undergoes transitions between these branches. Of particular interest will be to study damped transitions that nearly track the manifold of impulsive orbits of the FEP. By the previous discussion such transitions imply that the dynamics of system (1.1) engage in sustained nonlinear resonance scattering without being captured by the countable infinity of resonances corresponding to the periodic impulsive orbits on that manifold. It follows that, in the context of resonance capture, a damped transition that approximately tracks the IO manifold represents the complete antithesis of resonance capture; that is, a state of sustained anti-resonance of the dynamics.

The peculiar transition of the trajectory along the IO manifold without resonance captures deserves some extra discussion. As has been demonstrated in [2], response regimes lying on the IO manifold of the underlying Hamiltonian system constitute their own invariant set. These regimes are characterized by their entirely non-resonant behavior during which insignificant interactions between the oscillators occur. Surprisingly enough, it has been found that for the lightly damped system, there are possibilities for the response to permanently stay in a small neighborhood of this invariant set without escaping to resonance captures. Unfortunately, at this point, the

Table 1.1: Experimentally identified system parameters for the fixture presented in Fig.1.2.

Parameter	Value
m_1	$0.882kg$
m_2	$0.357kg$
k_{lin}	$469N/m$
C	$7.486 \times 10^6 N/m^\alpha$
α	2.963
λ_1	$0.074Ns/m$
λ_2	$0.025Ns/m$

exact reason for this peculiar non-resonant behavior is unknown; however, it is conjectured that the answer can be partially obtained from adiabatic theory. Thus, assuming a slow variation of the energy of the entire system, the picture of the underlying Hamiltonian system is revisited. Considering the underlying Hamiltonian structure of the system, the IO trajectories can be distinguished from other orbits by their maximal possible remoteness from the strongest (main) resonances. This fact suggests that starting far away from the resonance and keeping on the adiabatic reduction of the system energy (by introducing small damping in the system), a fine balance between the rate of evolution of the entire phase space with that of the deviation of the trajectory from the surface of the manifold can be found. Therefore, for this optimally balanced case the trajectory initially emanating from the IO manifold fails to overtake the evolution of the entire phase space and get attracted to one of the strong resonances. The system thus stays in close proximity of the slowly evolving IO surface, and at the same time it remains sufficiently far from the basins of attraction of the resonances. However, a slight increase in damping may cause the breakdown of this balance resulting in the transition to (and capture into) resonance.

1.2.3 An Experimental Study with brief Computational Support

Fig.1.2 depicts the test fixture constructed to experimentally confirm sustained resonance scattering. The system consists of two masses that oscillate

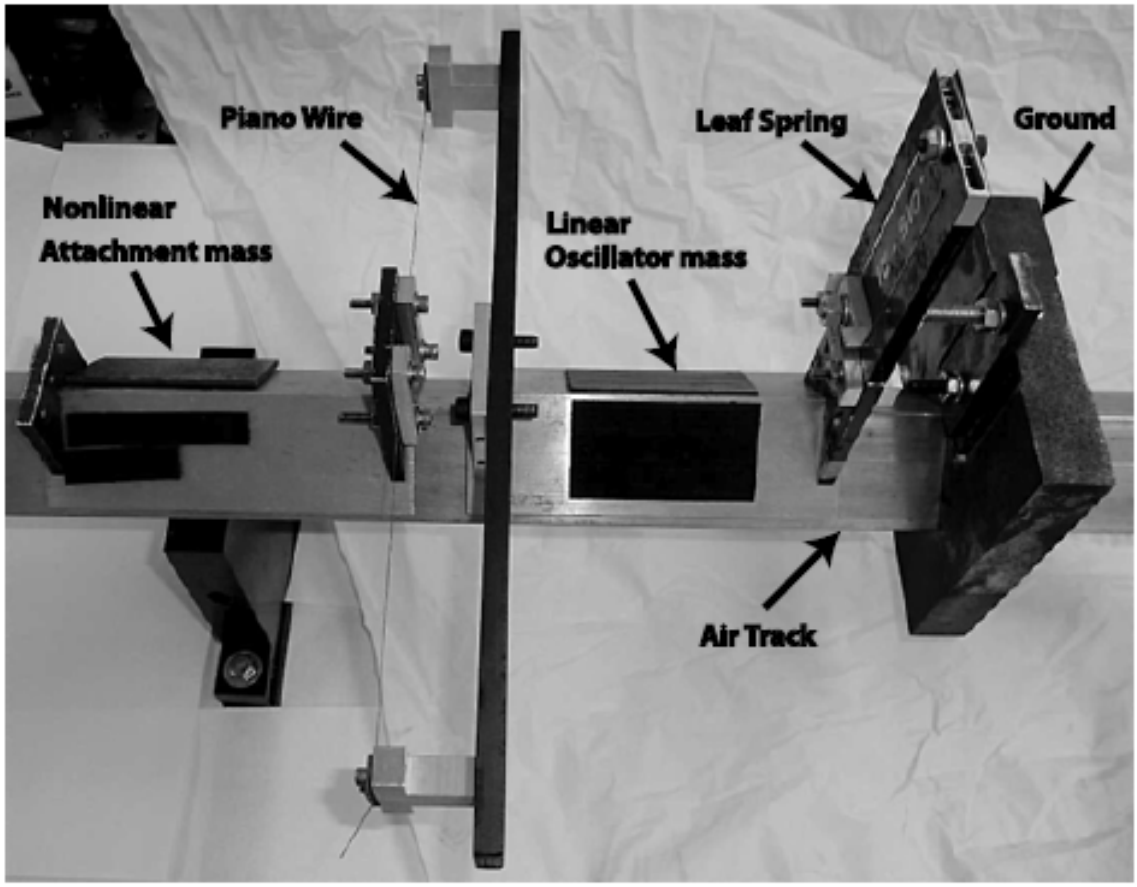

Figure 1.2: Experimental realization of the system (1.3) utilized for single impulse excitation conditions (1.2) and parameters identified in Table 1.1.

along an air track in order to minimize energy dissipation due to friction. The linear oscillator consists of a larger mass grounded by a linear leaf spring, whereas the attachment consists of the smaller mass connected to the larger one by means of a strongly nonlinear stiffness. This was realized by means of a small diameter steel piano wire oriented perpendicular to the direction of oscillation. When there is no pretension in the wire, an essentially nonlinear stiffness of nearly third order is realized [2] due to geometric nonlinearities in the resulting forcedisplacement relationship. An impulsive excitation is applied to the linear oscillator by means of an impact hammer, so that the resulting equations of motion are modeled as,

$$m_1 x'' + \lambda_1 x' + \lambda_2(x' - v') + k_{lin} x + C sgn(x - v)|x - v|^{\alpha} = F(t) \tag{1.3a}$$

$$m_2 v'' + \lambda_2(v' - x') + C sgn(v - x)|v - x|^{\alpha} = 0 \tag{1.3b}$$

where the numerical values of the parameters were identified by modal analysis (for the linear oscillator) and nonlinear system identification (for the nonlinear attachment). These are listed in Table 1.1. As in the theoretical development, the essentially nonlinear (nonlinearizable) terms are restricted solely to the coupling stiffness which is approximately cubic ($\alpha = 2.963$). Moreover, consistent with the assumptions of our analysis, the viscous damping term in the linear coupling element is of $O(\epsilon_2)$ where, as in the analysis, the small parameter is defined as the ratio of the masses of the two oscillators, $\epsilon = 0.3569/0.882 \approx 0.405$. Hence, based on our theoretical predictions, it is anticipated that the occurrence of nonlinear resonance scattering in the experimental system will exist.

In the experimental tests, an impulsive excitation (by means of a PCB modal hammer) was given to the linear oscillator with the system being initially at rest (1.2), and the velocity time series of the two masses were measured using two separate Polytec VibraScan laser vibrometers and recorded on two separate computers. The individual vibrometers can be set to start recording either at the onset of motion for each individual mass or can be synchronized with a trigger in the modal hammer. Early runs did not utilize the trigger in the impact hammer, but later this feature was implemented. By not using an impact trigger, an unmeasured phase lag is introduced between the measured signals preventing the accurate measurement of the relative

motion between the two masses. Without knowing this relative response, the instantaneous system energy stored in the coupling spring cannot be computed, and the experimental FEP cannot be constructed. Hence, only experimental data obtained using the hammer trigger will be presented in this study.

In order to plot the experimental data on the FEP, the velocity data must first be time integrated to obtain the displacement time history for each individual mass. To avoid drift in the data due to integration of signal noise, the displacement time histories were baseline corrected using a high pass, 4^{th} order Butterworth filter with a cutoff frequency of $1Hz$. From the synchronized displacement time histories, the instantaneous total system energy is computed as

$$E_{TOT}(t) = \frac{1}{2}m_1 x'(t)^2 + \frac{1}{2}m_2 v'(t)^2 + \frac{1}{2}k_{lin}x(t)^2 + \frac{C}{1+\alpha}|x(t) - v(t)|^{\alpha+1} \quad (1.4)$$

It is mentioned at this point that even though the start of the recordings was synchronized and accurate measurements were made, uncertainty in the parameters listed in Table 1.1 and in the experimental setup remain; examples are experimental noise from the surrounding environment (e.g., from the moving air on the track), unmodeled friction during the movement of the carts on the air track, and occasional small rattling due to contact of the carts with the air track. These are not accounted for in the energy model (1.4). Since this system is non-conservative, the total system energy should decay with time; to ensure this, a non-increasing envelope of the energy of system (1.3) was computed. Having computed the energy versus time relationship and the wavelet transform of the relative displacement time history, an experimental damped transition on the Hamiltonian FEP of system (1.3) can be constructed and compared to the theoretical prediction.

Selecting the appropriate magnitude of the impulsive excitation in order to excite a damped transition in the neighborhood of the IO manifold (and, hence, induce sustained nonlinear resonance scattering) in the experimental system proved to be challenging. Indeed, such damped transitions can only be realized for a small range of impulsive excitations, since typically impulsive excitations lead to resonance captures on low-frequency subharmonic tongues in the FEP [2]. However, in our experiments, a range of magnitudes of applied impulses that excited damped transitions corresponding to

Table 1.2: Summary of experimental runs and observed dynamics.

Experimental Trial	$I_0(m/s)$	Type of Response
33	0.0384	SRS
34	0.0230	1:3 RC
35	0.0244	1:3 RC
36	0.0376	SRS
37	0.0317	1:3 RC
38	0.0365	SRS
39	0.0402	SRS
40	0.0353	Inconclusive
41	0.0629	Inconclusive
42	0.0347	1:3 RC
43	0.0331	Inconclusive
44	0.0358	Inconclusive
45	0.0400	SRS

sustained resonance scattering were found. A summary of the experimental tests and results is depicted in Table 1.2, where I_0 is the initial velocity of the linear oscillator immediately after the application of the impulse. From the theoretical predictions (based on numerical simulations of system (1.1)), the target initial velocity of the linear oscillator instantaneously after application of the impulse ranged between 0.032 and $0.048m/s$. This range, as predicted in the simulations, corresponds to excitations where large dynamic instabilities in the response of the nonlinear attachment were observed, and as shown in [15] such instabilities can be tied to sustained resonance scattering in the early stages of the damped transitions. This velocity range corresponds to the region of the FEP between the 1:3 and 1:2 periodic impulsive orbits. As shown in Table 1.2, nine out of the fourteen experimental runs fell within this desired theoretical range, and led to either sustained resonance scattering (SRS) or were at most inconclusive [that is, the dynamical response was identified as possibly SRS or resonance capture (RC)]. The results in Table 1.2 demonstrate that SRS can be observed repeatedly in the target velocity range, and is not an isolated dynamical phenomenon that is very sensitive to initial conditions.

For two cases where conclusive sustained resonance scattering in the measured dynamics was observed, the corresponding time histories and wavelet

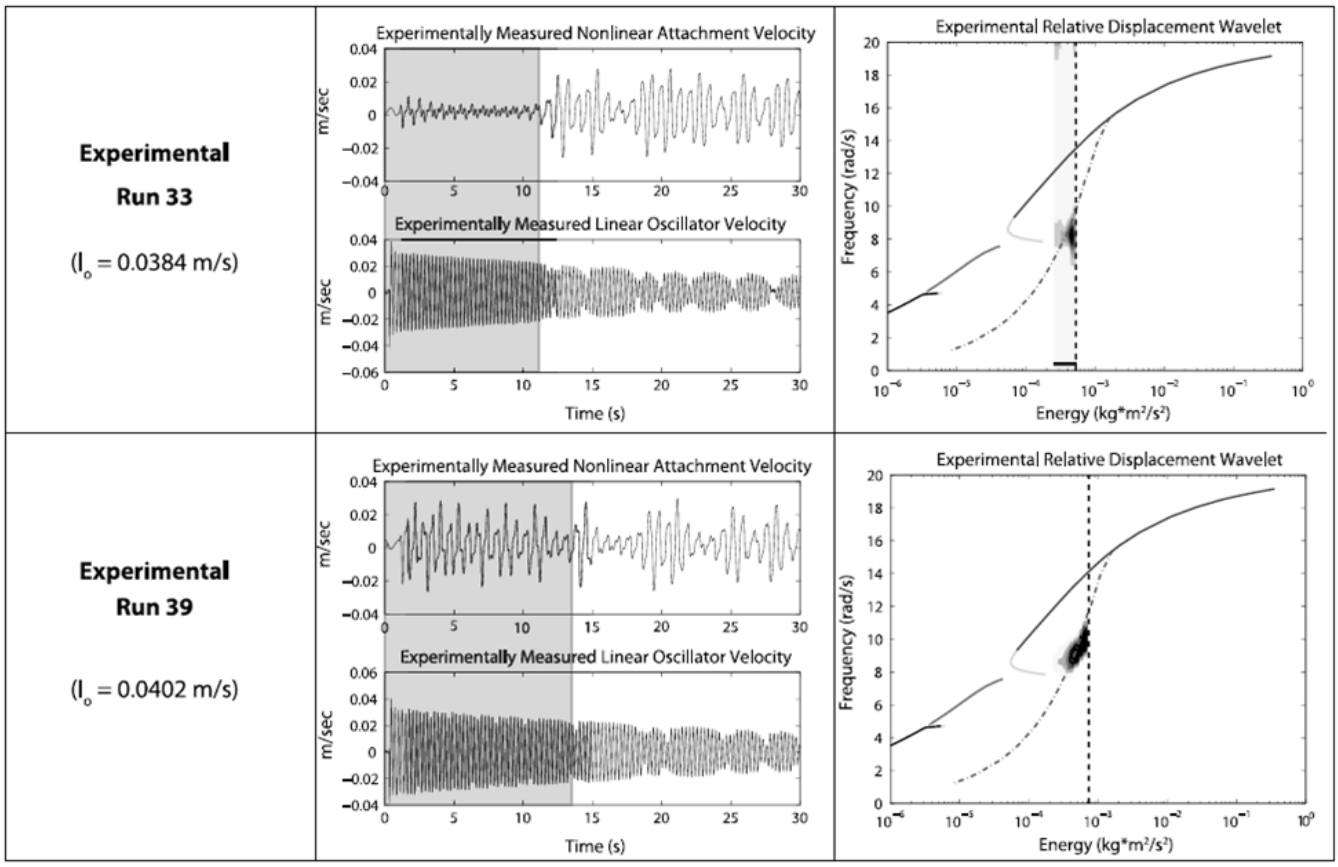

Figure 1.3: Velocity time series and corresponding damped transitions of relative displacements on the Hamiltonian FEP for selected experimental runs exhibiting sustained resonance scattering; shading indicates the initial state of SRS.

depictions in the Hamiltonian FEP are presented in Fig.1.3. A strong dynamic instability can be seen in the time history of the nonlinear attachment for experimental run 33 after the progression along the impulsive orbit manifold; this is manifested as "bursts" in the velocity time series of the response of the nonlinear attachment. In fact, such bursts correspond to the dynamics engaging in 1:3 resonance capture after the initial sustained resonance scattering, and is in full agreement with previous theoretical findings reported in [15]. For experimental run 39, a higher amplitude response of the nonlinear attachment is observed during transition along the impulsive orbit manifold; however, the corresponding frequency content remains similar to experimental run 33 during this transition. Regardless of the efficacy of the attachment in drawing energy from the main mass, both experimental runs 33 and 39 clearly show that SRS behavior can be observed in a repeatable fashion.

In Fig.1.4 the damped transitions obtained for experimental run 33 are depicted in more detail. The wavelet and Fourier transforms of the experimental displacement time histories of both the linear oscillator and nonlinear attachment are presented and compared to the corresponding plots derived by numerically simulating the mathematical model (1.3) with numerical parameters listed in Table 1.1 and initial velocity of the linear oscillator equal to $I_0 = 0.0384 m/s$. The two phases of the dynamics (initial sustained resonance scattering followed by 1:3 resonance capture) are clearly discerned, with the transition between the two phases occurring at about $12s$ for the experiment and about $5.5s$ for the numerical simulation. Moreover, the transition to 1:3 resonance capture is manifested as a dynamical instability: as a series of bursts in the experimental results and as a higher amplitude periodic oscillation in the numerical simulation. This, as well as the different transition times between experiment and simulation, can be attributed to the uncertainties in the experiments discussed previously, and especially the uncertainty of accurate measurement of the actual dissipation that occurs in the experimental fixture. The sustained resonance scattering that occurs as the weakly damped dynamics track approximately the impulsive orbit manifold of the underlying Hamiltonian FEP is confirmed by the Fourier transforms presented in Fig.1.4c and Fig.1.4f, where the broadband content of the response of the nonlinear attachment is clearly discerned in the frequency interval $\omega_0/3 < \omega < \omega_0$, with ω_0 the natural frequency of the linear oscillator. The lower boundary of this frequency range is due to the even-

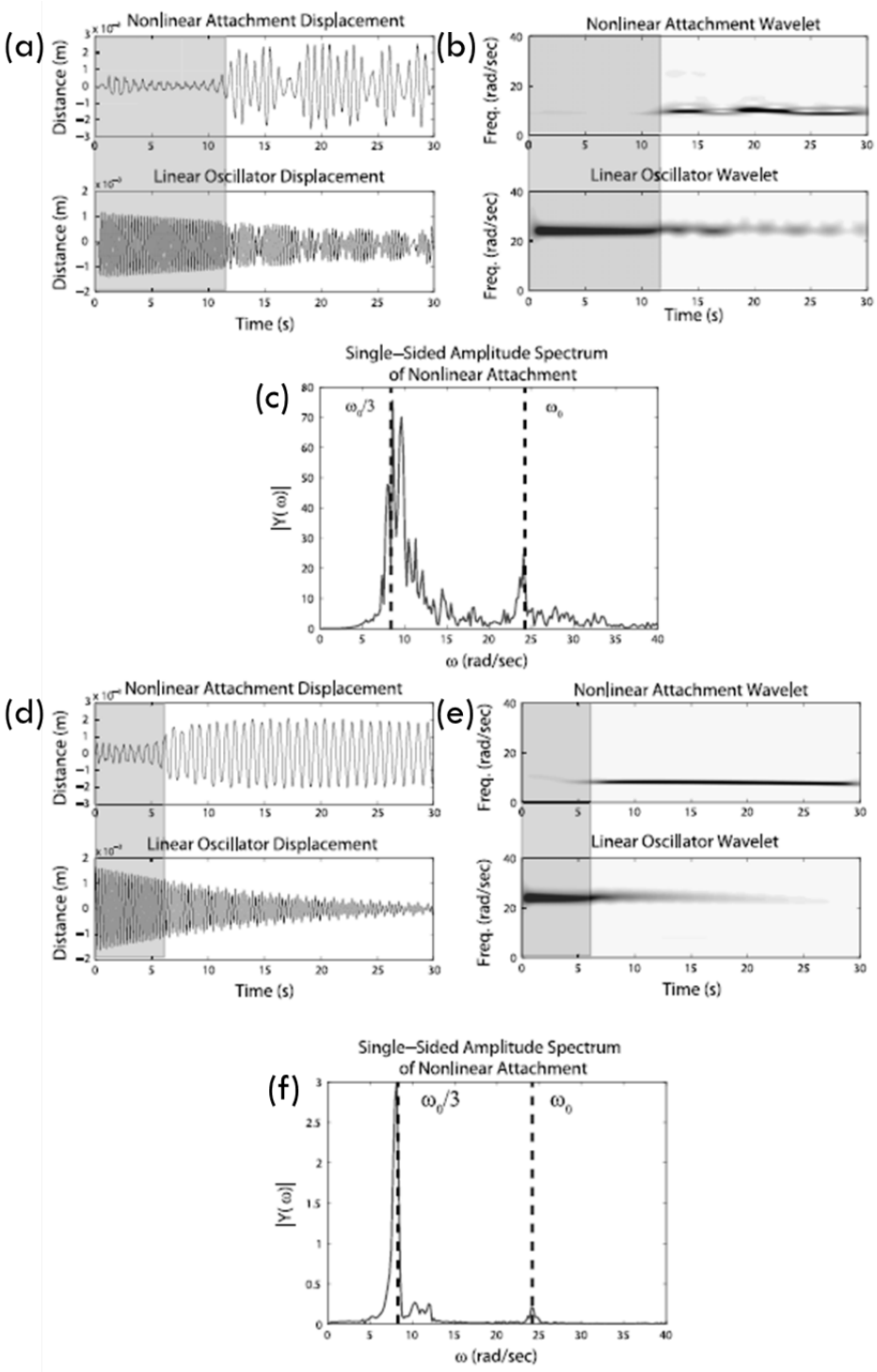

Figure 1.4: Results for experimental run 33, $I_0 = 0.0384m/s$: (a,b,c) experimental displacement time histories, and wavelet / Fourier transforms; (d,e,f) corresponding numerical results derived from model (1.3); shaded regions indicate sustained resonance scattering.

tual 1:3 resonance capture of the dynamics at the end of the initial phase of sustained resonance scattering. Hence, there exist strong frequency components in the Fourier transform plots at frequencies $\omega = \omega_0/3$ (1:3 resonance capture) and $\omega = \omega_0$ (corresponding to the fast frequency of the response of the nonlinear attachment as shown in the analytical study during [15]).

As another example, in Fig.1.5 the corresponding results for experimental run 39 in comparison with simulation are provided. Again, the experimental run shows sustained resonance scattering in the Fourier transform as was predicted from the simulation. As discussed previously, for initial or forcing conditions away from the neighborhood of the impulsive orbit manifold of the underlying Hamiltonian FEP, the dynamics is captured close to other resonance manifolds (lower frequency subharmonic tongues). This was fully confirmed by the experimental study. Cases that fell outside the desired range $0.032m/s < I_0 < 0.048m/s$ exhibit immediate resonance capture at subharmonic tongues with complete absence of sustained resonance scattering at the initial phase of the motion. For the results of experimental run 39, it is noted that the wavelet transform for the nonlinear attachment during sustained resonance scattering is more readily discerned when compared to experimental run 33; this is only an artifact of the normalization of the wavelet transform which is normalized to the peak value (which for experimental run 39 is comparable both before and after 1:3 resonance capture). The results of experimental runs 33 and 39 confirm the robustness of the sustained resonance scattering phenomenon, but also demonstrate that dynamic instabilities may be more difficult to control and consistently generate in an experimental setup.

1.3 Primary Goals for High-frequency Energy Harvesting

In summary, the experimental study of Section 1.2 provides strong evidence of realization of the theoretically predicted sustained nonlinear resonance scattering in a practical, strongly nonlinear system of coupled oscillators. It is conjectured that this peculiar state of the dynamics is due to the essential (nonlinearizable) stiffness nonlinearity of the attachment and can only be realized in the neighborhood of the impulsive orbit manifold of the under-

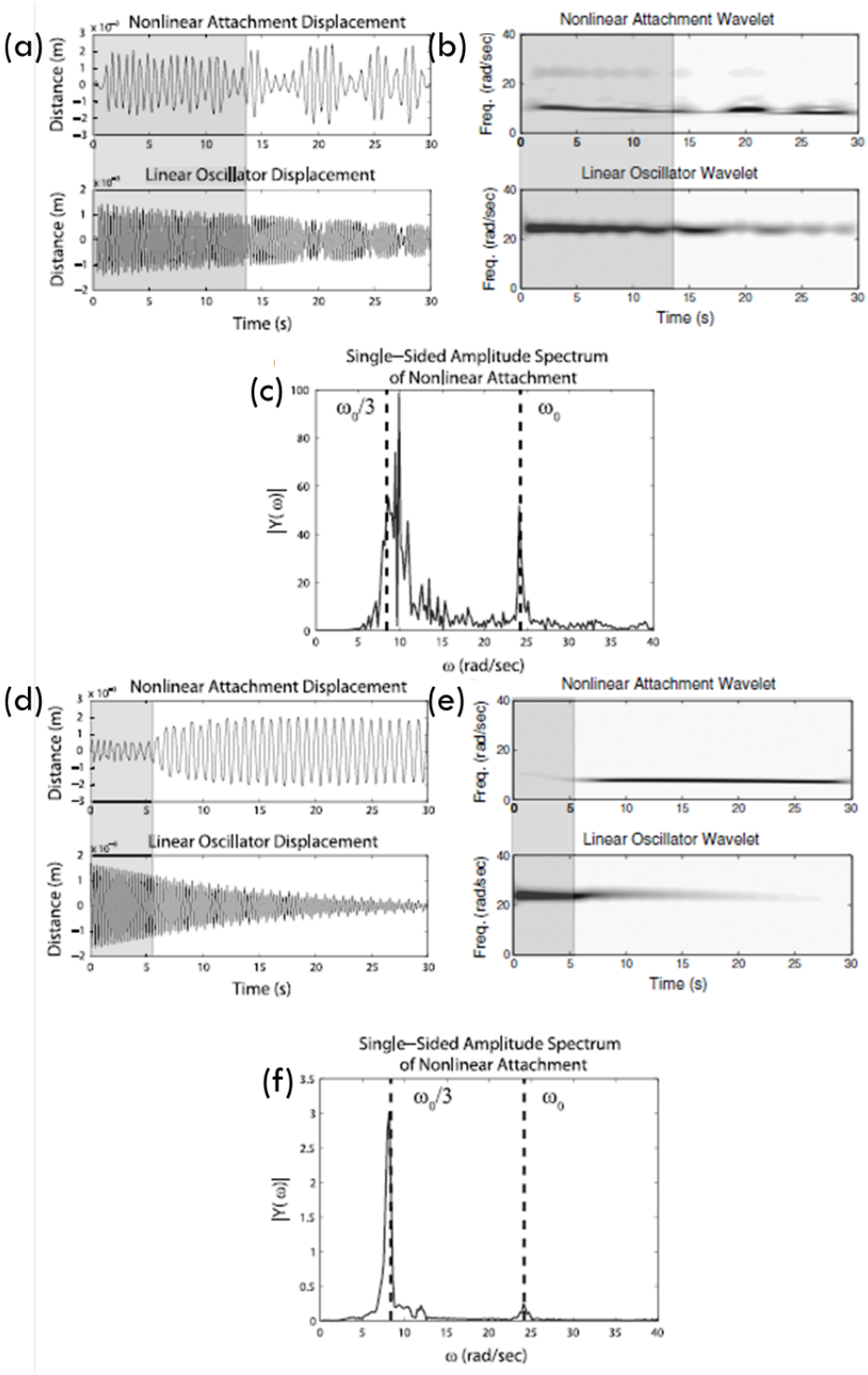

Figure 1.5: Results for experimental run 39, $I_0 = 0.0402m/s$: (a,b,c) experimental displacement time histories, and wavelet / Fourier transforms; (d,e,f) corresponding numerical results derived from model (1.3); shaded regions indicate sustained resonance scattering.

lying Hamiltonian system. Sustained resonance scattering is the complete antithesis of resonance and represents the state of the nonlinear dynamics that is "most distant" from a state of resonance. It is also conjectured that this state cannot be realized in systems with linearizable dynamics since in that case the dynamics have preferential resonant frequencies that possess strong domains of attraction that prevent sustained resonance scattering. A resonance manifold with such a relatively strong domain of attraction in the system studied herein is the one corresponding to 1:3 resonance, and indeed capture of the dynamics in the neighborhood of this manifold signifies the end of the phase of sustained resonance scattering. Upon capture onto a resonance manifold, a "burst" in the dynamics of the system results from the instability, which is the feature of paramount interest for vibrational energy harvesting.

Utilizing the knowledge of electromechanical conversion techniques outlined in Section 1.1 and the capability of the mechanical system proposed in Section 1.2 to engage in chaotic large-amplitude responses with a linear primary system, the primary goal of this document is to experimentally show superior energy harvesting capability for a system operating in a sustained high-frequency response regime using suitable harvesting elements. A secondary goal of performance robustness to various excitation conditions is paramount to system design, which is an attractive property of nonlinear vibration energy harvesting systems compared to similar linear systems. An impulsive class of excitations will be utilized in this work to induce high-frequency responses, as outlined in Section 1.2. Freedom in system design and parameter control is another goal of this work, allowing for a scalable system to be utilized in various applications.

The information provided in Section 1.1 indicates some important considerations for the design of the proposed nonlinear energy harvesting system. Piezoelectric elements are widely available commercially, making their use appealing as long as they can be readily adapted to an experimental apparatus. These elements are capable of providing a suitable power output needed for small electronics operating on the mW scale. These elements are typically utilized in applications where the system is subject to high-frequency harmonic excitations. The use of these piezoelectric elements in two unique energy harvesting systems is explored in Chapter 4.

Electromagnetic elements are also available commercially, although more

freedom exists in controlling the parameters inherent to the electromechanical coupling. This provides an important advantage when adapting harvesting elements to a unique experimental apparatus, as is proposed in this document. These elements are capable of providing a suitable power output needed for small electronics, as long as the mechanical system is of the proper scale. These elements are typically utilized in applications with various forcing schemes, providing a more robust performance. The use of these electromagnetic elements in a unique energy harvesting system is explored in Chapter 3.

The system initially explored in Section 1.2 indicates the capability of the lightweight nonlinear attachment to engage in low-frequency instabilities, resulting in large-amplitude responses relative to 1:1 internal resonance. The work in the next section explores the capability of a similar mechanical system to engage in high-frequency instabilities, resulting in larger-amplitude responses. Superior, robust energy harvesting capability is predicted from these high-frequency, large-amplitude responses.

CHAPTER 2

INDUCING HIGH-FREQUENCY INSTABILITY IN IMPULSIVELY LOADED SYSTEMS

The work in this chapter extends the aforementioned results in two ways. First, it is shown that high-frequency dynamical instability can be realized in systems of impulsively excited strongly nonlinear coupled oscillators; this contrasts with previously reported results in the work in [15] and Section 1.2, where only low-frequency dynamic instabilities were reported. Second, in contrast to previous studies where free damped transitions were considered, in this report the nonlinear dynamics under a repetitive series of impulses is considered, and it is shown that the dynamic instability can be sustained under this type of periodic excitation. It is anticipated that these findings will find application in areas such as energy harvesting of vibrations of systems under periodic or near-periodic excitations. These theoretical findings are validated by a series of experimental tests.

2.1 System Modeling

The configuration of the system of coupled oscillators is depicted in Fig.2.1. It is composed of a grounded weakly damped linear oscillator coupled to a lightweight attachment through a linear weak viscous damper and an essentially nonlinear spring of the third order (i.e., possessing cubic nonlinearity and no linear stiffness component). Geometric and kinematic nonlinearities in this system are realized due to transverse deformations of the linear springs with constants k_3 relative to the direction of oscillation of the attachment. An excitation $f(t)$ is applied to the linear oscillator at $t = 0$ with the system at rest.

The equations of motion of the system shown in Fig.2.1 are expressed in

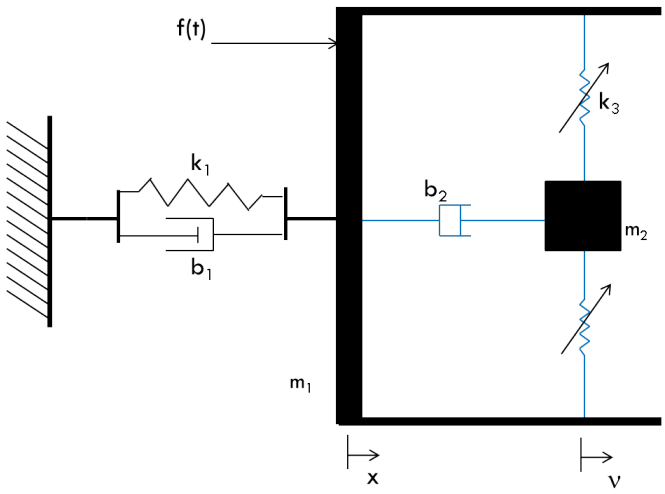

Figure 2.1: Configuration of the two degree-of-freedom coupled oscillator with essential geometric nonlinearity.

normalized form as follows,

$$\ddot{x} + \lambda_1 \dot{x} + \lambda_2(\dot{x} - \dot{v}) + \omega_0^2 x + C(x - v)^3 = F(t) \tag{2.1a}$$

$$\varepsilon \ddot{v} + \lambda_2(\dot{v} - \dot{x}) + C(v - x)^3 = 0 \tag{2.1b}$$

where x denotes the response of the linear oscillator, v the response of the nonlinear oscillator, and the $\dot{(\cdot)} \equiv d/dt$, or differentiation with respect to the time variable t. The normalized parameters are defined as $\omega_0 = (k_1/m_1)^{(1/2)}$, $C = k_3/m_1$, $\lambda_1 = b_1/m_1$, $\lambda_2 = b_2/m_1$, $\varepsilon = m_2/m_1$, and $F(t) = f(t)/m_1$, where the physical parameters are presented in Fig.2.1. By considering the small mass parameter $0 < \varepsilon \ll 1$, the lightweightness of the nonlinear attachment compared to the directly excited linear oscillator is denoted. This work considers impulsive forcing excitation in the form of single or repetitive impulses.

The first excitation scenario of a single impulse was presented in Section 1.2, and it was shown both theoretically and experimentally that the corresponding damped transition approximately tracks the lower frequency branch of the *impulsive orbit manifold (IOM)* of the underlying Hamiltonian system (that is, system (2.1) with the damping constants set equal to zero). This work will generalize these results by showing high-frequency IOM tracking by the damped dynamics of system (2.1). In turn, these high-frequency dy-

namics will be manifested as dynamic instability of the coupled system in the form of relatively high-amplitude and high-frequency oscillations of the (indirectly forced) nonlinear attachment. Moreover, in the single impulse excitation scenario it is assumed that system (2.1) is initially at rest at $t = 0-$, and a single impulse equal to $F(t) = I_0\delta(t)$ is applied to the linear oscillator at $t = 0+$. Hence, the equations of motion (2.1) are complemented by the initial conditions

$$\begin{aligned} x(0+) &= 0, \qquad \dot{x}(0+) = I_0, \\ v(0+) &= 0, \qquad \dot{v}(0+) = 0 \end{aligned} \tag{2.2}$$

In the second excitation scenario the linear oscillator is excited by a periodic series of identical impulses. For the first impulse, it is assumed again that at $t = 0-$ the system is initially at rest, so immediately after the initial impulse is applied the initial conditions are given by (2.2). This case defines the impulsive period t_p as the inter arrival time between consecutive impulses, and the normalized impulsive period as the multiple μ_T of the fundamental period $T_0 = 2\pi/\omega_0$ of the linear oscillator between consecutive impulses, $\mu_T = t_p/T_0$. For example, a normalized impulsive period of 5 would define a periodic forcing scheme in which an impulse of magnitude I_0 is applied to the linear oscillator every 5 fundamental periods. In mathematical form the periodic series of impulses is defined as

$$F(t, \mu_T, I_0) = \sum_{p=0}^{N} I_0\delta(t - pt_p) \tag{2.3}$$

where N denotes the total number of applied impulses in the given computation or experiment. In this scheme, the p^{th} impulse applied to the linear oscillator at $t = pt_p+, p \geq 1$, corresponds to the initial conditions for system (2.1) immediately after the application of the p^{th} impulse,

$$\begin{aligned} &x(pt_p+) = x(pt_p-), \qquad \dot{x}(pt_p+) = \dot{x}(pt_p-) + I_0, \\ &v(pt_p+) = v(pt_p-), \qquad \dot{v}(pt_p+) = \dot{v}(pt_p-), \\ &p = 1, ..., N \end{aligned} \tag{2.4}$$

Hence, the initial state of the system will differ for each consecutive impulse,

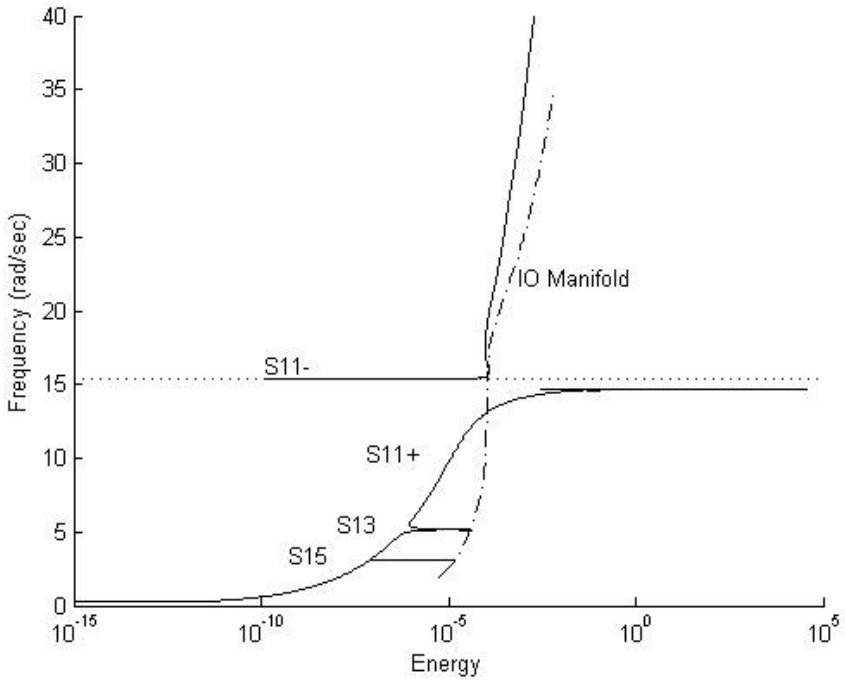

Figure 2.2: Frequency-energy plot of the underlying Hamiltonian system (2.1) with parameters outlined in Table 2.1.

depending on the remaining vibration energy in the two coupled oscillators at the time of application of the p^{th} impulse. In (2.4) continuity for all state variables at the time of application of the impulse is imposed, except for the velocity of the linear oscillator which exhibits a discontinuity equal to the intensity of the applied impulse.

Various impact periods and impulse magnitudes are considered to study the occurrence of sustained dynamic instability in this system, manifested as repetitive excitation of high-frequency and relatively high-amplitude oscillations of the (indirectly forced) lightweight attachment in the neighborhood of a high-frequency part of the IOM of the underlying Hamiltonian system. Since the dynamics of the corresponding undamped system (2.1) plays an important role in exciting sustained dynamic instability in this system, the next section is devoted to a brief overview of the underlying Hamiltonian dynamics and discusses the IOM of this system.

2.1.1 Underlying Hamiltonian Dynamics

Before studying the dynamics of system (2.1), the underlying Hamiltonian system corresponding to $\lambda_1 = \lambda_2 = F(t) = 0$ is considered by depicting its dynamics in a *frequency energy plot FEP* [4, 2]. This plot depicts branches of periodic and quasi-periodic orbits at varying energy levels. In particular, the dominant frequency of each orbit is plotted as a function of the (conserved) energy. The Hamiltonian FEP will be used as a framework to study the forced dynamics of the weakly damped system (2.1) since, depending on the applied initial energy, the weakly damped dynamics will transition between different branches of the FEP; this will be shown by computing the wavelet transform spectra of the damped responses and superimposing these spectra on the Hamiltonian FEP. The wavelet transform will be applied to analyze a time series of a given transient response to obtain frequency transitions as wavelet spectra. The wavelet transform involves a windowing technique with variable-sized regions, in which small time intervals are considered for high-frequency components and, conversely, larger time intervals are considered for lower frequency components. This provides a valuable dynamic time-frequency analysis tool, which is more beneficial compared to stationary signal analysis provided by the Fast Fourier Transform in the sense that it reveals the temporal evolutions of the dominant frequency components of a given damped transition as energy decreases due to damping dissipation. Depending on the level of damping and the initial state of the system this damped transition will be shown to visit and make transitions between different branches of the FEP with decreasing energy.

In Fig.2.2 the FEP of the underlying Hamiltonian system (2.1) for parameters $\varepsilon = 8.814 \times 10^{-2}$, $\omega_0 = 15.367 rad/s$, and $C = 4.315 \times 10^6 N/(kg \cdot m^3)$ is presented; these parameters correspond approximately (with the exception of the exponent of the essential stiffness nonlinearity as discussed below) to the experimental system that will be considered in a following Section with un-normalized parameters $m_1 = 1.9853kg$, $m_2 = 0.175kg$, $k_1 = 469N/m$, $k_3 = 8.568 \times 10^6 N/m^3$. Two global backbone branches of orbits are presented which are defined over broad frequency and energy ranges, namely branches $S11\pm$ corresponding to in-phase and out-of-phase periodic orbits in 1:1 resonance, with both oscillators of the system vibrating with identical frequencies. Two of the countable infinity of local subharmonic tongues

are also depicted, namely branches $S13$ and $S15$ corresponding to 1:3 and 1:5 resonances, respectively, between the linear oscillator and the nonlinear attachment (which oscillates with lower frequency). As discussed in Section 1.2, the countable infinity of periodic orbits lie on pairs of in-phase/out-of-phase subharmonic tongues (such as the depicted branches $S13$ and $S15$), which are defined over finite energy ranges and are connected to the backbone branches (in fact each of these subharmonic tongues represents mode mixing between the in-phase and out-of-phase modes of the system).

Of particular interest to this study will be the *impulsive orbit manifold IOM* of the Hamiltonian system. The IOM consists of a countable infinity of periodic orbits and an uncountable infinity of quasi-periodic orbits of the Hamiltonian system corresponding to initial impulsive excitation of the linear oscillator and all other initial conditions zero; i.e., $\dot{x}(0+) = I_0, x(0+) = v(0+) = \dot{v}(0+) = 0$. In Section 1.2 it was shown analytically and experimentally that damped transition in the neighborhood of the low-frequency portion of the IOM imply sustained nonlinear resonance scattering on that manifold. It was predicted that damping plays a critical role in exciting this type of damped transition (i.e., "tracking" the IOM); specifically, light damping allows for slow variation of energy in the system, leading to sustained resonance scattering away from basins of attraction to resonance captures. Indeed, increased damping causes the breakdown of resonance scattering, which results in immediate resonance capture. As shown in the next Section, under single or repetitive impulsive excitation of the linear oscillator in the damped system (2.1), the resulting dynamical transitions in neighborhoods of the high-frequency portion of the IOM will be responsible for sustained instability of the dynamics, appearing as multi-frequency, high-amplitude oscillations of the nonlinear attachment.

The superposition of the wavelet spectrum of a specific damped transient response on the Hamiltonian FEP of Fig.2.2 provides valuable qualitative and quantitative information regarding the frequency content of the damped dynamics. Although such FEP-wavelet superpositions are purely phenomenological, one needs to consider that the dynamic effects of weak viscous damping are purely parasitic; i.e., they do not introduce any new dynamics in the system compared to the underlying Hamiltonian one. Hence, the FEP depictions of the wavelet spectra of the damped transitions provide information on the branches of solutions of the underlying Hamiltonian

system that are "visited" in a given damped transition; the actual transitions between branches are then dictated by the level and distribution of damping within the system. For more information of the use of the FEP to study transient nonlinear dynamics the reader is referred to Section 1.2 and references therein. To construct the FEP depictions in the results of the following sections one applies the following sequence of computations: (i) for a given impulse (or series of impulses) applied to the linear oscillator, one computes the numerical wavelet spectrum of the responses of the system; (ii) at any given time one computes the total (continuously decreasing) instantaneous energy of the system following the application of the impulse; (iii) by plotting the frequency responses obtained by the wavelet spectra versus the corresponding instantaneous energy (i.e., eliminating the time variable) one obtains a frequency energy depiction of the damped transition which can be superimposed to the Hamiltonian FEP in order to study the nonlinear dynamic transitions that occur in the dynamics.

2.2 Computational Study

This section initiates the study of the damped dynamics of system (2.1) by performing numerical simulations for single and repetitive impulse excitations, and study the resulting high-frequency dynamical instabilities by wavelet analysis and superpositions of wavelet spectra on the FEP of Fig.2.2. The two impulse excitation scenarios are considered separately.

2.2.1 Single Impulse

The computational study of the damped dynamics of (2.1) is initiated by considering single impulse excitation and studying the resulting damped transitions by superimposing their wavelet spectra on the FEP of the underlying Hamiltonian system. Although this type of superposition is purely phenomenological, it will help one interpret the damped response in terms of resonance captures or resonance scattering in the branches of the FEP visited during that specific response. The system parameters for the model of Fig.2.1 were selected as shown in Table 2.1, which correspond to the normalized parameters for the theoretical model (2.1) shown in Table 2.2. These parame-

Table 2.1: Physical system parameters for the model of Fig.2.1

Parameter	Value
m_1	$1.985kg$
m_2	$0.175kg$
k_1	$469N/m$
k_3	$25.068 \times 10^6 N/m^3$
b_1	$0.0726Ns/m$
b_2	$0.0030Ns/m$

Table 2.2: Normalized parameters for the model of Fig.2.1

Parameter	Value
ε	8.814×10^{-2}
ω_0	$15.367rad/s$
C	$12.627 \times 10^6 N/kg \cdot m^3$
λ_1	$0.0366Ns/kg \cdot m$
λ_2	$0.0015Ns/kg \cdot m$

ters differ from the experimentally identified parameters for the experimental model discussed in Section 2.3, the reason being that no linear component complementing the nonlinear stiffness was considered so that the nonlinear coefficient k_3 had to be adjusted to account for its purely (essentially) nonlinear nature. In addition, purely cubic stiffness nonlinearity was assumed in this theoretical model, in contrast to the experimentally estimated nonlinear exponent of 2.95 as discussed in Section 2.3. All frequency-energy Hamiltonian plots utilized in this section were computed using the previous adjusted system parameters.

Here, note that in the theoretical model above, there is a large reduction of the mass ratio ε compared to the system considered in Section 1.2 with mass ratio $\varepsilon = 0.4046$; as shown below this reduction of the mass of the nonlinear attachment has a drastic effect on the damped dynamics, and in particular its frequency content. Whereas in Section 1.2 it was shown that the dynamics can track the lower frequency portion of the IOM, in the present case with the much lighter nonlinear attachment the dynamics will be shown to track the higher frequency portion of the IOM resulting in high-frequency dynamic

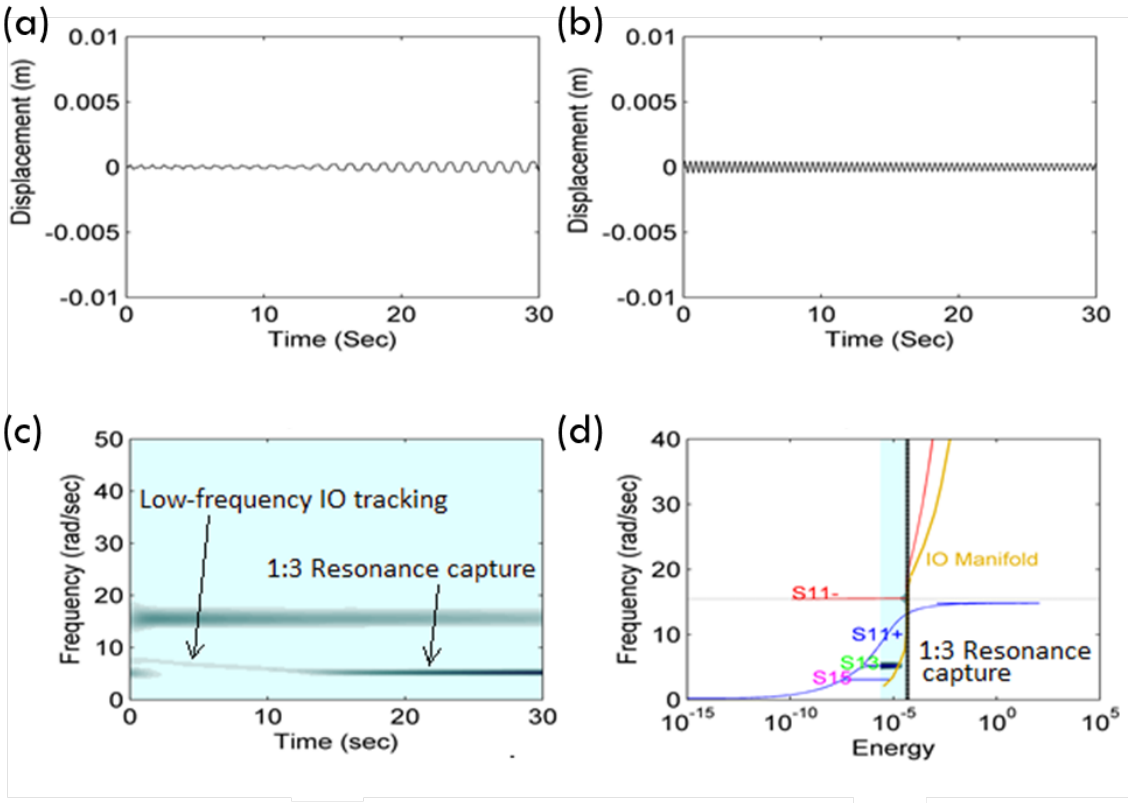

Figure 2.3: Damped response of the theoretical model for single impulse excitation of normalized intensity $I_0 = 0.007m/s$: (a) Displacement of the nonlinear attachment, (b) displacement of the linear oscillator, (c) wavelet spectrum of the relative displacement, (d) wavelet spectrum of (c) superimposed on the Hamiltonian FEP.

instability of the system.

The theoretical model (2.1) was numerically integrated with initial conditions (2.2) for a range of applied impulses in order to study the effect of the energy input on the damped dynamics. Fig.2.3 depicts the response of the theoretical model subject to a single impulse of relatively small intensity $I_0 = 0.007m/s$. Although the responses of the linear oscillator and the nonlinear attachment are small, interesting resonance captures in the damped dynamics are observed when considering the wavelet spectrum of the relative response $x - v$ (cf. Fig.2.3c) and superimposing it on the FEP of the underlying Hamiltonian system (cf. Fig.2.3d). It is deduced that the dynamics initially engage in resonance capture in the vicinity of the $S11-$ out-of-phase backbone branch before transitioning to the lower frequency $S13$ subharmonic tongue which results in gradually increasing (albeit small) am-

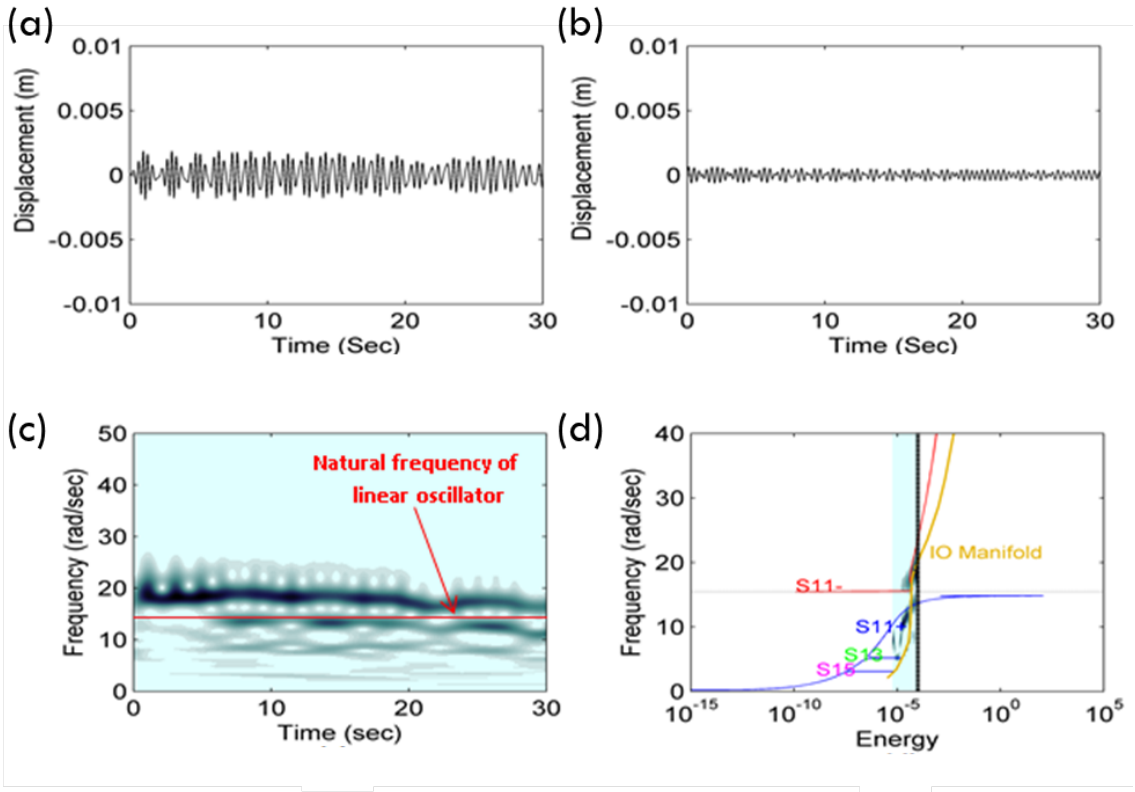

Figure 2.4: Damped response of the theoretical model for single impulse excitation of normalized intensity $I_0 = 0.010m/s$: (a) Displacement of the nonlinear attachment, (b) displacement of the linear oscillator, (c) wavelet spectrum of the relative displacement, (d) wavelet spectrum of (c) superimposed on the Hamiltonian FEP.

plitude of oscillation of the nonlinear attachment. This type of low-frequency damped transition is typical of transitions reported in previous work [2] and the corresponding dynamic instabilities reported therein. In this case the initial energy input into the system provided by the impulse is too low to cause high-frequency transient dynamic instability associated with tracking of the high-frequency portion of the IOM.

The response of the system for normalized impulse intensity of $I_0 = 0.01m/s$ is shown in Fig.2.4. It is clear that a small increase in input energy results in qualitatively different dynamic response. In particular, in the initial highly energetic regime the response of the nonlinear attachment occurs in the neighborhood of the intersection between the out-of-phase backbone branch $S11-$ and the high-frequency portion of the IOM; this is deduced by the strong high-frequency harmonics in the initial part of the wavelet

spectrum of the damped relative response of Fig.2.4c. In the later part of the damped responses, broadband beat phenomena (appearing as pulsations) in the wavelet spectrum of Fig.2.4c are noted; these nonlinear beats result due to the existence of closely spaced resonance captures as the IOM approaches the out-of-phase $S11-$ branch [6]. These phenomena result in high-frequency dynamical instability in the damped response, which manifests itself in the form of strongly modulated damped responses of both the linear oscillator and (especially) the nonlinear attachment. It is important to note again that this dynamic instability arises from the presence of the essential stiffness nonlinearity and weak viscous damping in the coupling, since it cannot be realized in linear or weakly nonlinear settings. Moreover, this is the first report of high-frequency dynamical instability by tracking of the high-frequency portion of the IOM. In Section 1.2, similar dynamical instability was reported but this was associated exclusively with low-frequency IOM tracking; in that section no high-frequency IOM tracking could be realized due to the relatively large value of the normalized mass ratio (which was close to 40% compared to the 8% value used in this section).

The response of the system for the relatively high impulse intensity $I_0 = 0.07m/s$ is shown in Fig.2.5. In this case the high-frequency IOM tracking is more clearly visible, confirming the occurrence of high-frequency dynamic instability in this system. The high-frequency IOM tracking is evident when one considers the slowly varying strong high-frequency harmonic in the relative response of the wavelet spectrum of Fig.2.5c. Moreover, as seen from the wavelet spectrum superposition of Fig.2.5d, the response of the nonlinear attachment starts tracking the high-frequency portion of the IOM right from the start of the damped dynamics, with continuously decreasing frequency and energy for the duration of the simulation. This sustained high-frequency resonance scattering results in large-amplitude and strongly modulated oscillations of the nonlinear attachment, and hence, to strong transient dynamic instability of the damped response.

2.2.2 Repeated Impulses

In the next step of the computational study, the repetitive impulse excitation scenario is considered, whereby the linear oscillator is forced by a periodic

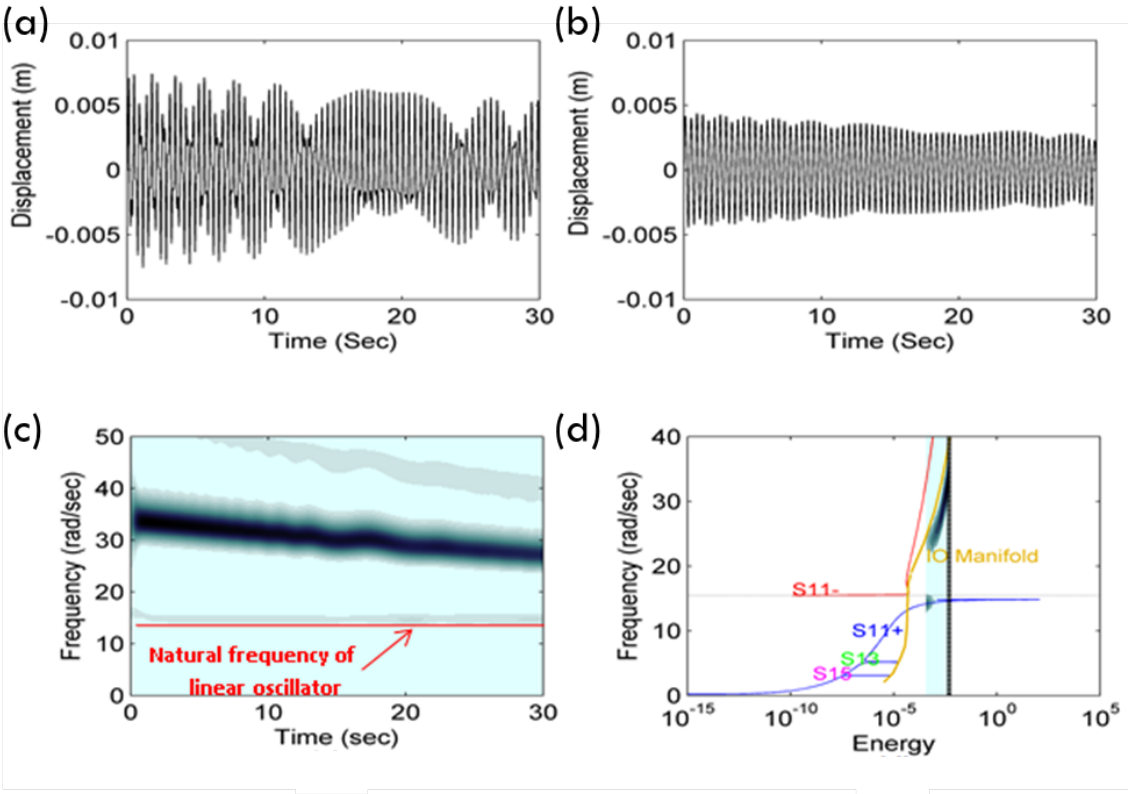

Figure 2.5: Damped response of the theoretical model for single impulse excitation of normalized intensity $I_0 = 0.070m/s$: (a) Displacement of the nonlinear attachment, (b) displacement of the linear oscillator, (c) wavelet spectrum of the relative displacement, (d) wavelet spectrum of (c) superimposed on the Hamiltonian FEP.

series of identical impulses with the system being initially at rest, as outlined by the conditions (2.2) and (2.4). The principal aim of the study is to demonstrate that it is possible to consistently bring the nonlinear attachment into a state of dynamic instability by repeatedly tracking the high-frequency portion of the IOM as in the previous case of single impulse excitation. For consistency, the system parameters for the following computational study remain the same as in the previous single impulse excitation scenario. The damped responses of system (2.1) subject to the initial conditions (2.2) and intermediate conditions (2.4) were considered for a range of applied normalized impulse intensities I_0 applied at time instants $t = pt_p, p = 0, 1, 2, ...$ Following each applied impulse the initial conditions and the energy of the system were considered, and the resulting damped transitions were studied by superimposing their wavelet spectra on the Hamiltonian frequency-energy plot (as in the previous case of single impulse excitation).

Fig.2.6 presents the damped response of the system for 10 applied impulses of normalized intensity $I_0 = 0.010m/s$ and normalized period $\mu_T = t_p/T_0 = 25$ (i.e., the period of the applied periodic impulse excitation was 25 that of the natural period of oscillation of the linear oscillator). Here note that, similar to the previous case, the response of the (unexcited) nonlinear attachment is larger than the response of the (directly excited) linear oscillator, indicating repetitive excitation of dynamic instability in this case. Moreover, the onset of dynamic instability after application of each impulse occurs for non-zero initial conditions of the system (in contrast to the single impulse excitation scenario), providing a first indication of robustness of the dynamic instability mechanism.

To study the damped dynamics of the system and demonstrate the excitation of high-frequency dynamic instability after the application of the initial impulses, Fig.2.7-Fig.2.9 present a detailed assessment of the dynamics following each of the first three impulses of Fig.2.6. The level of normalized impulse intensity is chosen so that the initial energy level in the system is the same as the initial energy level of the simulation of Fig.2.4, where high-frequency dynamic instability in the response of the nonlinear attachment resulted from tracking by the damped dynamics of the high-frequency portion of the IOM. The normalized impulsive period $\mu_T = 25 cycles$ was chosen according to the forcing scheme that was physically realizable in the experimental realization of the repetitive impulse scenario as discussed in the

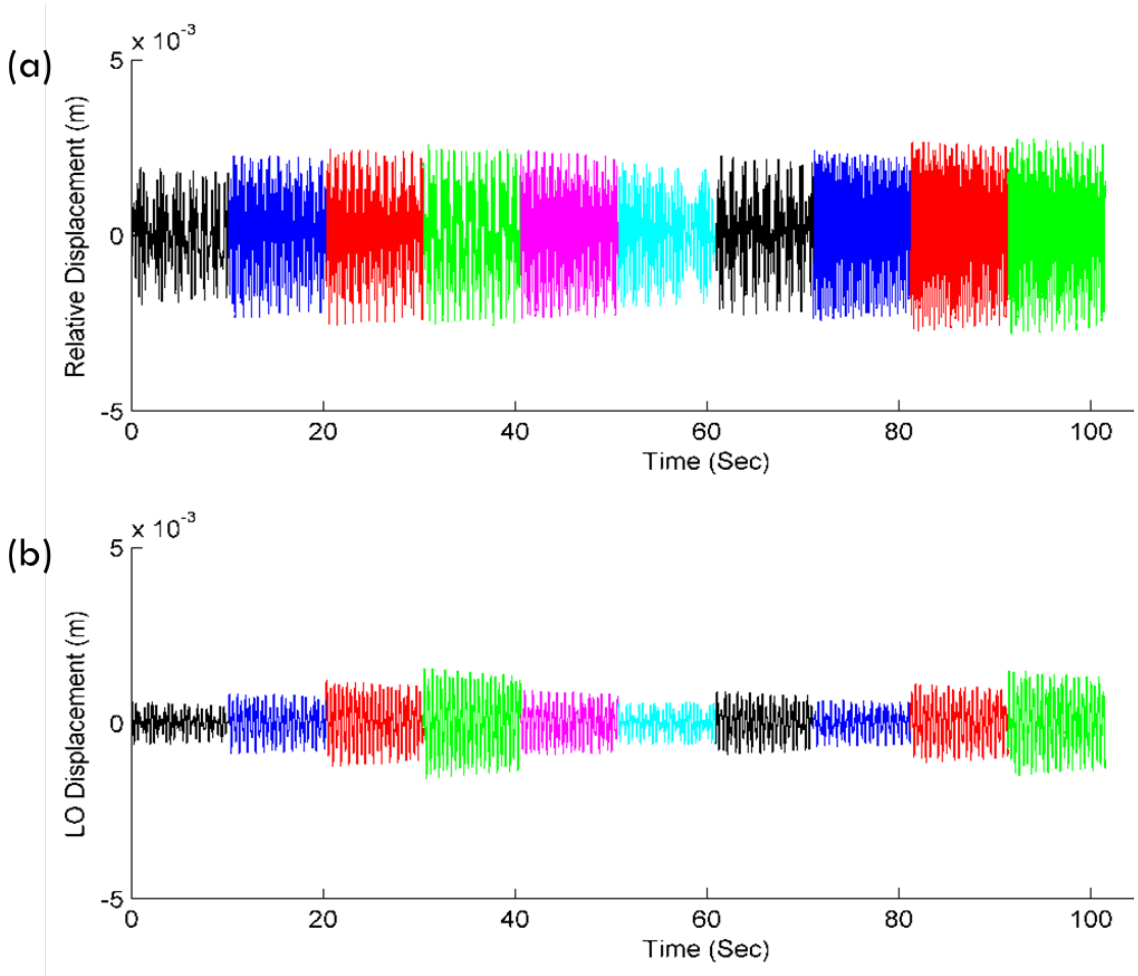

Figure 2.6: Damped response of the theoretical model for periodic impulse excitation of normalized intensity $I_0 = 0.010m/s$: (a) Relative displacement between the nonlinear attachment and the linear oscillator, and (b) displacement of the linear oscillator for 10 applied impulses.

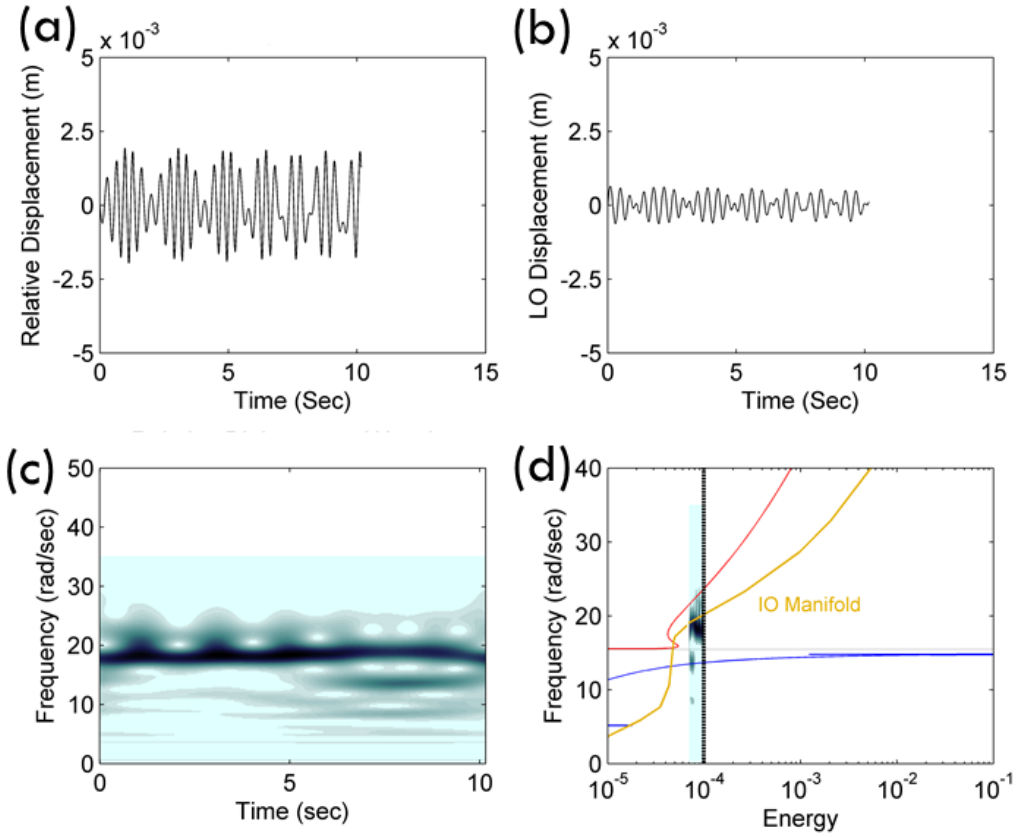

Figure 2.7: First cycle of the damped response of Fig.2.6, following the first impulse: (a) Relative displacement between nonlinear attachment and the linear oscillator, (b) displacement of linear oscillator, (c) wavelet spectrum of relative displacement, (d) wavelet spectrum of (c) on the Hamiltonian FEP.

following Section 2.3.

As seen in the relative displacement time series in Fig.2.6, large amplitude oscillations are maintained for the duration of the simulation and for each of the impulses. Considering in detail the first cycle of the response presented in Fig.2.7, the wavelet spectrum superposition on the FEP indicates that the instantaneous frequency of the nonlinear attachment is fluctuating between several of the superharmonic resonance branches existing in the neighborhood of the IOM (which are not depicted in the FEP for this system). The relative displacement time series indicates that this is a pulsing (beating) phenomenon attributed to *superharmonic resonance captures* RC, similar to that depicted in Fig.2.4. Recall at this point that that damped transitions in

the neighborhood of the high-frequency portion of the IOM are characterized by continuously decreasing frequency and energy in the wavelet spectrum of the corresponding time series which, clearly, is not the trend in the response of the first cycle of Fig.2.7. However, considering in detail the following cycle depicted in Fig.2.8, the wavelet spectra superposition on the FEP indicate that the damped response of the relative response of the nonlinear attachment is now tracking the high-frequency portion of the IOM for the entire duration of the second cycle (i.e., the response of the system between the second and the third impulses). This state of *sustained resonance scattering SRS* results in relatively high energy transfer from the linear oscillator to the nonlinear attachment, as depicted by the high amplitude oscillations in the relative displacement time series and the resulting high-frequency dynamic instability.

In addition, examining in detail the third cycle of the damped response depicted in Fig.2.9, it is deduced that the wavelet spectrum of the relative response between the nonlinear attachment and the linear oscillator tracks again the high-frequency portion of the IOM for the entire duration of this cycle. In fact, the response of the system during the third cycle is similar to the response during the second cycle, despite the different initial conditions of the system at the start of each cycle (refer to Fig.2.10 below). This indicates that the described high-frequency instability can be robustly excited even for varying initial conditions of the system at the beginning of each cycle following repetitive impulse excitation.

The robustness of the excitation of high-frequency dynamic instability in this case is further confirmed by the results reported in Table 2.3 where a summary of the analysis of the dynamic responses for all ten cycles of the damped response of Fig.2.6 is provided. Two different types of damped dynamics can be realized in this case, namely *superharmonic resonance capture RC* (similar to the response of the first cycle in Fig.2.7), and *sustained resonance scattering SRS* (similar to the responses of the second and the third cycles in Fig.2.8 and Fig.2.9, respectively); eight of the ten impulsive cycles correspond to high-frequency dynamic instability of the response of the nonlinear attachment, tracking the high-frequency IOM. More specifically, as seen in the relative displacement time series of Fig.2.6, impulsive responses of the first and seventh cycles exhibit similar qualitative features, exhibiting the superharmonic frequency fluctuations. It is interesting to note that

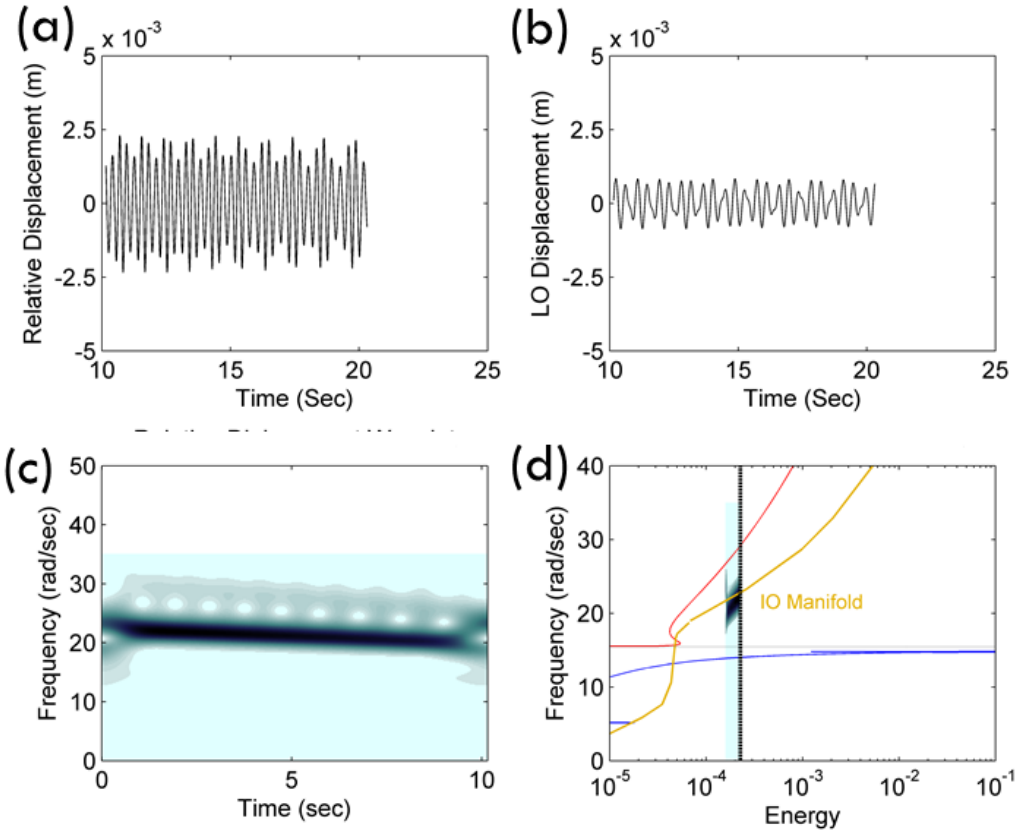

Figure 2.8: Second cycle of the damped response of Fig.2.6, following the first impulse: (a) Relative displacement between nonlinear attachment and the linear oscillator, (b) displacement of linear oscillator, (c) wavelet spectrum of relative displacement, (d) wavelet spectrum of (c) on the Hamiltonian FEP.

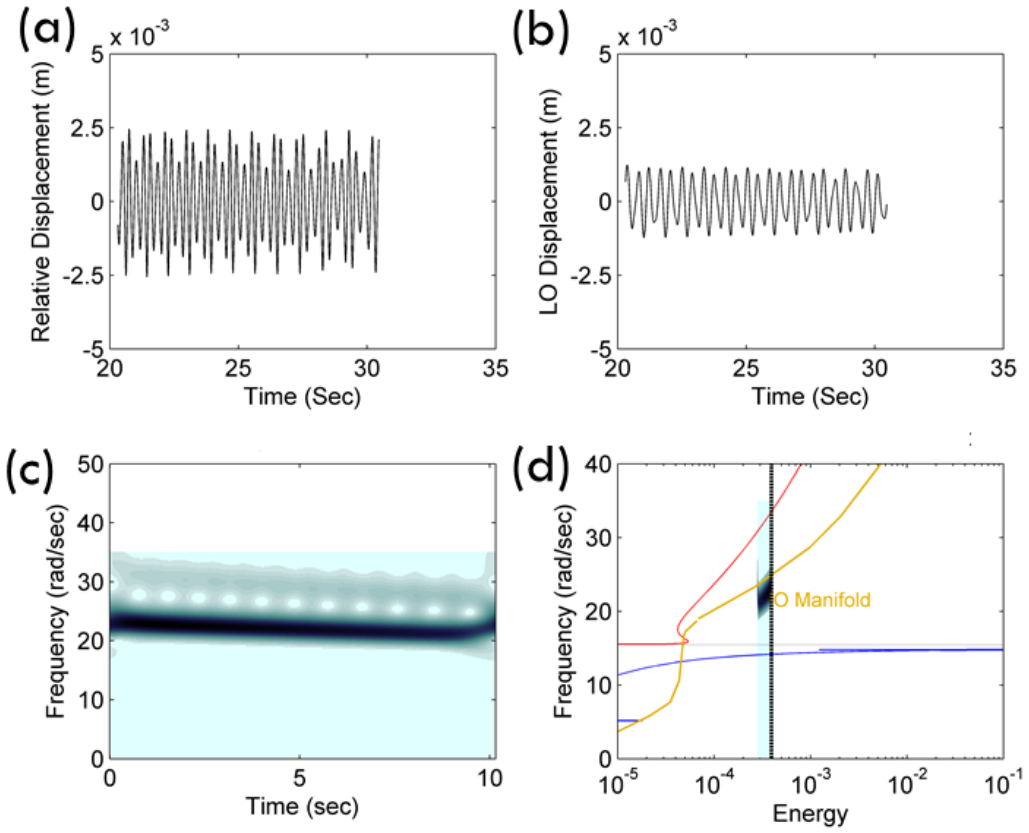

Figure 2.9: Third cycle of the damped response of Fig.2.6, following the first impulse: (a) Relative displacement between nonlinear attachment and the linear oscillator, (b) displacement of linear oscillator, (c) wavelet spectrum of relative displacement, (d) wavelet spectrum of (c) on the Hamiltonian FEP.

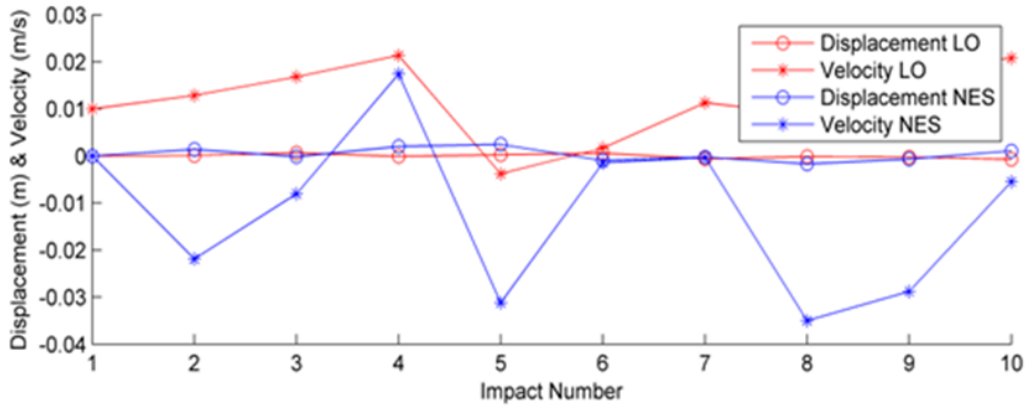

Figure 2.10: Initial conditions of the linear oscillator and the nonlinear attachment at the beginning of each of the ten impulsive cycles of the damped response depicted in Fig.2.6.

Table 2.3: Summary of resonance captures for the repeated impulse excitation scenario with $I_0 = 0.010 m/s$ and $\mu_T = 25 cycles$.

Impulse number	Type of dynamic response
1	Superharmonic RC
2	SRS
3	SRS
4	SRS
5	SRS
6	SRS (primarily)
7	Superharmonic RC
8	SRS
9	SRS
10	SRS

the dynamics during the sixth impulsive cycle escapes SRS near the end of the cycle; this might explain why the dynamics in the seventh cycle exhibits superharmonic resonance capture. However, following this, the dynamics of the eighth cycle returns to a state of SRS, and the high-frequency dynamic instability is excited again. This repeated excitation of SRS occurs despite the different initial conditions of the system at the beginning of each cycle following an impulse excitation as depicted in Fig.2.10. An interesting observation is that SRS (and high-frequency dynamic instability) appears to occur for impulsive cycles where the nonlinear attachment has initial velocity magnitude greater than a certain threshold; i.e., $|\dot{v}(pT+)| > 0.005m/s$.

2.3 Experimental Study

Motivated by the previous numerical results and the theoretically predicted robust excitation of high-frequency dynamic instability of the system under single and repeated impulsive forcing, an experimental study was undertaken in order to confirm the theoretical predictions. The experimental apparatus was derived from components used in Section 1.2. The results of this study are discussed in this section.

2.3.1 Single Impulse

The experimental fixture is presented in two configurations for the excitation scenarios considered. The configuration of Fig.2.11 is used for single impulse conditions. The experimental system consists of two masses that oscillate along an air track, which greatly reduces damping due to friction. The more massive linear oscillator is grounded through a linear leaf spring, while the lighter nonlinear attachment is coupled to the linear oscillator using a piano wire of diameter equal to $0.5mm$. The strong stiffness nonlinearity required for the realization of the high-frequency dynamic instability is implemented by means of the piano wire oriented to be perpendicular to the direction of the motion of the attachment; when this wire has no pretension, its transverse deformation gives rise to essential stiffness nonlinearity whose dominant component is third order (i.e., pure cubic nonlinearity). Although the piano wire is mounted so that there is no pretension in the wire in order

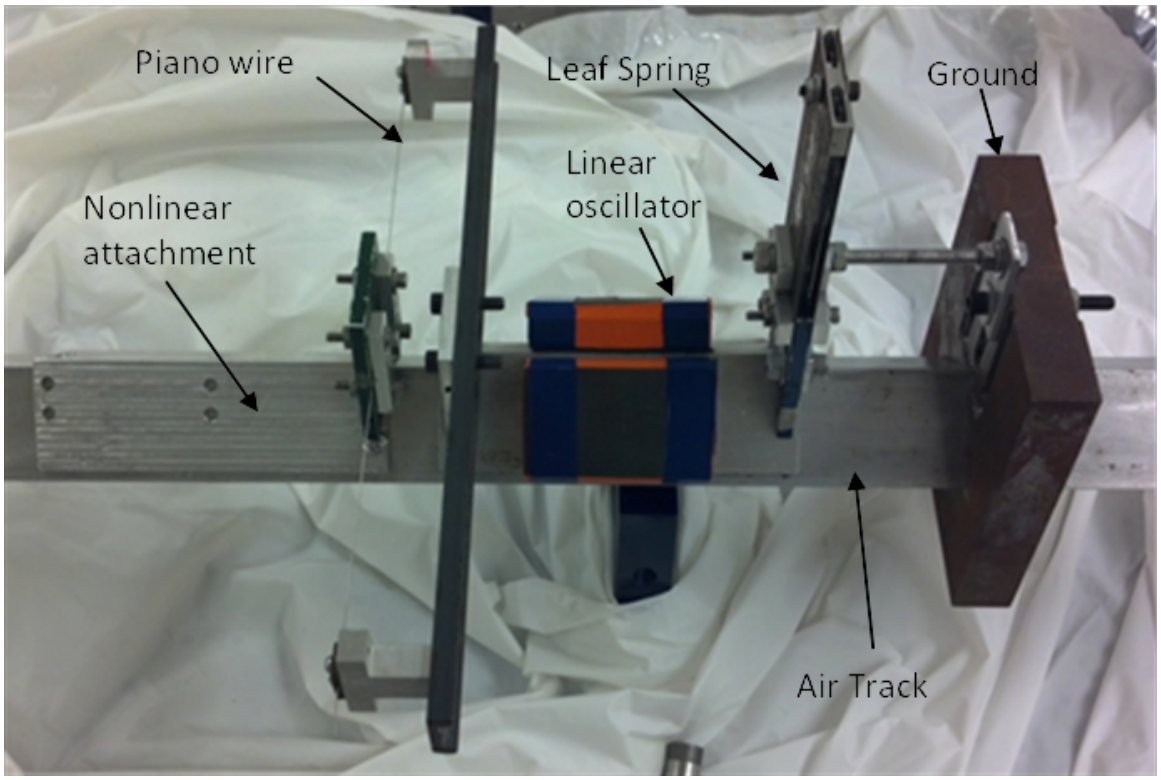

Figure 2.11: Experimental realization of the system (2.1) of Fig.2.1 utilized for single impulse excitation conditions (2.2).

Table 2.4: Experimentally identified system parameters for the fixture presented in Fig.2.11.

Parameter	Value
m_1	$1.985kg$
m_2	$0.175kg$
k_1	$469N/m$
k_3	$25.068 \times 10^6 N/m^3$
α	2.95
k_{lin}	$80.0N/m$
b_1	$0.0726Ns/m$
b_2	$0.0200Ns/m$

to minimize any linear component in the coupling stiffness of the nonlinear attachment, a small linear term nevertheless occurs as discussed below; however, as pointed out in Section 1.2, this small linear term is not expected to affect the strongly nonlinear dynamical phenomena that need to be validated by the experimental study. Moreover, an additional small linear term in the coupling stiffness is inevitable due to the force that the air track imparts on the nonlinear attachment. The air track pressure is set to a near minimum value of $50psi$ to support the weight of the linear oscillator, and this pressure adds an artificial linear component to the coupling stiffness due to the lightweight nature of the nonlinear attachment.

Single impulsive forces are applied to the linear oscillator by means of an impact hammer, whereas periodic impulsive forces are applied by means of a long-stroke shaker. The parameter values of the experimental system were identified by performing linear modal analysis (for the parameters of the linear oscillator) and nonlinear system identification utilizing the restoring force surface method [41, 42] (for the nonlinear attachment). The system parameters were identified as shown in Table 2.4. Note that the experimentally identified exponent of the essential stiffness nonlinearity is $\alpha = 2.95$ which, although close, is not exactly equal to the theoretically assumed cubic nonlinearity used in the theoretical study of the previous Section. Moreover, in the experimental system a small but non-negligible linear stiffness component for the nonlinear (coupling) stiffness of the attachment equal to $k_{lin} = 80N/m$ is identified, which again is contrary to the assumption of pure non-linearizable

stiffness nonlinearity of the attachment in the theoretical model of the previous Section. As discussed in [12], however, this small linear component is not expected to affect the dynamics in a significant way. It is noteworthy that damping in the experimental system is rather weak; the numerical study confirms the assumption that weak viscous damping is essential for obtaining the high-frequency dynamical instability, so the experimental model satisfies this requirement. It is important to note that some uncertainty existed in the identified system parameters due to the effect of the air track pressure on the carts, unmodeled friction effects in the system, and occasional contact of the carts with the air track. All Hamiltonian frequency-energy plots depicted in this section are identical to the one depicted in Fig.2.2; i.e., they are based on the above experimentally identified system parameters but for the exponent of the nonlinearity which was adjusted to 3 (i.e., exact cubic nonlinearity was assumed instead of the experimental exponent value of 2.95), and the linear component of the stiffness nonlinearity which was omitted (i.e., it was assumed to be $k_{lin} = 0$). This provides a measure of consistency in the interpretation of the experimental responses when their wavelet spectra are depicted in the underlying Hamiltonian FEP.

As in the computational study of the previous section, first the single impulse excitation scenario is considered. The computational study predicted the impulsive excitation levels that would allow for sustained resonance scattering in the higher frequency portion of the IOM. As stated earlier, for the single impulse excitation a PCB modal hammer was used to apply the excitation to the linear oscillator with the system initially at rest. The velocity time series measurements of the two oscillators were obtained using two Polytec VibraScan laser vibrometers at a sampling frequency of $512Hz$. The data acquisition for the two systems was synchronized using the impact hammer as the triggering mechanism, with a small pre-trigger time of $640ms$. The synchronized response of the oscillator system was very important for the accurate computation of the wavelet spectra of the relative displacement time series and the relative displacement frequency-energy plots, since it eliminated any discrepancy between the measured responses of the linear oscillator and the nonlinear attachment. The raw velocity time series data were then numerically integrated once to obtain the corresponding displacement time series for each of the two oscillating components of the system. The displacement time series data were corrected using a high pass, 4^{th} order

Butterworth filter with a cutoff frequency of $1.28Hz$ to eliminate drift in the data from the signal noise. The instantaneous total system energy during the dynamics could then be computed similarly to the numerical case, followed by numerical computation of the wavelet spectra of the relative displacement time series and superposition of these wavelet spectra on the Hamiltonian FEP, exactly as in the computational study.

The system was forced using a wide range of excitation magnitudes corresponding to situations in which sustained resonance scattering was observed numerically. Exciting a damped transition on the lower frequency portion of the IOM for this system proved to be unobtainable (contrary to Section 1.2 where a heavier nonlinear attachment was used and low-frequency IOM tracking was the only possibility). Following the notation of the previous section, the predicted range for a transition on the lower portion of the IOM (as in the transition of Fig.2.3) was for an initial normalized impulsive intensity range $I_0 = 0.007 - 0.012m/s$. In practical terms, this impulse range was hard to excite using a modal hammer, since physical hammer excitations less than $I_0 = 0.015m/s$ caused very low amplitude oscillations, as predicted by the numerical investigation. However, in the experimental tests these low amplitude oscillations were predominantly linear, indicating that the air track pressure was having a stronger polluting effect on the dynamics of the lightweight nonlinear attachment at these low amplitudes. Therefore the remaining experiments focused on exciting the upper portion of the IOM where the theoretically predicted high-frequency dynamical instability was expected to occur.

The predicted range for a transition on the upper portion of the IOM (as in the transitions of Fig.2.4 and Fig.2.5) was for normalized impulse intensities of $0.014m/s < I_0 < 0.080m/s$. In practical terms this impulsive magnitude range corresponded to an energy range $10^{-4} - 10^{-2}J$ on the FEP depicted in Fig.2.2. In the experimental tests this energy range was robustly excitable with the modal hammer, with the resulting high-amplitude oscillations of the system exhibiting strongly nonlinear characteristics, indicating that the air track had negligible (linear) effect on the dynamics. It is important to note here that the numerically predicted impulse magnitudes did not correspond directly to the required physical impulse magnitudes to obtain transitions in the same energy range. This was because the forcing in the numerical simulation was in the form of a *Dirac Delta function*, while the forcing practically

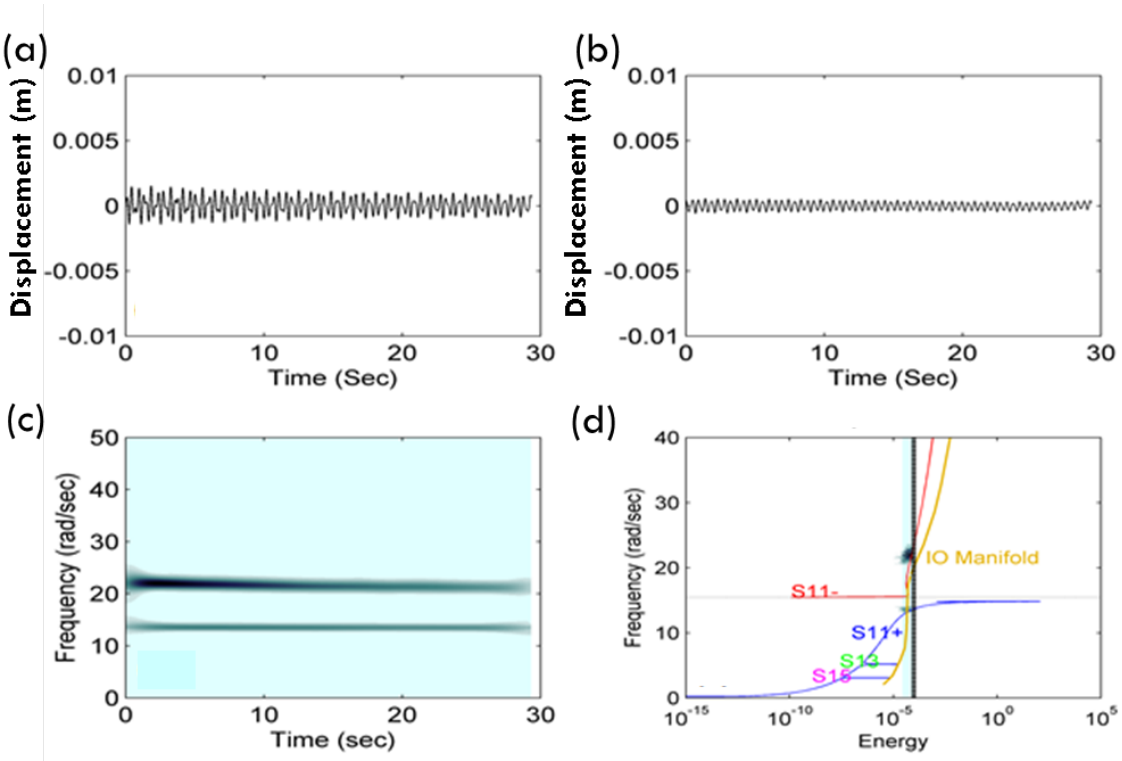

Figure 2.12: Damped experimental response for single impulse excitation of normalized intensity $I_0 = 0.0198m/s$: (a) Displacement of the nonlinear attachment, (b) displacement of the linear oscillator, (c) wavelet spectrum of the relative displacement, (d) wavelet spectrum of (c) superimposed on the Hamiltonian FEP.

realized by the modal hammer was approximately in the form of a half-sine pulse of finite duration. This, however, did not present a problem in the experimental forcing scheme but, rather, provided an important distinction between the numerical simulation and experimental trials.

The experimental response of the system of Fig.2.11 for normalized impulse intensity equal to $I_0 = 0.0198m/s$ is depicted in Fig.2.12. This initial excitation energy input into the linear oscillator achieved by means of the modal hammer is comparable to the energy input depicted in the theoretical response of Fig.2.4. Indeed the responses and the wavelet spectra of the responses of the linear and nonlinear oscillators compare favorably. Similar to the theoretical case of Fig.2.4, the dynamics of the nonlinear attachment occurs in the neighborhood of the intersection between the out-of-phase backbone branch $S11-$ and the high-frequency portion of the IOM for the entire duration of the simulation. That this is indeed the case is verified by

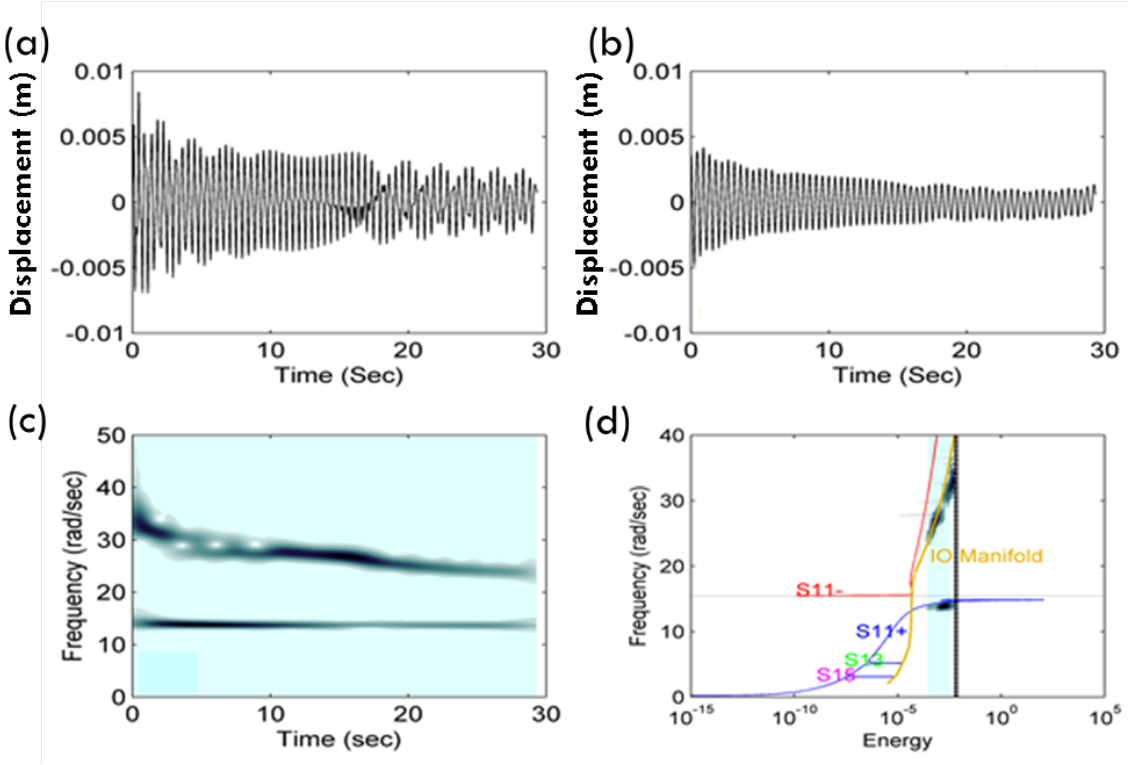

Figure 2.13: Damped experimental response for single impulse excitation of normalized intensity $I_0 = 0.1454m/s$: (a) Displacement of the nonlinear attachment, (b) displacement of the linear oscillator, (c) wavelet spectrum of the relative displacement, (d) wavelet spectrum of (c) superimposed on the Hamiltonian FEP.

the nearly constant wavelet spectrum of the relative response in Fig.2.12c. This result is typical for the experimental setup with initial excitation levels $\sim 10^{-4.3}J$ and below. As stated earlier, damped transitions of the dynamics in the neighborhood of the lower frequency part of the IOM could not be realized experimentally with the current experimental setup.

A different picture of the damped dynamics is obtained for stronger applied impulses. Fig.2.13 depicts the experimental response of the system for a higher normalized impulse intensity equal to $I_0 = 0.1454m/s$. This initial excitation energy input into the linear oscillator by means of the modal hammer is comparable to the energy input in the theoretical computation depicted in Fig.2.5. Similar to the theoretical result, the experimental responses of Fig.2.13 verify the occurrence of high-frequency dynamical instability resulting by tracking the higher frequency portion of the IOM. That this is indeed the case is verified by the slowly (and continuously) decreasing fre-

quency spectrum of the relative response of Fig.2.13c. Hence, the theoretical prediction of high-frequency dynamical instability of Section 2.2.1 is experimentally validated. As seen in the superposition of the wavelet spectrum of the relative response on the Hamiltonian FEP of Fig.2.13d, the nonlinear dynamics starts tracking the high-frequency portion of the IOM right from the beginning of the motion and keeps on tracking the IOM with decreasing frequency and energy (due to damping dissipation). Interesting dynamics then occur at $t = 3s$, when the instantaneous frequency of the relative oscillation starts fluctuating between different resonances in the neighborhood of the upper IOM and the $S11+$ backbone branch. Following this phase of the dynamics, the damped dynamics starts again tracking the upper portion of the IOM at $t = 10s$ and for the remainder of the presented window of experimental measurement. The tracking of the higher frequency portion of the IOM results in high-frequency dynamic instability of the system in the form of bursts in the velocity time series of the nonlinear attachment (see Fig.2.13b).

The experimental study indicates that this state of sustained resonance scattering by tracking the upper portion of the IOM and the ensuing instability in the response of the nonlinear attachment is robust (and fully reproducible) for normalized impulse intensities in the range $10^{-4}J < I_0 < 10^{-2}J$. In fact, high-frequency dynamic instability due to tracking of the upper portion of the IOM was observed in seventeen out of twenty experimental trials performed in the aforementioned energy range, indicating that the reported dynamic instability is robust in the experimental system.

2.3.2 Repeated Impulses

In an additional series of experiments the periodic impulsive excitation scenario (2.3) is considered using the modified experimental fixture of Fig.2.14, which enabled the excitation of the linear oscillator by a periodic series of identical impacts. As seen in Fig.2.14, the core experimental fixture remains the same as the experimental fixture depicted in Fig.2.11 for the single impulse excitation scenario; however, in the present case, the ground for the linear oscillator was shifted to a separately standing structure that surrounds the air track. An APS Dynamics ELECTRO-SEIS Model 400 long-stroke

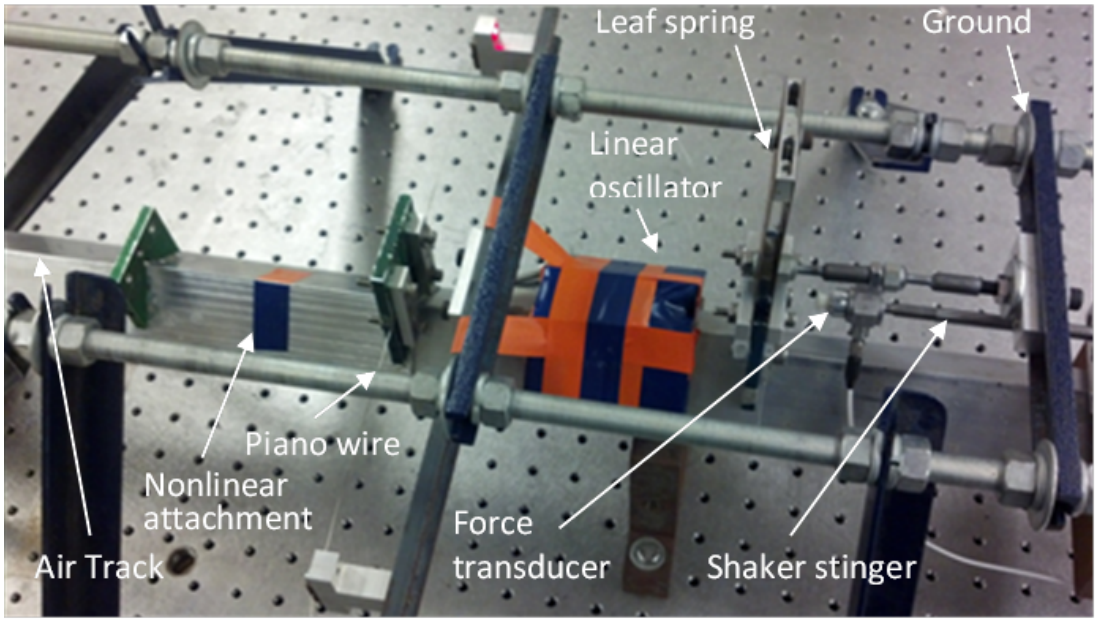

Figure 2.14: Experimental realization of the system (2.1) of Fig.2.1 utilized for repeated impulse excitation conditions (2.4).

electromagnetic shaker was aligned along the axial direction of the air track to the right of the linear oscillator, with respect to Fig.2.14. The shaker stinger was supported by a self-aligning linear ball bearing and aligned with a suitable impact location in line with the vertical and horizontal axial center of mass of the linear oscillator. A PCB force transducer with hard plastic tip (as was the case with the modal hammer) was mounted to the tip of the stinger in order to measure the precise waveform of the impulsive force that was applied during each cycle. Elastic bands within the shaker were adjusted so that the separation between the linear oscillator and stinger tip was held at $0.5in$ prior to the application of each impulse. A positive half square wave of duration less than $25ms$ was input to the shaker controller followed by a negative half square wave of duration $100ms$. The positive square wave applied a fast impulsive force to the linear oscillator similar to the impulse imparted by the modal hammer in the single impulse excitation scenario. The negative square wave quickly retracted the shaker armature and stinger in order to avoid undesirable double impulse excitations to the linear oscillator. The elastic bands then brought the stinger back to the prescribed $0.5in$ separation before the next impulse was applied by the shaker.

This waveform was then applied to the system at the desired impact period and at the desired impulsive magnitude. For the experiments, a period equal to $t_p \sim 10sec$ per impulse was selected so to match the normalized period $\mu_T = 25cycles$ used in the previous computational study for this excitation scenario.

The velocity time series measurements for the two oscillators were obtained using the two Polytec laser vibrometers, but at a higher sampling frequency of $1024Hz$ to obtain more accurate forcing data. Due to sample size restrictions of the Polytec scanning system in use, the duration of the experiment was limited to $\sim 30s$ or three impulse cycles. Moreover, the force transducer at the tip of the striker was used to synchronize (trigger) the data acquisition for the two laser systems, with a small pre-trigger time of $640ms$. The data was processed the same way as for the single impulse experimental trials described above. The data from the force transducer was used to split the entire experimental trial into impulsive cycles, allowing for separate FEP analysis of the transient dynamics of the system at each cycle. As in the case of the single impulse experimental trials, only the cases where damped transitions occurred on the upper branch IOM triggering dynamic instability will be presented here.

As described by conditions (2.4), the two oscillators have a nonzero state of motion before the application of the p^{th} impulse, which differentiates the dynamics from the case of single impulse excitation. It follows that the initial energy in the system is now a function of the displacement and velocity of the two oscillators at the application of each repetitive impulse, rather than just the velocity of the linear oscillator as in the previous case of single impulse. Nevertheless, the computational study of the previous Section predicted that sustained resonance scattering (and, hence, high-frequency dynamic instability in the response of the nonlinear attachment) could be robustly realized in this case, especially if the nonlinear attachment possesses relatively high initial energy at the beginning of each impulsive cycle.

Fig.2.15 depicts the experimental responses for the first three impulsive cycles of the system. The impulse intensities were chosen so that the initial energy levels of the system were in the range $10^{-4} - 10^{-2}J$, in which the previous theoretical study predicted the occurrence of high-frequency dynamic instability resulting from repeated tracking of the higher frequency portion of the IOM. As stated earlier, data was acquired only for three impulsive cycles

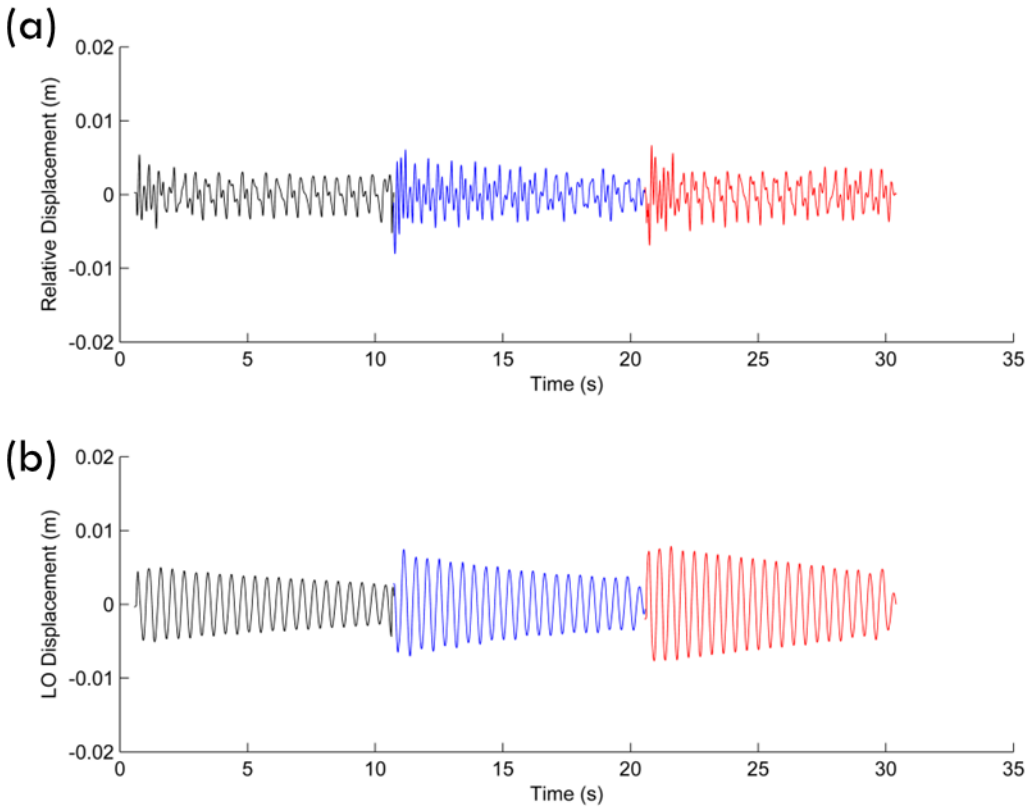

Figure 2.15: Experimental damped response for periodic impulse excitation of normalized intensities $I_0 = 0.2262m/s$ first cycle, $I_0 = 0.3806m/s$ second cycle, and $I_0 = 0.2829m/s$ third cycle: (a) Relative displacement between the nonlinear attachment and the linear oscillator, and (b) displacement of the linear oscillator.

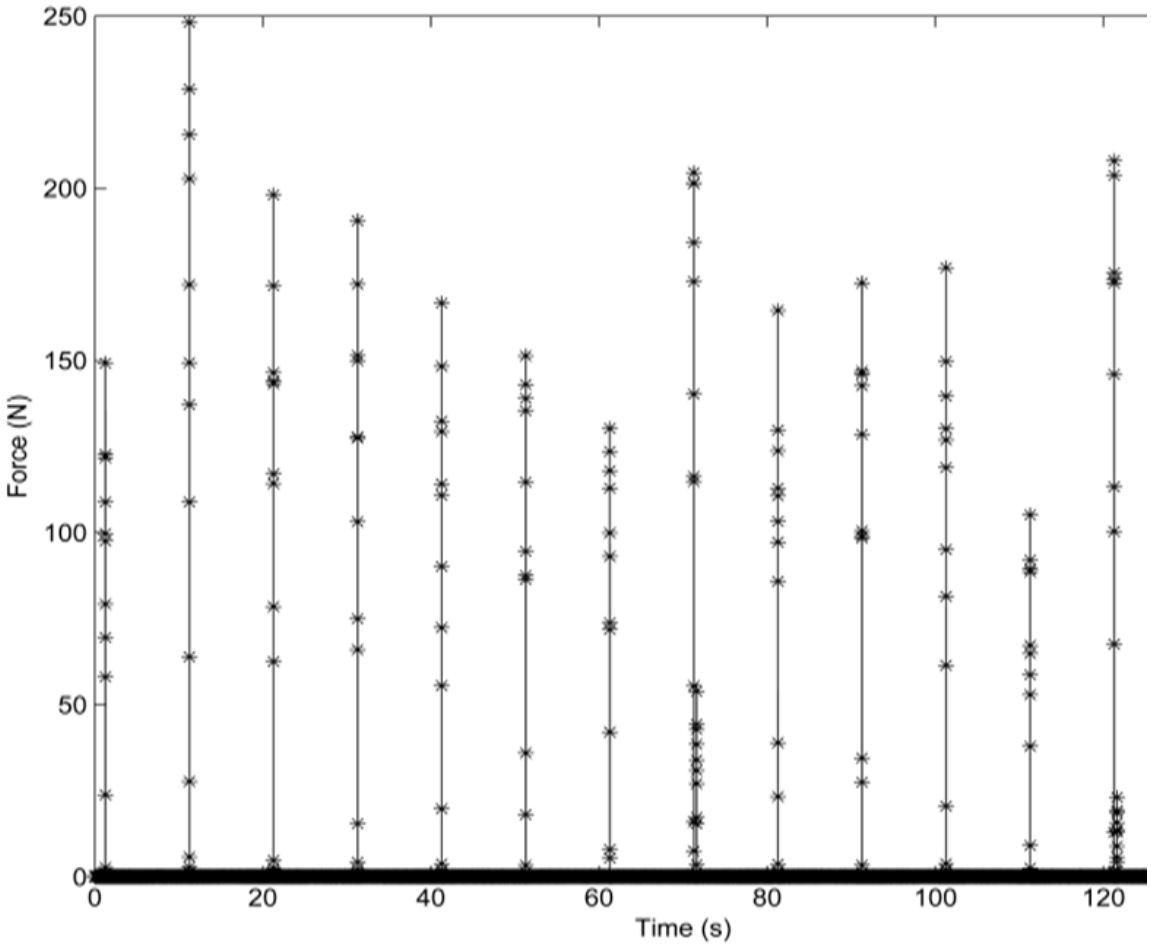

Figure 2.16: Experimentally realized forces for the repeated impulse test depicted in Fig.2.15.

due to hardware restrictions. As seen in the relative displacement time series of Fig.2.15a, the nonlinear attachment undergoes high-frequency complex oscillations. Note that this is different than the computational results depicted in Fig.2.6, where the amplitudes of oscillation of the nonlinear attachment were larger than those of the linear oscillator. This can be attributed to the fact that the forcing scheme was slightly different in the experimental case. In particular, due to the finite force practically realized by the shaker, each impulse delivered to the linear oscillator was of finite duration (in contrast to the delta-function excitation in the theoretical case), of slightly varying intensity and at slightly varying time periods between impulses. The exact forcing scheme realized in this particular experimental trial is shown in Figure 15, and confirms these assertions regarding the uncertainties in the repetitive series of impulsive excitations.

The first three impulsive cycles of the experimental response of Fig.2.15 were analyzed in detail as in the theoretical case, and the results are depicted in Fig.2.17-Fig.2.19. As seen from the experimental impulsive forces depicted in Fig.2.16, the forces applied to the linear oscillator are not of the same magnitude and are only nearly periodic. Focusing on the results of Fig.2.17d, it is noted that the wavelet spectrum - FEP superposition does not clearly show the frequency transition on the upper portion of the IOM for the relative displacement; however, the wavelet spectrum of the relative displacement depicted in Fig.2.17c indicates that the dynamics of the nonlinear attachment briefly tracks the IOM, but primarily gets captured on high-frequency superharmonic resonance branches. The instantaneous frequency of the nonlinear attachment then fluctuates between two superharmonic resonance branches, in similarity to the numerical simulation presented in Fig.2.7, which depicts the first cycle of the theoretical case.

Considering the second impulsive cycle of Fig.2.18, the results clearly indicate capture of the dynamics on the upper portion of the IOM from the beginning of the cycle. This confirms experimentally the theoretical prediction and shows that the high-frequency dynamical instability can be robustly excited even by repetitive impulsive forcing with the previously mentioned uncertainties. It is noteworthy that interesting dynamics occur at $t = 4s$ within the second impulsive cycle, when the frequency starts fluctuating between different resonances in the neighborhood of the upper IOM. After this intermediate dynamics, the nonlinear attachment returns to tracking the up-

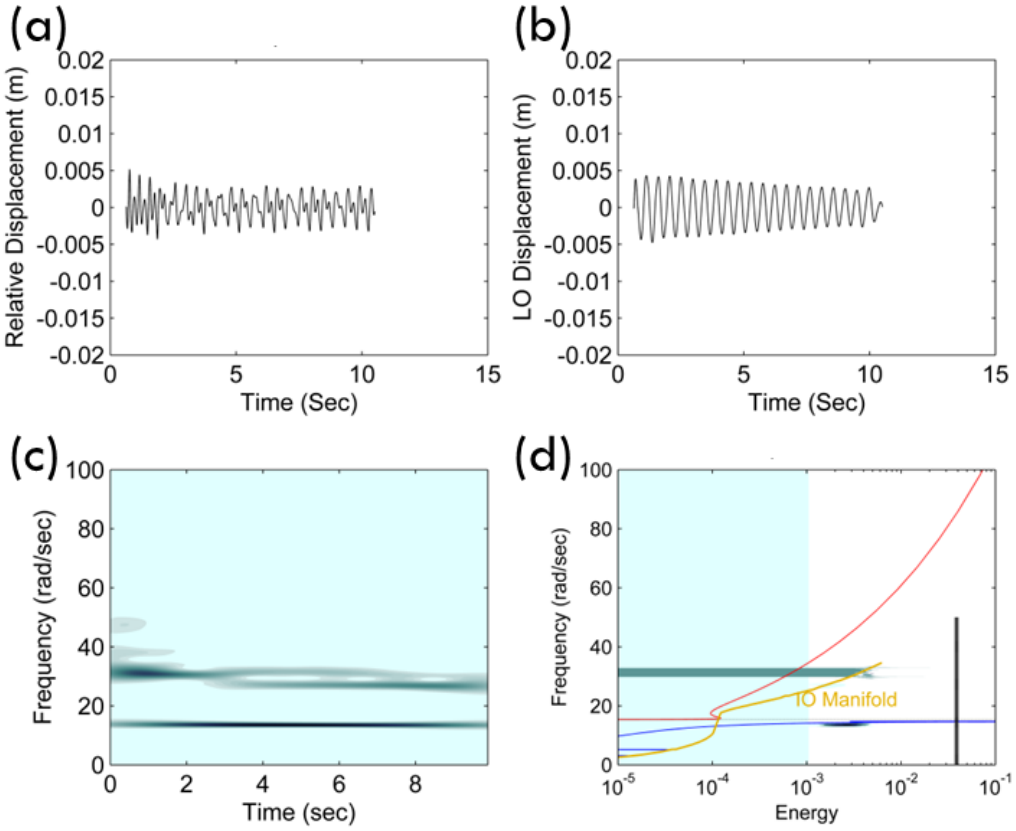

Figure 2.17: First cycle of the damped response of Fig.2.15, following the first impulse: (a) Relative displacement between nonlinear attachment and the linear oscillator, (b) displacement of linear oscillator, (c) wavelet spectrum of relative displacement, (d) wavelet spectrum of (c) on the Hamiltonian FEP.

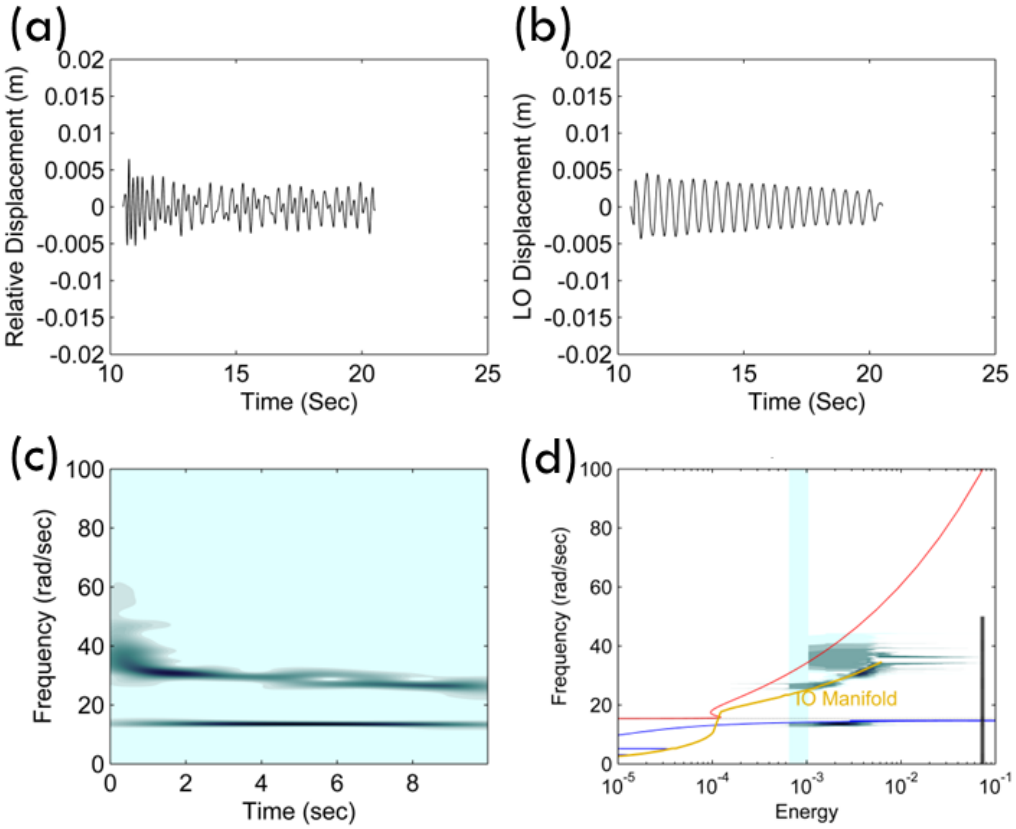

Figure 2.18: Second cycle of the damped response of Fig.2.15, following the first impulse: (a) Relative displacement between nonlinear attachment and the linear oscillator, (b) displacement of linear oscillator, (c) wavelet spectrum of relative displacement, (d) wavelet spectrum of (c) on the Hamiltonian FEP.

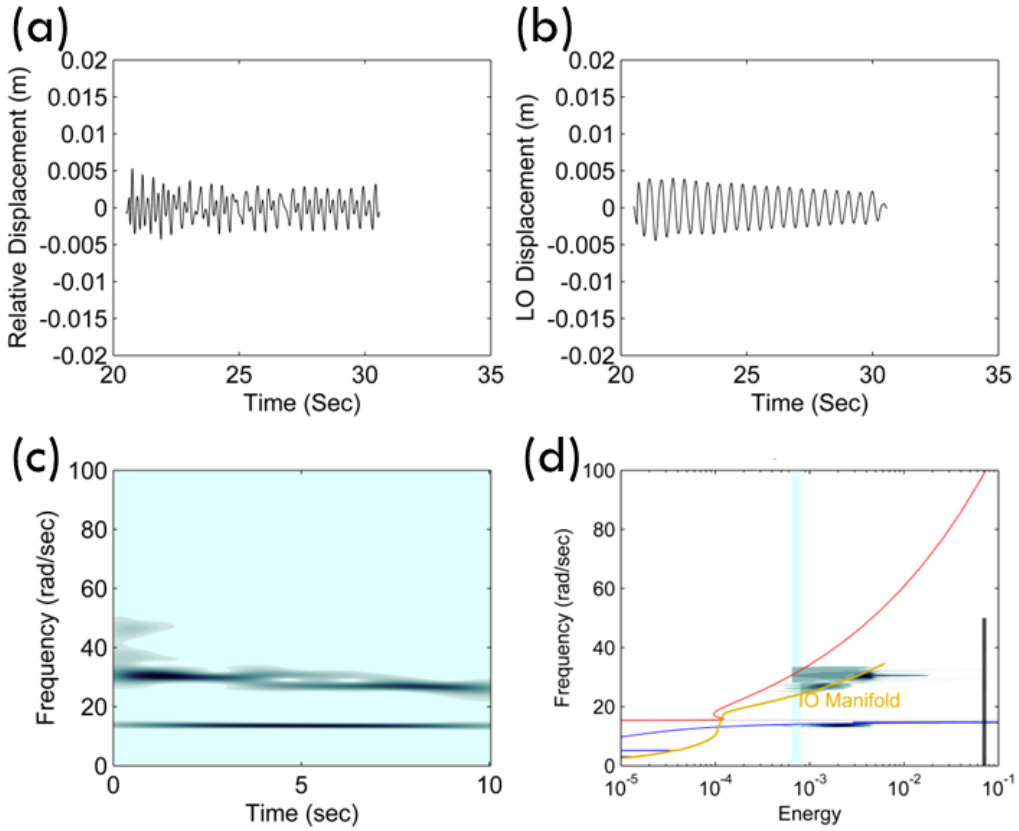

Figure 2.19: Third cycle of the damped response of Fig.2.15, following the first impulse: (a) Relative displacement between nonlinear attachment and the linear oscillator, (b) displacement of linear oscillator, (c) wavelet spectrum of relative displacement, (d) wavelet spectrum of (c) on the Hamiltonian FEP.

per IOM at $t = 6.5s$ for the remainder of the cycle.

The third impulsive cycle is considered in Fig.2.19 and indicates similar behavior to the second cycle, with consistent excitation of the high-frequency dynamical instability associated with tracking by the dynamics of the upper portion of the IOM. This further confirms the capacity of the strongly nonlinear attachment to engage in sustained resonance scattering on the IOM in the second impulsive excitation scenario. An additional series of experimental tests similar to the one presented in Fig.2.17-Fig.2.19 were performed. The high-frequency dynamical instability was readily repeatable, indicating that sustained resonance scattering is robust in the impulsively forced system.

CHAPTER 3

HIGH-FREQUENCY NONLINEAR VIBRATION ENERGY HARVESTING BASED ON A SYSTEM WITH ELECTROMAGNETIC ELEMENTS

The work in this chapter expands upon the aforementioned results computationally and experimentally for a system of two coupled oscillators with essential cubic stiffness nonlinearity and electromagnetic coupling. It is demonstrated that the high-frequency instability can be experimentally obtained for a system with moderate viscous damping subject to a single impulsive load, and that this high-frequency instability corresponds to good energy harvesting performance. The analysis is then expanded to consider the same system under repeated impulsive forcing. This work demonstrates that repetitive forcing places the system in a state of sustained high-frequency dynamic instability, which is favorable for energy harvesting, as predicted initially during the work presented in Section 4.1. This novel experimental apparatus proves the superior energy harvesting ability of this system operating in the high-frequency response regime.

3.1 System Modeling

We consider a nonlinear energy harvesting system (cf. Fig.3.1) composed of a linear, lightly damped oscillator (primary system) coupled to a lightweight, nonlinear, moderately damped oscillator (nonlinear energy sink, NES) via a permanent magnet, inductance coil, and piano wire. The piano wire generates an essential cubic stiffness nonlinearity through geometric and kinematic nonlinearities that arise due to transverse deformations, of the linear springs with constants k_2, relative to the direction of oscillation. The permanent magnet and inductance coil produce a linear, electromechanical damping term in the coupling, which is in addition to the linear viscous mechanical damping inherent in the system. A perfectly cylindrical inductance coil and

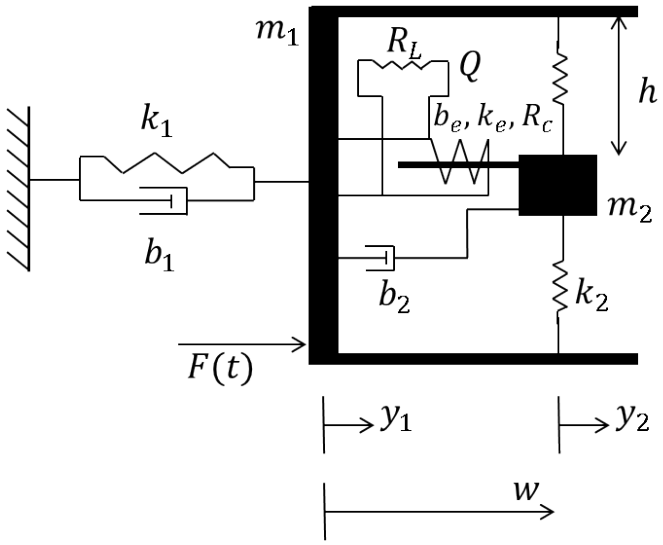

Figure 3.1: Configuration of the two coupled oscillators with essential geometric nonlinearity and electromagnetic elements.

magnet are assumed for the model and resulting analysis. The total coupling force can be expressed as

$$F_c = F_d + F_s + F_e = b_2\dot{w} + k_2 z + b_e\dot{w} \tag{3.1}$$

where b_2 is the linear viscous damping coefficient, k_2 is the axial stiffness of the piano wire, and b_e is the electromechanically induced damping coefficient. The absolute displacements of the primary system and NES are denoted by y_1 and y_2, respectively. The relative displacement w is defined as $y_2 - y_1$ with time-derivative $\dot{w}$, where $\dot{(\cdot)} \equiv d/dt$. The force across the piano wire can be expressed in terms of z, which is the axial displacement of the half-span of the wire with undeformed length h. This axial displacement z of the wire can be expressed in terms of the relative displacement w of the oscillators via the strongly nonlinear relationship $z = \sqrt{w^2 + h^2}$. A force $F(t)$ is applied in the direction of oscillation to the primary system, which is grounded via a linear spring of stiffness k_1 and linear viscous damper with coefficient b_1. The masses of the primary system and NES are denoted as m_1 and m_2, respectively.

The electromechanically-induced damping is well-defined by Kremer and Liu in [31] and Beeby and O'Donnell in *Chapter 5* of [33]. Faraday's law describes the electromotive force (emf) induced by a circuit as the time rate

change of the magnetic flux linkage or

$$emf = -\frac{d\phi}{dt} \tag{3.2}$$

where ϕ is the magnetic flux linkage. For a N turn coil, the induced emf is defined as a function of the total flux linkage Φ as

$$emf = -\frac{d\Phi}{dt} = -N\frac{d\phi}{dt} \tag{3.3}$$

The total flux linkage for a N turn coil is evaluated as the combination of flux linkages for individual turns, i.e.

$$\Phi = \sum_{i=1}^{N} \int_{A_i} B(A_i) \cdot dA \tag{3.4}$$

where B denotes the magnetic field flux density for a given i^{th} turn area A_i. The area of the effective magnetic field depends on the magnet's relative position with respect to the coil w (axial dependence) and the size of the coil in terms of its outer radius r_o and inner radius r_i (radial dependence). Lenz's law describes the electromagnetic force F_e as a function of the current in the coil $\dot{Q}$ and the transduction factor k_e, or

$$F_e = k_e \dot{Q} \tag{3.5}$$

The transduction factor is a function of the magnetic field flux density and coil size, thus describing the strength of the electromechanical coupling. The transduction factor can be defined as the change in total flux linkage as a function of position,

$$k_e = \frac{d\Phi}{dw} \tag{3.6}$$

Substituting the expression for the transduction factor in (3.6) into the expression for Faraday's law in (3.3), the electomotive force can be described as

$$emf = k_e \dot{w} \tag{3.7}$$

Assuming a uniform flux density over the area of the coil and substituting the expression in (3.4) into (3.6), the transduction factor can be reduced to

the simple expression

$$k_e = \frac{L_w h_c (r_o - r_i)}{A_c} B \tag{3.8}$$

where L_w is the length of the wire in the coil, h_c is the axial length of the coil, and A_c is the cross-sectional area of the coil, or $A_c = \pi(r_o^2 - r_i^2)$.

As seen in Fig.3.1, power is extracted from the mechanical system by connecting the coil to a fixed load resistance R_L. The current is able to flow through the coil and load resistance, creating its own magnetic field in opposition to the field created by the permanent magnet. The coil inherently contains its own resistance R_c and inductance L_c parameters. The electromagnetic force described in (3.1) and (3.6) is produced from the interaction of the field from the induced current and the field from the permanent magnet, allowing the conversion of mechanical energy into electrical energy. The voltage in the circuit due to the electromotive force can be described by applying Kirchoff's law to the system, i.e.

$$emf = L_c \ddot{Q} + (R_c + R_L)\dot{Q} \tag{3.9}$$

This expression (3.9) can be combined with (3.7) to express the current in the system as

$$\dot{Q} = \frac{k_e}{(R_c + R_L)} \dot{w} - \frac{L_c}{(R_c + R_L)} \ddot{Q} \tag{3.10}$$

Wheeler in [43] provides an estimate for the coil inductance as

$$L_c = \frac{(7.875 \times 10^{-6})(r_o + r_i)^2 N}{13 r_o - 7 r_i + 9 h_c} \tag{3.11}$$

and the maximum coil impedance Z_L can be estimated as

$$Z_L = 2\pi f_{max} L_c \tag{3.12}$$

where f_{max} is the maximum driving frequency (in Hz) imposed by the mechanical system. As will be shown later, the experimental coil inductance and resulting coil impedance are negligible relative to the load resistance used. Therefore the coil impedance is neglected in further analysis for simplification. Using this assumption, (3.10) can be reduced to

$$\dot{Q} = \frac{k_e}{(R_c + R_L)} \dot{w} = \frac{b_e}{k_e} \dot{w} \tag{3.13}$$

where the electromagnetic damping b_e is expressed as

$$b_e = \frac{k_e^2}{R_c + R_L} \tag{3.14}$$

The nonlinear equations of motion governing the dynamics of the harvesting device can finally be obtained by summing forces in the direction of oscillation and expanding into Taylor series for the nonlinear terms. The three governing equations are expressed as

$$m_1\ddot{y}_1 + b_1\dot{y}_1 + k_1 y_1 - (b_e + b_2)\dot{w} - \frac{k_2}{h^2}w^3 = F(t) \tag{3.15a}$$

$$m_2(\ddot{w} + \ddot{y}_1) + (b_e + b_2)\dot{w} + \frac{k_2}{h^2}w^3 = 0 \tag{3.15b}$$

$$\dot{Q} - \frac{b_e}{k_e}\dot{w} = 0 \tag{3.15c}$$

As seen in (3.15), the essential cubic stiffness nonlinearity appears in the coupling stiffness.

The preliminary work in Chapter 2 theoretically and experimentally demonstrated the ability of introducing high-frequency dynamic instability in the same system but with the electric circuit removed. The work shows that the transient damped dynamics of the system tracks the high-frequency IOM in the frequency-energy plane when the primary system is subject to specific impulse excitation magnitude. Bursts in the response of the NES arise at bifurcation points along damped transitions in the neighborhood of the IOM, resulting in strong energy transfers from the directly excited primary system to the NES. This feature was exploited theoretically in Section 4.1 to produce superior energy harvesting performance for the same system with piezoelectric coupling elements and a simple circuit. The principal aim of our study is to show experimentally that high-frequency dynamic instabilities in the response of (3.15) exist and can provide an effective mechanism for vibration energy harvesting.

The dynamics of the system (3.15) were first explored by introducing non-dimensionalized parameters. This was carried out by scaling the time, displacement, and charge variables as $t = c_t\tau$, $y_1 = c_x x$, $w = c_x u$, and $Q = c_q q$, respectively. The normalization coefficients were chosen in a manner that normalizes the linear and nonlinear stiffness parameters, as well as one of the

circuit parameters. This scaling allows for computational study of the effects of system damping and electromechanical coupling on the performance of the harvester. The normalization coefficients are given by

$$c_t = \sqrt{\frac{m_1}{k_1}}, \qquad c_x = h\sqrt{\frac{k_1 m_2}{k_2 m_1}}, \qquad c_q = \frac{h k_1 m_2}{k_e m_1}\sqrt{\frac{m_2}{k_2}} \tag{3.16}$$

This analysis yields a simplified set of non-dimensional equations given by

$$x'' + \lambda x' + x - \mu[(\beta + \zeta)u' + u^3] = \gamma f(\tau) \tag{3.17a}$$

$$u'' + x'' + (\beta + \zeta)u' + u^3 = 0 \tag{3.17b}$$

$$q' - \beta u' = 0 \tag{3.17c}$$

where $\gamma f(\tau) \equiv F(t(\tau))$, $(\cdot)' \equiv d/d\tau$, and the non-dimensional parameters are defined as

$$\begin{aligned} \mu &= \frac{m_2}{m_1}, \qquad \lambda = \frac{b_1}{\sqrt{m_1 k_1}}, \qquad \zeta = \frac{b_2}{m_2}\sqrt{\frac{m_1}{k_1}}, \\ \beta &= \frac{b_e}{m_2}\sqrt{\frac{m_1}{k_1}}, \qquad \gamma = \frac{1}{h k_1}\sqrt{\frac{k_2 m_1}{k_1 m_2}} \end{aligned} \tag{3.18}$$

Within these nonlinear, non-dimensional equations of motion, the mass ratio between the NES and the primary system is defined by μ, λ defines the linear viscous damping in the primary system, ζ represents the linear viscous damping in the coupling, β describes the electromechanical coupling for the system, and γ defines the force magnitude.

A single impulsive excitation scenario is considered first in this work. The harvesting system (3.17) is initially at rest at $\tau = 0-$, in which the $0-$ denotes the moment just prior to instantaneous zero. A single impulse $\gamma f(\tau) = \tilde{I}_0 \delta(\tau)$ is then applied to the system at $\tau = 0+$. Using this assumption of an instantaneously applied force, the equations of motion (3.17) are complemented by initial conditions

$$\begin{aligned} x(0+) &= 0, \qquad x'(0+) = \tilde{I}_0, \\ u(0+) &= 0, \qquad u'(0+) = -\tilde{I}_0, \\ q(0+) &= 0 \end{aligned} \tag{3.19}$$

and γ is effectively set equal to zero so that no additional forcing is applied to the system. For further clarification, the instantaneously applied force is being expressed as a velocity initial condition. Experimentally, the forcing takes the shape of a half-sine wave pulse with a specific duration, which will be explored in later sections. Recall that $u'(\tau)$ describes the non-dimensional relative velocity between the oscillators. This condition must be defined as above so that the initial velocity of the NES is zero.

The second excitation scenario considered studies the response of the system (3.15) to repeated impulsive excitation of variable amplitude and frequency. The forcing scenario will be described here in terms of the dimensional system (3.15) for clarity. The oscillators are again initially at rest at $t = 0-$, in which $-$ and $+$ will be used to denote the moments directly before and after a designated time, respectively. The *Dirac* force described above is applied to the linear oscillator at time $t = 0+$. The initial conditions are thus adjusted to reflect this instantaneous forcing as

$$\begin{aligned} y_1(0+) &= 0, \qquad \dot{y}_1(0+) = I_0, \\ w(0+) &= 0, \qquad \dot{w}(0+) = -I_0, \\ Q(0+) &= 0 \end{aligned} \tag{3.20}$$

It is noted here for clarification that $\dot{w}$ corresponds to the relative velocity between the NES and linear oscillator; therefore, the relative velocity must be defined as in (3.20) so that the initial velocity of the NES is not incremented by the impulse. The forcing frequency for application of impulses is defined in this work as a function of the primary system fundamental period $T_0 = 2\pi(m_1/k_1)^{1/2}$, or cycles of the linear oscillator. This impulse period μ_T is thus defined as $\mu_T = t_p/T_0$, where t_p represents the duration of time between application of consecutive impulses. For clarification, an impulse period of $\mu_T = 10$ defines a pulse train applied to the primary system every 10 fundamental periods with intensity I_0. This forcing scheme is mathematically represented as

$$F(t, \mu_T, I_0) = \sum_{p=0}^{N} I_0 \delta(t - pt_p) \tag{3.21}$$

where N represents the total number of applied impulses after the initial

excitation. Under this excitation scenario, the p^{th} impulse applied to the primary system at time $t = pt_p+, p \geq 1$ corresponds to initial conditions

$$\begin{aligned} y_1(pt_p+) &= y_1(pt_p-), \qquad \dot{y}_1(pt_p+) = \dot{y}_1(pt_p-) + I_0, \\ w(pt_p+) &= w(pt_p-), \qquad \dot{w}(pt_p+) = \dot{w}(pt_p-) - I_0, \\ Q(pt_p+) &= Q(pt_p-), \qquad p = 1, ..., N \end{aligned} \tag{3.22}$$

which are representative of the system directly after the application of the impulse. As deduced from (3.22), the initial state of the system will differ after each consecutive impulse depending upon the remaining mechanical energy in the system at the time of the application of the p^{th} impulse.

Energy harvesting performance measures can be defined for the system (3.15) using energy and power expressions for use in later sections. For this system, the instantaneous power generated by the harvesting device is a function of the energy dissipated across the resistive element in the coupled circuit, i.e.

$$P(t, I_0) = R_L \dot{Q}^2 = \overbrace{\underbrace{\left[\frac{h^2 k_1^2 m_2}{k_2 m_1}\sqrt{\frac{k_1}{m_1}}\right]}_{Units of Watts} \cdot \underbrace{\left[\frac{\mu}{\beta}(q')^2\right]}_{Non-dimensional Power}}^{Dimensional Power} \tag{3.23}$$

As seen in the above equation, the instantaneous power depends on the impulse magnitude and the load resistance. As described earlier, the numerical integration is performed using the non-dimensional system (3.17) and then scaled back to the dimensional system (3.15) using the scaling parameters (3.16). The total energy harvested E_h for the p^{th} impulse of magnitude I_0 can be expressed as the time integral of the non-dimensional power during the forcing interval of interest with proper scaling, i.e.,

$$E_h(p, \mu_T, I_0) = \overbrace{\underbrace{\left[\frac{h^2 k_1^2 m_2}{k_2 m_1}\right]}_{Units of Joules} \cdot \underbrace{\left[\int_{p\tau_p}^{(p+1)\tau_p} \frac{\mu}{\beta}(q'(\tau))^2 d\tau\right]}_{Non-dimensional Energy Harvested}}^{Dimensional Energy Harvested} \tag{3.24}$$

The energy harvesting efficiency η_h for the p^{th} impulse forcing period can then be defined in this work as the energy harvested during the p^{th} impulse (3.24)

of magnitude I_0 normalized by the kinetic energy input into the primary system at time $t = pt_p+$, i.e.

$$\eta_h(p, \mu_T, I_0) = \frac{E_h(p, \mu_T, I_0)}{\frac{1}{2}m_1(I_0)^2} \times 100\% \tag{3.25}$$

As mentioned above, the principal goal of this work is to experimentally demonstrate that effective energy harvesting can be achieved by inducing high-frequency instability of the NES. The dynamics of the underlying Hamiltonian system are discussed in the next section for the experimental apparatus and its inherent parameters. This is necessary to study the mechanism governing the instability and promoting good energy harvesting performance.

3.1.1 Underlying Hamiltonian Dynamics

The dynamics of the underlying Hamiltonian system derived from (3.15) can be depicted in a *frequency energy plot - FEP*, which is thoroughly explained in Section 1.2. The underlying Hamiltonian system is obtained by removing the damping, electrical, and forcing terms from (3.15); i.e., by setting $b_1 = b_2 = b_e = F(t) = 0$. The frequency-energy plane provides a visual method by which branches of periodic and quasi-periodic orbits of the underlying Hamiltonian system can be expressed over varying energy levels. Transitions between various branches of the FEP are realized in the transient response of the system (3.15) due to the non-conservative terms in the original equations of motion. Wavelet spectral analysis can be performed by taking the *Morlet wavelet* transform of a time-history response of the system (3.15). The wavelet transform is a dynamic time-frequency analysis tool, which is more appropriate than the fast Fourier transform for stationary signal analysis. The resulting wavelet spectra can then be superimposed on the Hamiltonian FEP or plotted versus time to reveal the transitions between branches in the transient response. This methodology is based on the assumption that the conservative elements of the Hamiltonian system govern which branch is "visited" by the system for a given energy input, and the non-conservative elements govern the transitions between branches. For clarification, the damping in the system provides purely parasitic dynamical effects; i.e., damping doesn't introduce any new dynamics into the underlying

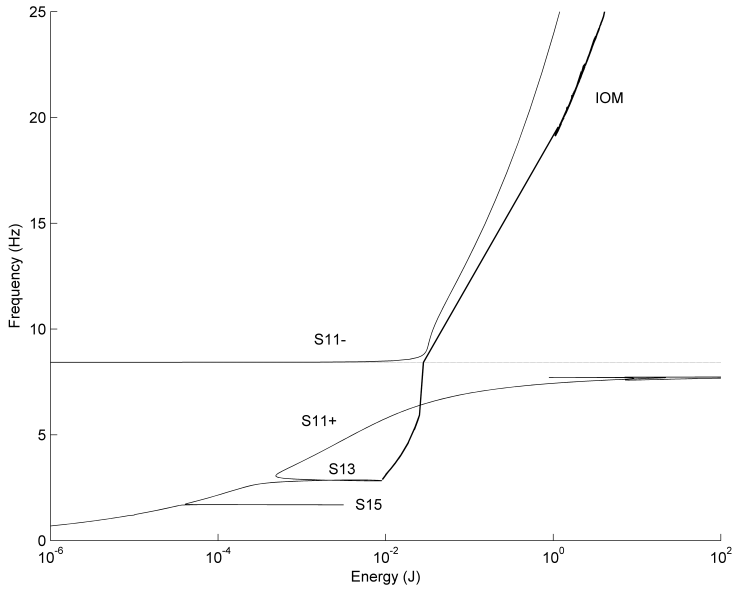

Figure 3.2: Frequency-energy plot of the underlying Hamiltonian system (3.15) derived from experimental parameters presented in Table 3.2.

Hamiltonian system.

The FEP for the underlying Hamiltonian system is shown in Fig.3.2 for the experimental parameters (m_1, k_1, m_2, k_2) identified in Table 3.2 from Section 3.2.2. The horizontal dotted line at approximately $8.42Hz$ corresponds the natural frequency of the primary system. Two *global backbone branches* denoted $S11\pm$ are then defined over broad frequency and energy ranges. These branches correspond to in-phase and out-of-phase periodic orbits in 1:1 resonance, respectively. For clarification, these are periodic orbits in which the primary system and the NES oscillate at the same fundamental frequency. The FEP in Fig.3.2 also contains two *subharmonic tongues*, denoted $S13$ and $S15$, extending horizontally from the $S11+$ backbone. These tongues correspond to 1:3 and 1:5 internal resonances, respectively, between the NES and the primary system. These subharmonic internal resonances indicate slower oscillations (lower frequency) of the NES with respect to the primary system. Conversely, superharmonic internal resonances also exist for this system, although they are not depicted in the FEP presented in Fig.3.2. These *superharmonic tongues* would extend horizontally from the $S11-$ backbone, indicating resonances in which the NES oscillates faster (higher frequency) than the primary system. As discussed in Section 3.2.2, a countable infinity

of periodic orbits exist in the underlying Hamiltonian system. These occur in pairs of Snm in-phase/out-of-phase subharmonic and superharmonic tongues (n:m internal resonance) that exist over finite energy ranges.

The impulsive orbits manifold contains another class of solutions in the FEP. These solutions are composed of a countable infinity of periodic orbits and an uncountable infinity of quasi-periodic orbits of the Hamiltonian system. These impulsive orbits correspond to impulsive excitation of the primary system as outlined according to initial conditions in (3.19). The previous work in Chapter 2 indicates that orbits of the lightly damped system in the neighborhood of the high-frequency IOM result in strong energy transfers from the primary system to the nonlinear attachment, which is beneficial for harvesting energy from the NES. These strong energy transfers take the form of "transient bursts" (instabilities) in the response of the nonlinear attachment, which arise at bifurcation points along damped transitions near the IOM. These bursts have been indicated in some works [44, 45] as resembling self-excited resonances.

3.2 Single Impulse

This section initiates the computational study of the damped dynamics of system (3.17) by performing numerical simulations for a single impulse of various magnitudes applied to the primary system. The effect of changing the electromechanical coupling and circuit load resistance will be explored, as well as determination of physical parameters for the experimental system. Wavelet analysis will be performed on the transient response of the system and then compared to the energy harvesting efficiency defined in (3.25) to show that these high-frequency transitions can lead to effective energy harvesting.

3.2.1 Computational Study

The computational study of system (3.17) is initiated by considering a single impulsive input to the primary system according to (3.19) and studying the resulting damped transitions via wavelet analysis, as described in the previous section. The numerical simulations carried out in this section are

performed with several parameters resulting from an experimental apparatus derived and constructed from the previous apparatus from Section 2.3. The experimental apparatus used in this study can be seen in Fig.3.9 and is described in more detail in Section 3.2.2.

A system identification was performed initially for the mechanical parameter values governing the experimental apparatus so that the computational study could begin with these as a baseline. Linear modal analysis was performed on the primary system alone to extract the parameter values b_1 and k_1. Nonlinear system identification utilizing the restoring force surface method [41, 42] was performed on the attachment alone to extract the parameter values b_2 and k_2. The primary system and NES masses were weighed to determine m_1 and m_2, respectively, and the piano wire half-span length was measured to determine h. These seven mechanical parameter values are presented in Table 3.2.

As derived in (3.18), the resulting non-dimensional mechanical system parameters can be determined from the identified physical parameter values. The non-dimensional system parameters are presented in Table 3.1. As seen from (3.18), the mass ratio μ and damping terms λ and ζ correspond to the mechanical parameters, leaving the electromechanical coupling coefficient β as the only unknown design parameter for the system (3.17). This electromechanical coupling coefficient is primarily dependent upon the transduction factor k_e, which is determined by the coil construction and permanent magnet selection. As described in [18, 25], optimized energy harvesting efficiency can be achieved with proper tuning of the electrical circuit parameters. While system optimization is not specifically the goal in this study, parameter optimization can be easily explored with the simplified non-dimensional system (3.17).

The total non-dimensional energy harvested from (3.24) and the energy harvesting efficiency (3.25) were considered when determining system performance for a range of electromechanical coupling and impulse magnitude values. Appropriate parameter ranges were established according to physical limitations of the experimental apparatus, and then expanded to include other possible outcomes for future apparatus optimization. Contour plots were developed for an electromechanical coupling range $\beta = [0.01 - 1.00]$ with step $\Delta\beta = 0.01$ and impulse magnitude range $\tilde{I}_0 = [0.05 - 10]$ with step $\Delta\tilde{I}_0 = 0.05$. The system (3.17) was numerically integrated with initial con-

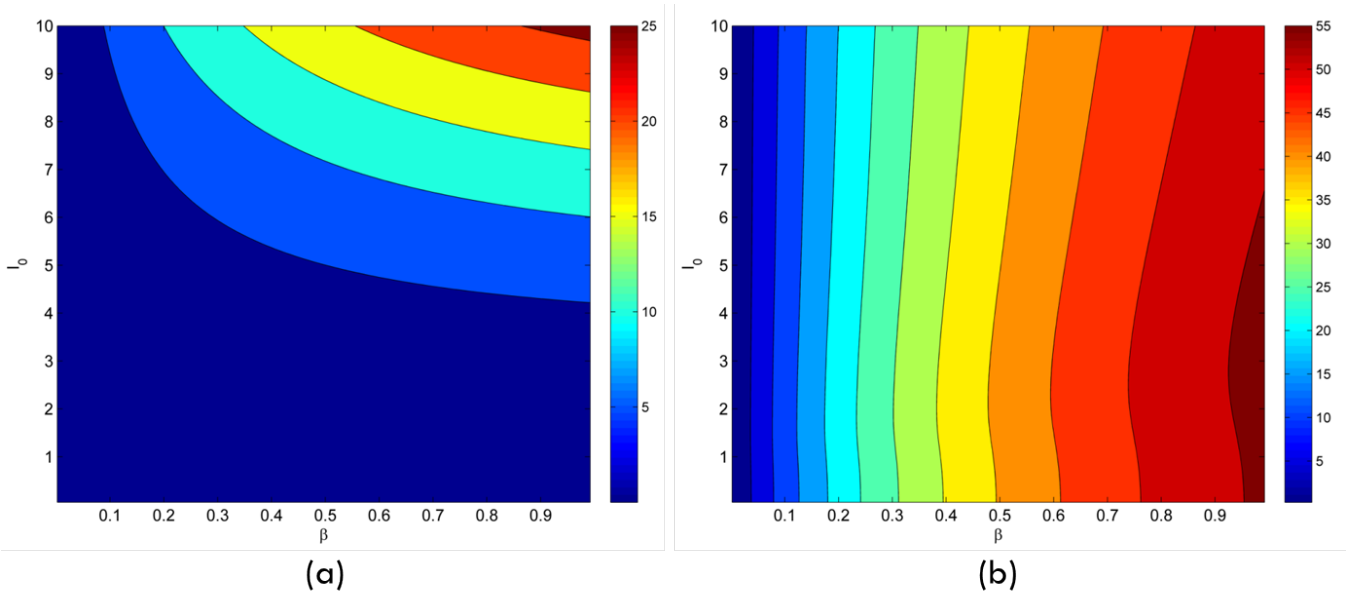

Figure 3.3: (a) Total non-dimensional energy harvested and (b) energy harvesting efficiency for a simulation time of $\tau_f = 110$ as a function of $\tilde{I}_0$ and β.

ditions (3.19) for each $(\beta, \tilde{I}_0)$ parameter pair for a given time period τ_f. The resulting time series was post-processed to produce performance contours based on energy measures (3.24) and (3.25).

The system is integrated for a simulation time of $\tau_f = 110$, which corresponds physically to approximately $t_f = 2.0$ seconds. Contour plots for performance measures described in (3.24) and (3.25) are depicted in Fig.3.3. As indicated by Fig.3.3a, the total energy harvested is strongly dependent upon the energy level at which the system operates, or the excitation magnitude, which is expected for strongly nonlinear systems. Recall from Fig.3.2 and the discussion in Section 3.1.1, that the initial energy state of the primary system dictates which orbits are "experienced" by the system. The work in Chapter 2 indicated that high initial energy states under the initial conditions (3.19) correspond to high-frequency dynamic instabilities in the neighborhood of the upper IOM. These high-frequency transitions provide for good energy harvesting performance, and are thus predicted in this case to be the driving mechanism behind the response. The contour in Fig.3.3a also indicates that total energy harvested depends moderately upon the electromechanical coupling parameter. The contour in Fig.3.3b denotes the importance of the electromechanical coupling parameter, which strongly dic-

tates the energy harvesting efficiency. Plateaus of increasing efficiency exist for discrete ranges of electromechanical coupling and for the entire range of impulse magnitudes studied. It should be noted that these findings depend on the non-dimensional time parameter τ, or the time interval of computation for harvesting measures (3.24) and (3.25). It is intuitive that energy can continue to be harvested until the system comes to rest. Studying individual time histories at discrete points in these contours can provide more insight into the dependence on time.

The dynamics governing various regimes of the contours presented in Fig.3.3 can be studied in detail by using wavelet analysis to analyze the nonlinear transient response of the system. High-frequency transient resonance captures are predicted for large impulse magnitudes and for any electromechanical coupling. The response of system (3.17) for a non-dimensional impulse magnitude of $\tilde{I}_0 = 9$ is examined for system parameters listed in Table 3.1 and electromechanical coupling $\beta = [0.1, 0.9]$. As deduced form Fig.3.3, these parameter combinations will provide insight into low and high harvesting efficiency regimes and for large total energy harvested. These responses are depicted in Fig.3.4 and Fig.3.5.

The response of the system for $\beta = 0.1$ and $\tilde{I}_0 = 9$ is shown in Fig.3.4. As seen in Fig.3.3b and Fig.3.4e, this system response corresponds to an overall energy harvesting efficiency of approximately 13%, in which 7% of the harvesting occurs within the first ~ 5 simulation time units. Examination of the multi-frequency time history in Fig.3.4c and relative displacement wavelet in Fig.3.4d reveals the dynamics during the first ~ 5 simulation time units. As seen clearly in Fig.3.4d, the transient response of the NES initially occurs in the neighborhood of high-frequency superharmonic tongues in the vicinity of the upper branch of the IOM. This is indicated by the dominant high-frequency harmonics in the initial, highly energetic phase of the relative response. As mentioned earlier, the primary system was scaled so that it has a fundamental frequency of unity, as seen in Fig.3.4a and Fig.3.4b. Frequency transitions above unity correspond to motions in which the NES oscillates faster than the primary system, which is beneficial to energy harvesting. Following the high-frequency TRCs, the dynamics of the system transition to the lower-frequency $S11+$ backbone branch, where energy is further harvested at a slower rate or dissipated via the viscous damping in the oscillators. To reiterate, these high-frequency TRCs are possible due to

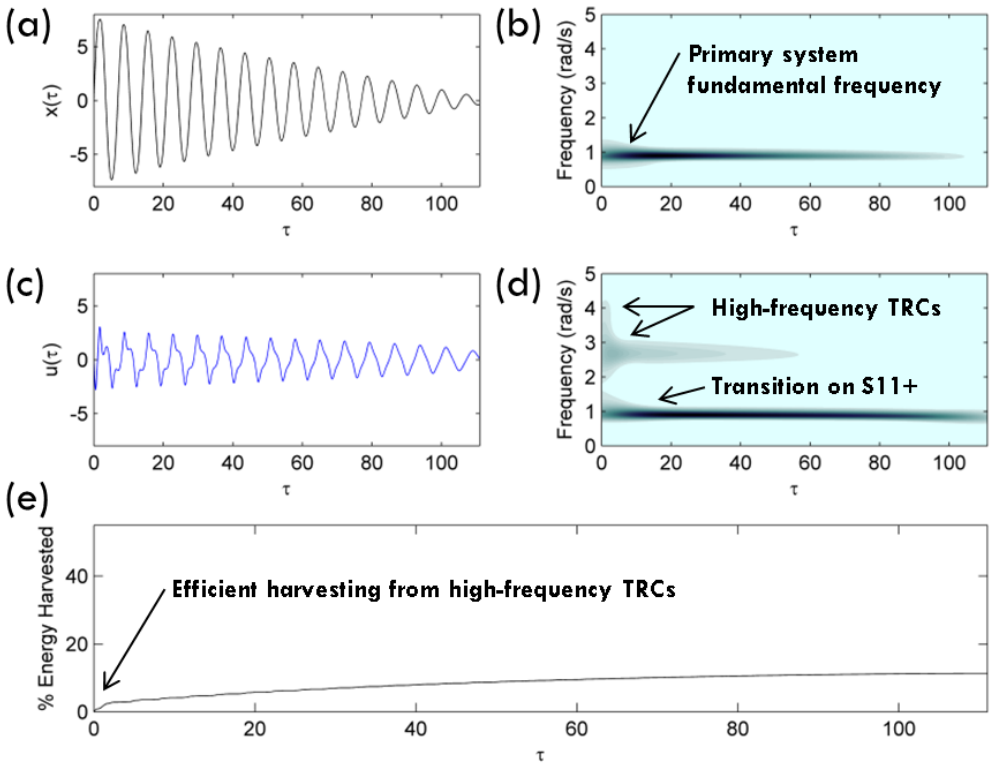

Figure 3.4: (a) Primary system displacement time history, (b) primary system displacement wavelet, (c) relative displacement time history, (d) relative displacement wavelet, and (e) energy harvesting efficiency measure (3.25) for system (3.17) with $\tilde{I}_0 = 9$ and $\beta = 0.1$.

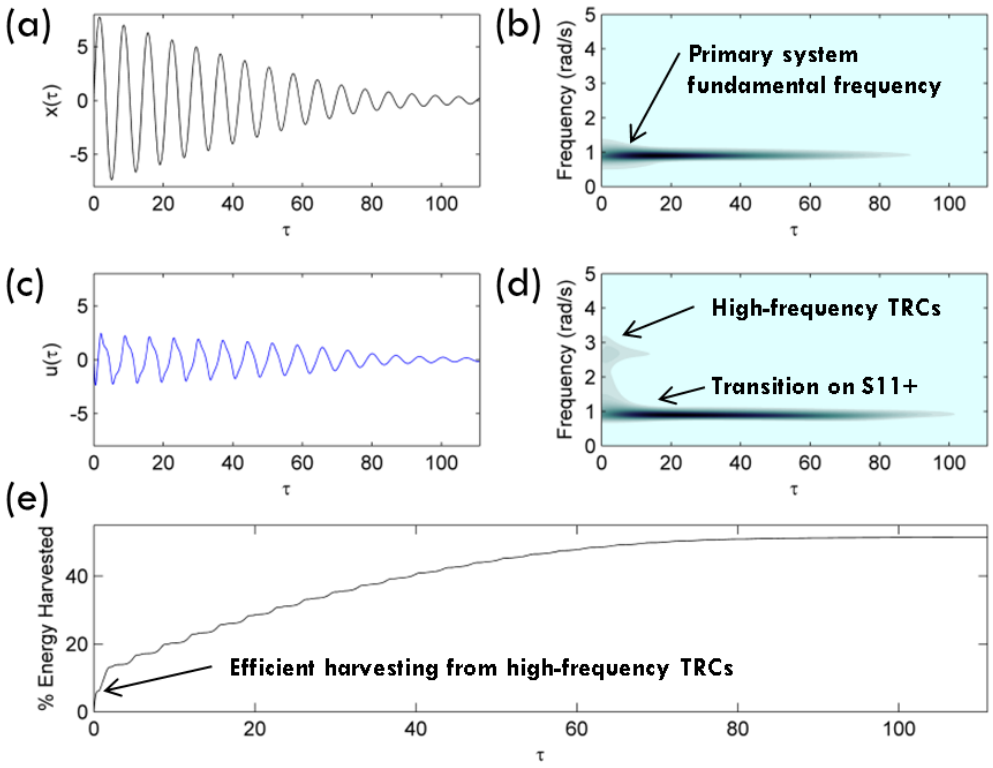

Figure 3.5: (a) Primary system displacement time history, (b) primary system displacement wavelet, (c) relative displacement time history, (d) relative displacement wavelet, and (e) energy harvesting efficiency measure (3.25) for system (3.17) with $\tilde{I}_0 = 9$ and $\beta = 0.9$.

the intentional strong cubic nonlinearity imposed in the coupling of the NES.

The response of the system for $\beta = 0.9$ and $\tilde{I}_0 = 9$ is shown in Fig.3.5, which exhibits similar high-frequency TRCs as those presented in Fig.3.4. As seen in Fig.3.5e, approximately 15% of the total 47% harvested energy now occurs within the first ~ 5 simulation time units. Examination of the relative displacement wavelet in Fig.3.5d clearly indicates that the dynamics track high-frequency TRCs in the neighborhood of the upper branch of the IOM within the first ~ 5 time units. Similar to the response depicted in Fig.3.4, the dynamics of the system transition to the lower-frequency $S11+$ backbone branch after the high-frequency TRCs die out. Energy is again passively dissipated and harvested at a slower rate until the system comes to rest. The effect of the increased electromechanical coupling in Fig.3.5e is evident when compared to Fig.3.4e. The total energy harvesting efficiency increases from 13% to 47% when the electromechanical coupling increases from 0.1 to 0.9. In addition, the time to maximum obtained efficiency or equilibrium system conditions decreases from 110 time units to 80 time units with increased electromechanical coupling. However, the high-frequency dynamic instability depends on the initial energy state of the system rather than the electromechanical coupling.

A similar analysis was carried out for lower impulse magnitude regions of the contours presented in Fig.3.3. For impulse magnitudes $\tilde{I}_0 <\sim 4$ and any electromechanical coupling β, the dynamics of the system initiate on and remain tracking the $S11+$ backbone branch for the duration of the simulation. While the system remains in motion during this tracking, energy is harvested at a rate similar to that presented in Fig.3.4e and Fig.3.5e during $S11+$ tracking. This defines an important general magnitude threshold for exciting high-frequency dynamic instability in the system, which is similar to the work presented in Chapter 2. This magnitude threshold can be scaled back to the physical primary system initial velocity value as $\dot{y}_1(0) = \tilde{I}_0 \cdot c_x/c_t = I_0$, which indicates the initial energy level required to excite the experimental apparatus into high-frequency instability.

This previous analysis is important for the design and fabrication of the induction coil and selection of the permanent magnet, which determines the transduction factor k_e, the electromagnetic damping b_e, and thus the non-dimensional electromechanical coupling coefficient β. Physical limits are imposed on the transduction factor value via the size of the inductance coil

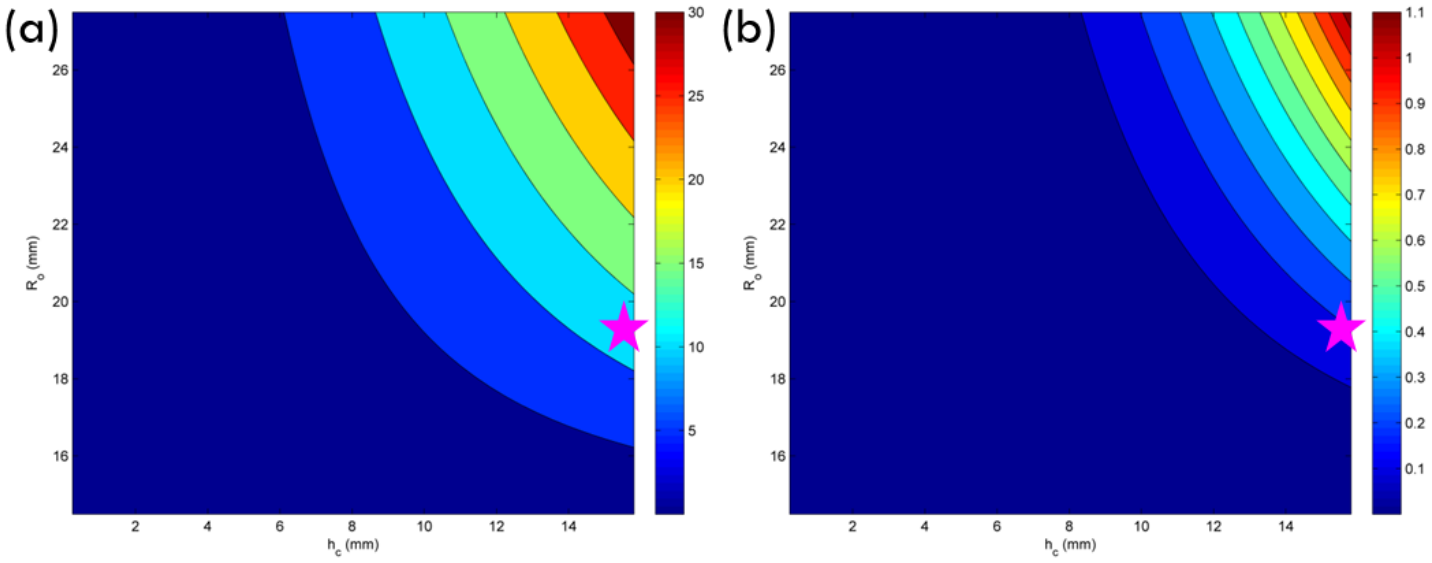

Figure 3.6: (a) Transduction factor (Tm) and (b) non-dimensional electromechanical coupling for an orthogonal fill factor inductance coil of thickness h_c and outer radius r_o. The pink star denotes the targeted parameter values for the coil in the experimental apparatus.

and the magnetic field flux density inherent to the permanent magnet, as indicated in (3.8). As described earlier, the primary goal of this study is to experimentally demonstrate the effect of high-frequency dynamic instability on energy harvesting rather than strictly optimizing the system for harvesting energy, which provides some freedom in the design and fabrication of the induction coil. Detailed information regarding the inductance coil construction and permanent magnet selection will be described in Section 3.2.2; however, the analysis behind the construction and parameter identification will be discussed here next.

The inductance coil used in the experimental apparatus (cf. Fig.3.9) was wound assuming an orthogonal fill factor, as described in [33]. The fill factor encompasses tightness of winding, insulation thickness, and winding shape, which essentially determines the efficiency of the coil. This orthogonal fill factor corresponds to a coil efficiency of $\sim 80\%$, and is obtainable practically with careful coil wrapping. Physically, the orthogonal fill factor describes coil winding in which each new turn of wire lies directly on top of the wire turn below it and perfectly in line with the wire turn next to it. Using this assumption, contour plots can be constructed to estimate the transduction

Table 3.1: Non-dimensional parameters for the system (3.17)

Parameter	Value
μ	0.1850
λ	0.0059
ζ	0.6653
β	0.1018
γ	0.0000

factor (cf. Fig.3.6a) and non-dimensional electromechanical coupling parameter (cf. Fig.3.6b) for specific coil dimensions. As seen in Fig.3.6, the outer radius and coil thickness of the wire wrapping can be varied to determine the parameter values from (3.8) and (3.18). The minimum and maximum coil dimensions are constrained by the spool geometry used in the experimental apparatus.

As deduced from Fig.3.6a, the transduction factor is strongly dependent upon the coil thickness relative to the coil radius. This indicates that the length (surface area) of the magnetic field induced by the coil is more important in the electromechanical coupling than the radial thickness of the magnetic field. Therefore the full thickness of the spool ($16mm$) was wrapped when constructing the coil to maximize the transduction factor for a given length of wire, which leads to a given coil resistance and coil inductance. As seen in Fig.3.6b, this also serves to maximize the electromechanical coupling parameter, which was investigated in Fig.3.3. Recall from the derivation in Section 3.1 that the coil inductance L_c (3.11) and resulting impedance Z_L (3.12) can be estimated from the coil dimensions. In addition the coil inductance was assumed to be negligible in the analysis outlined following (3.13). Therefore the coil dimensions have self-imposed physical limitations to maintain the assumptions from Section 3.1.

From the analysis deduced from Fig.3.3 and Fig.3.4, a coupling parameter of $\beta = 0.1$ was deemed acceptable to show the effects of high-frequency dynamic instability on energy harvesting capability while keeping the coil construction simple and maintaining the assumptions from Section 3.1. Therefore as indicated by Fig.3.6b, the coil must have a thickness of $16mm$, inner radius of $14mm$, and outer radius $\sim 20mm$. This design criteria is marked by a pink star in Fig.3.6. The coil was wound with $N = 819turns$ to achieve

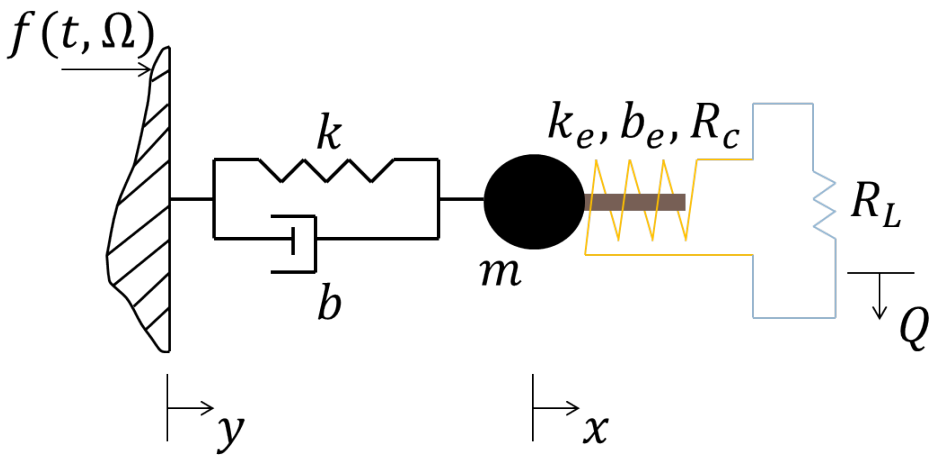

Figure 3.7: Model for the configuration of the system used to identify the transduction factor.

these dimensions. The coil resistance, measured with an ohmmeter, can be seen in Table 3.2. The coil inductance and impedance were determined from (3.11) and (3.12), respectively, assuming a maximum system frequency of $25Hz$. The resulting induction impedance was indeed negligible relative to the coil resistance at $Z_L = 0.1m\Omega$.

The coil parameters were identified and confirmed experimentally by comparing a simple constrained experimental system to the corresponding numerical system, which is depicted in Fig.3.7 and expressed as

$$m\ddot{x} + b\dot{x} + b_e\dot{x} + kx = X_0 \sin(\Omega t) \tag{3.26a}$$

$$\dot{Q} - \frac{b_e}{k_e}\dot{x} = 0 \tag{3.26b}$$

The permanent magnets were attached to an APS Dynamics ELECTRO-SEIS®Model 400 long-stroke shaker via a rigid rod, and the fully constructed induction coil was rigidly fixed to an optical table separate from the shaker. The magnets were aligned within the coil as they would be during the harvesting experiment, or such that there would be a constant magnetic field for each half oscillation. Displacement data was collected for this constrained system with the shaker operating at $10Hz$ and $1.5mm$ displacement. Voltage data was collected across a load resistance of $R_L = 47\Omega$. The corresponding numerical system was constrained similarly for the same input conditions and load resistance. The transduction factor was varied until the numer-

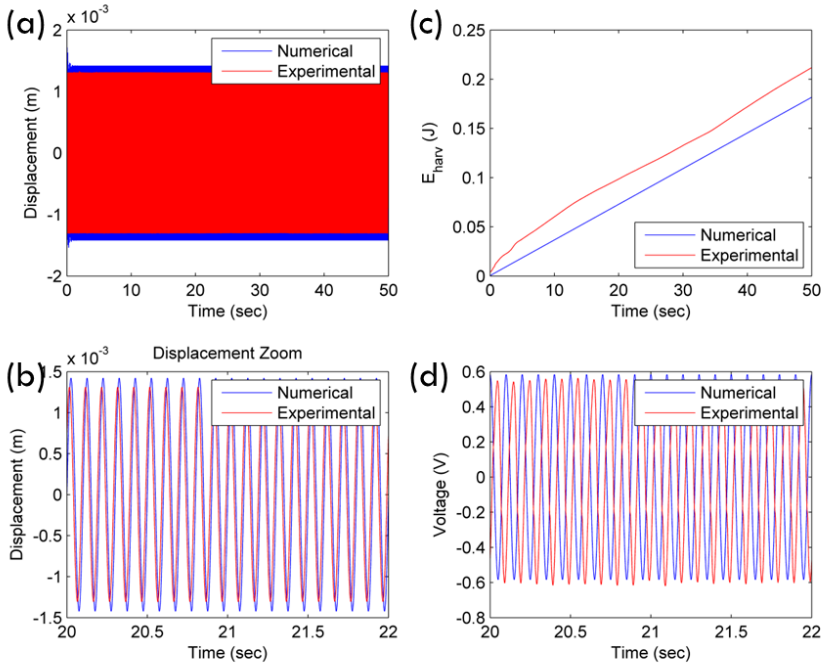

Figure 3.8: Comparison of numerical and experimental results for identification purposes of the transduction factor k_e: depicted as (a) full displacement times series, (b) zoomed in displacement time series, (c) energy harvested versus time, and (d) output voltage time series.

ical harvested energy was the same as the experimental harvested energy. The resulting transduction factor and electromagnetic damping parameters are outlined in Table 3.2. The comparison of experimental data from the setup modeled by Fig.3.7 with the numerical simulation data from system (3.26) with $k_e = 11Tm$ is depicted in Fig.3.8. As seen in Fig.3.8a,b, the displacement magnitudes of the numerical and experimental systems correspond strongly. Fig.3.8c depicts the same energy harvesting rate for the two systems and Fig.3.8d depicts similar voltage output. The analysis here validates the transduction factor, which is within the range estimated in Fig.3.6 for the constructed induction coil dimensions.

The final non-dimensional electromechanical coupling parameter β can thus be computed, which is shown in Table 3.1. It should be noted that the electromechanical parameter values presented in Table 3.1 and Table 3.2 have strong correspondence to the targeted design parameter values presented in Fig.3.6, validating the assumptions, design, and construction of the coil.

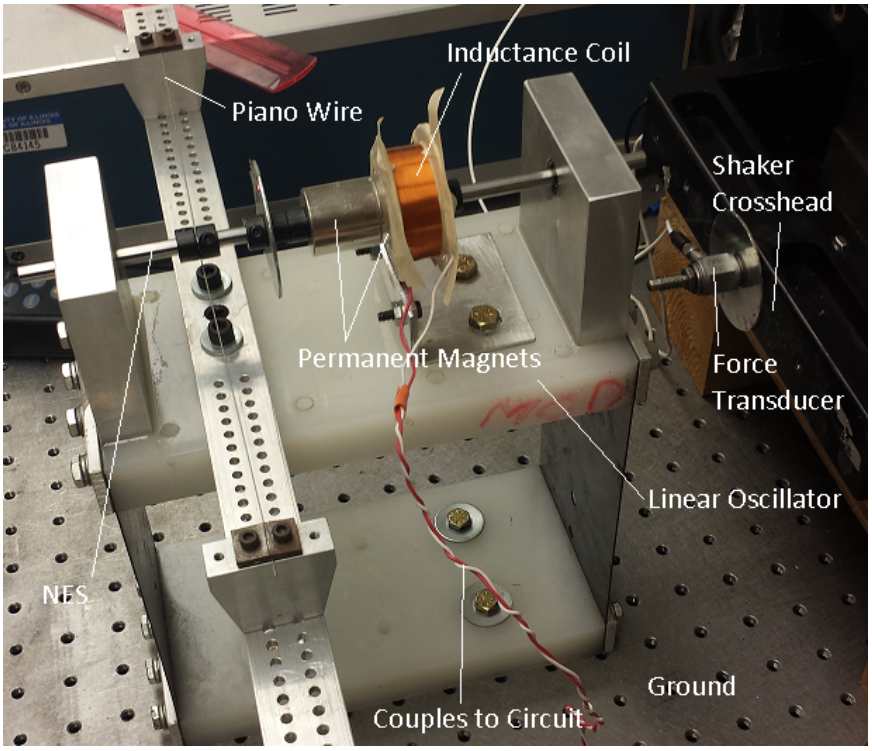

Figure 3.9: Experimental realization of the system depicted in Fig.3.1.

Motivated by the previous computational results that theoretically predicted high-frequency dynamic instability of the system, an experimental study was carried out in order to confirm the prediction. The result of this study is evaluated in the next section.

3.2.2 Experimental Study

The experimental apparatus is presented in Fig.3.9. The primary system is denoted in the figure as the linear oscillator (high-density polyethylene mounting mass), piano wire (aluminum cross-bar beam and steel wire), and inductance coil (copper coil and aluminum mount). The primary system is grounded to an optical table via two thin steel rectangles, which provide for the linear grounding stiffness and light viscous damping. The lightweight nonlinear attachment (NES) is composed of the permanent magnets, collar mounts, and a steel rod, which is supported by two linear roller bearings in each aluminum upright at the ends of the HDPE mounting mass. Additional damping in the coupling arises from the interaction of the rod with the bearings, which is approximated as linear viscous damping rather than

coulomb damping. The NES is coupled to the primary system via a piano wire of diameter $0.5mm$, which is physically attached to the NES via the collar mounts. These collar mounts also serve to precisely hold the permanent magnets in place. As seen in Fig.3.9, the piano wire is oriented perpendicular to the direction of motion of the attachment, through which the resulting transverse deflection gives rise to a dominant third order essential stiffness nonlinearity (cubic nonlinearity). The piano wire is mounted in the crossbar beam such that there is no pretension in the wire, minimizing any linear components in the coupling stiffness.

The inductance coil is constructed within a HDPE spool of inner radius $r_i = 14mm$. As described in Section 3.2.1, the coil is wrapped with $N = 819turns$ to achieve a thickness of $h_c = 16mm$ and outer radius $r_o = 20mm$, which provides the desired electromechanical coupling. The coil was wound by while striving to maintain the orthogonal fill factor, as described in the last section. Enameled AWG 30 copper wire is used to maximize turns while minimizing coil resistance. Two cylindrical neodymium (NdFeB) permanent magnets with dimensions $25.4mm$ outside diameter and $25.4mm$ length are used to create a uniform magnetic field within the coil. Neodymium magnets provide a strong magnetic field flux density for their size; the selected magnets provided a flux density of $B = 1.32T$. The coil leads are connected to a breadboard and placed in series with a simple resistor, which functions as the load resistance for computing energy harvesting capability. The experimentally identified parameters for the physical apparatus from Section 3.2.1 are summarized in Table 3.2. This system is modeled numerically as described by (3.15).

Impulsive forces are applied to the linear oscillator by use of an instrumented PCB 086D20 modal hammer with a hard plastic tip with the system initially at rest, striving to replicate the initial conditions imposed in (3.19). Absolute velocity time series measurements of the two oscillators are recorded using two Polytec PSV laser vibrometers with a sampling frequency of $S_F = 8.192kHz$ over a period of $t_f = 2.0s$. Voltage time series measurement is taken across the load resistance, which could later be used to compute output power from the harvesting elements. The data acquisition is synchronized using the modal hammer as the trigger to start acquisition, with a small pretrigger time of $196ms$. This synchronized measurement of the response of the system is important for accurate computation of the relative

Table 3.2: Dimensional parameters for the experimental apparatus described by system (3.15)

Parameter	Value
m_1	1.535 kg
b_1	0.480 Ns/m
k_1	4300 N/m
m_2	0.284 kg
b_2	10.0 Ns/m
k_2	322,647 N/m
h	0.133 m
b_e	1.53 Ns/m
k_e	11 Tm
R_c	32.1 Ω
R_L	47 Ω

displacement wavelet spectra by eliminating any phase-mismatch in the measurements. The raw velocity time series data is numerically integrated during post-processing to obtain absolute displacement time series data for each of the oscillators. The wavelet spectra are computed during post-processing from the time series data as in the computation study.

A series of ten experimental trials were conducted using the apparatus and measurement scheme described above. The trials covered a wide range of excitation magnitudes corresponding to the range explored in the non-dimensional system (3.17) from Section 3.2.1. This range spanned $I_0 = [0.5 - 1.2]m/s$, which was determined from the maximum velocity of the primary system directly following the impulse from the modal hammer. The average width of the half-sine pulse provided from the modal hammer was $\sim 1.8ms$. Recall that the forcing in the non-dimensional system (3.17) was assumed to be *Dirac* in nature, so a minimized pulse width from the hammer excitation was important to approaching this assumption in the numerical system.

This work seeks to expand the following results into a study of this system under repeated impulse excitation to maintain energy harvesting from high-frequency instability. To enhance this effort, the experimental results are compared to the corresponding numerical system (3.15). The corresponding numerical system is simulated using the forcing data from the modal hammer

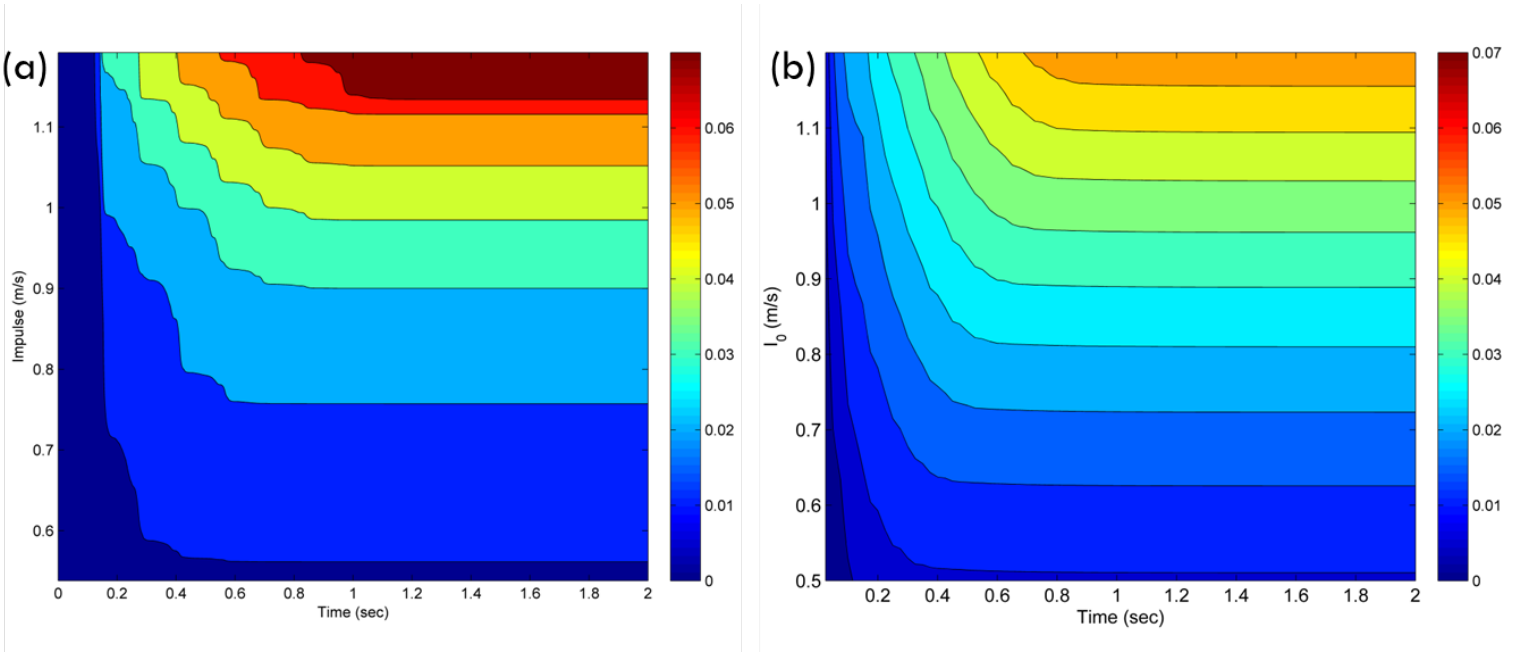

Figure 3.10: (a) Experimental and (b) numerical energy harvesting performance over time for various impulse magnitudes. Energy harvesting performance evaluated from (3.24) is presented in *Joules*.

in the experimental trials as a means to validate the parameter identification from Section 3.2.1. The numerical system is further explored using the *Dirac* forcing assumption, as is done for the non-dimensional system (3.17) in Section 3.2.1. This will allow for accurate exploration of the numerical system (3.15) forced by repetitive impulses in the next work if there is good correspondence between the experimental and numerical responses.

Performance contour plots for the system (3.15) are developed experimentally and numerically (*Dirac* forcing) using energy harvesting measure (3.24) reported in *Joules*. These results are presented in Fig.3.10. While Fig.3.10b is constructed "smoothly" for impulse values discretized as $\Delta I_0 = 0.01$ for the whole range presented, there is some degree of interpolation in the data presented in Fig.3.10a due to a larger discretization ΔI_0 from only performing ten experimental trials. This figure is analyzed by focusing on horizontal "slices" in the contour and deducing the rate at which energy is being harvested. The pretrigger imposed in the data collection accounts for the first $\sim 0.2s$ of no harvesting in Fig.3.10a, whereas the *Dirac* forcing used in Fig.3.10b initiates harvesting at the onset of the simulation. As deduced from Fig.3.10, the harvesting performance (3.24) from the experimental appara-

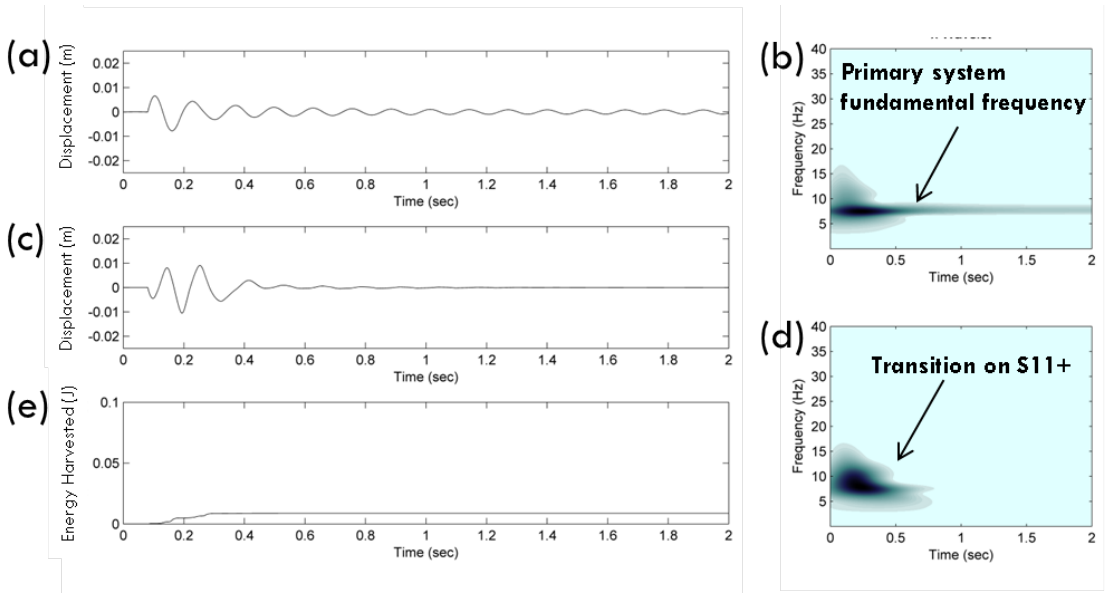

Figure 3.11: (a) Primary system displacement time history, (b) primary system displacement wavelet, (c) relative displacement time history, (d) relative displacement wavelet, and (e) energy harvesting performance measure (3.24) for the experimental apparatus presented in Fig.3.9 subject to low intensity impulsive excitation of magnitude $I_0 = 0.54m/s$ from modal hammer.

tus has strong qualitative and quantitative correspondence to the harvesting performance from the numerical system (3.15). As seen in Fig.3.10a, the apparatus harvests more energy at a faster rate for higher impulse magnitudes, which was predicted in Section 3.2.1 (cf. Fig.3.3 and Fig.3.5). The contour in Fig.3.10a indicates a maximum experimentally harvested energy of $\sim 70mJ$ over a duration of $\sim 1.0s$, providing an average output power of $\sim 70mW$. It is again predicted that this superior performance at higher energy levels is due to the presence of the high-frequency TRCs in the response of the system. For these large impulse excitations, the system harvests energy for $\sim 1.0s$ before most likely coming to rest, which is indicated experimentally and numerically by Fig.3.10. The performance of the experimental apparatus can be analyzed further by investigating the time series and wavelet spectra for individual trials.

The response of the experimental apparatus shown in Fig.3.9 for a low impulse intensity of $I_0 = 0.54m/s$ is presented in Fig.3.11. As seen in Fig.3.11a,b, the primary system oscillates at its fundamental frequency of $8.4Hz$ before eventually coming to rest. As seen in Fig.3.11c,d, the NES

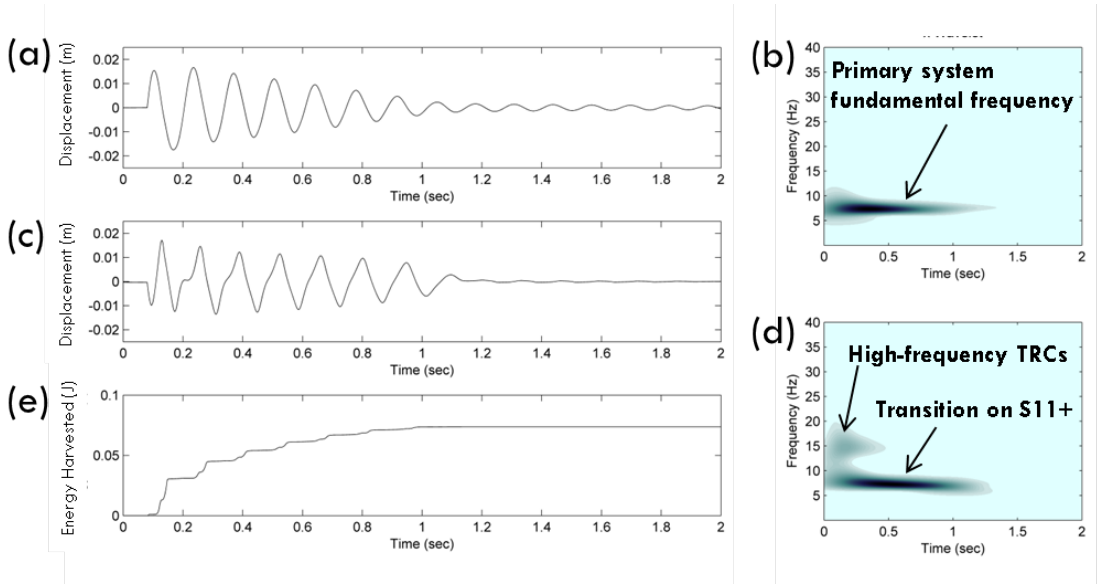

Figure 3.12: (a) Primary system displacement time history, (b) primary system displacement wavelet, (c) relative displacement time history, (d) relative displacement wavelet, and (e) energy harvesting performance measure (3.24) for the experimental apparatus presented in Fig.3.9 subject to high intensity impulsive excitation of magnitude $I_0 = 1.19m/s$. from modal hammer

simply engages in 1:1 internal resonance capture with the primary system before coming to rest after $\sim 0.4s$. The energy input into the linear oscillator isn't large enough to excite the high energy solutions presented in Fig.3.2. The apparatus exhibits poor energy harvesting performance in this case, as seen in Fig.3.11e. A maximum energy of $11mJ$ is harvested slowly for a duration of $\sim 0.4s$, resulting in an average power of $\sim 27.5mW$. This performance is predicted in the non-dimensional study presented in Section 3.2.1, which is confirmed here experimentally.

A much different response is obtained for stronger applied impulses. The response of the experimental apparatus for a high impulse intensity of $I_0 = 1.19m/s$ is presented in Fig.3.12. As with the low intensity impulse shown in Fig.3.11a, the primary system oscillates at its fundamental frequency before coming to rest, as indicated by Fig.3.12a,b. This behavior is predicted by the non-dimensional system (3.17) for any magnitude impulse excitation. This indicates that the attachment doesn't affect the underlying dynamics of the primary system, rather just the rate at which energy is removed from the primary system. As seen in the relative displacement time series in Fig.3.12c

and more clearly in the relative displacement wavelet in Fig.3.12d, the NES initially engages in high-frequency TRCs with the primary system in the neighborhood of the upper branch of the IOM within the first $\sim 0.4s$. This high-frequency TRC occurs in the neighborhood of the 2:1 superharmonic internal resonance tongue, as indicated by the frequency content of $\sim 16Hz$ in Fig.3.12d. The corresponding energy harvested during the first $\sim 0.4s$ can be deduced from Fig.3.12e, which indicates $55mJ$ of energy is harvested with a resulting average power of $\sim 137.5mW$. The initial energy input into the primary system is now large enough to excite the high energy solution presented in Fig.3.2. As energy is removed via harvesting and passive dissipation, the system cannot remain operating in the high-frequency solution regime, which is indicated by Fig.3.12d. As seen in the figure, the NES transitions to the $S11+$ branch after $\sim 0.4s$, engaging in 1:1 internal resonance capture with the primary system. Similar to the performance presented in Fig.3.11d,e, energy is harvested at a slower rate for an additional $\sim 0.7s$ during the 1:1 internal resonance capture, as deduced from Fig.3.12d,e. A maximum energy of $72mJ$ is harvested for a total duration of $1.1s$, resulting in a total average power of $65.5mW$. This performance is predicted in the non-dimensional study presented in Section 3.2.1, which is confirmed here experimentally. This increased energy harvesting performance during high-frequency TRCs is the primary goal of this study and is now confirmed here for a novel experimental apparatus.

As discussed earlier, another goal of this study is to validate the identified parameters from Table 3.2. This is accomplished in the analysis that follows by comparing the experimental system response presented in Fig.3.12 with the corresponding numerical system (3.15) response utilizing the experimental forcing data. The system (3.15) is integrated numerically for $t_f = 2.0s$ using the large impulse intensity of $I_0 = 1.19m/s$, which is presented in Fig.3.13. Similar to the experimental apparatus, Fig.3.13a,b indicates that the primary system oscillates at its fundamental frequency before coming to rest. Again similar to the experimental apparatus, Fig.3.13c,d indicates that the NES initially engages in high-frequency TRCs with the primary system in the neighborhood of the upper branch of the IOM within the first $\sim 0.3s$. The transitions depicted in Fig.3.12d and Fig.3.13d vary slightly in that the experimental system shows dominant transition on the 2:1 superharmonic tongue while the numerical system shows transitions near the 3:1 and 2:1 su-

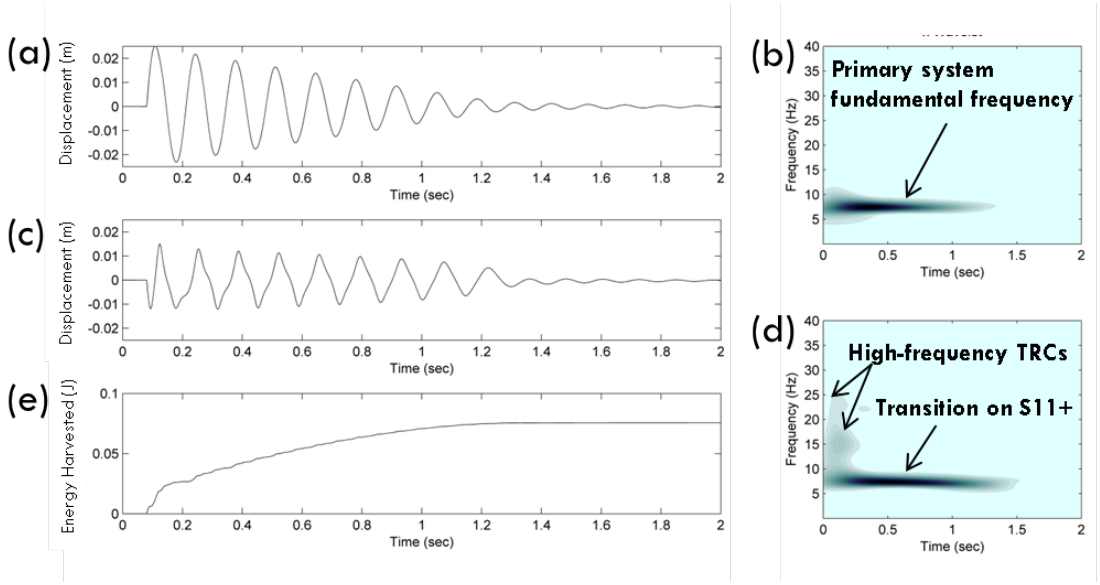

Figure 3.13: (a) Primary system displacement time history, (b) primary system displacement wavelet, (c) relative displacement time history, (d) relative displacement wavelet, and (e) energy harvesting performance measure (3.24) for the numerical system (3.15) subject to high intensity impulsive excitation of magnitude $I_0 = 1.19m/s$ provided from experimental data collected from the modal hammer. Figure generated using numerical simulation with experimental forcing data.

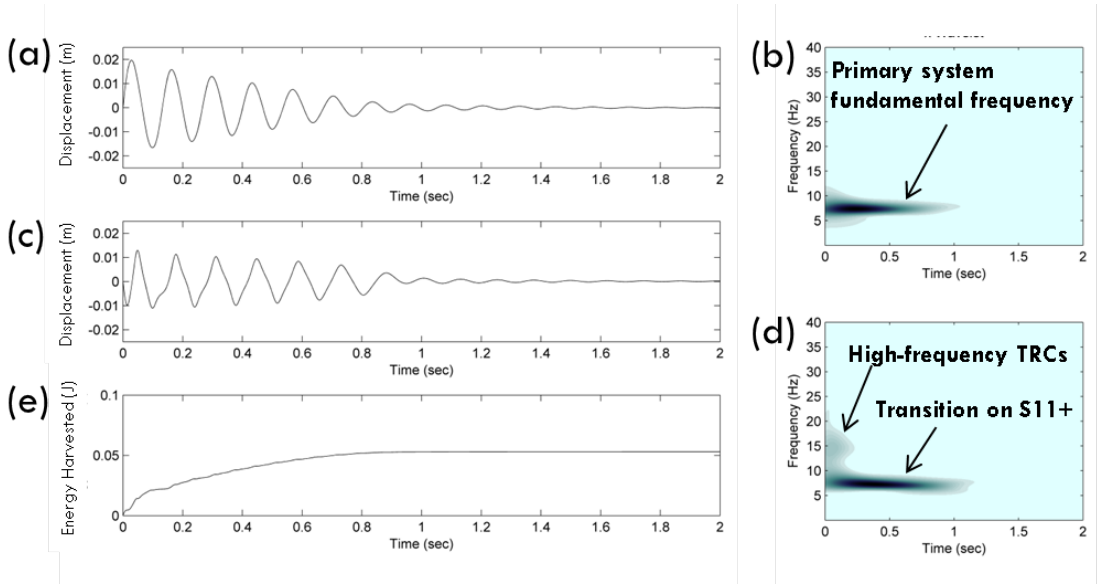

Figure 3.14: (a) Primary system displacement time history, (b) primary system displacement wavelet, (c) relative displacement time history, (d) relative displacement wavelet, and (e) energy harvesting performance measure (3.24) for the numerical system (3.15) subject to high intensity impulsive excitation of magnitude $I_0 = 1.19m/s$ provided from a pulse of *Dirac* nature. Figure generated using purely numerical simulation.

perharmonic tongues within the first $\sim 0.3s$. This slight variation in TRCs doesn't persist long enough to have a profound effect on the energy harvested before the NES transitions to the $S11+$ branch, as indicated by the similar energy harvesting capability in Fig.3.12e and Fig.3.13e. Comparing Fig.3.12a and Fig.3.13a, it can be seen that the numerical system experiences higher initial displacements than the experimental system for the first few cycles. The passive viscous damping in the experimental apparatus may be slightly greater than identified and used in the numerical system, allowing for different frequency transitions. This could also be the effect of coulomb friction present in the experimental system at the bearing and rod interface. Nevertheless, it is concluded here that the identified parameter set presented in Table 3.2 is validated. Numerical simulations of system (3.15) utilizing lower intensity impulse data from the experiments continues to show good quantitative and qualitative correspondence between the results.

It serves to now accurately explore system (3.15) numerically using a series of *Dirac* pulses and thus construct a baseline for future experiments. It must be shown that the *Dirac* pulse assumption is a good approximation of

the experimental forcing. This is accomplished in the analysis that follows by comparing the experimental system response presented in Fig.3.12 with the corresponding numerical system (3.15) response utilizing *Dirac* forcing. The system (3.15) is integrated numerically for $t_f = 2.0s$ using the large impulse intensity of $I_0 = 1.19m/s$, which is presented in Fig.3.14. Similar to the experimental apparatus, Fig.3.14a,b indicates that the primary system oscillates at its fundamental frequency before coming to rest. Again similar to the experimental apparatus, Fig.3.14c,d indicates that the NES initially engages in high-frequency TRCs with with the primary system in the neighborhood of the upper branch of the IOM within the first $\sim 0.2s$. The TRCs depicted in Fig.3.12d and Fig.3.14d are similar in that both exhibit dominant transitions on the 2:1 superharmonic tongue, but the transitions vary in length of time captured. Fig.3.14d depicts a faster transition to the 1:1 internal resonance branch than that presented in Fig.3.12d. This is most likely due to the difference in actual energy input into the system between the two forcing schemes. The excitation magnitude is based on the maximum velocity of the linear oscillator directly following the impulse, rather than the energy in the actual transmitted pulse. *Dirac* forcing assumes an infinitesimally small pulse width, while the experimental forcing has an average pulse width of $\sim 1.8ms$. Therefore the energy imparted into the system due to the *Dirac* forcing is conservative compared to the energy imparted into the system due to the experimental forcing from the modal hammer. This is evident in the overall lower energy harvested from the *Dirac* forcing (cf. Fig.3.14e) when compared to the overall higher energy harvested from the experimental apparatus (cf. Fig.3.12e). The characteristic increase in energy harvesting performance during high-frequency TRC is still present in Fig.3.14e for the *Dirac* forcing, which is most important for these purposes. Nevertheless, it is concluded here that the *Dirac* forcing scheme is an acceptable approximation of the experimental forcing from the modal hammer, with the energy consideration taken into account. Numerical simulations of system (3.15) utilizing lower intensity *Dirac* impulses continues to show good quantitative and qualitative correlation between the results.

3.3 Repeated Impulses

Motivated by the previous numerical and experimental results indicating superior energy harvesting performance due to harvesting during high-frequency instabilities induced by a single impulse, the work is now expanded to the same system (3.15) subjected to repeated impulses (3.21). The ability of the mechanical system to engage in sustained high-frequency dynamic instability was shown in Chapter 2. It is predicted theoretically in Section 4.1 that harvesting energy during this sustained high-frequency response will result in superior harvesting capability. The results of this study are discussed in this section.

3.3.1 Computational Study

The system (3.15) is analyzed in this section utilizing the experimental system parameters presented in Table 3.2, which were previously identified and validated during the work in Section 3.2.2. The system is subjected to the repeated impulsive forcing scheme (3.21) for various amplitudes and frequencies. The wavelet spectral analysis and energy harvesting performance measures described in (3.23), (3.24), and (3.25) are used to predict the harvesting capability of the experimental apparatus, which is depicted in Fig.3.9 and described in more detail in Section 3.3.2.

Analysis was performed for system (3.15) subject to a range of impulse periods μ_T and forcing amplitudes I_0. The energy harvested per impulse (3.24) and energy harvesting efficiency per impulse (3.25) were used to evaluate system performance when subject to these varying excitation conditions. Appropriate parameter ranges were established based on the physical excitation magnitudes and time scale applied to the system in Section 3.2.2. Recall from Section 3.1 that the impulse period is defined as the time between applied pulses t_p normalized by the fundamental period of the primary system T_0, or $\mu_T = t_p/T_0$. For the experimental parameters defined in Table 3.2, the fundamental period for this system is $T_0 = 0.0839s$. Contour plots were developed for an impulse period range $\mu_T = [1-6]cycles$ with step $\Delta\mu_T = 0.1$ and impulse magnitude range $I_0 = [0.1-1.5]m/s$ with step $\Delta I_0 = 0.005$. The system (3.17) was numerically integrated with initial conditions (3.22) for each (μ_T, I_0) parameter pair for a series of 40 impulses, allowing the sys-

tem to reach steady-state conditions for each parameter pair. The resulting time series for each of these parameter pair numerical simulations is post-processed to produce the performance measures described above.

Recall from the discussion in Section 3.1.1 and Fig.3.2 that the initial energy state following the applied impulse dictates which orbits are "experienced" by the system. This is expected as nonlinear vibrational systems are strongly dependent upon excitation frequency and amplitude. This knowledge is important for the understanding of Fig.3.15 and Fig.3.16. The work in Chapter 2 also indicates that large initial energy states under the initial conditions (3.22) correspond to high-frequency dynamic instabilities in the neighborhood of the upper IOM. The experimental apparatus is forced into this high-frequency state in Section 3.2 using a single impulse, which provides for superior energy harvesting performance while operating in the high-frequency regime. Recall that it is the primary goal of this work to demonstrate that this high-frequency instability can be sustained under proper forcing conditions, allowing for optimal energy harvesting conditions.

Contour plots for energy harvesting efficiency (3.25) and energy harvested in *Joules* (3.24) are depicted in Fig.3.15 and Fig.3.16, respectively, for the transient response of the system during the first four impulses and for the steady-state response at later impulses seventeen and eighteen. Steady-state conditions are obtained for all parameter (μ_T, I_0) combinations for the system after the first ~ 10 impulses.

As seen in the first impulse in Fig.3.15a, the energy harvesting efficiency is dependent upon the excitation amplitude and the amount of time that the system is allowed to oscillate. The efficiency behavior changes significantly upon application of the second impulse. As seen in Fig.3.15b, higher efficiency "ribs" start to form for discrete ranges of impulse periods, indicating that the phase of the primary system is important when exciting the system. This phase-dependence is predicted later in Section 4.1 when exploring deterministic and stochastic impulsive excitations for a related energy harvesting system and will be described in more detail in the analysis below. The efficiency is still dependent upon the magnitude of the applied impulse, with high efficiencies at low and high impulse magnitudes. These ribs continue to develop during the transient response of the system, as seen for the 3^{rd} and 4^{th} impulses in Fig.3.15c and Fig.3.15d, respectively.

The steady-state behavior of the system is obtained after ~ 10 impulses,

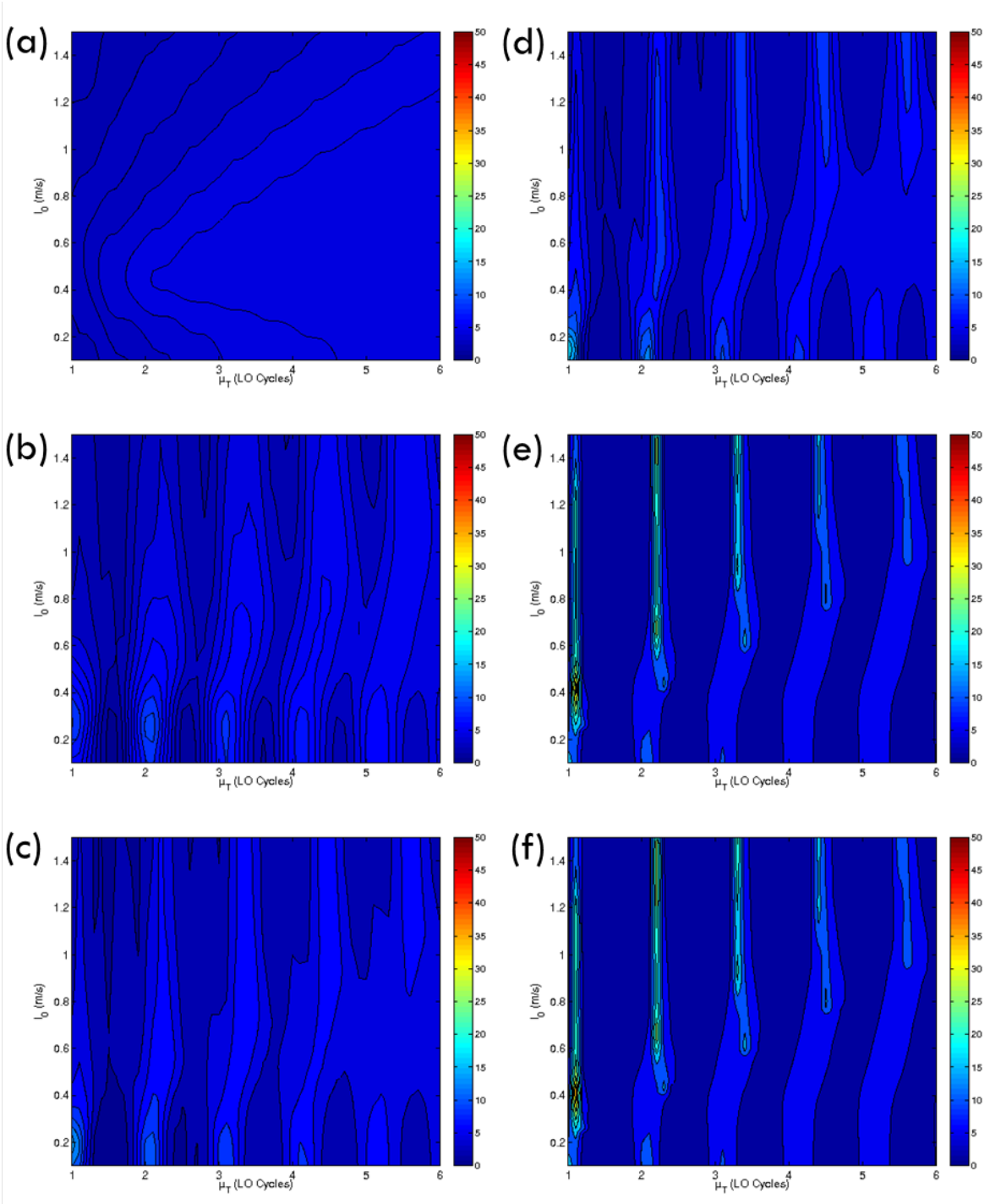

Figure 3.15: Energy harvesting efficiency performance measure (3.25) for the system (3.15) for various parameter sets (μ_T, I_0). Depicted here are impulse numbers (a) 1, (b) 2, (c) 3, (d) 4, (e) 17, (f) 18.

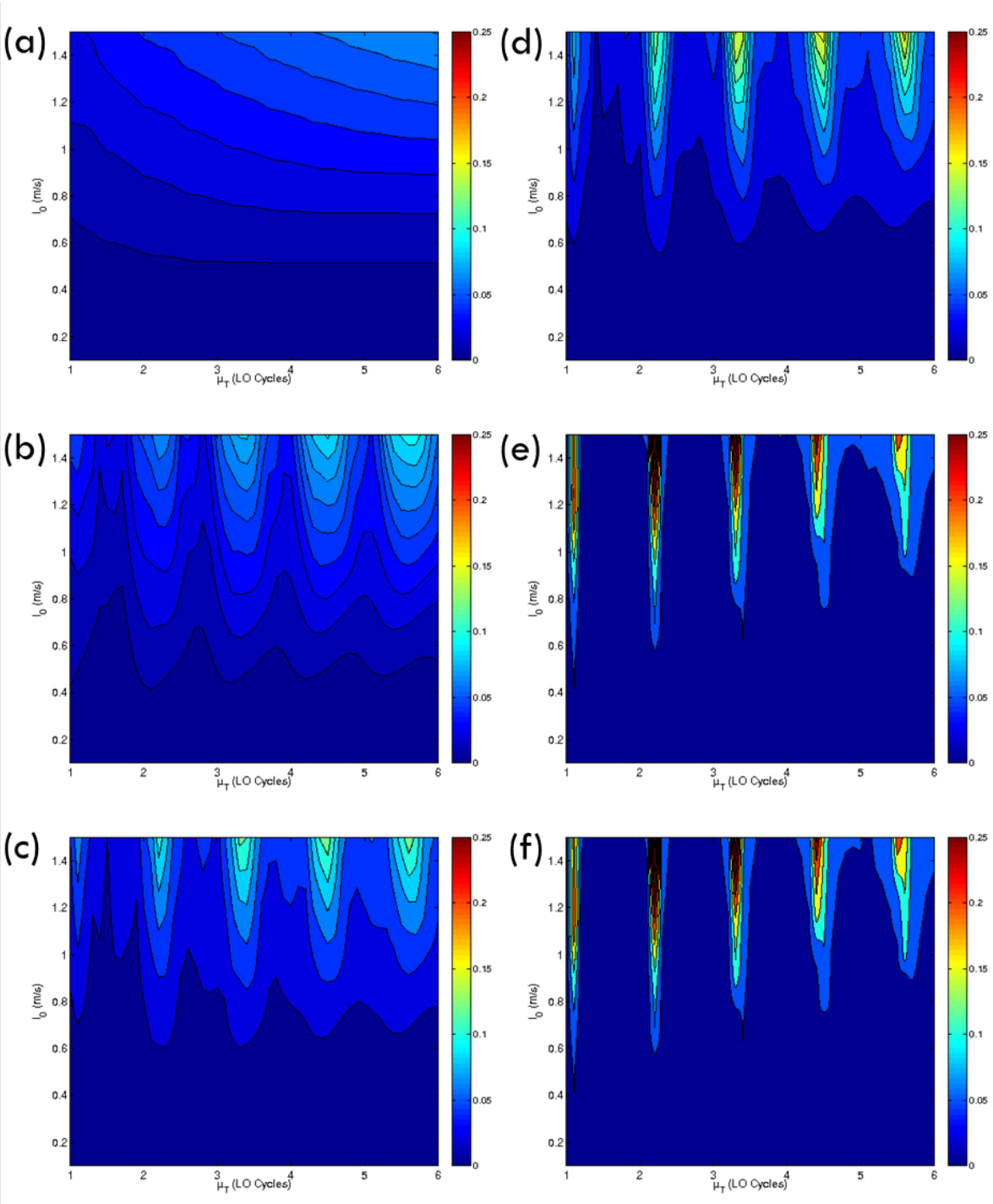

Figure 3.16: Energy harvesting efficiency performance measure (3.24) for the system (3.15) for various parameter sets (μ_T, I_0). Depicted here are impulse numbers (a) 1, (b) 2, (c) 3, (d) 4, (e) 17, (f) 18.

which is depicted and confirmed in Fig.3.15e,f for the 17^{th} and 18^{th} impulses, respectively. As seen in Fig.3.15f, discrete ribs of high efficiency impulse periods have fully formed, corresponding to excitation frequencies near multiples of the primary system fundamental period. The efficiency is still amplitude dependent, which dictates the optimal impulse period for a specific rib. For clarification, the second high efficiency rib has an optimal impulse period of $\mu_T = 2.1 cycles$ for excitation amplitudes $I_0 \leq 0.4 m/s$; however, the optimal impulse period increases to $\mu_T = 2.3 cycles$ for excitation amplitudes $I_0 > 0.4 m/s$. The disparity between optimal impulse periods increases for higher ribs; i.e., the longer the response develops. This is due to the different frequency transitions that occur at various system initial energy states, which dictates the energy harvesting capability of the apparatus.

For low impulse magnitudes, transitions in the neighborhood of the low-frequency IOM can occur, resulting in low-frequency instabilities during various TRCs on the subharmonic tongues, as indicated in Section 1.2 and in Fig.3.2. The higher efficiency behavior of the system for $\mu_T = [2.1, 3.2] cycles$ and $I_0 \leq 0.2 m/s$ is due to these low-frequency TRCs. These transitions result in a maximum efficiency of $\sim 15\%$. This work is focused on exciting the high-frequency TRCs, as performed experimentally in Section 3.2.2 for a single impulse, which results in superior energy harvesting performance. The work in Section 4.1 indicates computationally that sustaining these high-frequency instabilities results in continuous superior energy harvesting performance. This behavior is predicted for the higher impulse regions ($I_0 > 0.5 m/s$) of Fig.3.15f for the impulse periods governing the various high efficiency ribs. Demonstrating this behavior experimentally is the primary goal of this work, which will be numerically explored in more detail next. Energy harvesting efficiency greater than $\sim 30\%$ is predicted in these regions for this non-optimized experimental apparatus.

A similar analysis is indicated by the energy harvesting measure (3.24) depicted in Fig.3.16. The first impulse (cf. Fig.3.16a) indicates that the harvesting performance depends strongly on the impulse magnitude. As seen in Fig.3.16b, ribs of better harvesting performance begin to develop with the application of the second impulse, continuing to develop in the transient response regime depicted for the 3^{rd} and 4^{th} impulses in Fig.3.16c and Fig.3.16d, respectfully. The 17^{th} and 18^{th} impulses depicted in Fig.3.16e,f again indicate the steady-state response of the system. As seen in Fig.3.16f,

the energy harvesting capability of the system drastically increases in the predicted high-frequency response operating region described above relative to the lower-frequency region induced by lower excitation magnitudes. Energy harvesting capability greater than $\sim 50 - 250mJ$ is predicted in these high-frequency response regions for the experimental apparatus per applied impulse. Operating outside of these high-frequency ribs reduces energy harvesting performance significantly for this set of non-optimized parameters, which correspond to the experimental apparatus and are defined in Table 3.2. Specific time series and wavelet spectra are explored in more detail next to confirm the high-frequency TRC predictions established above.

The response of the system (3.15) for several specific (μ_T, I_0) forcing parameter sets is explored next for the predicted high-frequency response region presented in Fig.3.15f. The time series displacement and wavelet spectra response of the system for $I_0 = 0.8m/s$ and $\mu_T = [1.1, 1.65, 2.2, 2.75, 10]cycles$ for the first 20 applied impulses are plotted with the energy harvesting measure (3.24) to compare system performance. The impulse period parameters chosen reflect steady-state system response operating on two of the high performance ribs and the space between them. The y-axis scaling is held constant for all figures for comparison purposes. The six different colors used in the time history responses separate the applied impulses for identification purposes.

The response of the system for $\mu_T = 10cycles$ and $I_0 = 0.8m/s$ is depicted in Fig.3.17. This operating regime isn't depicted in Fig.3.15 due to the impulse period being greater than $6cycles$. As deduced earlier from Fig.3.15f and Fig.3.16f, the harvesting system (3.15) exhibits a phase-dependent regime of the dynamics for relatively small impulse periods. Maximum and minimum energy harvesting regions result in this regime due to the ability of the NES to engage in TRCs with the primary system. This dictates the "pumping" of energy from the primary system to the NES, in which the relative phase between the primary system and the applied impulse becomes very important. The work in Section 4.1 describes this behavior in further detail, which is more of a power absorption argument than the nonlinear nature of the harvester. A critical impulse period is reached after $\sim \mu_T = 9cycles$ for physically reasonable excitation magnitudes; i.e., $I_0 < 1.5m/s$. Above this critical period, the mechanical energy in the primary system following the application of an impulse is completely dissipated or harvested before

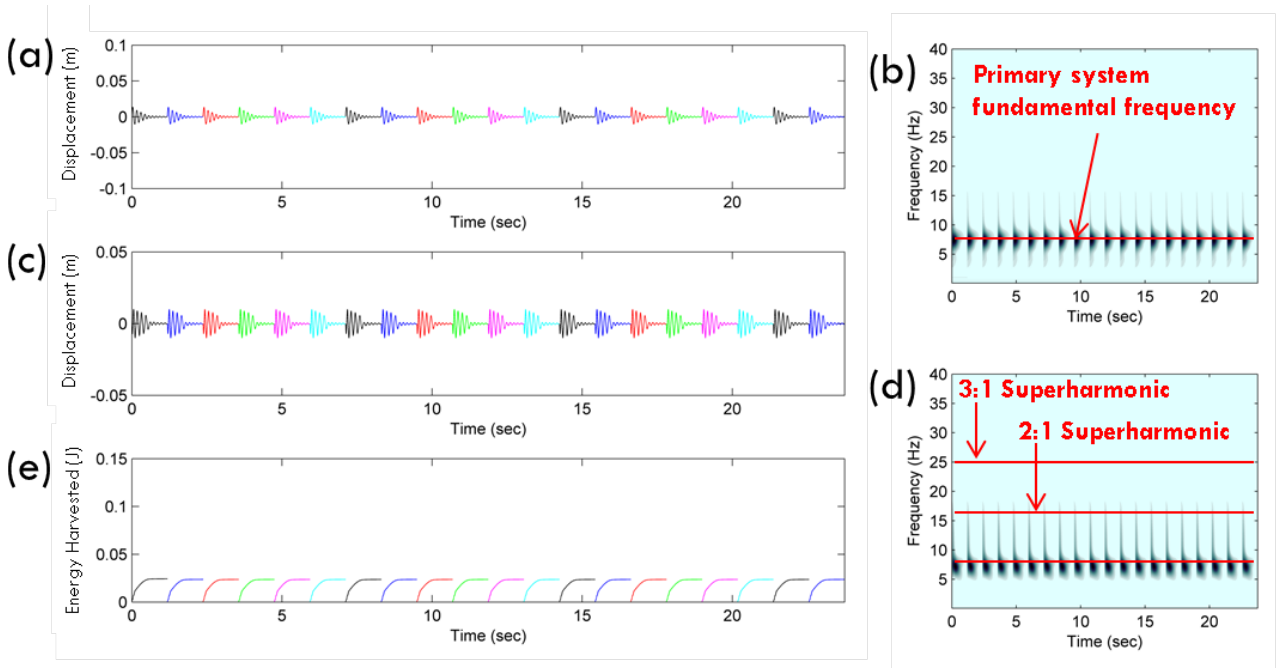

Figure 3.17: Numerical simulation for (a) primary system displacement time history, (b) primary system displacement wavelet, (c) relative displacement time history, (d) relative displacement wavelet, and (e) energy harvesting measure (3.24) for system (3.15) with $mu_T = 10.0 cycles$ and $I_0 = 0.8 m/s$.

the next impulse is applied. The response of the system above this critical operating point is considered periodic with a guaranteed energy harvesting value. The system response in this region replicates the single impulse results presented in Section 3.2.2, as expected.

As seen in Fig.3.17a,c, the primary system and NES come to rest before the next impulse is applied, as denoted by the color change in the time series. In addition the primary system oscillates at its fundamental frequency of $\sim 8Hz$, as indicated by Fig.3.17b. As seen clearly in Fig.3.17d, the transient response of the NES initially engages in 2:1 internal resonance capture in the neighborhood of the high-frequency IOM for each applied impulse. This behavior was predicted numerically and proved experimentally during the work in Section 3.2, and is recovered here for this system operating in this forcing regime. This is indicated in Fig.3.17d by the dominant high-frequency harmonics in the initial phase of the relative response for each impulse. Frequency transitions above the primary system fundamental frequency correspond to motions in which the NES oscillates faster than the primary system, which increases the energy harvesting capability of the sys-

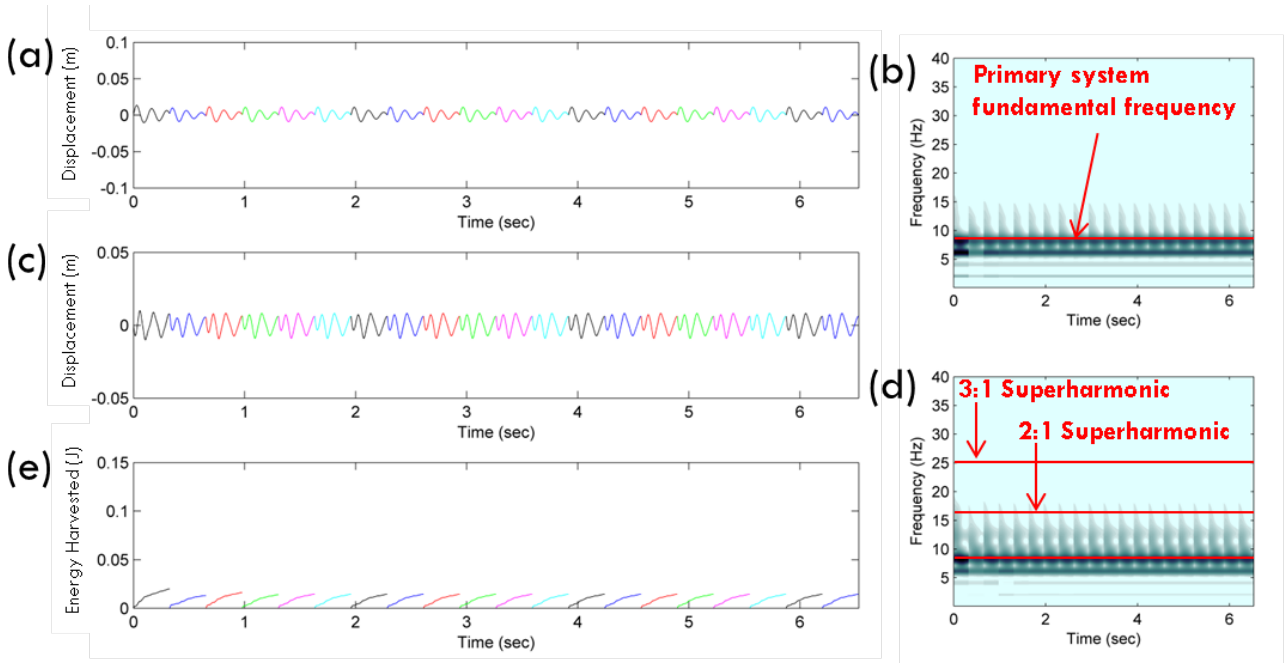

Figure 3.18: Numerical simulation for (a) primary system displacement time history, (b) primary system displacement wavelet, (c) relative displacement time history, (d) relative displacement wavelet, and (e) energy harvesting measure (3.24) for system (3.15) with $mu_T = 2.75 cycles$ and $I_0 = 0.8 m/s$.

tem. As energy is dissipated and harvested by the system, the dynamics transition to 1:1 internal resonance capture on the $S11+$ backbone branch, where energy is still harvested, but at a slower rate. The initial energy input in the primary system is enough to excite the high-frequency dynamic instabilities, but not maintain them for long. This is indicated by Fig.3.17e, in which energy is initially harvested quickly before slowly increasing and eventually reaching a maximum plateau as the system comes to rest. For this excitation magnitude, the system operating above the critical impulse period has a steady-state maximum energy harvesting capability of $\sim 25mJ$ per impulse. At this critical operating period, this results in an average harvested power of $\sim 23mW$ per impulse. Recall that the primary goal of this work is to harvest energy while sustaining the high-frequency TRCs associated with the 3:1 and 2:1 superharmonic tongues described in Section 3.1.1, allowing for continuous superior energy harvesting performance.

The response of the system for $\mu_T = 2.75 cycles$ and $I_0 = 0.8 m/s$ is depicted in Fig.3.18. This excitation parameter set corresponds to the high energy phase-dependent regime, but between high performance ribs, as seen

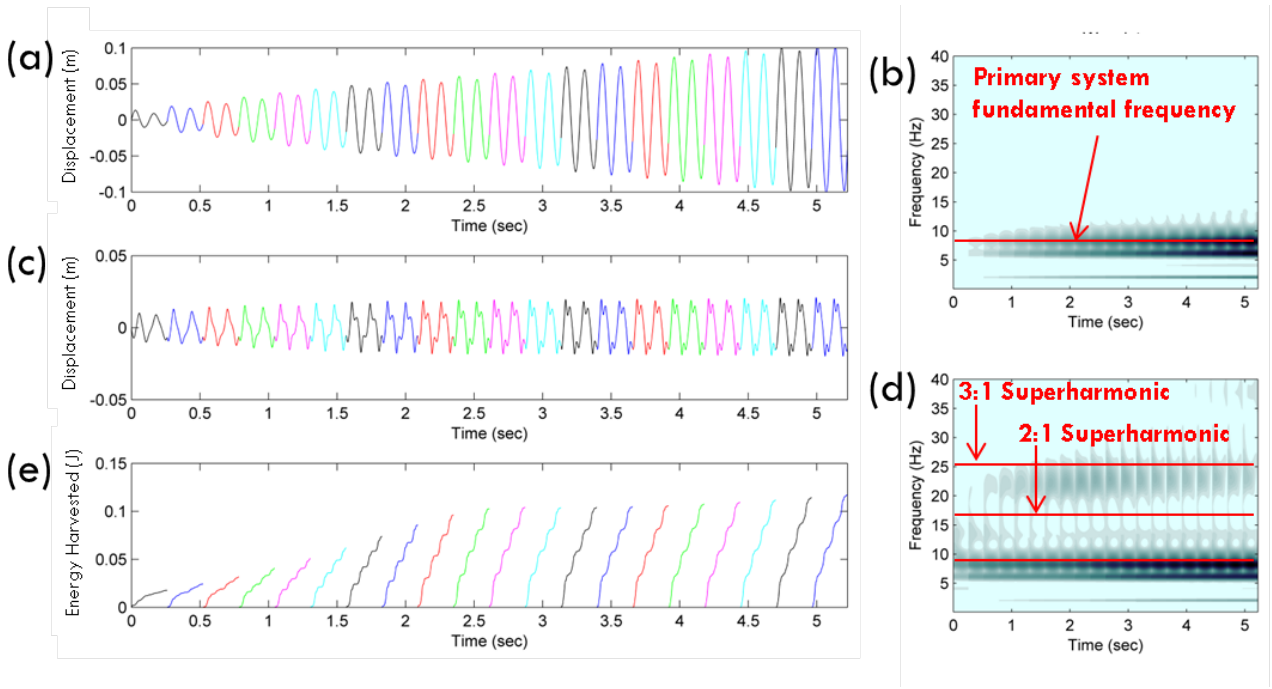

Figure 3.19: Numerical simulation for (a) primary system displacement time history, (b) primary system displacement wavelet, (c) relative displacement time history, (d) relative displacement wavelet, and (e) energy harvesting measure (3.24) for system (3.15) with $mu_T = 2.2cycles$ and $I_0 = 0.8m/s$.

in Fig.3.16f. In Fig.3.18a, the primary system oscillates for $2.75cycles$ before the next impulse is applied to it, which is again denoted by the color change. In addition the primary system still oscillates at its fundamental frequency of $\sim 8Hz$, as indicated by Fig.3.18b. The relative displacement wavelet depicted in Fig.3.18d indicates some high-frequency dynamics with 3:2 resonance characteristics; however, the response quickly transitions to 1:1 internal resonance capture similar to the response depicted in Fig.3.17d. These operating conditions result in lower energy harvesting performance with a steady-state capability of $\sim 20mJ$ per impulse, as indicated by Fig.3.18e. However for this shorter duration impulse period, the average harvested power is $\sim 61mW$ per impulse, which is an improvement relative to the the non-phase-dependent impulse period operating regime.

The response of the system for $\mu_T = 2.2cycles$ and $I_0 = 0.8m/s$ is depicted in Fig.3.19. This excitation parameter set corresponds to the high energy phase-dependent regime, but on the second high performance rib, as seen in Fig.3.16f. In Fig.3.19a, the primary system oscillates for $2.2cycles$

before the next impulse is applied to it, which now causes the response to grow with each consecutive impulse. In addition the primary system still oscillates at its fundamental frequency of $\sim 8Hz$, as indicated by Fig.3.19b. The relative displacement wavelet depicted in Fig.3.19d now indicates very different behavior for the steady-state dynamics of the system. As seen in the figure, the transient response behavior occurs for the first 10 impulses, during which the system transitions from lower-frequency 3:2 and 1:1 resonance characteristics to a sustained high-frequency 3:1 transient resonance capture. This is indicated in Fig.3.19d by the dominant high-frequency harmonics that occur at $\sim 25Hz$, or $3T_0$. This 3:1 TRC is maintained for the duration of the response until the next impulse is applied, which then keeps the system response operating in the 3:1 regime. The build up of energy in the primary system after the first 3 impulses keeps the initial energy state of the system (directly following each impulse) high enough to remain in the 3:1 frequency regime. As seen in Fig.3.19e, this operating regime corresponds to superior energy harvesting performance in which energy is quickly harvested for the entire duration of each response. These operating conditions result in a steady-state energy harvesting capability of $\sim 120mJ$ per impulse, providing an average harvested power of $\sim 459mW$ per impulse. This is a vast improvement over the other operating conditions presented above.

The response of the system for $\mu_T = 1.65cycles$ and $I_0 = 0.8m/s$ is depicted in Fig.3.20. This excitation parameter set corresponds to the high energy phase-dependent regime, but again between high performance ribs, as seen in Fig.3.16f. As seen in Fig.3.20a, the primary system oscillates for $1.65cycles$ before the next impulse is applied to it. Unlike the results presented for $\mu_T = 2.2cycles$ in Fig.3.19a, the response of the primary system does not build up with each consecutive impulse, rather it remains in a relatively low-amplitude state. The relative displacement wavelet depicted in Fig.3.20d indicates some short-duration 2:1 resonance characteristics for alternating responses, but primarily 3:2 and 1:1 resonance characteristics are exhibited by the system for every response. As expected, Fig.3.20e indicates diminished energy harvesting capability of the system when operating under these forcing conditions. Although the steady-state energy harvesting capability is only $\sim 15mJ$ per impulse, the shorter impulse period results in an average harvested power of $\sim 77mW$ per impulse, which is an improvement over the non-phase-dependent impulse period operating regime.

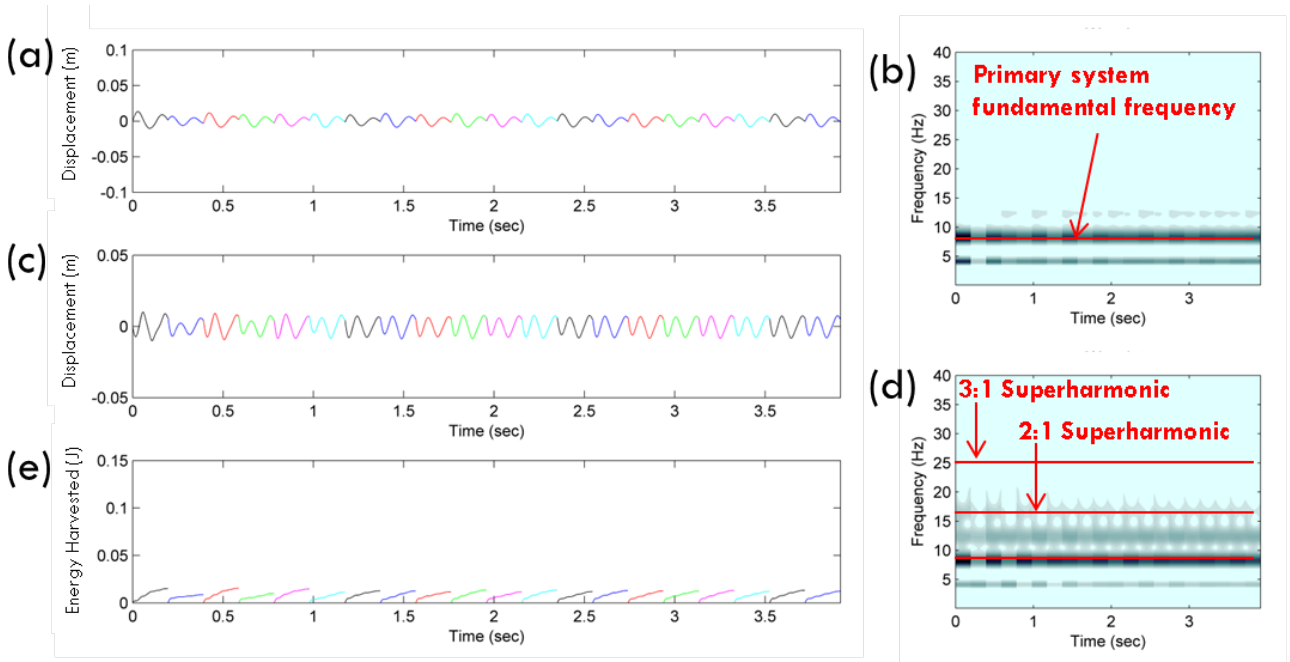

Figure 3.20: Numerical simulation for (a) primary system displacement time history, (b) primary system displacement wavelet, (c) relative displacement time history, (d) relative displacement wavelet, and (e) energy harvesting measure (3.24) for system (3.15) with $mu_T = 1.65 cycles$ and $I_0 = 0.8 m/s$.

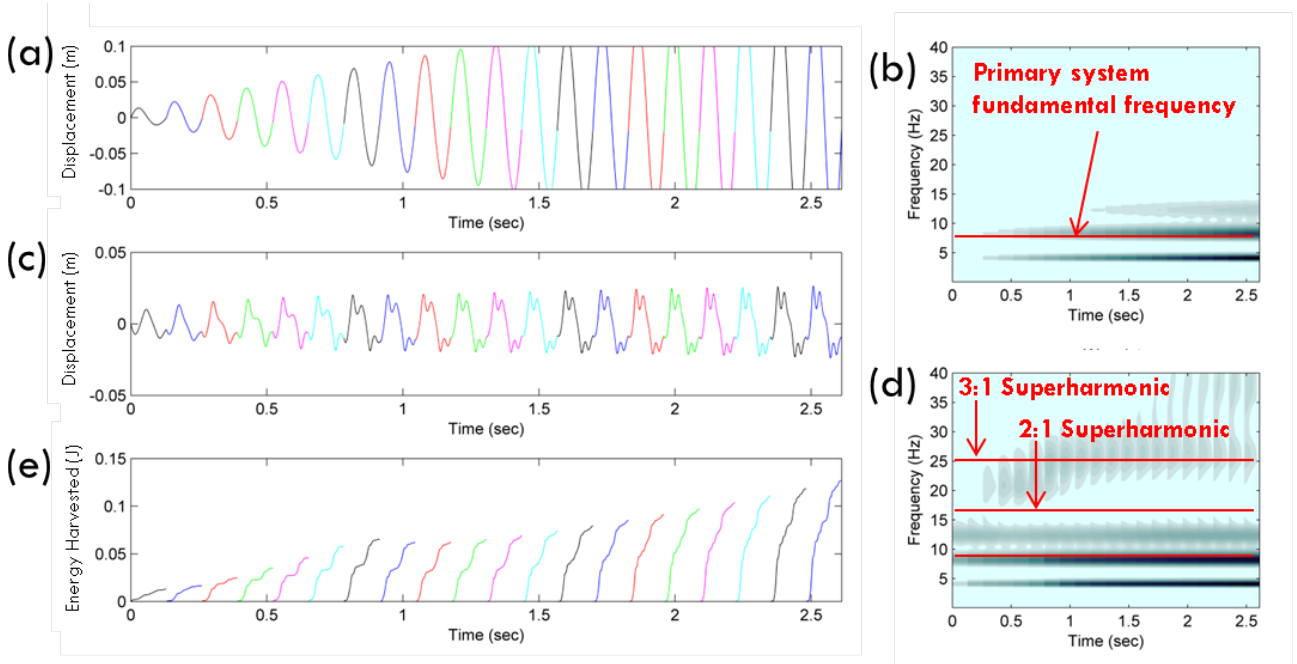

Figure 3.21: Numerical simulation for (a) primary system displacement time history, (b) primary system displacement wavelet, (c) relative displacement time history, (d) relative displacement wavelet, and (e) energy harvesting measure (3.24) for system (3.15) with $mu_T = 1.1 cycles$ and $I_0 = 0.8 m/s$.

The response of the system for $\mu_T = 1.1 cycles$ and $I_0 = 0.8 m/s$ is depicted in Fig.3.21. This excitation parameter set corresponds to the high energy phase-dependent regime, but on the first high performance rib, as seen in Fig.3.16f. In Fig.3.21a, the primary system oscillates for $1.1 cycles$ before the next impulse is applied to it which, similar to the response for $\mu_T = 2.2 cycles$ depicted in Fig.3.19a, causes the response to grow with each consecutive impulse. The excitation frequency for this forcing period is near the natural frequency of the primary system, which causes the response magnitude to grow even more than before. The relative displacement wavelet depicted in Fig.3.21d again indicates steady-state behavior similar to the response for $\mu_T = 2.2 cycles$ depicted in Fig.3.19d. As seen in Fig.3.21d, the transient response behavior occurs for the first 15 impulses, during which the system transitions from lower-frequency 3:2 and 1:1 resonance characteristics to a sustained high-frequency 3:1 transient resonance capture before continuing on to display 4:1 resonance characteristics. This is indicated in the figure by the dominant high-frequency harmonics that occur at $\sim 25 Hz$ and $\sim 34 Hz$ for times $t > 1.7 s$. These high-frequency instabilities are again maintained for the duration of the response before the next impulse is applied, which sustains the high-frequency oscillation and thus high-frequency energy harvesting. As seen in Fig.3.21e, this operating regime corresponds again to superior energy harvesting performance in which energy is quickly harvested for the entire duration of each response. These excitation conditions result in a steady-state energy harvesting capability of $\sim 125 mJ$ per impulse, providing an average harvested power of $\sim 957 mW$ per impulse.

A similar analysis was carried out for lower impulse magnitude regions of the contours presented in Fig.3.15 and Fig.3.16, in which $I_0 \leq 0.4 m/s$. Steady-state dynamics similar to those presented for $I_0 = 0.8 m/s$ and $\mu_T = [2.75, 1.65] cycles$ result in these lower harvesting performance regions, in which the responses briefly exhibit some high-frequency resonance characteristics before quickly transitioning to 1:1 internal resonance capture for the duration of the response. Energy can be harvested efficiently for these low-magnitude excitation regions when the impulse period keeps the system operating on one of the ribs presented in 3.15f; however, the overall amount of energy that can be harvested diminishes due to the system operating at purely 1:1 sustained resonance capture and the fact that there is less energy input to the primary system available for harvesting.

These computational results predict sustained high-frequency energy harvesting when the system (3.15) is subject to the proper conditions, resulting in superior energy harvesting capability relative to low-frequency conditions. Motivated by these numerical results and the experimental confirmation of the high-frequency instabilities in the physical apparatus from Section 3.2.2 subject to single impulses, an experimental study was carried out in order to confirm the predicted sustained high-frequency energy harvesting behavior. The results of this study are evaluated in the next section.

3.3.2 Experimental Study

The physical apparatus utilized for the experiments in Section 3.2.2 and for further analysis in this work is presented in Fig.3.9. System identification was performed using linear modal analysis and the restoring force surface method during the work in Section 3.2.1, in which further information is discussed for the electrical system design and identification. The resulting system parameters are displayed in Table 3.2. The apparatus pictured in Fig.3.9 is the physical realization of the model presented in Fig.3.1 with governing equations of motion (3.15). The NES mass consists of a steel rod with several collar mounts and two neodymium (NdFeB) permanent magnets, which oscillates within two linear roller bearings embedded withing the aluminum uprights on each end of the linear oscillator. The primary system is referred to as the linear oscillator in the figure, which is composed of a HDPE upper floor mounting mass, aluminum cross-bar beam and piano wire assembly, and a copper inductance coil with aluminum mounting bracket. This linear oscillator is grounded to a large optical table via two rectangular sheets of spring steel. The NES is coupled to the primary system via the collar mounts attached to the piano wire, which has a diameter of $0.5mm$. The essential cubic stiffness coupling nonlinearity arises from the transverse deflection of this piano wire relative to the direction of oscillation of the two masses. It is important that this piano wire is mounted such that there is no pretension, which minimizes the possibility of any linear effects in the coupling stiffness. The moderate linear viscous damping in the coupling arises primarily from the interaction of the rod with the linear roller bearings.

As mentioned above, two cylindrical neodymium permanent magnets con-

stitute a significant percentage of the NES mass. The selected magnets provided a flux density of $B = 1.32T$, as identified by the manufacturer, and have an outer diameter of $25.4mm$ and length of $25.4mm$. The two magnets are placed together to provide for a uniform magnetic field within the coil, which was a key assumption during the system derivation. The inductance coil was simulated and constructed during Section 3.2.1 to achieve a physically realizable electromechanical coupling, although coil optimization was not strictly a goal of the study. Enameled AWG 30 copper wire is used to maximize size while minimizing coil resistance, which essentially adds additional linear viscous damping to the system without the benefit of contributing to energy harvesting output. The wire is wound within an HDPE spool of inner radius $14mm$ with $N = 819turns$. The coil leads are soldered to longer wires, which are connected to a breadboard. A simple 47Ω resistor is placed in series with the coil, which functions as the load resistance for computing energy harvesting capability.

The repeated impulsive forcing is applied to the primary system by use of an APS Dynamics Model 400 long-stroke electromagnetic shaker, which is positioned such that it strikes the horizontal and vertical center of mass of the linear oscillator. The black crosshead armature is pictured in Fig.3.9 to the right of the experimental apparatus. The stinger, which actually strikes the linear oscillator, is composed of a hard steel tip connected to a PCB 208C05 force transducer, which measures precisely the applied waveform of the forcing during each cycle. Recall from the modeling description in Section 3.1, the experimental forcing waveform takes the shape of a half-sine pulse of short time-width rather than a *Dirac* pulse of infinitesimally small time-width. The input frequency and voltage levels are adjusted until the desired impulse period and excitation magnitude are obtained. The excitation magnitude is physically realized as the initial velocity of the primary system directly following the first impulse. The force transducer also allows for precise separation of the data into discrete applied impulses for further analysis, as performed in the computational study. A custom-made square waveform is input into the shaker controller, resembling a discrete pulse train as described by (3.21). Elastic bands inside of the shaker are adjusted to precisely control the separation between the primary system and stinger tip, which was set to $1cm$.

Two Polytec PSV laser vibrometers with a sampling frequency of $S_F =$

$20.48Hz$ and a time period $t_f = 12.8s$ are used to record absolute velocity time series measurements of the two oscillators. This time period allows for acquisition of at least the first 40 impulses for every impulse period considered, providing confirmation of steady-state operating conditions. The instantaneous voltage across the resistive element in the circuit is also measured, which is used to compute output power from the harvesting device. A small pretrigger time of $128ms$ is used to capture the system state directly prior to any excitation, in which the system is at rest according to (3.20). The data acquisition systems of the two laser vibrometers are synchronized using the force transducer in the striker as the trigger to begin recording. Accurate computation of the relative displacement wavelet spectra requires this precise synchronization, which serves to eliminate any phase-lag in the acquisition. Numerical integration and filtering during post-processing of the data is used to obtain displacement time series measurements of the oscillators, with which the resulting wavelet spectra can be computed similarly to the computational study.

Using the experimental apparatus and measurement scheme described above, a series of twenty experimental trials were conducted. A wide range of excitation magnitudes for several discrete impulse periods corresponding to the numerical simulations were conducted for comparison purposes and to prove the ability of the harvesting apparatus to engage in sustained high-frequency energy harvesting. Recall that steady-state, sustained, high-frequency energy harvesting was predicted numerically for the system (3.15) operating on the high performance ribs depicted in Fig.3.16f, providing for superior energy harvesting capability. Experimental confirmation of this behavior is the primary goal of this study. The excitation range explored spanned from $I_0 = [0.3 - 1.0]m/s$ for impulse periods $\mu_T = [2.75, 2.2, 1.65, 1.1]cycles$. The average width of the half-sine pulse provided from the shaker striker was $\sim 1.3ms$ for each applied impulse. The following results correspond to excitation magnitude $I_0 = 0.8m/s$ for the impulse periods described above, corresponding directly to the numerical simulations presented in Fig.3.18-Fig.3.21. Displacement time series, wavelet spectra, and energy harvested (3.24) are plotted for the first twenty applied impulses, similarly to the numerical simulations. The y-axis scaling is held constant for all figures for comparison purposes, but differs from the scaling used in the numerical simulations. The six different colors used in the time history responses again

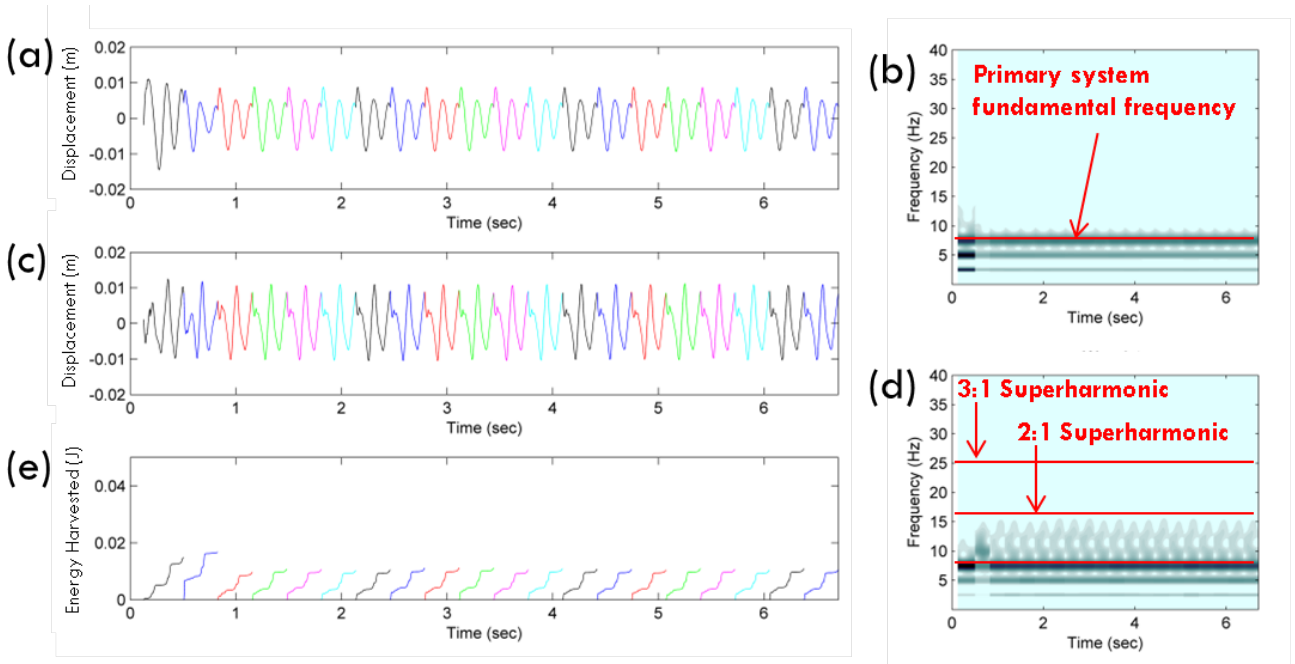

Figure 3.22: Experimental trial for (a) primary system displacement time history, (b) primary system displacement wavelet, (c) relative displacement time history, (d) relative displacement wavelet, and (e) energy harvesting measure (3.24) for system (3.15) with $mu_T = 2.75 cycles$ and $I_0 = 0.8 m/s$.

separate the applied impulses for identification purposes.

The response of the system for $\mu_T = 2.75 cycles$ and $I_0 = 0.8 m/s$ is depicted in Fig.3.22. This excitation parameter set corresponds to the high energy phase-dependent regime, but between high performance ribs, as seen in Fig.3.16f. In Fig.3.22a, the primary system oscillates for $\sim 2.75 cycles$ before the next impulse is applied to it, which is denoted by the color change. Recall that the impulses were separated for analysis using indexing from the force transducer data, which provided clear insight when each successive impulse was applied. Fig.3.22b indicates that the primary system oscillates at its fundamental frequency of $\sim 8 Hz$ similar to the numerical simulations. The relative displacement wavelet depicted in Fig.3.22d indicates some high-frequency brief dynamics with 3:2 resonance characteristics before the response primarily transitions to 1:1 internal resonance capture. This behavior correlates strongly to the response depicted in the numerical simulation in Fig.3.18d for the same excitation conditions. These operating conditions result in lower energy harvesting performance, as indicated in Fig.3.22e, in which energy is slowly harvested for the duration of the response. These

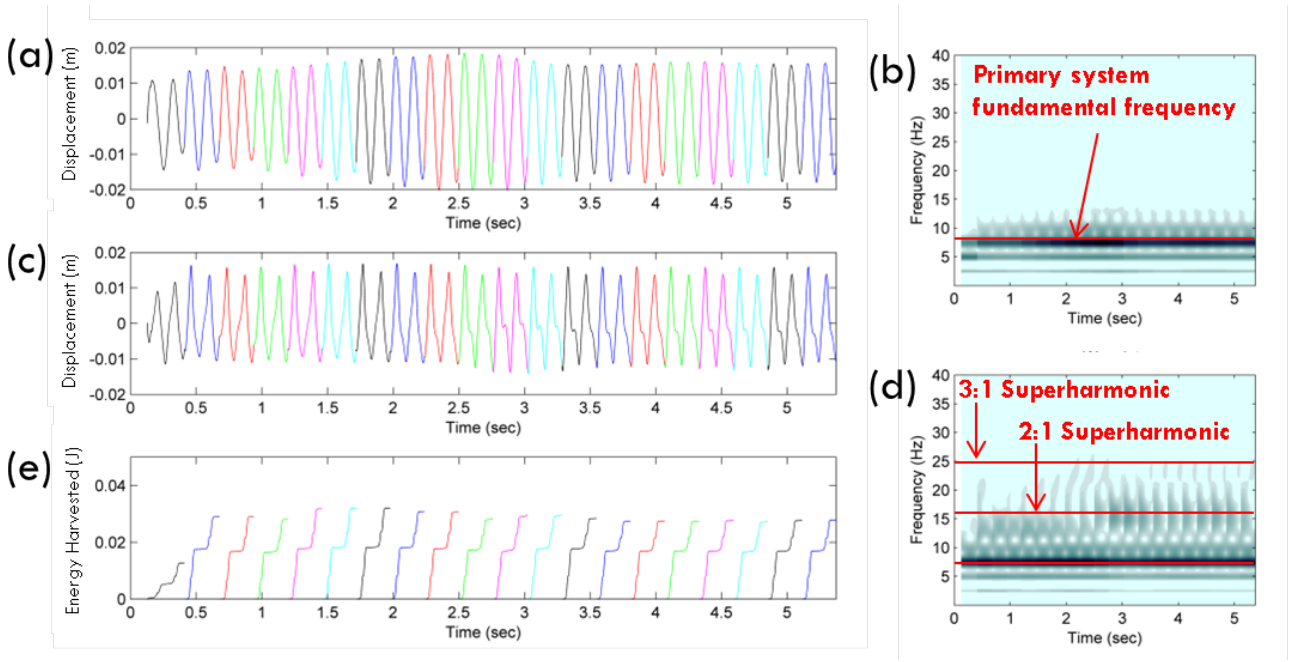

Figure 3.23: Experimental trial for (a) primary system displacement time history, (b) primary system displacement wavelet, (c) relative displacement time history, (d) relative displacement wavelet, and (e) energy harvesting measure (3.24) for system (3.15) with $mu_T = 2.2cycles$ and $I_0 = 0.8m/s$.

operating conditions result in a steady-state energy harvesting capability of $\sim 10mJ$ per impulse, providing an average harvested power of $\sim 31mW$. This is approximately half of what is predicted in Fig.3.18e.

The response of the system for $\mu_T = 2.2cycles$ and $I_0 = 0.8m/s$ is depicted in Fig.3.23. This excitation parameter set corresponds to the high energy phase-dependent regime, but on the second high performance rib, as depicted in Fig.3.16f. As seen in Fig.3.23a, the primary system oscillates for $\sim 2.2cycles$ before the next impulse is applied to it, which now causes the response to grow slightly with each consecutive impulse. Unlike the numerical simulation presented in Fig.3.19a, the primary system response grows to a bounded size rather than continually increasing for the response duration depicted. In addition the primary system still oscillates at its fundamental frequency of $\sim 8Hz$, as indicated by Fig.3.23b. The relative displacement wavelet depicted in Fig.3.23d now indicates very different behavior for the steady-state dynamics of the system. As seen in the figure, the transient response behavior occurs for the first 12 impulses, during which the system experiences various frequency transitions for each impulse response. The first

impulse corresponds to purely 1:1 internal resonance capture, in which energy is harvested slowly (cf. Fig.3.23e). The system response changes upon application of the second impulse due to the residual energy in the primary system. Recall from the analysis in Section 3.3.1 that the build up of energy in the primary system allows for a higher initial energy state upon application of successive impulses, providing the means for high-frequency dynamic instabilities to manifest. As seen in Fig.3.23d, impulses $2-9$ correspond to 2:1 transient resonance captures before transitioning back down to the 1:1 internal resonance branch briefly before the next impulse is applied. Impulses $10-12$ constitute the end of the transient response of the system, in which 2:1 transient resonance capture is sustained for the duration of the impulse. This is denoted in Fig.3.23d by the dominant high-frequency harmonics that occur at $\sim 16Hz$, or $2T_0$, for the duration of the response.

Steady-state conditions are obtained for the system with the application of the $13^{th}+$ impulses, in which the system experiences a very brief transition on the 3:1 resonance tongue before transitioning to sustained transient resonance capture on the 2:1 tongue for the duration of the response until the next impulse is applied, which keeps the system response operating in the 2:1 regime. As seen in Fig.3.23e, this operating regime corresponds to superior energy harvesting performance in which energy is quickly harvested for the entire duration of each response. These operating conditions result in a steady-state energy harvesting capability of $\sim 30mJ$ per impulse, providing an average harvested power of $\sim 115mW$ per impulse. This is approximately 4 times less than what is predicted in the numerical simulation for these forcing conditions in Fig.3.19e. This is attributed to the difference in how the energy builds up in the primary system, which results in different sustained frequency transitions. Recall that numerically sustained 3:1 TRCs are predicted for these conditions; however, experimentally sustained 2:1 TRCs are obtained. The work in Section 3.2 indicated that there is differences in the responses obtained when using the assumption of *Dirac* forcing numerically compared to the physical half-sine pulse that is actually imparted into the system. In fact, the *Dirac* forcing was a good approximation for the system response; however, inconsistencies can exist when extending the results to the case of repeated forcing. Nevertheless, sustained high-frequency dynamic instabilities resulting in superior energy harvesting on sustained 2:1 TRCs is demonstrated with this response presented in Fig.3.23, which is the primary

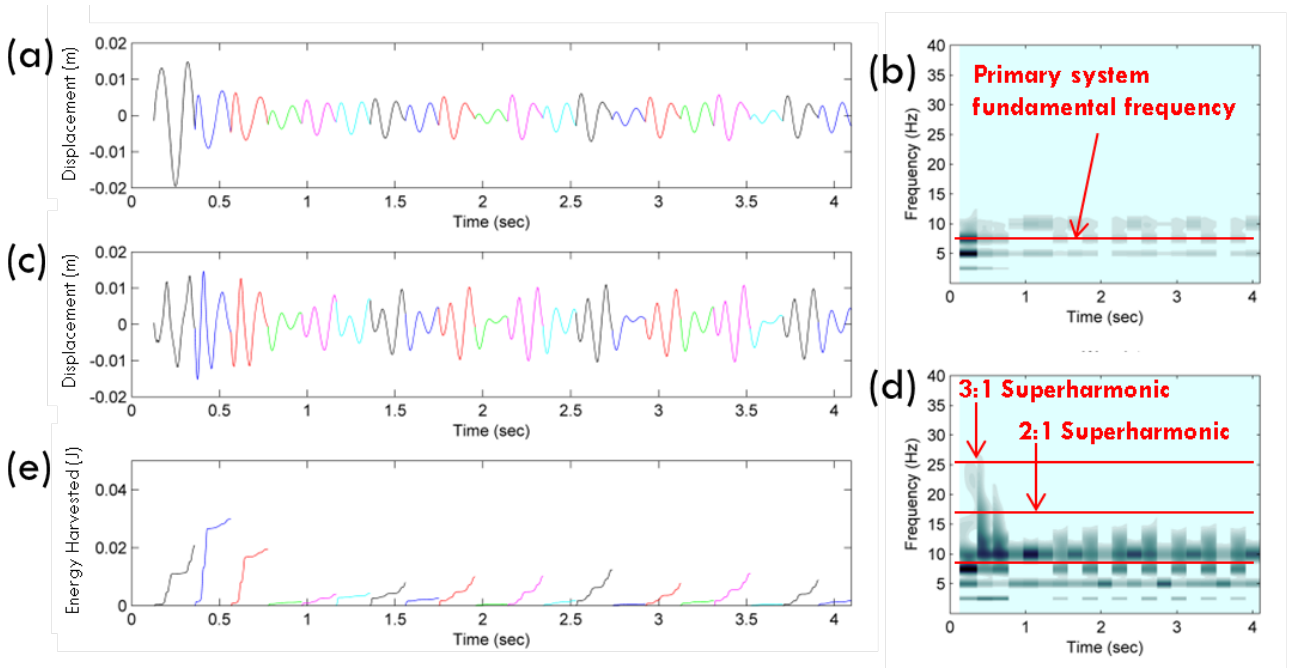

Figure 3.24: Experimental trial for (a) primary system displacement time history, (b) primary system displacement wavelet, (c) relative displacement time history, (d) relative displacement wavelet, and (e) energy harvesting measure (3.24) for system (3.15) with $mu_T = 1.65 cycles$ and $I_0 = 0.8 m/s$.

goal of this work.

The response of the system for $\mu_T = 1.65 cycles$ and $I_0 = 0.8 m/s$ is depicted in Fig.3.24. This excitation parameter set corresponds to the high energy phase-dependent regime, but again between high performance ribs as seen in Fig.3.16f. In Fig.3.24a, the primary system oscillates for $\sim 1.65 cycles$ before the next impulse is applied to it. Unlike the results presented for $\mu_T = 2.2 cycles$ in Fig.3.23a, the response of the primary system does not build up with each consecutive impulse; rather, it remains in a relatively low-amplitude state. The relative displacement wavelet depicted in Fig.3.24d indicates some brief 2:1 resonance characteristics during the first three impulses, in which energy is quickly harvested (cf. Fig.3.24e); however, the system enters into pseudo steady-state behavior after the first 7 impulses. Similar to the numerical prediction for these operating conditions deduced from Fig.3.20d, the system exhibits alternating 3:2 and 1:1 resonance characteristics for every two responses. As seen in Fig.3.24e, $\sim 10 mJ$ is harvested when the system exhibits brief high-frequency behavior and $\sim 1 mJ$ is harvested when the system exhibits primarily 1:1 resonance capture. This

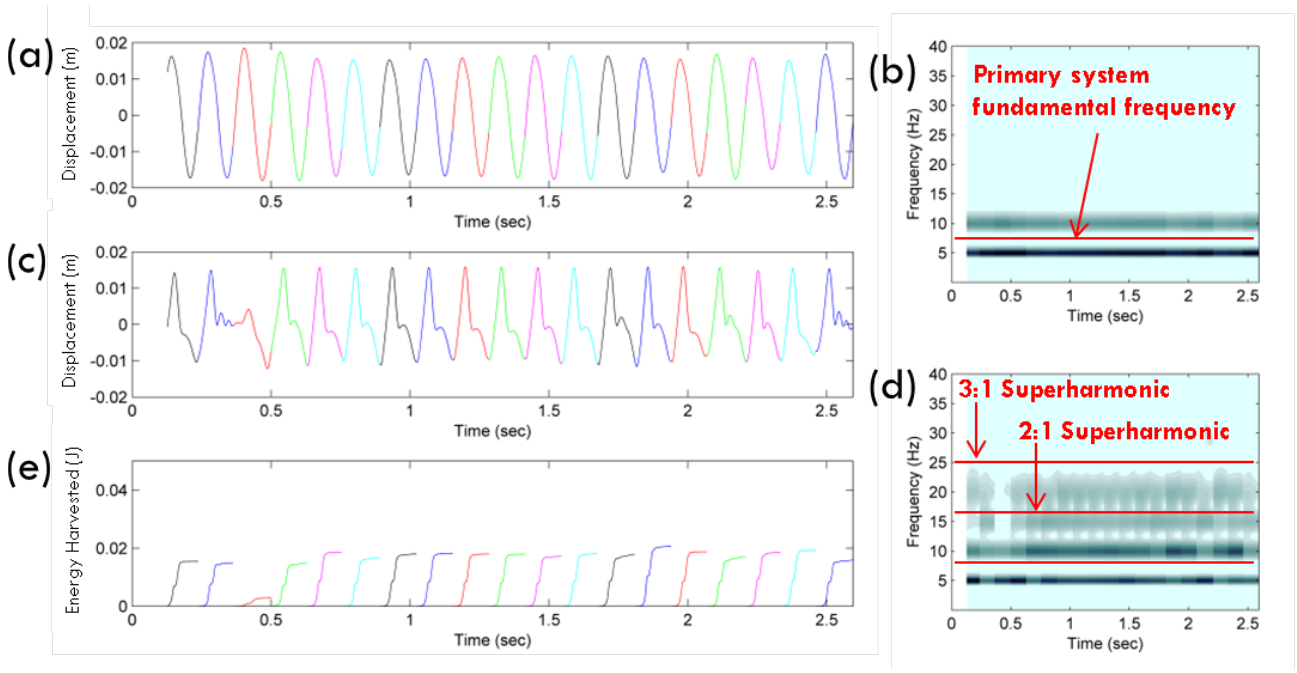

Figure 3.25: Experimental trial for (a) primary system displacement time history, (b) primary system displacement wavelet, (c) relative displacement time history, (d) relative displacement wavelet, and (e) energy harvesting measure (3.24) for system (3.15) with $mu_T = 1.1 cycles$ and $I_0 = 0.8 m/s$.

alternating harvesting response results in an average harvesting power of $\sim 28mW$, which is 2.75 times less than what was predicted numerically.

The response of the system for $\mu_T = 1.1 cycles$ and $I_0 = 0.8 m/s$ is depicted in Fig.3.25. This excitation parameter set corresponds to the high energy phase-dependent regime, but on the first high performance rib, as seen in Fig.3.16f. As seen in Fig.3.25a, the primary system oscillates for $\sim 0.9 - 1 cycles$ before the next impulse is applied to it, which maintains a bounded large-amplitude response similarly to the case for $\mu_T = 2.2 cycles$ presented in Fig.3.23a. The excitation frequency for this forcing period is near the natural frequency of the primary system, which causes the response of the primary system to behave slightly differently. As seen in the various impulses depicted in Fig.3.25a, the primary system doesn't oscillate for $1.1 cycles$ before the next impulse is applied as is originally intended; rather, an impulse period comparable to $\sim \mu_T = 0.85 cycles$ is realized. This is depicted in Fig.3.25b in which the primary system has a dominant oscillation frequency of $10 Hz$. This behavior is attributed to problems encountered with the interaction of the shaker and the experimental apparatus while trying to maintain large

forcing magnitudes near resonance.

Nevertheless, the relative displacement wavelet depicted in Fig.3.25d indicates steady-state behavior reflecting sustained 2:1 TRCs for the responses following the 4^{th} impulse. This is indicated in the Fig.3.25d by the dominant high frequency harmonics near $20Hz$, or 2 times the realized forcing frequency. The large amplitude response of the primary system again provides large initial energy states following each applied impulse that allow for high-frequency dynamic instabilities to manifest. The successive impulses maintain this energy level and thus the 2:1 TRCs. As seen in Fig.3.25e, this sustained high-frequency 2:1 TRCs result in superior energy harvesting capability, in which energy is quickly harvested for the duration of the response. These excitation conditions result in a steady-state energy harvesting capability of $\sim 18mJ$ per impulse, providing an average harvested power of $\sim 138mW$. This is approximately 7 times less than what is predicted in the numerical simulation for these forcing conditions in Fig.3.21e; however, once again this is attributed to the difference in the forcing between the numerical system and the experimental system described earlier for $\mu_T = 2.2cycles$. Again with this impulse period, sustained 2:1 TRCs are obtained experimentally rather than the numerically predicted 3:1 TRCs. Nevertheless, sustained high-frequency dynamic instabilities resulting in superior energy harvesting on sustained 2:1 TRCs is again observed for this response presented in Fig.3.25. Perhaps most importantly, this excitation scenario shows the robustness of this harvesting apparatus for excitation frequencies above the natural frequency of the primary system, in which the NES can adapt for superior energy harvesting by still engaging in sustained superharmonic responses.

The response of the system for $\mu_T = 2.2cycles$ and $I_0 = 0.6m/s$ is depicted in Fig.3.26. This excitation parameter set corresponds to the low energy phase-dependent regime and on the second high performance rib, as depicted in Fig.3.15f. As seen in Fig.3.26a, the primary system oscillates for $\sim 2.2cycles$ before the next impulse is applied to it. Unlike the case in which $I_0 = 0.8m/s$ depicted in Fig.3.23a, the primary system response in Fig.3.26a does not grow with each applied impulse, rather the response decays until a low-amplitude steady-state is obtained. The primary system still oscillates at its fundamental frequency of $\sim 8Hz$, as indicated by Fig.3.26b. The relative displacement wavelet depicted in Fig.3.26d no indicates very different

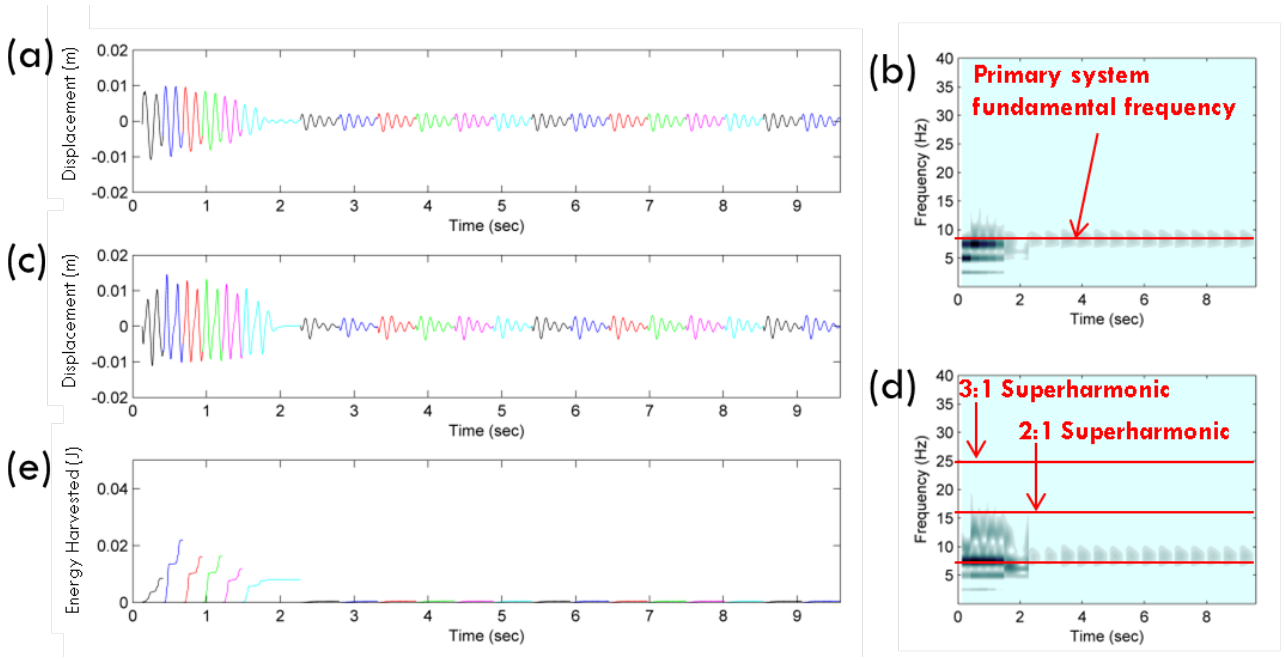

Figure 3.26: Experimental trial for (a) primary system displacement time history, (b) primary system displacement wavelet, (c) relative displacement time history, (d) relative displacement wavelet, and (e) energy harvesting measure (3.24) for system (3.15) with $mu_T = 2.2 cycles$ and $I_0 = 0.6 m/s$.

behavior for the steady-state dynamics of the system relative to those indicated for the system subject to higher forcing in Fig.3.23d. The first impulse corresponds to purely 1:1 internal resonance capture, in which energy is harvested slowly (cf. Fig.3.26e). The system response changes upon application of the second impulse due to the residual energy in the primary system, in which brief 2:1 resonance characteristics result followed by transition to the lower frequency 1:1 resonance branch. This cycle repeats for impulses $3-6$, after which the response of the harvester becomes locked into 1:1 internal resonance with the primary system. Once the harvester is locked into this state, each successive impulse doesn't impart enough additional energy into the system to induce high-frequency energy states. As seen in Fig.3.26e, this steady-state behavior results in poor energy harvesting performance, with an average energy harvested of $\sim 0.5mJ$ per impulse. This results in an average harvested power of $\sim 1.91mW$ per impulse. This is a significant reduction from the $\sim 115mW$ reported for the same impulse period but in the high energy regime.

The response of the system for $\mu_T = 1.1 cycles$ and $I_0 = 0.3 m/s$ is depicted

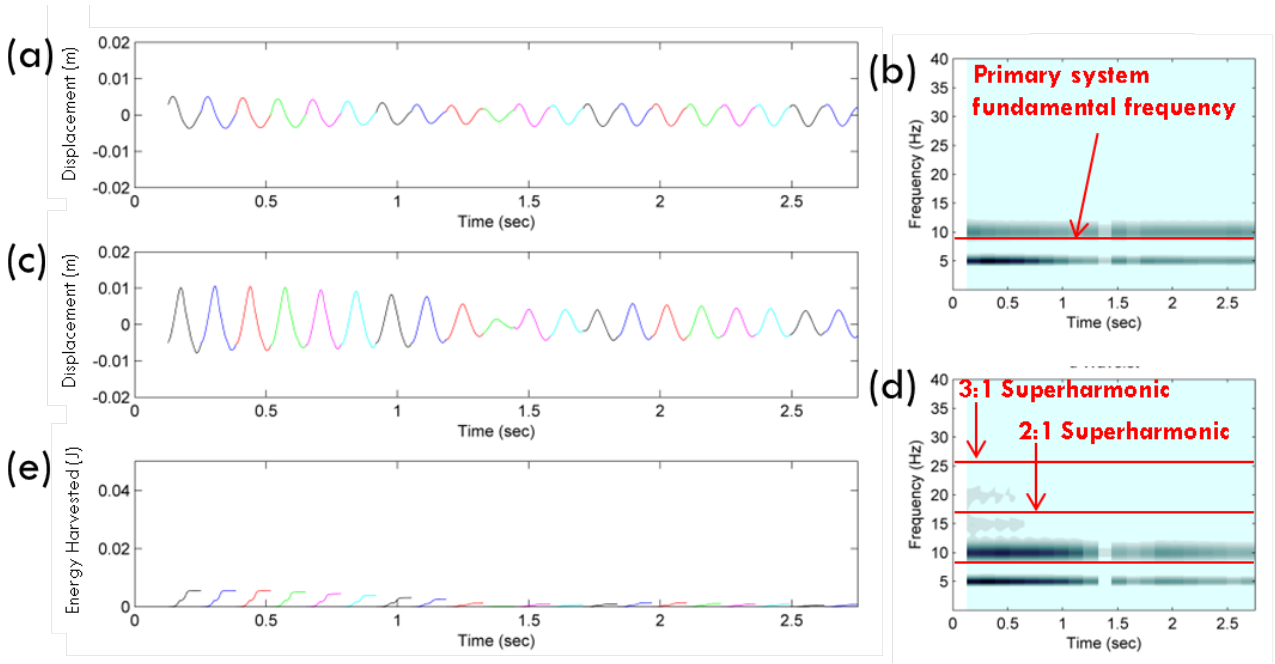

Figure 3.27: Experimental trial for (a) primary system displacement time history, (b) primary system displacement wavelet, (c) relative displacement time history, (d) relative displacement wavelet, and (e) energy harvesting measure (3.24) for system (3.15) with $mu_T = 1.1 cycles$ and $I_0 = 0.3 m/s$.

in Fig.3.27. This excitation parameter set corresponds to the low energy phase-dependent regime and on the first high performance rib, as depicted in Fig.3.15f. As seen in Fig.3.27a, the primary system oscillates for $\sim 0.9 - 1 cycles$ before the next impulse is applied to it. Unlike the case in which $I_0 = 0.8 m/s$ depicted in Fig.3.25a, the primary system response in Fig.3.27a does not grow with each applied impulse; rather, the response decays until a low-amplitude steady-state is obtained. As seen in Fig.3.27b, the primary system oscillates at a slightly higher frequency due to the variability in the forcing. Nevertheless, the relative displacement wavelet depicted in Fig.3.27d indicates similar behavior to that depicted for the previous case in Fig.3.26. After the first ~ 7 impulses, the system becomes locked into 1:1 resonance with the primary system, resulting in poor energy harvesting performance, as depicted in Fig.3.27e. As seen in the figure, a steady-state energy harvesting capability of $\sim 1 mJ$ per impulse is obtained with an average harvested power capability of $\sim 7.66 mW$. This is a significant reduction from the $\sim 138 mW$ reported for the same impulse period but in the high energy regime.

A summary of steady-state energy harvesting capability for all the ex-

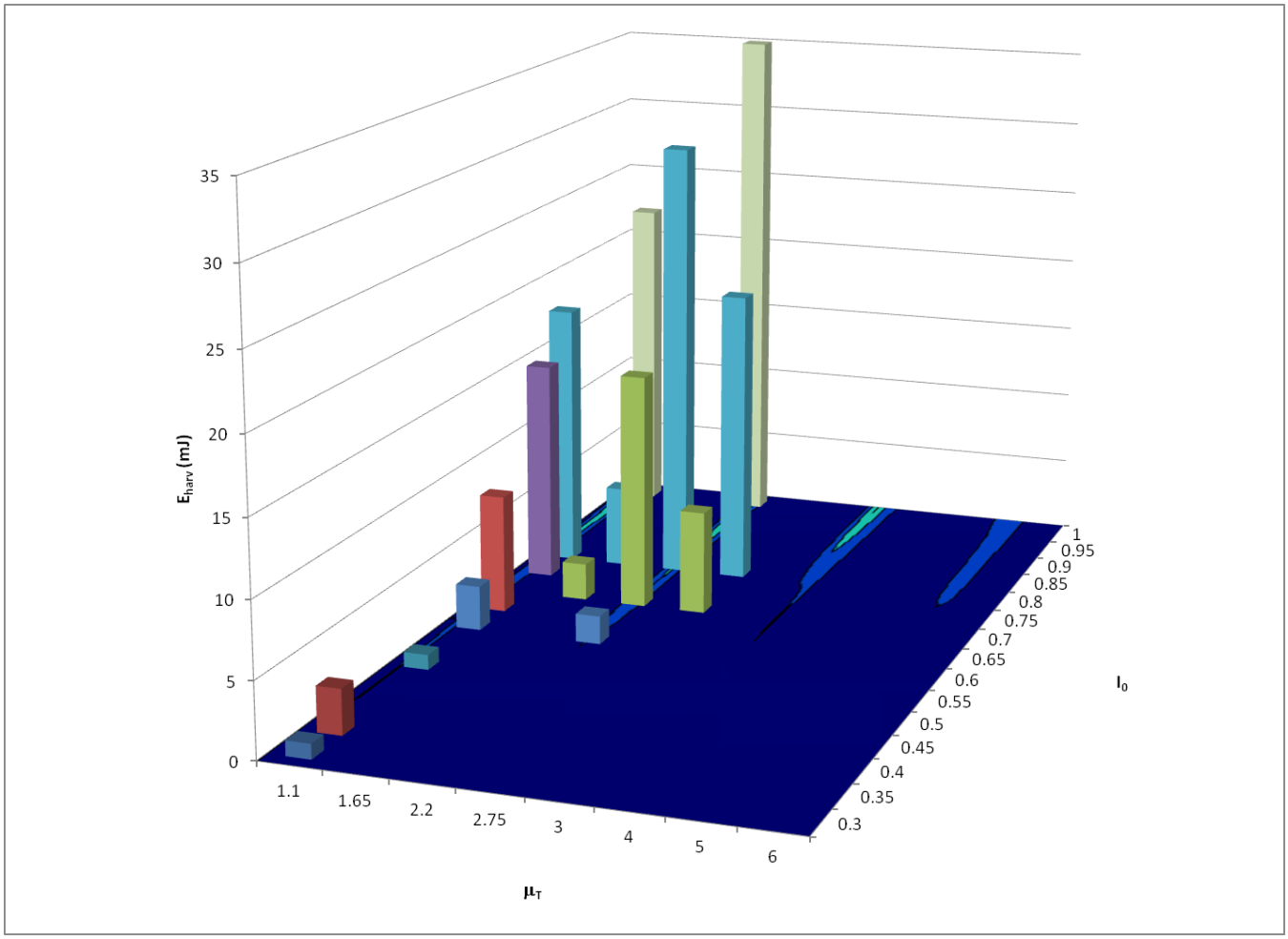

Figure 3.28: Summary of steady-state energy harvesting capability (3.24) for all experimental trials for the case of repeated impulsive loading of the apparatus of Fig.3.1 superimposed on the steady-state contour plot of Fig.3.16f.

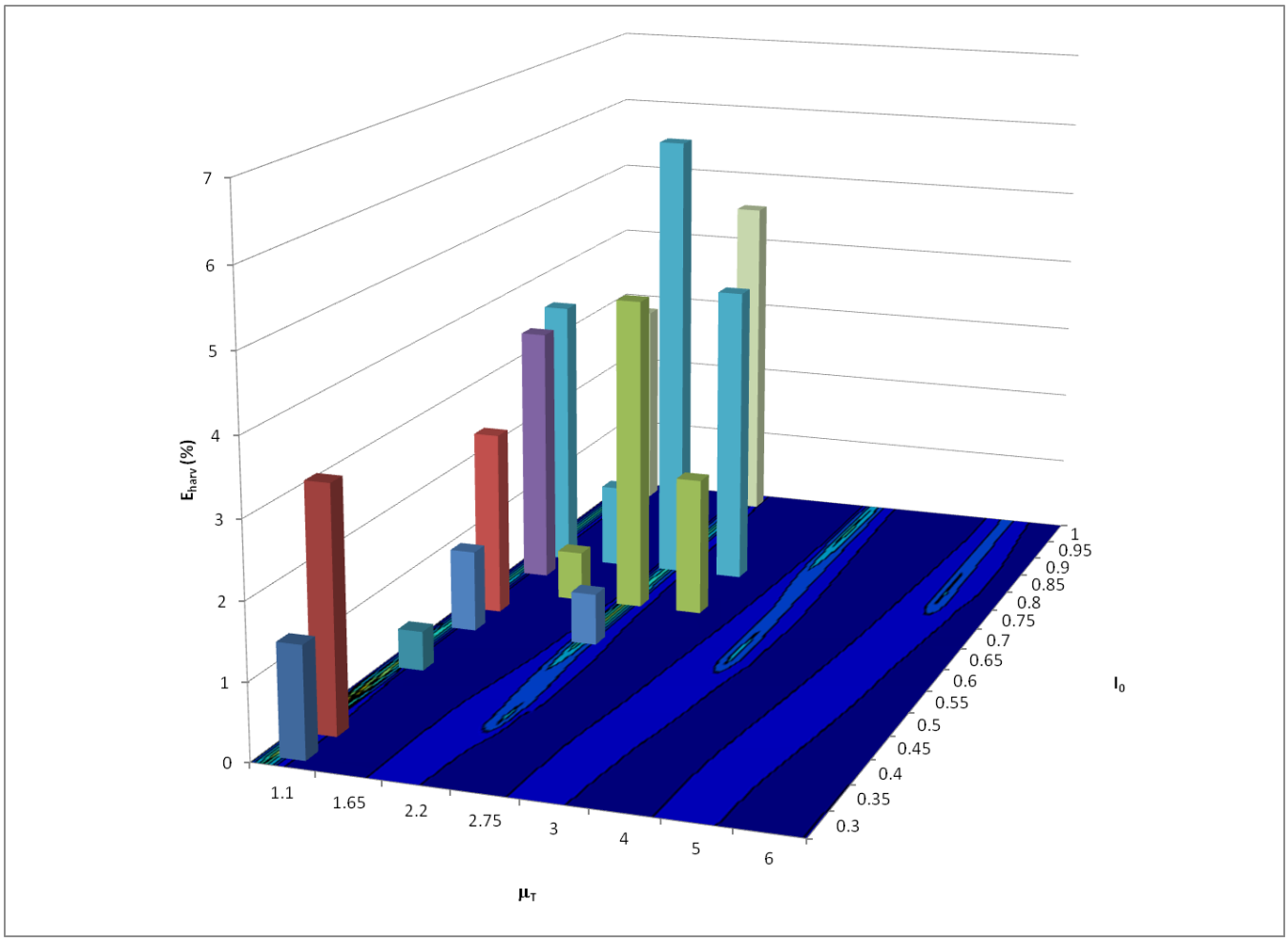

Figure 3.29: Summary of steady-state energy harvesting efficiency (3.25) for all experimental trials for the case of repeated impulsive loading of the apparatus of Fig.3.1 superimposed on the steady-state contour plot of Fig.3.15f.

perimental trials is presented in Fig.3.28. The energy harvesting capability is expressed in terms of performance measure (3.24) and plotted in units of $milli - Joules$ for the four impulse periods and various excitation amplitudes considered. As depicted in the Fig.3.28, the experimental results strongly correspond to the theoretical steady-state performance contour depicted in Fig.3.16f. As seen in the figure, more energy is harvested when the system operates on the high performance ribs than when it operates off of the ribs.

A summary of steady-state energy harvesting efficiency for all the experimental trials is presented in Fig.3.29. The energy harvesting efficiency is

expressed in terms of performance measure (3.25) and plotted in % for the four impulse periods and various excitation amplitudes considered. As depicted in the Fig.3.29, the experimental results again strongly correspond to the theoretical steady-state performance contour depicted in Fig.3.15f. As seen in the figure, energy is harvested more efficiently when the system operates on the high performance ribs than when it operates off of the ribs. Relatively high efficiency is still obtainable for the system operating under low magnitude impulse conditions if the forcing frequency corresponds to the high-efficiency ribs.

It is concluded here that the energy harvesting system (3.15) operating in the high energy regime on the large response ribs results in sustained high-frequency energy harvesting and thus provides large power output. Although the system operating in the low energy regime or away from the large response ribs doesn't engage in high-frequency energy harvesting, the 1:1 internal resonance energy harvesting still results in power output comparable to optimal configurations of other devices in the literature, as described in Section 1.1.

CHAPTER 4

HIGH-FREQUENCY NONLINEAR VIBRATION ENERGY HARVESTING BASED ON SYSTEMS WITH PIEZOELECTRIC ELEMENTS

The work in this chapter was performed prior to the analysis described in Chapter 3, providing the initial framework for the novel energy harvesting apparatus presented there. This work focuses on a similar system of two coupled oscillators with essential cubic stiffness nonlinearity, but now with piezoelectric coupling elements. A piezoelectric cable is used in the oscillator coupling to perform the harvesting in the next section. The system is subjected to single and repeated impulsive loading of various magnitudes and frequencies. The numerical and experimental work presented here aided in the culmination of work presented in Chapter 3. The harvesting elements were changed from piezoelectric to electromagnetic in order to better control the electromechanical coupling inherent in the latter. It will again be demonstrated that energy harvesting from high-frequency dynamic instabilities provides for superior harvesting performance relative to simple 1:1 internal resonance.

This work investigates a vibration-based energy harvesting system composed of two oscillators coupled with essential (nonlinearizable) stiffness nonlinearity in the form of a piezoelectric cable and subject to impulsive loading of the mechanical component. Due to geometric/kinematic mechanical effects, the piezoelastic cable generates a nonlinearizable cubic stiffness nonlinearity, whereas electromechanical coupling simply sees a resistive load. Under single and repeated impulsive inputs the transient damped dynamics of this system exhibit transient resonance captures (TRCs) causing high-frequency bursts or instabilities in the response of the harvesting element. In turn, these high-frequency dynamic instabilities result in strong and sustained energy transfers from the directly excited primary system to the lightweight harvester, which, through the piezoelastic element, are harvested by the

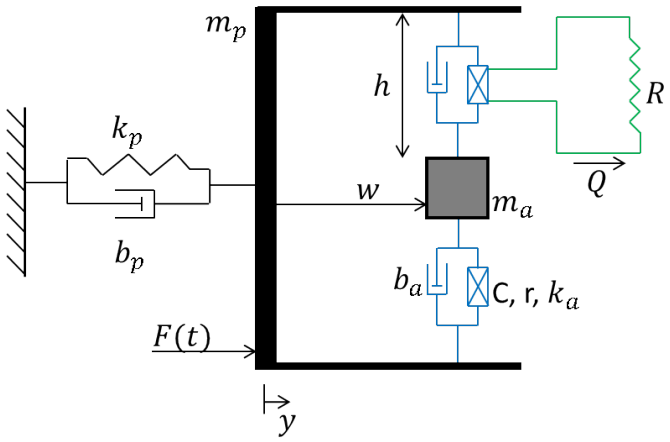

Figure 4.1: Model of the nonlinear energy harvesting system (4.9) (electric circuit shown only for half of the piezoelastic cable).

electrical component of the system. The primary goal of this work is to demonstrate the efficacy of employing this type of high-frequency dynamic instability to achieve enhanced nonlinear vibration energy harvesting under impulsive excitations. A brief experimental study is performed on a SDOF system utilizing the piezoelectric cable to demonstrate the efficacy of employing this type of electromechanical coupling in the impulsive system of interest.

4.1 Computational Study

We consider an energy harvesting system composed of a linear damped oscillator (denoted as the "primary system") attached to a secondary lightweight mass (denoted as the "harvester") through a piezoelastic cable (cf. Fig.4.1). The cable is modeled as a piezoelectric element in series with a linear spring (modeling the linear elasticity of the cable), with the resulting combination in parallel with a linear viscous damper (modeling the dissipative forces in the cable). As a result, the transmitted force across the linear spring and piezoelectric element of the cable are equal and denoted by F_s, and the force exerted by the linear viscous damper is F_d. Denoting by z_1 and z_2 the axial displacements across the linear spring and the piezoelectric element, respec-

tively, the force F_s is expressed as

$$F_s = k_1 z_1 = k_2 z_2 - \left(\frac{k_{33}}{d(1 - k_{33})} \right) Q \tag{4.1}$$

where k_1 and k_2 denote the axial stiffness of the spring and piezoelastic elements of the cable, respectively; d and k_{33} are piezoelectric coupling and electromechanical coupling parameters of the piezoelastic element, respectively, and are related to the constitutive law governing the elastic deformation and the generated charge; Q describes the electric charge in the piezoelectric element. The total force across the piezoelastic cable can be expressed in terms of $z = z_1 + z_2$ (the total stretch of the half-span of the cable) as

$$F_s = (k_a)z - (rk_a)Q \tag{4.2}$$

where $k_a = [k_1^{-1} + (1 - k_3 3)k_2^{-1}]^{-1}$. Note that this represents a device-level constitutive law for the piezoelastic cable element. In terms of the piezoelectric material constants, the coupling parameter r represents the device-level piezoelectric voltage constant, expressed as

$$r = \frac{d}{\epsilon^T (A/l)} \tag{4.3}$$

where ϵ^T is a scalar parameter defining the permittivity material property, A denotes the cross section and l the unstretched length of the piezoelastic element (in this work it is assumed that $l = h$, where h is the half-length of the piezoelastic cable). Therefore the total axial force generated in the cable is

$$F = F_s + F_d = (k_a)z - (rk_a)Q + b_a \dot{z} \tag{4.4}$$

We note that even through the piezoelastic cable connecting the primary system with the harvester is assumed to obey a linear constitutive law (4.4), its transverse deflection is expected to generate strongly nonlinear dynamics due to geometric/kinematic effects. Indeed, in terms of the relative displacement w of the harvester with respect to the primary system in the direction of motion, the stretch in the cable and its time derivative are expressed by

the strongly nonlinear relationships

$$z = \sqrt{w^2 + h^2} - l \Rightarrow \dot{z} = \frac{w\dot{w}}{\sqrt{w^2 + h^2}} \tag{4.5}$$

leading to the nonlinear equations of motion governing the oscillations of the primary system and the harvester

$$m_p\ddot{y}+b_p\dot{y}+k_py-\left[b_a\frac{w\dot{w}}{w^2+h^2}+k_a(\sqrt{w^2+h^2}-l)-(rk_a)Q\right]\frac{2w}{\sqrt{w^2+h^2}}=F(t) \tag{4.6a}$$

$$m_a(\ddot{y}+\ddot{w})+\left[b_a\frac{w\dot{w}}{w^2+h^2}+k_a(\sqrt{w^2+h^2}-l)-(rk_a)Q\right]\frac{2w}{\sqrt{w^2+h^2}}=0 \tag{4.6b}$$

Here, y denotes the absolute displacement of the primary system, m_p and m_a the mass of the primary system and the harvester, k_p and b_p the stiffness and damping coefficients of the primary system, and $F(t)$ the external load applied to the primary system in the direction of motion with the system being initially at rest.

To complete this set of equations, consider the electrical constitutive equation for the piezoelectric element, which can be written as

$$V = (1/C)Q - (rk_a)z \tag{4.7}$$

where C denotes capacitance, or in terms of w

$$V = (1/C)Q - (rk_a)(\sqrt{w^2 + h^2} - l) \tag{4.8}$$

Finally, assuming that the voltage across the piezoelectric element is harvested through a resistive load with resistance R, we can relate the harvested voltage to the rate of change of the charge by $V = R\dot{Q}$, and derive the final set of equations of motion describing the dynamics of the nonlinear harvesting device as

$$m_p\ddot{y}+b_p\dot{y}+k_py-\left[b_a\frac{w\dot{w}}{w^2+h^2}+k_a(\sqrt{w^2+h^2}-l)-(rk_a)Q\right]\frac{2w}{\sqrt{w^2+h^2}}=F(t) \tag{4.9a}$$

$$m_a(\ddot{y}+\ddot{w})+\left[b_a\frac{w\dot{w}}{w^2+h^2}+k_a(\sqrt{w^2+h^2}-l)-(rk_a)Q\right]\frac{2w}{\sqrt{w^2+h^2}}=0 \tag{4.9b}$$

$$R\dot{Q} + (1/C)Q - (rk_a)(\sqrt{w^2 + h^2} - l) = 0 \tag{4.9c}$$

We emphasize again that although all constitutive relations for the various elements of the system were assumed to be linear, the resulting equations of motion are strongly nonlinear due to geometric and kinematic effects. As shown in previous chapters, these types of strong nonlinearities can lead to interesting dynamic instabilities which, as shown below, can be utilized constructively for energy harvesting.

The principal aim of our study is to show that high-frequency dynamic instabilities in the response of system (4.9) generated by the strong nonlinearities can provide an effective mechanism for vibration energy harvesting. The preliminary nonlinear dynamic analysis performed in Chapter 2 has theoretically and experimentally demonstrated the efficacy of introducing sustained high-frequency dynamic instability in the same system but with the electric circuit (the harvester) removed, under single or sustained impulsive excitation. As shown in that work, under specific impulse excitations of the primary system the transient damped dynamics of the system tracks a high-frequency IOM in the frequency-energy plane. Dynamic instabilities arise at bifurcation points along damped transitions in the neighborhood of the IOM, causing bursts in the response of the lightweight attachment (the harvester) which resemble self-excited resonances. Moreover, for appropriate parameter designs the system remains in a state of sustained high-frequency dynamic instability under the action of repeated impulses. In turn, this sustained instability results in strong energy transfers from the directly excited primary system to the harvester, a feature that we intend to exploit in our energy harvesting application, with the addition of an electric circuit to the harvester.

As a first step in our study of the dynamics of the electromechanical harvesting system (4.9) we introduce non-dimensionalized variables and parameters by scaling the time variable as $t = c_t\tau$, the displacements as $w = c_y x$, $y = c_y u$, and the charge as $Q = c_Q q$, with the normalization coefficients defined by

$$c_t = \sqrt{\frac{m_p}{k_p}}, \qquad c_y = h\sqrt{\frac{k_p m_a}{k_a m_p}}, \qquad c_Q = \frac{hm_a}{2}\sqrt{\frac{C}{k_a}} \tag{4.10}$$

Then the equations of motion are non-dimensionalized, and the nonlinear

terms are expanded in Taylor series about $x = 0$, keeping terms only up to third order. This yields the set of simplified normalized equations given by

$$\ddot{x} + \lambda\dot{x} + x - \mu[\zeta u\dot{u} + (\sigma + u^2) - \beta q]u = f(\tau) \tag{4.11a}$$

$$\ddot{x} + \ddot{u} + [\zeta u\dot{u} + (\sigma + u^2) - \beta q]u = 0 \tag{4.11b}$$

$$\rho\dot{q} + q - \beta(\sigma + u^2) = 0 \tag{4.11c}$$

where $f(\tau) \equiv F(t(\tau))$, $(\dot{\cdot}) \equiv d/d\tau$, and the non-dimensional parameters are defined as

$$\begin{aligned} &\mu = \frac{m_a}{m_p}, \qquad \lambda = \frac{b_p}{\sqrt{k_p m_p}}, \qquad \zeta = 2\frac{b_a}{k_a}\sqrt{\frac{k_p}{m_p}}, \\ &\beta = r\sqrt{Ck_a}, \qquad \sigma = 2\frac{m_p k_a}{m_a k_p}\left(1 - \frac{l}{h}\right), \qquad \rho = RC\sqrt{\frac{k_p}{m_p}} \end{aligned} \tag{4.12}$$

Within these strongly nonlinear nondimensional equations of motion, the parameter μ represents the mass ratio between the harvester and the primary system, and λ the mechanical damping in the primary system. The mechanical damping in the harvester is given by $\mu\zeta$, and the (nondimensional) linear component of the restoring force in the harvester is $\mu\sigma$. For example, if the elastic component of the coupling piezoelastic cable is unstretched in the equilibrium configuration so that $u = 0$, then $\sigma = 0$. Finally, β characterizes the piezoelectric coupling between the mechanical and electrical components of the system, and ρ is the equivalent circuit of the electrical load. We aim to study the efficacy of using this nonlinear harvesting device under single and repetitive impulsive excitations of the primary system. To this end, we define certain energy measures.

Two different excitation scenarios will be considered in this work. In the first, the harvesting system (4.11) is initially at rest at $\tau = 0-$, and a single impulse $f(\tau) = I_0\delta(\tau)$ is applied to the primary system at $\tau = 0+$. Hence, the equations of motion (4.11) are complemented by the initial conditions:

$$\begin{aligned} &x(0+) = 0, \qquad \dot{x}(0+) = I_0, \\ &u(0+) = 0, \qquad \dot{u}(0+) = -I_0, \\ &q(0+) = 0 \end{aligned} \tag{4.13}$$

Recall that $\dot{u}(t)$ corresponds to the normalized relative velocity between the two oscillators; therefore, the relative velocity initial condition must be defined as above so that the initial velocity of the harvester is zero.

In the second excitation scenario the primary system is excited by a periodic series of identical impulses; i.e., by a pulse train. For the first impulse at $\tau = 0-$, we assume again that the system is at rest, so immediately after the application of the first impulse the initial conditions of system (4.11) are given by (4.13). Following the first impulse we define the impulsive period μ_T as the time between consecutive impulses, and the normalized impulsive period as the multiple n of the fundamental period $T_0 = 2\pi$ of the linear oscillator between consecutive impulses, $n = \mu_T/T_0$. For example, a normalized impulsive period of 5 would define a periodic pulse train, with the intensity of the impulse being equal to I_0 and applied to the primary system every 5 fundamental periods. In mathematical form the pulse train is defined as

$$F(\tau, \mu_T, I_0) = \sum_{k=0}^{N} I_0 \delta(\tau - k\mu_T)$$

where N denotes the total number of applied impulses after the first in the given excitation event. In this scheme, the p^{th} impulse applied to the linear oscillator at $\tau = p\mu_T+, p \geq 1$, corresponds to the following initial conditions for system (4.11) immediately after the application of the p^{th} impulse:

$$\begin{aligned} &x(p\mu_T+) = x(p\mu_T-), \qquad \dot{x}(p\mu_T+) = \dot{x}(p\mu_T-) + I_0, \\ &u(p\mu_T+) = u(p\mu_T-), \qquad \dot{u}(p\mu_T+) = \dot{u}(p\mu_T-) - I_0, \\ &p = 1, ..., N \end{aligned} \tag{4.14}$$

It follows that the initial state of the system will differ at each consecutive impulse, depending on the remaining vibration energy in the two coupled oscillators at the time of application of the p^{th} impulse.

We now develop energy harvesting measures to quantify the efficiency of system (4.11) in later sections. Starting from the first excitation scenario corresponding to initial conditions (4.13), the total normalized energy in the

system at an arbitrary time τ can be expressed as

$$E(\tau; I_0) = \overbrace{\left[\frac{(\dot{x})^2}{2} + \frac{(x)^2}{2}\right]}^{\text{primary}} + \overbrace{\mu\left[\frac{(\dot{x}+\dot{u})^2}{2} + \frac{(\sigma+u^2)^2}{4}\right]}^{\text{harvester}} \underbrace{- \left[\frac{\mu\,\beta}{2}\,q\,(\sigma+u^2)\right]}_{\text{coupling}} + \underbrace{\left[\frac{\mu}{4}\,q^2\right]}_{\text{electrical}} \underbrace{\qquad\qquad}_{\text{mechanical}} \tag{4.15}$$

where the implicit dependence of the normalized energy on the impulse intensity I_0 was noted as a parameter in (4.15). The nondimensional power harvested through the resistive load is then given by

$$P_h(\tau; I_0) = \frac{\mu\rho}{2}\dot{q}^2 \tag{4.16}$$

Using (4.16), the normalized energy harvested by the system in the normalized time interval $[\tau, \tau + T]$ is computed by

$$M(\tau, T; I_0) = \frac{1}{E(\tau; I_0)} \int_{\tau}^{\tau+T} P_h(\tau; I_0) d\tau \tag{4.17}$$

which represents the energy harvested in the resistive load over an interval of time T, normalized by the total energy in the system at time τ. Again, the implicit dependence of the normalized harvesting measure (4.17) on the impulse intensity I_0 was noted. This is the basic energy harvesting measure that will be used in the next section to study the efficiency of system (4.11) under a single impulse excitation.

Considering now the second excitation scenario for initial conditions (4.14), we need to generalize measure (4.17), and develop harvesting measures suitably adapted to the physics of the problem of repetitive applied impulses. To this end, we first define a time-averaged energy harvested measure

$$M_1 = \frac{1}{T_{total}} \int_0^{T_{total}} P(\tau; I_0) d\tau = \frac{1}{T_{total}} \int_0^{T_{total}} \frac{\mu\rho}{2}\dot{q}^2(\tau) d\tau \tag{4.18}$$

where T_{total} denotes the total time interval of the time series considered. Hence, M_1 represents the average rate of energy harvested per unit of normalized time. A second energy harvested measure is the impulse-averaged

harvested energy, or the average energy harvested per impulse, defined as

$$M_2 = \frac{1}{N_{impulses}} \int_0^{T_{total}} P(\tau; I_0) d\tau = \frac{1}{N_{impulses}} \int_0^{N_{impulses}\mu_T} \frac{\mu\rho}{2} \dot{q}^2(\tau) d\tau \tag{4.19}$$

where $N_{impulses}$ denotes the number of impulses with the inter-arrival period μ_T taken into account. Finally, we define a third measure, namely the impulse-averaged canonical energy harvested, by

$$\bar{M}_3 = \frac{1}{N_{impulses}} \sum_{i=0}^{N_{impulses}} M_3(i) \tag{4.20}$$

$$M_3(i) = \frac{2E_{harv}(i)}{(\dot{x}^2 + x^2)_i + \mu \left[(\dot{x} + \dot{u})^2 + \frac{1}{2}(\sigma + u^2)^2\right]_i - [\mu\beta q(\sigma + u^2)]_i + \left[\frac{\mu}{2} q^2\right]_i} \tag{4.21}$$

where $E_{harv}(i)$ is the energy harvested in the time period $i\mu_T < \tau < (i+1)\mu_T$; i.e., in the cycle of the harvester response following the application of the i^{th} impulse. Hence, $\bar{M}_3$ represents the mean value of the total energy harvested over the total impulsive energy applied to the system. Equivalently, if $M_3(i)$ indicates the ratio of energy harvested in the cycle following the application of the i^{th} impulse, the measure $\bar{M}_3$ defines the mean value of $M_3(i)$ for $0 < i < N_{impulses}$. These measures will be utilized in the study of energy harvesting of system (4.11) under repeated impulses, performed in the next sections.

As mentioned previously, our principal aim is to show that effective energy harvesting can be achieved by inducing sustained high-frequency dynamic instability of the lightweight harvester under single or repetitive impulsive excitation. To demonstrate the dynamic mechanism governing this instability, it is necessary to briefly consider the underlying Hamiltonian dynamics of system (6), and discuss the realization of a countable infinity of high-frequency transient resonance captures (TRCs). It is through the excitation of such high-frequency TRCs that conditions for effective nonlinear energy harvesting are realized.

4.1.1 Underlying Hamiltonian Dynamics

We consider the underlying Hamiltonian system derived from the normalized equations (4.11) by setting $\lambda = \zeta = \beta = \rho = f(\tau) = 0$; i.e., by removing

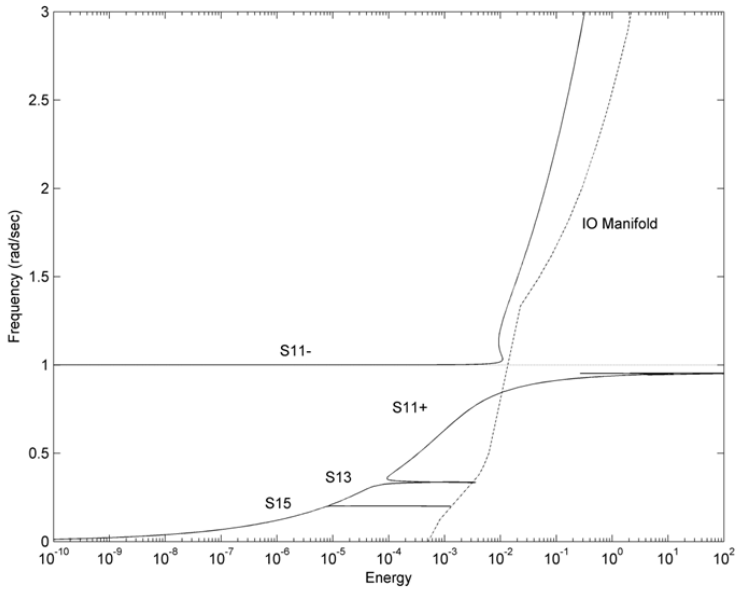

Figure 4.2: Frequency-energy plot of the underlying Hamiltonian system (4.11) derived from non-dimensional system parameters.

the damping, electrical and forcing terms, and by depicting its dynamics in a *frequency energy plot FEP*, as performed in Section 1.2. This plot depicts branches of periodic and quasi-periodic orbits of the underlying Hamiltonian system at varying energy levels. When weak damping (or any other non-conservative term) is added to the equations of motion, transitions between different branches of the FEP can be realized by computing the wavelet transform spectra of the corresponding transient responses and superimposing the spectra on the Hamiltonian FEP. Such representations are based on the concept that the weakly non-conservative dynamic transitions are mainly influenced by the underlying Hamiltonian dynamics, with the non-conservative effects affecting transitions between branches in the FEP. This concept has been tested extensively in [2].

An example of an FEP for the underlying Hamiltonian system is depicted in Fig.4.2 for parameters $\mu = 0.10$ and $\sigma = 0$. Backbone branches denoted by $S11\pm$ correspond to in-phase and out-of-phase periodic orbits in 1:1 resonance, respectively; i.e., periodic orbits where the primary system and the harvester oscillate at the same fundamental frequency. Subharmonic tongues, such as $S13$ and $S15$ in Fig.4.2, correspond to subharmonic 1:3 and 1:5 resonances, respectively, between the primary system and the harvester;

subharmonic orbits with frequencies below the normalized fundamental frequency of unity (such as the ones shown in Fig.4.2) correspond to slower oscillations of the harvester with respect to the primary system, whereas subharmonic orbits with frequencies above unity (not presented in the FEP of Fig.4.2) correspond to faster oscillations of the harvester with respect to the primary system. A countable infinity of subharmonic orbits can be realized in the Hamiltonian system, occurring in in-phase/out-of-phase pairs [2].

The third class of orbits in the FEP is composed of orbits on the IOM (cf. Fig.4.2). There are a countable infinity of periodic and an uncountable infinity of quasi-periodic impulsive orbits of the Hamiltonian system corresponding to initial impulsive excitation of the primary system with all other initial conditions being equal to zero; i.e., $\dot{x}(0+) = I_0$, $\dot{u}(0+) = -I_0$, $x(0+) = u(0+) = 0$. As shown in Section 1.2, orbits of the weakly nonconservative system in the neighborhood of the IOM result in strong energy transfers from the primary system to the strongly nonlinear attachment, so it is expected that these will be beneficial towards the goal of effective energy harvesting. As shown in Chapter 2, dynamic instabilities arise at bifurcation points along damped transitions in the neighborhood of the high-frequency part of the IOM, causing transient bursts (instabilities) in the response of the harvester resembling self-excited resonances [45, 44]. As shown in the next section, it is through the excitation of high-frequency subharmonic tongues close to the high-frequency portion of the IOM that leads to effective, strong energy harvesting. This discussion highlights the importance of the Hamiltonian FEP in our nonlinear energy harvesting approach.

In the next section, damped transitions in the neighborhood of the high-frequency section of the Hamiltonian FEP of (4.11) under single and repetitive impulsive excitation of the primary system are studied, showing that these high-frequency transitions can lead to effective energy harvesting through sustained dynamic instabilities of the harvester response. Numerical simulations of equations (4.11) subject to single and repetitive impulse excitations will be performed and studied using the resulting frequency transitions via wavelet analysis and superposition of wavelet spectra on the Hamiltonian FEP. Because the single impulse input scenario will be the basis for optimizing the electromechanical properties of (4.11) for effective energy harvesting, it is studied first, before considering repetitive impulsive inputs.

4.1.2 Single Impacts

The computational study of the damped dynamics of the normalized system (4.11) is initiated by considering a single impulse input to the LO and studying the resulting damped transitions by performing wavelet analysis and superimposing the derived wavelet spectra on the Hamiltonian FEP; as discussed in Section 1.2, this type of wavelet superposition, although purely phenomenological, can provide a valuable interpretation of the nonlinear transitions as the damped nonlinear response "tracks" different branches of the underlying Hamiltonian system. The numerical simulations presented in this section are carried out for fixed system parameters $\mu = 0.1$, $\lambda = 0.014$, $\zeta = 0.001$, $\sigma = 0$. As discussed in the previous section, weak damping should be considered in the mechanical system to ensure that the desired high-frequency damped transitions can be obtained when the electromechanical and circuit parameters, (β,ρ), respectively, are incorporated into the system. As in [18, 46, 25], proper tuning of the circuit parameters is desired to optimize energy harvesting efficiency.

The energy harvesting efficiency measure (4.17) was employed to obtain an optimal set of harvester parameters (β,ρ) in this case. This was performed numerically by defining appropriate parameter ranges, $\beta = [0.01 - 1.0]$ with step $\Delta\beta = 0.01$, and $\rho = [0.01 - 2.0]$ with step $\Delta\rho = 0.01$. For each specific parameter pair (β,ρ) the model (4.11) was numerically integrated with initial conditions (4.13) for a given time period μ_T and for varying impulse intensity I_0. The energy harvesting efficiency measure (4.17) was then computed by post-processing the resulting time series, depicted in a contour plot with every combination of (β,ρ) in the aforementioned parameter ranges.

In Fig.4.3, contour plots of the normalized harvested energy measure (4.17) are depicted as a function of the system parameters (β,ρ) for a fixed simulation period equal to $\mu_T = 47.7$ normalized time units and varying impulse intensity I_0. As deduced from these plots, the parameter pairs (β,ρ) corresponding to optimal harvested energy are dependent upon the excitation amplitude, or energy level, that the system experiences. This is to be expected since this nonlinear harvester design should depend strongly on the energy level of the dynamics. Indeed, a general feature of these results is that for lower impulse intensities (cf. Fig.4.3a,b) the system shows weak to moderate energy harvesting capacity, as evidenced by the complete absence

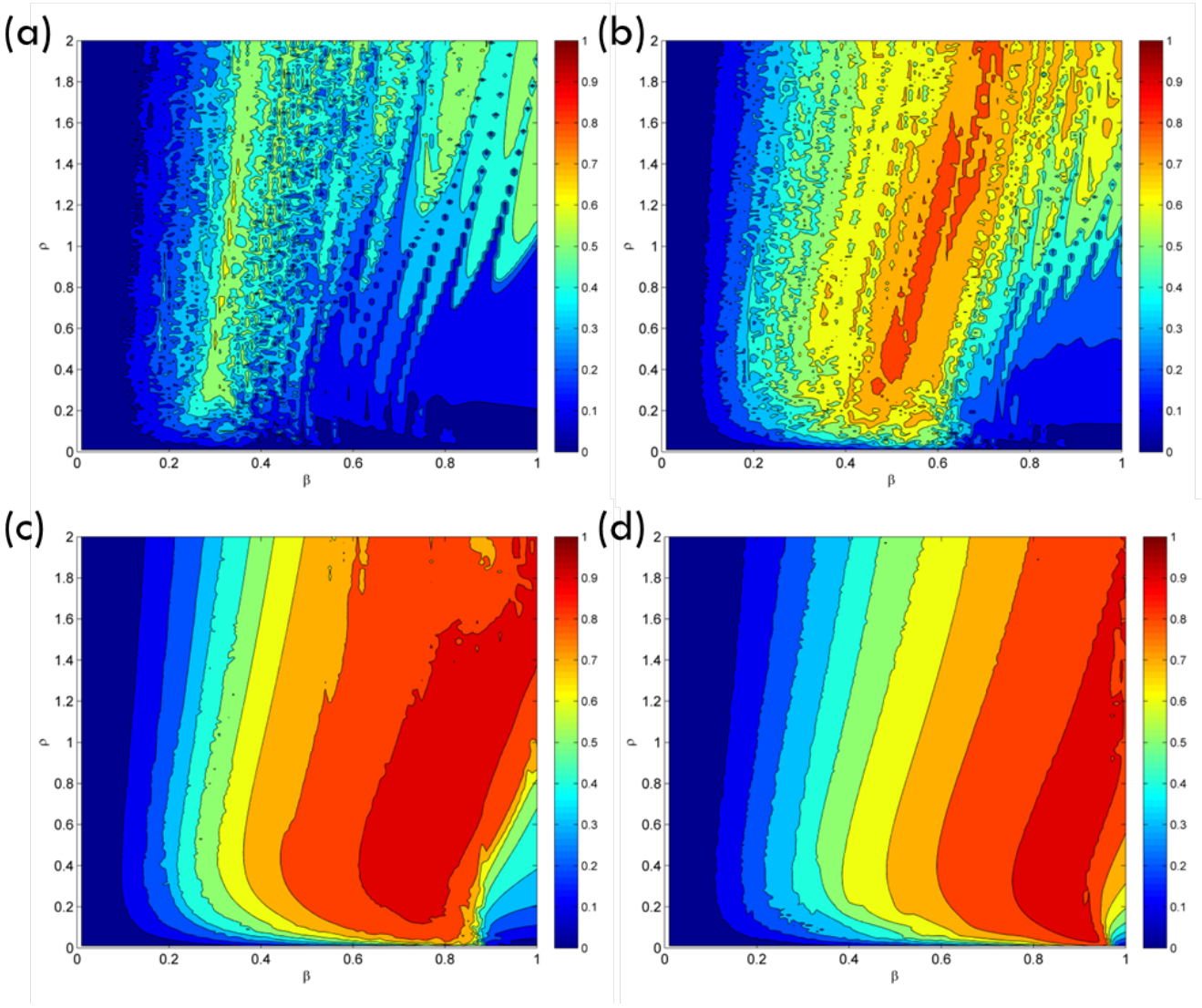

Figure 4.3: Energy harvesting measure (4.17) as a function of harvesting parameters (β,ρ) for normalized impulse intensity: (a) $I_0 = 0.5$, (b) $I_0 = 0.6$, (c) $I_0 = 1.0$ and (d) $I_0 = 2.0$ for $\mu_T = 47.7$.

(Fig.4.3a), or narrow band (Fig.4.3b), of parameter ranges corresponding to strong energy harvesting. On the contrary, for higher impulse intensities (cf. Fig.4.3c,d) we note the formation of plateaus of strong energy harvesting, indicating robustness of harvesting for small parameter variations within these plateaus. It's concluded that the contour plots of Fig.4.3 can be utilized to examine the robustness of the nonlinear energy harvesting system.

Considering the results in more detail, the contour plot of Fig.4.3a indicates that for this low impulse intensity there exist several narrow bands of parameter pairs for which the energy harvesting efficiency reaches at most 50%. By increasing the impulse intensity we obtain the contour plot of Fig.4.3b for which we note that a narrow band of maximum efficiency of nearly 70% can be achieved. By further increasing the impulsive intensity we note from the plots of Fig.4.3c and Fig.4.3d that relatively broad plateaus of strong harvesting efficiency as high as 90% can be achieved at the respective energy levels. Clearly, the formation of such plateaus of strong energy harvesting provides an important freedom for designing the electrical parameters of the harvester, since small variations or uncertainties in these parameters do not appear to significantly reduce the harvesting capacity. An important remark, however, is that these findings depend on the normalized time parameter μ_T; i.e., on the normalized time interval of computation of the normalized harvesting measure (4.17). Indeed, if this parameter is small it can negatively affect the energy harvesting measure, so a study of the dependence of the normalized measure (4.17) on μ_T should also be undertaken.

The dynamics governing the regimes of strong energy harvesting are now studied by relating the results of Fig.4.3 to specific nonlinear dynamic transitions in the frequency-energy plot (FEP). As mentioned previously, superposition of wavelet spectra on the FEP of the underlying Hamiltonian system can provide valuable insight into the nonlinear dissipative dynamics. First, we consider the nonlinear dynamic response of the harvesting system (4.11) for a single impulse of normalized intensity $I_0 = 0.5$ and harvesting parameters $\beta = 0.84$ and $\rho = 1.7$. These parameters correspond to a peak in the contour plot of Fig.4.3a; this, however, is one of weak harvesting performance of the system as described above. In Fig.4.4 we depict selected transient responses of this system, together with their wavelet spectra. Considering the wavelet spectrum of the relative displacement of the harvester with respect to the primary system depicted in Fig.4.4c, and its superposition on the FEP of

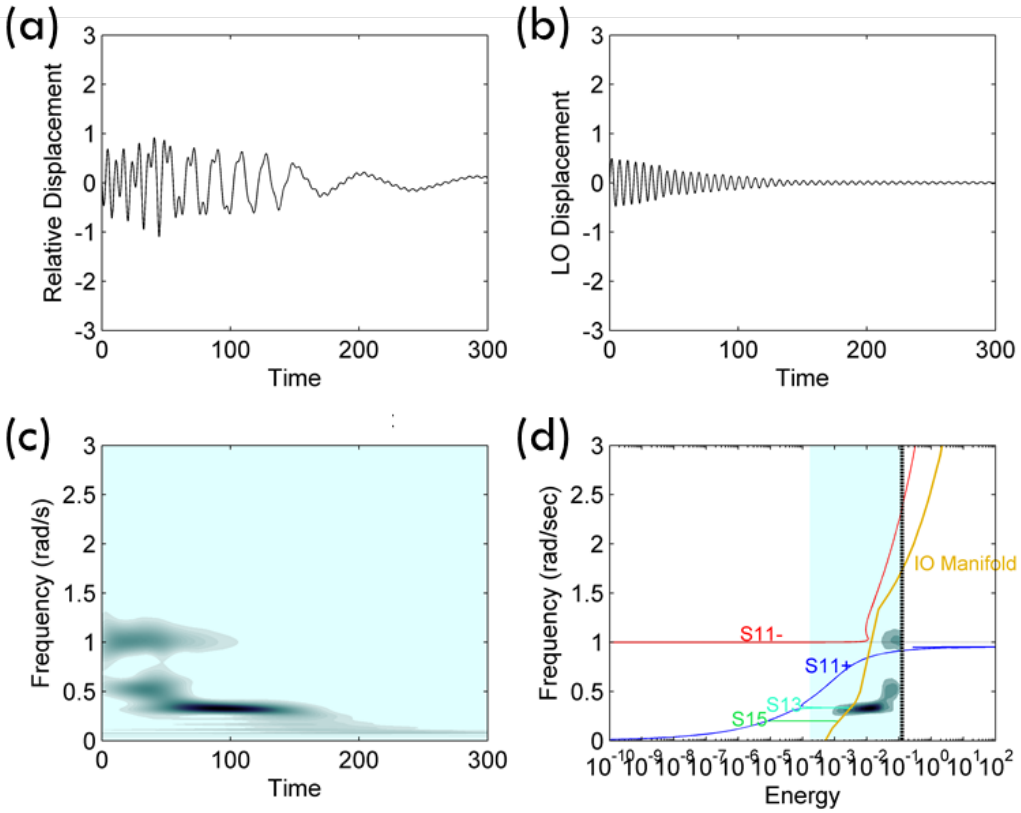

Figure 4.4: Damped transient response of system (4.11) with $\beta = 0.84$, $\rho = 1.7$, and $I_0 = 0.5$: (a,c) Time series and wavelet spectrum of relative displacement between primary system and harvester; (b) displacement of the primary system; (d) wavelet spectrum of (a) superimposed on the FEP of the underlying Hamiltonian system.

the underlying Hamiltonian system, we note interesting resonance captures in the damped dynamics.

Initially, there is a brief 1:1 *transient resonance capture - (TRC)* of the damped dynamics in the vicinity of the $S11-$ out-of-phase backbone branch of the Hamiltonian FEP, followed by escape from this TRC (due to diminishing energy) and a brief engagement in a low-frequency 1:2 TRC. Then, there is another sustained (i.e., prolonged) low-frequency 1:3 TRC, where the harvester oscillates with a frequency that is one third of the frequency of the primary system. The dynamics then remains captured in this lower frequency $S13$ subharmonic tongue until the remainder of the energy of the system is either harvested out of the primary system or is dissipated by viscous damping. This type of low-frequency damped transition resulting in low-frequency dynamical instability associated with 1:3 TRC is typical of transitions reported in purely mechanical systems of previous works presented in Chapter 2, and does not lead to effective energy harvesting. Clearly, in this case the initial impulsive energy into the system is too low to allow excitations of high-frequency transient dynamic instabilities due to TRCs at high-frequency subharmonic tongues (where the harvester oscillates faster than the primary system). As shown below, it is precisely the excitation of such high-frequency TRCs that facilitates strong energy harvesting in system (4.11).

Similar dynamics occurs at the peaks of energy harvesting of the contour plot of Fig.4.3b corresponding to impulse intensity $I_0 = 0.6$. At this energy level the dynamics exhibits more prolonged 1:1 TRC on the $S11-$ backbone before transitioning once again to a $S13$ subharmonic TRC with decreasing energy; hence, there is a marginal enhancement of energy harvesting efficiency since this is associated with low-frequency dynamics of the harvester.

A different picture of the transient dynamics is realized, however, at the strong energy harvesting peaks of the contour plots of Fig.4.3c, corresponding to higher impulse intensities. This is deduced by considering the response of system (4.11) for a single impulse of intensity $I_0 = 1.0$ and $\beta = 0.84$, $\rho = 1.0$, depicted in Fig.4.5; these parameters correspond to the highest energy harvesting efficiency region, indicated by the plateau in Fig.4.3c. Indeed, the increase in input energy results in qualitatively different transient dynamics, since now the transient response of the harvester takes place in the neighborhood of high-frequency subharmonic tongues in the vicinity of the

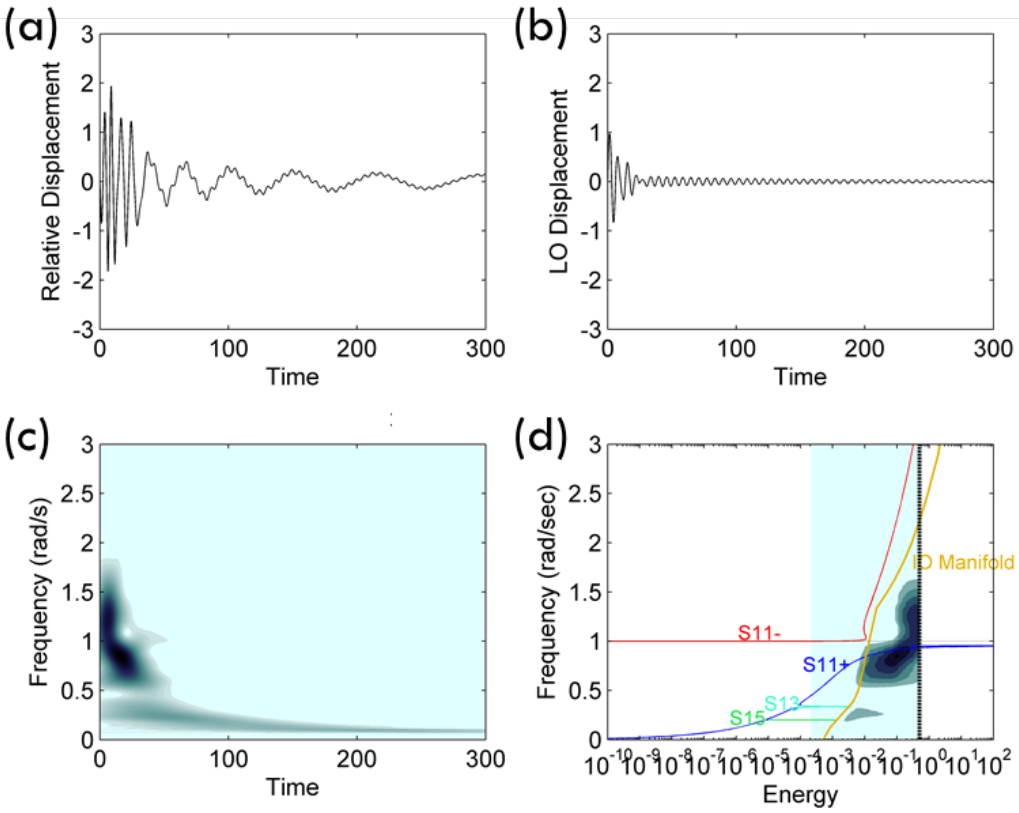

Figure 4.5: Damped transient response of system (4.11) with $\beta = 0.84$, $\rho = 1.0$, and $I_0 = 1.0$: (a,c) Time series and wavelet spectrum of relative displacement between primary system and harvester; (b) displacement of the primary system; (d) wavelet spectrum of (a) superimposed on the FEP of the underlying Hamiltonian system.

upper branch portion of the IOM. This is concluded by noting the dominant high-frequency harmonics in the initial, highly energetic phase of the relative response of Fig.4.5a and the corresponding wavelet spectrum of Fig.4.5c. As mentioned earlier, oscillations above the normalized natural frequency of unity correspond to motions where the harvester oscillates faster than the primary system, a feature which is greatly beneficial to energy harvesting. After these initial high-frequency transients the dynamics makes a transition to the lower-frequency $S11+$ in-phase backbone until the remainder of the input energy is either harvested or passively dissipated. An important feature here concerns the rate at which the energy is harvested out of the primary system which, as seen in Fig.4.5b, is high, as the impulsive energy is quickly transferred to the harvester and quickly harvested by the piezoelectric element. Indeed, as seen in Fig.4.5a, most of the impulsive energy input into the system is harvested within the first ~ 50 normalized time units, resulting in nearly 90% energy harvesting efficiency as defined by measure (4.17). We note that the high-frequency nonlinear instability occurring in this case is due to the high-energy TRCs realized in the initial highly energetic phase of the transient response, which, in turn, are caused by the (intentional) strong geometric nonlinearity of the harvesting system, as indicated in Chapter 2.

The response of the system for an impulse of intensity $I_0 = 2.0$ and for (β,ρ) in the highest efficiency region (plateau) of Fig.4.3d exhibits similar high-frequency instabilities and transitions. This indicates that strong energy harvesting of the system of Fig.4.1 is associated with excitation of high-frequency and high-energy dynamic instabilities in the lightweight harvesting element, caused by high-frequency TRCs in subharmonic tongues in the vicinity of the upper portion of the IOM of the underlying Hamiltonian system. As such, this result is similar to that reported in Chapter 2, for a purely mechanical system of strongly nonlinear coupled oscillators. Based on the results reported in this section, we conclude that strong energy harvesting under a single impulse excitation leads to rapid decay to the trivial equilibrium state of the directly excited primary system, a result that has interesting implications when one considers the extension of this study to the case of repeated impulses. Indeed, based on the previous results one can surmise that an energy harvesting system can be appropriately designed so that between impulses, the primary system returns to trivial equilibrium; in that case the strong energy harvesting efficiency (the plateaus) observed in

Fig.4.3c,d should be maintained under repetitive, time-periodic impulses as well. This issue is explored in detail in the next section.

4.1.3 Repeated Impacts, Simple SDOF System (Aside)

We now consider energy harvesting in system (4.11) under a time-periodic pulse train (4.14) (i.e., the second excitation scenario). Based on the results of the previous section, the highest energy harvesting efficiency achieved in this system under single impulse excitation was for system parameters $\mu = 0.1$, $\lambda = 0.01$, $\zeta = 0.001$, $\sigma = 0$ and impulse intensity $I_0 = 1.0$ (corresponding to the contour plots of Fig.4.3c); accordingly, we select these system parameters for our study. In addition, we select electrical parameters of the harvester as $\beta = 0.84$ and $\rho = 1.0$ since these correspond to the point of optimal energy harvesting efficiency at the plateau of Fig.4.3c. The resulting response of the system under single impulse excitation is then depicted in Fig.4.5. Finally, the imposed initial conditions after each impulse are given by (4.14) with the pulse inter-arrival time and pulse intensity I_0 assumed to be fixed and considered as parameters of the problem. Our aim will be to examine the energy harvesting efficiency of the system (4.11) (in terms of the harvesting measures developed previously) for different values of I_0.

Before considering the strongly nonlinear harvesting system (4.11), however, it will be instructive to first examine a simplified single-degree-of-freedom (SDOF) linear damped oscillator excited by a periodic train of repeated impulses. The simple form of this system will allow derivation of analytical expressions for the energy harvesting measures which will be used later to interpret the direct numerical simulations of the nonlinear system (4.11). Following this preliminary digression we will proceed to direct numerical simulations of the considered electromechanical system using the optimized system parameters derived from the single impulse excitation (as described above). We will examine the dynamics in the temporal, energy-frequency, and time-frequency domains, and attempt an interpretation of the resulting nonlinear dynamics in terms of the analytical results derived for the linear system studied in our preliminary digression.

To this end, we consider the linear SDOF damped oscillator under a peri-

odic impulse excitation, given by

$$\ddot{x} + 2\zeta\omega\dot{x} + \omega^2 x = I_0 \sum_{i=0,1,2,\ldots} \delta(t - i\mu_T) \tag{4.22}$$
$$x(0-) = \dot{x}(0-) = 0$$

where ζ and ω are the fraction of critical damping and natural frequency, respectively. We note that the "viscous damper" in (4.23) denotes the effective dissipation introduced in the linear dynamics of the primary system due to energy harvested by the harvesting element. Hence, the dissipative element in the simplified system (4.23) can be construed as an "effective viscous damper" modeling the energy harvesting process. In addition we assume that (4.23) is a weakly damped system ($\zeta \ll 1$), so that the time scale of the amplitude decay of (4.23) is larger than the natural period of the system, $T = 2\pi/\omega$, and a slow-fast partition of the damped dynamics is realized. This is a reasonable assumption for the considered problem, based on the results for the single impulse excitation analysis of the previous section (i.e., we do not anticipate the slow-fast partition of the dynamics of the primary system to be violated in this second excitation scenario).

The analysis will be based on simple energy balance arguments, and the fact that between applied impulses the system performs free oscillations. Based on the underdamped assumption, these free oscillations after the application of the i^{th} impulse can be expressed as

$$\begin{aligned} x &\approx \sqrt{E_i^+} e^{-\zeta\omega t} \sin\left(\sqrt{1-\zeta^2}\omega t + \delta\phi_i\right), \\ \dot{x} &\approx \left(\omega\sqrt{E_i^+} e^{-\zeta\omega t}\right) \cos\left(\sqrt{1-\zeta^2}\omega t + \delta\phi_i\right) \end{aligned} \tag{4.23}$$

where we denote by E_i^+ the total energy of the system immediately after the application of the i^{th} impulse, and by the resulting phase change. From the above it is straightforward to conclude that just before the application of the next impulse the total energy of the system is

$$E_{i+1}^- = E_i^+ e^{-2\zeta\omega\mu_T} \tag{4.24}$$

Note that in this idealized linear framework the energy harvested after the i^{th} impulse (defined as the energy dissipated by the "effective viscous damper"

of the oscillator) is expressed as

$$E_H = E_i^+ \left(1 - e^{-2\zeta\omega\mu_T}\right) \tag{4.25}$$

Moreover, immediately after the application of the $(i+1)^{th}$ impulse it holds that

$$\begin{aligned} x_{i+1}^+ &= \left(\sqrt{E_{i+1}^-}/\omega\right) \sin\left[\sqrt{1-\zeta^2}\omega(i+1)\mu_T + \delta\phi_i\right], \\ \dot{x}_{i+1}^+ &\approx \left(\sqrt{E_{i+1}^-}\right) \sin\left[\sqrt{1-\zeta^2}\omega(i+1)\mu_T + \delta\phi_i\right] + I_0 \end{aligned} \tag{4.26}$$

Therefore, we can express the total energy of the system immediately after the application of the $(i+1)^{th}$ impulse as

$$\begin{aligned} E_{i+1}^+ = (E_{i+1}^-/2)\{&\sin^2\left(\sqrt{1-\zeta^2}\omega(i+1)\mu_T + \delta\phi_i\right) \\ &+ \left[\cos(\sqrt{1-\zeta^2}\omega(i+1)\mu_T + \delta\phi_i) + \left(I_0/\sqrt{E_{i+1}^-}\right)\right]^2\} \end{aligned} \tag{4.27}$$

Due to the complexity of the above equation we will proceed by restricting our study to specific values of the inter-arrival times $\mu_T = n\pi/\sqrt{1-\zeta^2}\omega, n = 1, 2, ...$, in which case (4.27) takes the form

$$\begin{aligned} E_{i+1}^+ &= \frac{E_{i+1}^-}{2}\left[\sin^2(\delta\phi_i) + \left(\cos(n\pi + \delta\phi_i) + \frac{I_0}{\sqrt{E_{i+1}^-}}\right)^2\right], \\ \mu_T &= \frac{n\pi}{\sqrt{1-\zeta^2}\omega}, \qquad n = 1, 2, ... \end{aligned} \tag{4.28}$$

where $\delta\phi_i$ denotes the phase difference between the applied impulse and the harvester response. Moreover, we will further restrict our analysis to the case where either the impulse intensity satisfies the condition $I_0 \gg \sqrt{E_{i+1}^-}$, in which case the energy immediately after the impulse E_{i+1}^+ is almost purely kinetic, so $\delta\phi_i \approx \pi$; or to the condition $I_0 \ll \sqrt{E_{i+1}^-}$, in which case the phase difference $\delta\phi_i$ is negligible, $\delta\phi_i \approx 0$. In both cases the following approxima-

tion holds:

$$E_{i+1}^{+} \approx \frac{E_{i+1}^{-}}{2}\left[(-1)^n + \frac{I_0}{\sqrt{E_{i+1}^{-}}}\right]^2,$$
$$\mu_T = \frac{n\pi}{\sqrt{1-\zeta^2}\omega}, \qquad n = 1, 2, ...,$$
$$I_0 \ll \sqrt{E_{i+1}^{-}} \qquad or \qquad \sqrt{E_{i+1}^{-}} \ll I_0 \tag{4.29}$$

Combining this equation with (4.24), we finally obtain

$$E_{i=1}^{+} \approx \frac{1}{2}\left[(-1)^n e^{-\left(\zeta/\sqrt{1-\zeta^2}\right)n\pi}\sqrt{E_i^{+}} + I_0\right]^2,$$
$$\mu_T = \frac{n\pi}{\sqrt{1-\zeta^2}\omega}, \qquad n = 1, 2, ...,$$
$$I_0 \ll \sqrt{E_{i+1}^{-}} \qquad or \qquad \sqrt{E_{i+1}^{-}} \ll I_0 \tag{4.30}$$

Relation (4.30) defines a one-dimensional nonlinear map, and assuming that it has a stable period-1 fixed point (corresponding to stable steady-state energy harvesting), this can be computed as

$$E^{+} \approx \frac{1}{2}\left[(-1)^n e^{-\left(\zeta/\sqrt{1-\zeta^2}\right)n\pi}\sqrt{E^{+}} + I_0\right]^2,$$
$$\mu_T = \frac{n\pi}{\sqrt{1-\zeta^2}\omega}, \qquad n = 1, 2, ...(Steadystate) \tag{4.31}$$

where E^{+} denotes the total energy of the system at steady-state, immediately after the application of an impulse. Solving the above algebraic equation for E^{+} we obtain two solutions, of which only one is physically meaningful

$$\sqrt{E^{+}} \approx \frac{\sqrt{2} + (-1)^n e^{-\left(\zeta/\sqrt{1-\zeta^2}\right)n\pi}}{2 - e^{-\left(2\zeta/\sqrt{1-\zeta^2}\right)n\pi}} I_0,$$
$$\mu_T = \frac{n\pi}{\sqrt{1-\zeta^2}\omega}, \qquad n = 1, 2, ...(Steadystate) \tag{4.32}$$

Based on this analytical approximation the energy harvested per impulse at

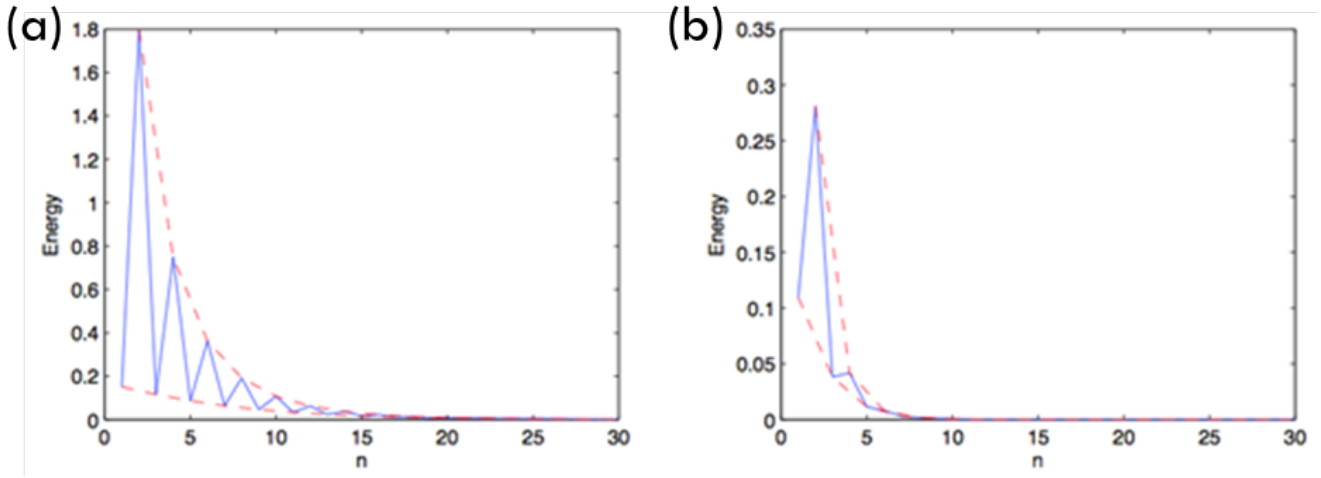

Figure 4.6: Analytical approximation of the total energy before the application of the impulse at steady state for system (4.33) for $I_0 = 1.0$: (a) $a = 0.7$, (b) $a = 0.9$.

steady-state can be estimated through (4.23) to be

$$E_H \approx I_0^2 \left[\frac{\sqrt{2} + (-1)^n a^n}{2 - a^{2n}} \right]^2 (1 - a^{2n}),$$
$$\mu_T = \frac{n\pi}{\sqrt{1-\zeta^2}\omega}, \qquad n = 1, 2, ...(Steadystate) \tag{4.33}$$

where $a \equiv e^{-\left(\zeta/\sqrt{1-\zeta^2}\right)n\pi} < 1$.

In Fig.4.6 we depict the previous analytical approximation of the total energy of the system after the application of an impulse of intensity $I_0 = 1.0$ (without any loss of generality) as a function of increasing inter-arrival time μ_T for $n = 1, 2, ...$ We observe that for sufficiently large inter-arrival times , i.e., for sufficiently large n, the total energy of the system before the impulse reaches approximately a zero level. This agrees with physical intuition, since if the inter-arrival time between impulses is sufficiently large, there is adequate time to harvest nearly all of the available mechanical energy, so an instant before the next impulse is applied the total energy of the system is nearly zero. This is a very robust regime of energy harvesting, and it clearly represents a state of the dynamics where no differentiation of the state of the system between applied impulses exists.

For smaller inter-arrival times, however, we observe a highly oscillatory

pattern between even and odd values of n. This is the case where the system continues to carry residual (unharvested) energy at the time instant of application of the next impulse. Moreover, the highly oscillatory behavior of the total energy for smaller values of n is a direct consequence of the fact that the discrete values of inter-arrival time were chosen so that the impulse was either in-phase or out-of-phase with respect to the response of the harvester. This highlights the extreme sensitivity of the energy harvesting to the relative phase of the oscillation between the harvester and the applied impulse in the regime of short to moderate inter-arrival times μ_T. Indeed, when n is even (in-phase case) we have the phenomenon of discrete-resonance where the impulsive energy is applied at the precise instant when the harvester can impart all of it, or equivalently, this is the case where the work produced by the external impulse is maximum. On the other hand when n is odd the velocity of the mass and the applied impulse are completely out-of-phase, so the energy imparted to the system is minimal. These two cases form the two extremes that bound the performance of the energy harvester. For inter-arrival times in between the considered discrete values (i.e., when n is small and non-integer) the dynamics is more complex and another approach based on stochastic analysis, is required, in order to relate the energy harvesting capacity of the system to the relative phase between the applied impulse and the harvester response. These results, along with the analysis of the energy harvesting optimization and robustness to small uncertainties in either the inter-arrival times or the impulse intensities, will be considered in detail in a future work. This ends the digression with the linear harvester (4.23), which highlighted some simple but important aspects related to the dynamics of energy harvesting under impulse excitation. This dynamics is expected to apply to the case of the nonlinear harvester (4.11) which we now proceed to examine.

4.1.4 Repeated Impacts, System (4.11)

The parameters for the system were selected based on the optimal values derived for the single impulse excitation as discussed in the beginning of this section. First, we examine the energy harvesting measures (4.18)-(4.21) defined above for this specific system. In Fig.4.7-Fig.4.9 we depict the mea-

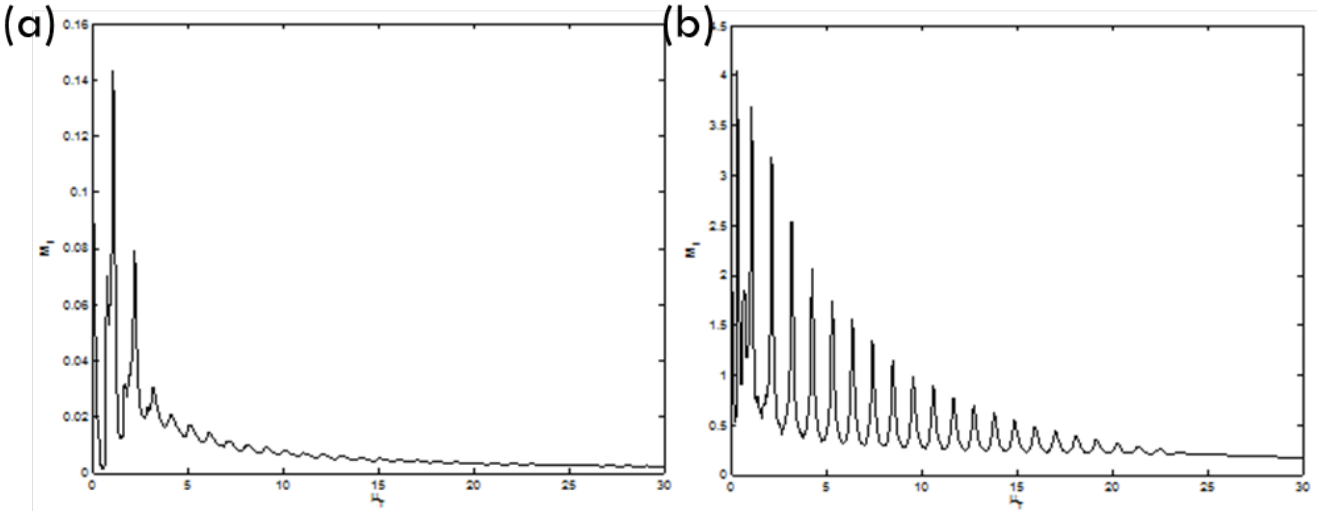

Figure 4.7: Time-averaged harvested energy (4.18) for the nonlinear harvesting system (4.11) as a function of inter-arrival time μ_T for impulse intensity (a) $I_0 = 1.0$ and (b) $I_0 = 10.0$.

sures (4.18), (4.19), and (4.20) as functions of the inter-arrival time μ_T for two different impulse intensities; these results were derived by direct numerical simulation of equations (4.11) with initial conditions (4.14). We note that consistent with the linear analysis presented previously, there exists a "phase-dependent" regime of the dynamics realized for sufficiently small inter-arrival times, where depending on the relative phase between the primary system and the applied impulse maximal or minimal absorption ("pumping") of energy in the harvesting system can be realized (cf. Fig.4.7). Clearly, this feature is independent of the nonlinear nature of the harvester and can be predicted using simple power absorption arguments similar to the ones used in the digression above.

However, as the inter-arrival time decreases, fluctuations in the energy harvesting performance gradually decrease to where they are completely eliminated. Hence, there exists a critical value of the inter-arrival time μ_T above which the entire mechanical energy in the primary system following the application of an impulse is nearly dissipated or harvested before the next impulse is applied, similar to the linear harvester discussed in the digression. In that case the impulse-averaged harvested energy measure (4.19) reaches a constant asymptotic value which corresponds to the total energy in the system immediately after the application of each impulse after subtracting

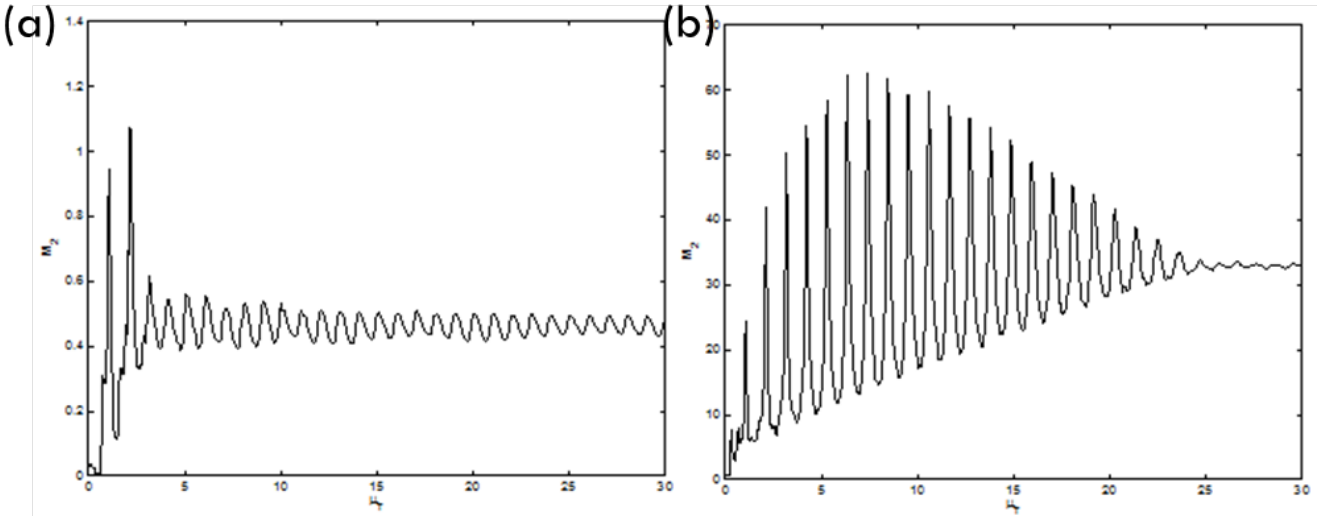

Figure 4.8: Impulse-averaged harvested energy (4.19) for the nonlinear harvesting system (4.11) as a function of inter-arrival time μ_T for impulse intensity (a) $I_0 = 1.0$ and (b) $I_0 = 10.0$.

the energy dissipated per cycle due to viscous damping (cf. Fig.4.8). In addition, for longer inter-arrival times the efficiency of the energy harvesting gradually decreases (e.g., consider measure (4.18)), since the impulses arrive infrequently and the primary system nearly reaches the trivial equilibrium between applied impulses.

Consider the third measure (4.20), which provides the average ratio of harvested energy normalized by the energy induced in the system (and hence, available for harvesting) immediately after the application of each impulse (cf. Fig.4.9). It turns out that this "utility" average measure reaches its maximum value when the inter-arrival time is sufficiently large so that most of the system energy has been dissipated before the next impulse is applied. This result combined with the conclusions made from measure (4.18) defines as a combined optimum (for all three energy harvesting measures) an inter-arrival time that is comparable with the time required for the system to almost completely harvest or dissipate the energy it acquires after an applied impulse.

To analyze the dynamics of the harvester in more detail we select a response from the robust regime of energy harvesting for the case $I_0 = 1.0$ corresponding to inter-arrival time $\mu_T = 30$. The relative response between the primary system and the harvester is depicted in Fig.4.10a, the response

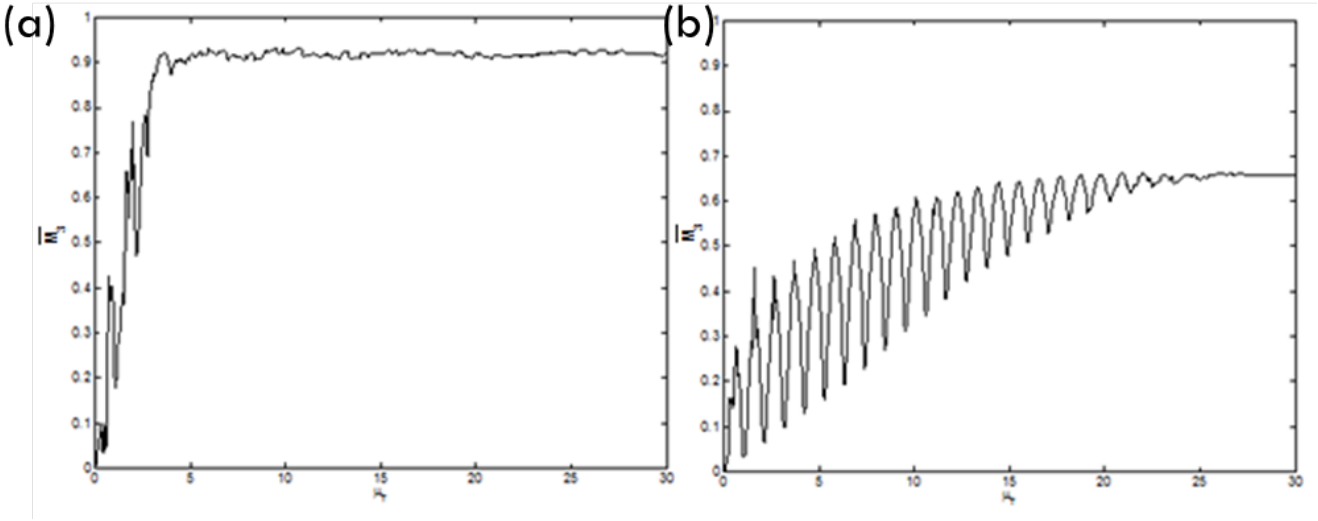

Figure 4.9: Impulse-averaged canonical harvested energy measure (4.20) for the nonlinear harvesting system (4.11) as a function of inter-arrival time μ_T for impulse intensity (a) $I_0 = 1.0$ and (b) $I_0 = 10.0$.

of the impulsively excited primary system in Fig.4.10b, and the wavelet spectrum of the relative response time series in Fig.4.10c. Clearly, we deduce that during each cycle of impulsive excitation the induced energy is rapidly and effectively harvested, so by the time of application of the next impulse the system reaches the near-trivial equilibrium state. As a result, the dynamics of system (4.11) is nearly periodic, starting from the first cycle; i.e., no transition to the steady state of efficient energy harvesting exists, and the system reaches a state of efficient harvesting immediately following the application of the first impulse at $\tau = 0+$. As noted from the wavelet spectrum of Fig.4.10c the governing dynamic mechanism leading to efficient energy harvesting is a high-frequency dynamic instability in the harvester response due to the excitation of a high-frequency subharmonic TRC, as discussed earlier. Contrary to the single-impulse excitation, however, this series of dynamic instabilities is sustained due to the appropriate design of the electromechanical parameters of the harvesting system and the appropriate selection of the inter-arrival time μ_T.

The dynamic instability of the harvester response is further highlighted in the frequency-energy plot of Fig.4.11, where the wavelet spectrum of the third cycle of the impulsive relative response of Fig.4.10a is superimposed on the FEP of the underlying Hamiltonian system. We notice the high-frequency

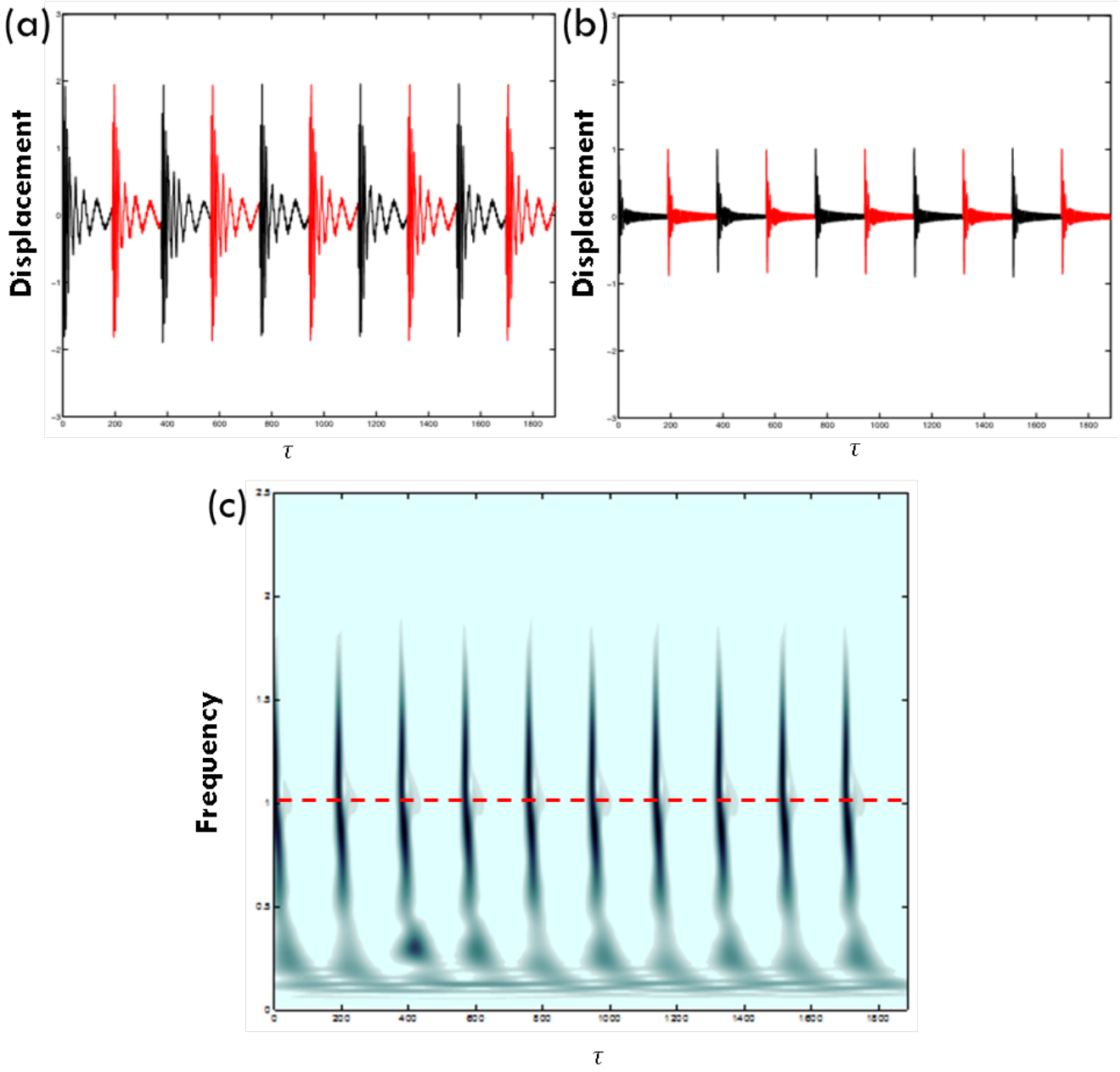

Figure 4.10: Case of efficient nonlinear energy harvesting for $I_0 = 1.0$ and $\mu_T = 30$: (a) Relative response between primary system and harvester, (b) response of the primary system, and (c) wavelet spectrum of (a); the dashed line indicates the normalized natural frequency of the primary system.

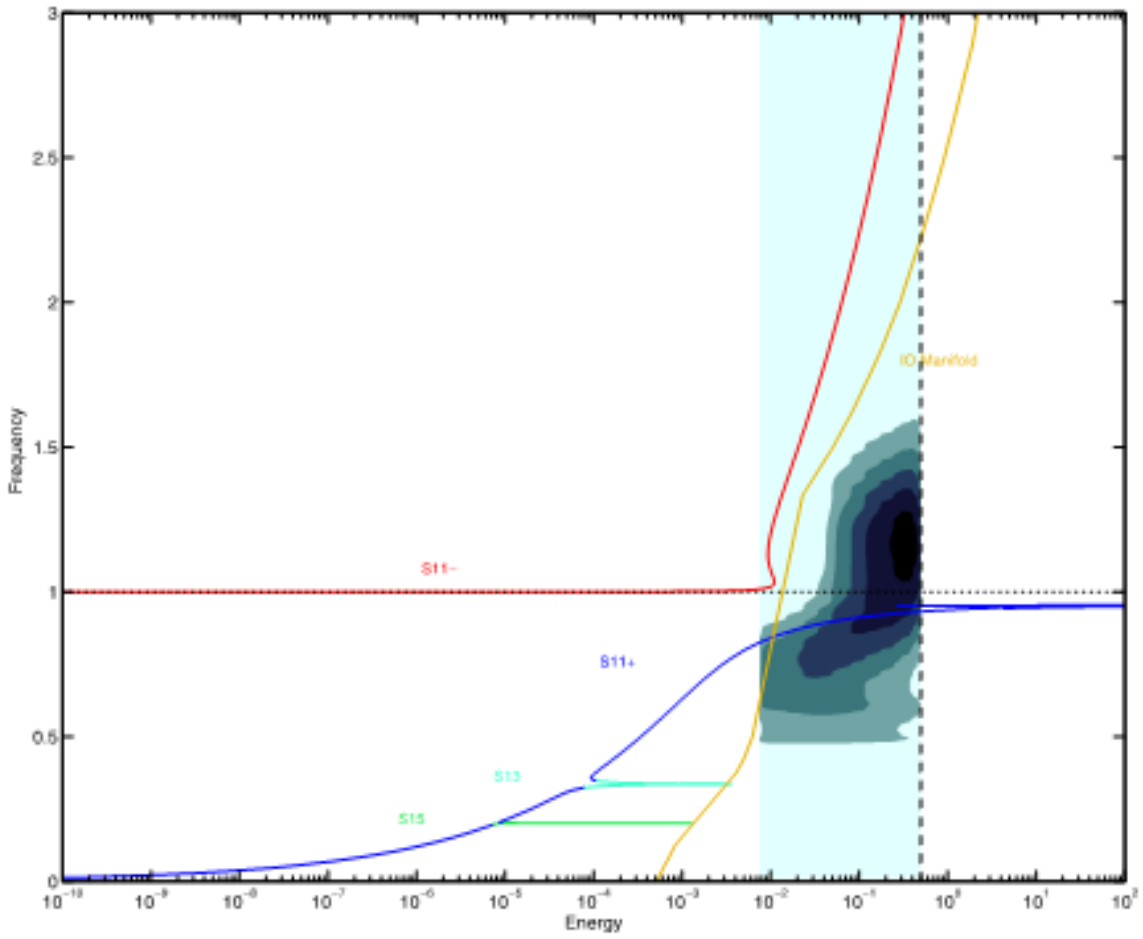

Figure 4.11: Wavelet spectrum of the relative response depicted in Fig.4.10a superimposed on the FEP of the underlying Hamiltonian system for the third cycle of impulsive excitation.

TRCs occurring in the initial highly energetic phase of the impulsive response, in the neighborhood of the high-frequency branch of the IOM, which leads to rapid targeted energy transfers from the primary system to the harvester. That this is indeed the case is confirmed by the rapid decay of the transient response of the primary system (cf. Fig.4.10b) and the simultaneous high-amplitude and high-frequency oscillation (manifested as transient dynamic instability) of the nonlinear harvester. We note that similar dynamics occurs during each cycle of the relative response of Fig.4.10a, justifying the high efficiency of energy harvesting in this system.

Next, we analyze the dynamic response of the harvester in the phase-dependent regime corresponding to relatively small inter-arrival times, realized for impulse intensity $I_0 = 1.0$ and inter-arrival time $\mu_T = 1.19$. In this case there is significant residual energy remaining in the system when a subsequent impulse is applied, so the non-trivial state of the system during the application of each impulse is expected to significantly influence its energy harvesting capacity. In Fig.4.12 we depict the transient dynamics of the harvester in this phase-dependent case. The first distinctive difference relative to the robust case is the aperiodic character of the transient response. Moreover, we observe that in contrast to the robust regime in this case the energy of the vibration is confined mainly in the neighborhood of the natural frequency of the primary system. Although some high-frequency oscillations are realized, these are weak, and the high-frequency dynamic instability that led to strong energy harvesting in the previous case is now completely missing. These conclusions are confirmed by the FEP of Fig.4.13 which depicts the wavelet spectrum of the relative response superimposed on the Hamiltonian FEP. As a result, in this dynamic regime there is much lower utilization of the total energy after each impulse, and the energy harvesting efficiency is low as confirmed by measure (4.20), which is sub-optimal in this sense (cf. Fig.4.9).

We emphasize, however, that even in this phase-dependent regime of energy harvesting the time-averaged energy harvested measure (4.18) can attain higher values than the previous robust harvesting regime, and to this end further analysis based on a stochastic approach is required to analyze the efficiency of energy harvesting. The previous studies revealed the sensitivity of the efficiency of energy harvesting in system (4.11) for fixed impulse intensity and varying inter-arrival time. We now proceed to the study of the

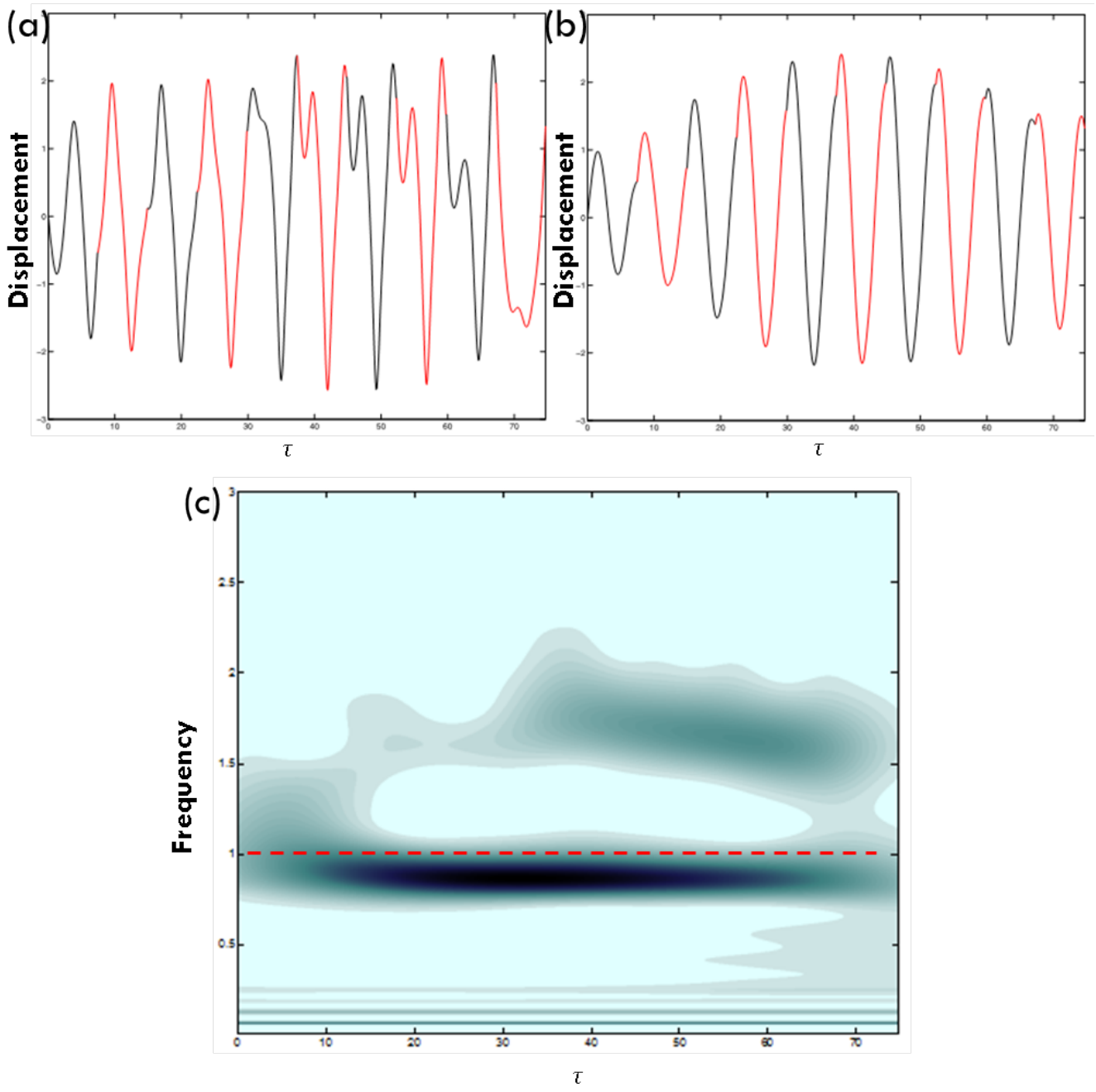

Figure 4.12: Case of efficient nonlinear energy harvesting for $I_0 = 1.0$ and $\mu_T = 1.19$: (a) Relative response between primary system and harvester, (b) response of the primary system, and (c) wavelet spectrum of (a); the dashed line indicates the normalized natural frequency of the primary system.

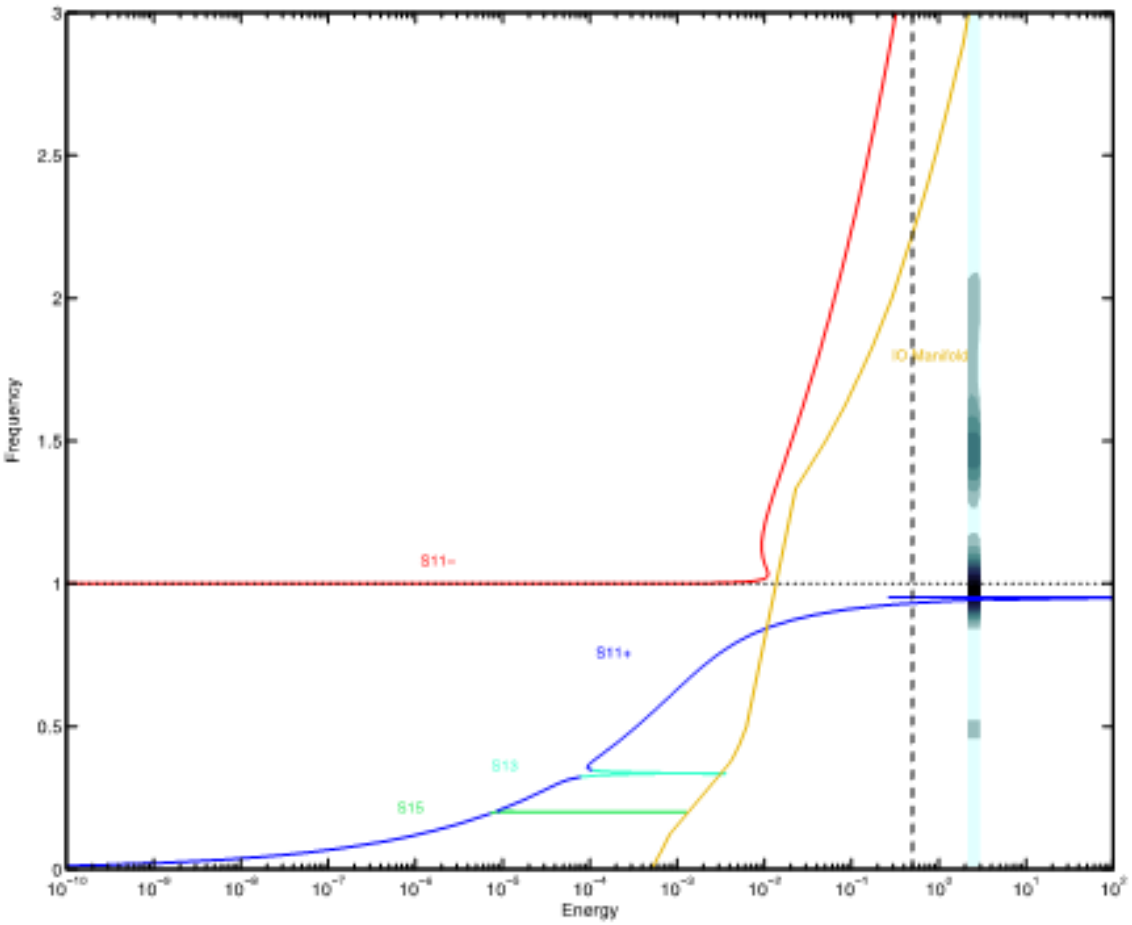

Figure 4.13: Wavelet spectrum of the relative response depicted in Fig.4.12a superimposed on the FEP of the underlying Hamiltonian system for the seventh cycle of impulsive excitation.

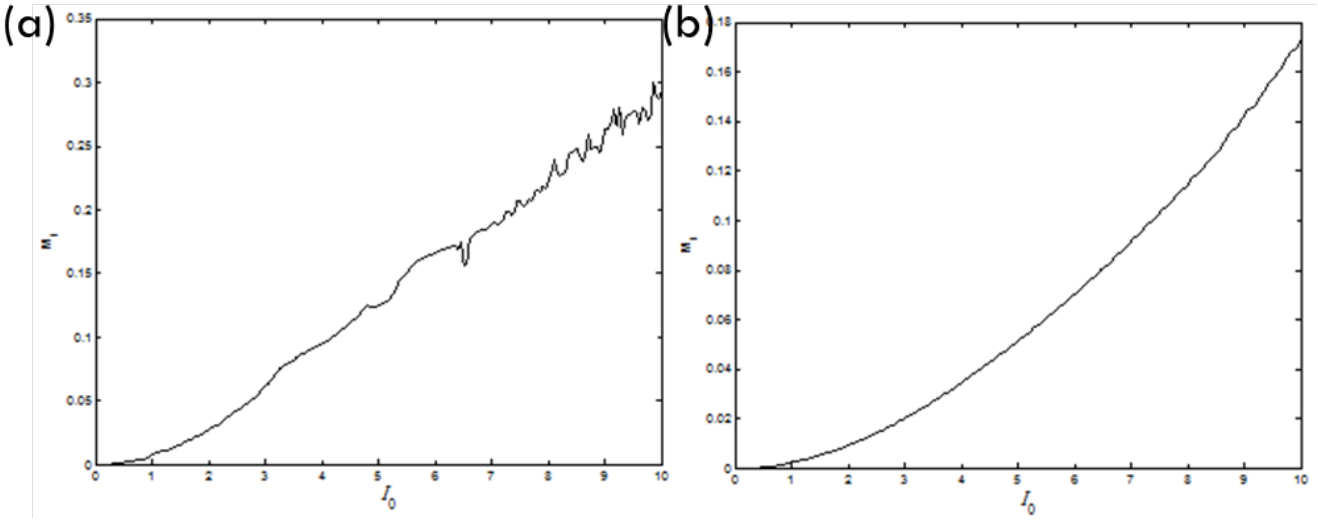

Figure 4.14: Time-averaged harvested energy (4.18) for the nonlinear harvesting system (4.11) as a function of impulse intensity I_0 for inter-arrival time (a) $\mu_T = 10$ and (b) $\mu_T = 30$.

harvesting system under periodic pulse train excitation for fixed inter-arrival times and varying impulse intensity.

The results in terms of the three harvesting measures are shown in Fig.4.14-Fig.4.16. The first two measures (cf. Fig.4.14 and Fig.4.15) show an almost monotonic increase of the energy harvested with respect to impulse intensity for small and large inter-arrival times. More information is provided by the third measure (cf. Fig.4.16), which depicts the capacity of the system to harvest the available energy after the application of an impulse; i.e., the utilization of the available energy after each impulse. In particular, this measure shows an increasing trend for the smaller impulse intensities, which slowly decreases after reaching a maximum close to $I_0 = 1.0$. This tendency is observed for both cases of inter-arrival times considered. As discussed earlier, low-intensity impulses lead to damped dynamic transitions on low-frequency subharmonic tongues, which result in lower energy harvesting efficiency. However, higher-magnitude impulses (near an optimal value of unity) result in damped transitions in the neighborhood of the high-frequency IOM, which result in high energy harvesting efficiency. This explains the trends observed in Fig.4.14-Fig.4.16.

In Fig.4.17 a computational study of the dependence of the three energy harvesting measures is presented for both the impulse intensity and

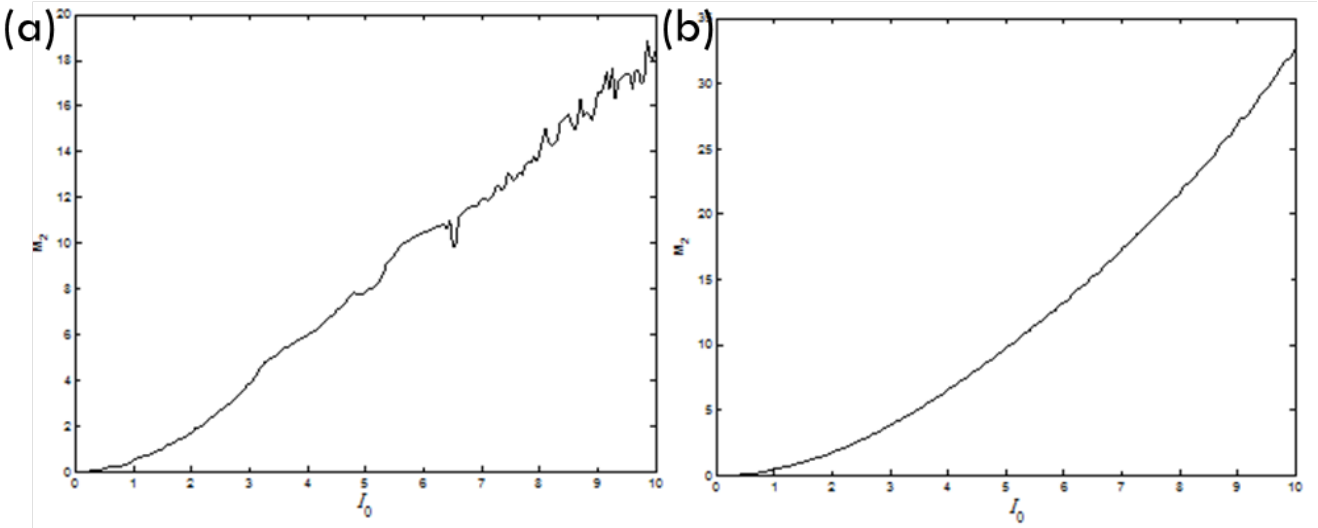

Figure 4.15: Time-averaged harvested energy (4.19) for the nonlinear harvesting system (4.11) as a function of impulse intensity I_0 for inter-arrival time (a) $\mu_T = 10$ and (b) $\mu_T = 30$.

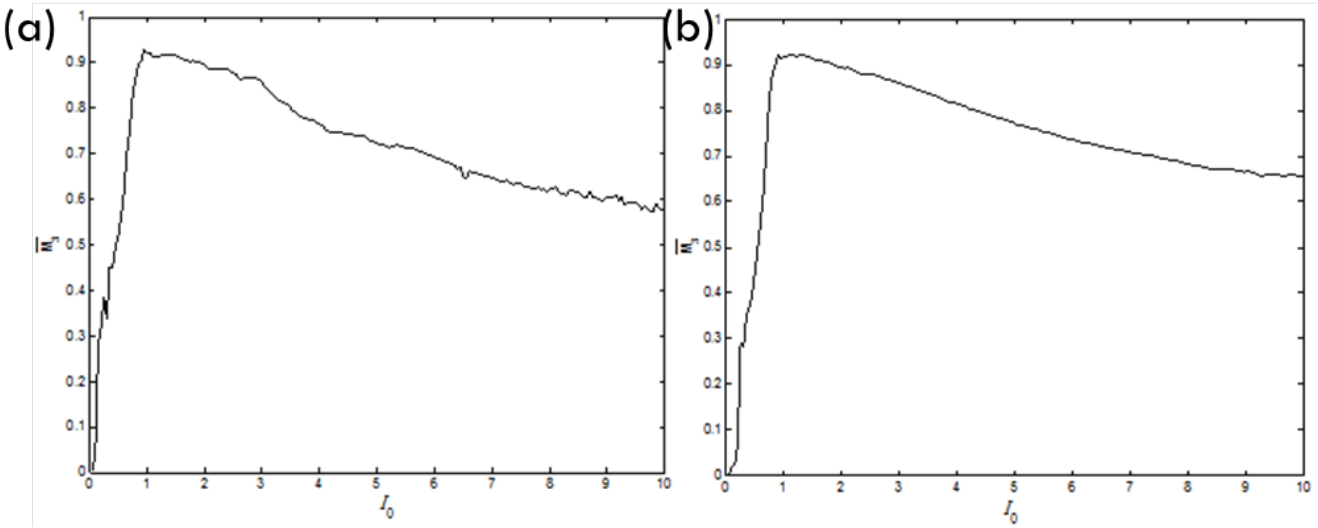

Figure 4.16: Impulse-averaged canonical harvested energy measure (4.20) for the nonlinear harvesting system (4.11) as a function of impulse intensity I_0 for inter-arrival time (a) $\mu_T = 10$ and (b) $\mu_T = 30$.

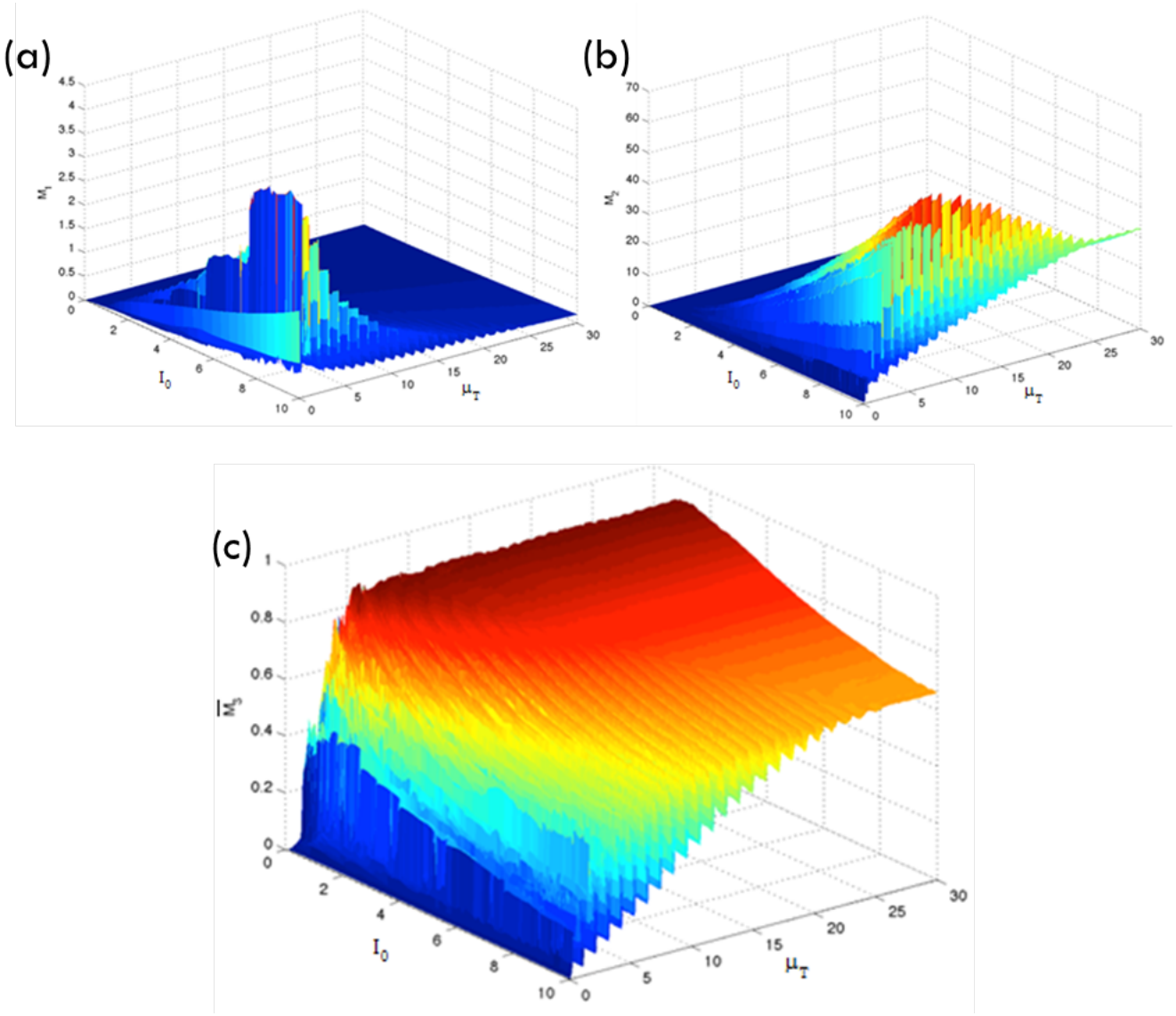

Figure 4.17: Energy harvesting performance as a function of impulse intensity and inter-arrival time: (a) measure (4.18), (b) measure (4.19), (c) measure (4.20).

the inter-arrival time in order to get the complete picture of the effectiveness of the electromechanical system (4.11) as the parameters of the applied pulse trains vary. The previous results depicted in Fig.4.14-Fig.4.16 thus represent "slices" of the corresponding three-dimensional plots of Fig.4.17. Considering the information provided by the harvesting measure (4.20) (Fig.4.17c), it is deduced that an efficient energy harvesting regime is realized for pulse train parameters $I_0 \approx 1$ and $\mu_T > 4$. On the other hand, the average energy harvesting measure (4.18) depicted in Fig.4.17a indicates that an inter-arrival time greater than $\mu_T = 5$ might be excessive, since in that case the periods between impulses are so large that the energy harvesting device returns to its trivial equilibrium state before the next impulse is applied. Hence a redundancy occurs with the device becoming under-utilized. Also, as mentioned previously, the impact-averaged measure (4.19) (cf. Fig.4.17b) provides us with another indication of the effectiveness of energy harvesting in this parameter regime. It follows that parametric studies such as the ones reported in Fig.4.17 enable one to design system (4.11) for optimal energy harvesting for time-periodic pulse train excitation of given impulse intensity and inter-arrival time.

Despite the usefulness of these results, however, they do not provide any measure of robustness of energy harvesting to parameter variations in the harvester itself. To this end, it would be desirable to perform such a robustness study by extending for the case of repetitive impulses the similar study performed earlier where "plateaus" of strong energy harvesting were noted over variations of the electromechanical parameters (β,ρ) of the harvester (cf. Fig.4.3).

Based on the previous study, for the normalized system parameters considered, we select an optimal impulse intensity of the pulse train equal to $I_0 = 1$ and consider variable inter-arrival times μ_T. The previous results were derived for electromechanical parameters of the harvester $\mu = 0.1$, $\lambda = 0.01$, $\zeta = 0.001$, $\sigma = 0$, $\beta = 0.84$, and $\rho = 1.0$, and now we wish to investigate the robustness of energy harvesting in the optimal regime by varying the parameters (β,ρ). In particular, we examine if "plateaus" of highly efficient energy harvesting, indicating robustness, appear in suitably constructed contour plots, similar to Fig.4.3 for the case of single impulse excitation.

To achieve this goal we will consider the dependence of the energy measure (4.20) (as the main indicator of energy harvesting efficiency) on the parame-

ters (β,ρ) for varying μ_T, while keeping all other system parameters and the impulse intensity fixed. We will restrict our attention to the neighborhood of $(\beta, \rho) = (0.84, 1.0)$, which was considered in the previous optimization study, and examine the energy harvesting efficiency of system (4.11) in that neighborhood for two different inter-arrival times $\mu_T = 1$ and $\mu_T = 5$.

In Fig.4.18 contour plots of (4.20) as a function of (β,ρ) for the first four impulse cycles are depicted when $\mu_T = 1$. Each of these plots was constructed by evaluating the measure (4.20) from direct numerical simulations of equations (4.11) subject to the specific initial conditions (4.14) at the start of the considered impulsive cycle; alternatively, these plots reveal how the capacity of energy harvesting depends on the system parameters and the inter-arrival time, as well as the state of the harvester at the beginning of each impulsive cycle. The optimal design point $(\beta, \rho) = (0.84, 1.0)$ is indicated by a cross in each of these plots. As seen from Fig.4.18, the contour plots change both qualitatively and quantitatively with each applied impulse; however, for this small inter-arrival time the harvesting efficiency is in general small. This is indicated by the absence of a "plateau" of high values of the harvesting measure, a result which correlates with our previous results. In conclusion, the results indicate a consistently low level of energy harvesting irrespective of the choice of parameters (β,ρ), and the process is mainly dominated by the short inter-arrival time μ_T as well as the state of the harvester at the beginning of each impulsive cycle.

In Fig.4.19 we depict the corresponding contour plots for (4.20) for the higher inter-arrival time $\mu_T = 5$, and a completely different picture of energy harvesting efficiency emerges. In this case, the larger inter-arrival time enables the dynamics to form "plateaus" of high values of measure (4.20) right from the first impulsive cycle. Indeed, for each of the leading four cycles depicted, we note the formation of a plateau of strong energy harvesting in the neighborhood of the optimal point $(\beta, \rho) = (0.84, 1.0)$, indicating robustness of the energy harvesting dynamics. As discussed earlier for the case of single impulses, on these plateaus there occur high-frequency TRCs at the beginning of each cycle, leading to high-frequency dynamic instability of the harvesting element and, hence, to efficient energy harvesting. On the contrary, for small inter-arrival times (cf. Fig.4.18), low-frequency TRCs are realized in the transient dynamics between cycles, which are not favorable to the energy harvesting objective. A final note regarding the plots of Fig.4.18

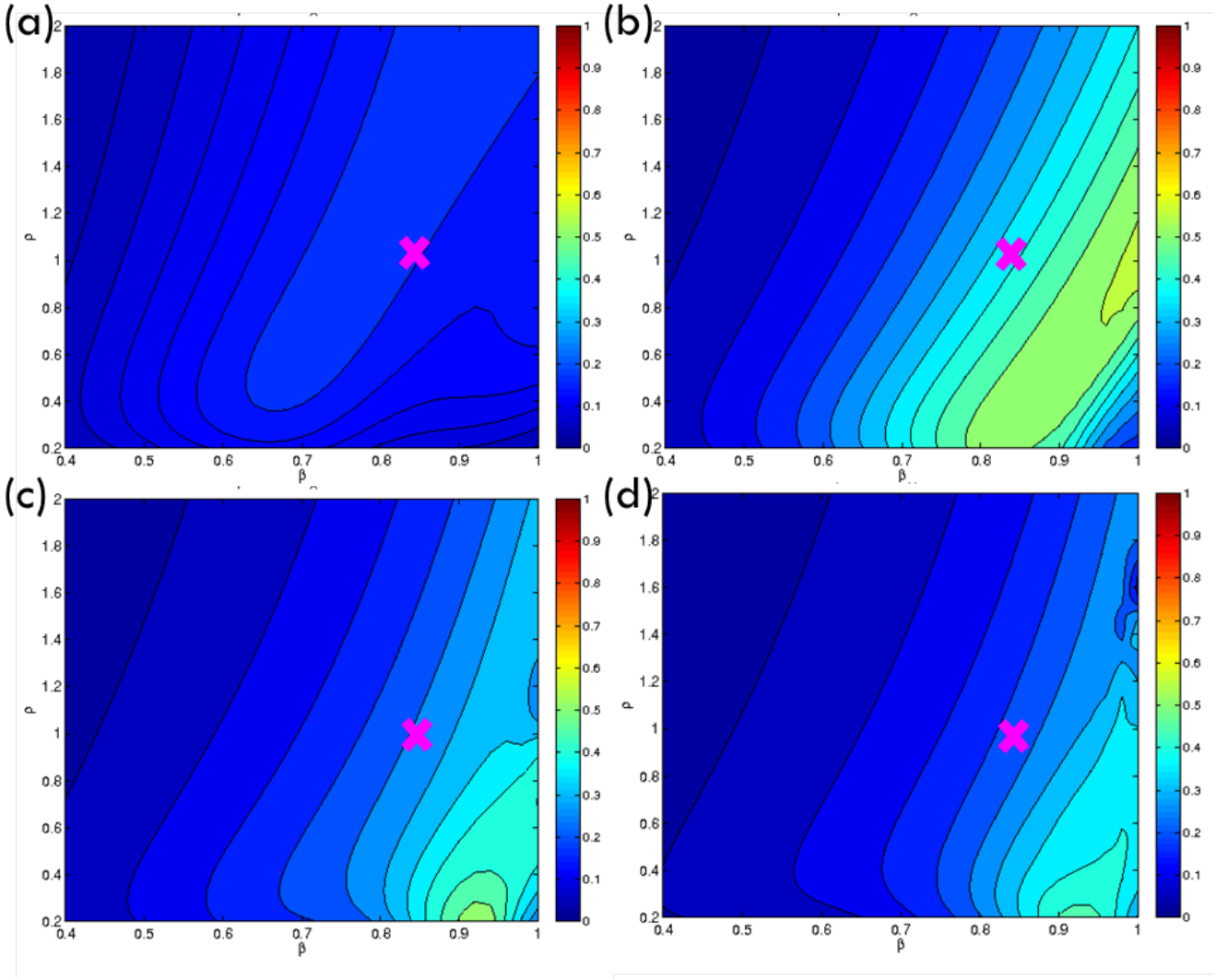

Figure 4.18: Contour plots of measure (4.20) as a function of (β,ρ) for impulse intensity $I_0 = 1.0$ and inter-arrival time $\mu_T = 1$ for leading impulsive cycles: (a) cycle 1, (b) cycle 2, (c) cycle 3, (d) cycle 4.

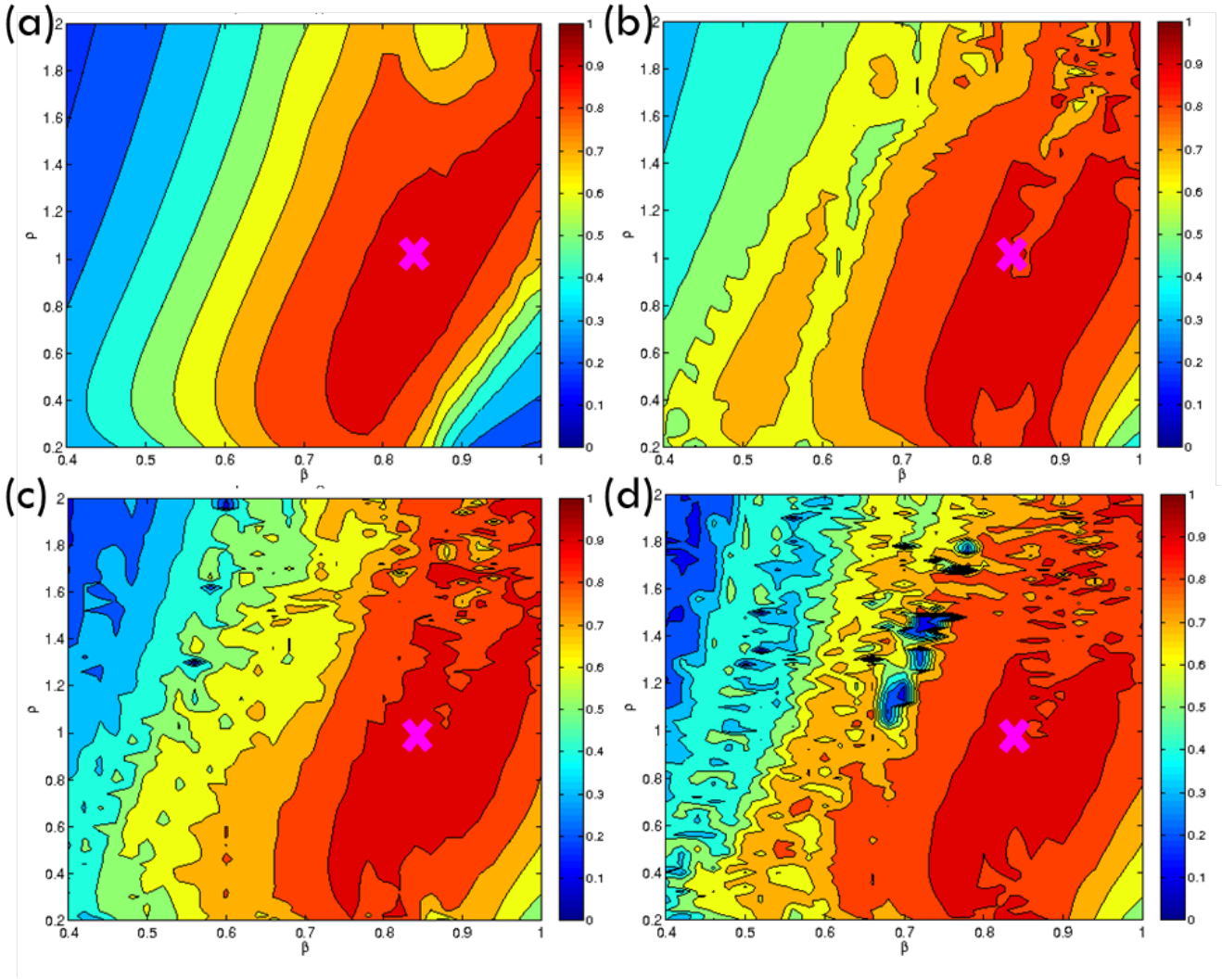

Figure 4.19: Contour plots of measure (4.20) as a function of (β,ρ) for impulse intensity $I_0 = 5.0$ and inter-arrival time $\mu_T = 1$ for leading impulsive cycles: (a) cycle 1, (b) cycle 2, (c) cycle 3, (d) cycle 4.

and Fig.4.19 is that they can be considered as extensions for the repetitive impulse case (second impulse excitation scenario) of the plot of Fig.4.3, constructed for the single impulse case (first impulse excitation scenario). As such, these plots provide an integrated picture of the effects of parameter changes on energy harvesting capacity as the inter-arrival time changes. Using this methodology the robustness of the energy harvesting operation can be systematically and thoroughly studied.

4.2 Experimental Study

The computational results presented in the previous section indicate that with proper parameter selection, the system (4.11) can be forced into a state of sustained high-frequency dynamic instability. This state is favorable for harvesting energy efficiently; however, harvesting capability is strongly dependent upon the electromechanical coupling parameter β and the circuit loading parameter ρ. Recall that these non-dimensional parameters are derived from physical dimensional parameters inherent to piezoelectric devices, as outlined in (4.12). As deduced from (4.12), the electromechanical coupling is primarily dependent upon the capacitance and the parameter r, which describes the piezoelectric voltage constant and the piezoelectric strain constant. These parameters inherent to the underlying piezoelectric crystal are fixed, placing the only freedom in designing the electromechanical coupling on the wire stiffness coefficient and the type of wire used. The circuit loading parameter ρ is strongly dependent upon the capacitance and the load resistance, which can be freely varied in the accompanying circuit and thus providing design freedom.

To this end, a simple single-degree-of-freedom experiment was designed to identify these system parameters resulting from a piezoelectric cable obtained from the study in [25] and applied to the air-track setup described in Chapter 2. A piezoelectric cable is physically composed of several radial wrapping layers in the cross-section, which include (from core to outside) a stranded central core, PVDF piezo film tape, a copper braid, and finally a polyethylene protective coating. Due to the number of layers and compactness in the winding, an important geometric constraint is placed on the piezoelectric strain constant. This results in a relatively lower electromechan-

ical coupling factor compared to other piezoelectric devices, such as foams or patches. In addition the compliant outer polyethylene coating constitutes one of the thickest layers, reducing the strain experienced by the dielectric elements and thus reducing the resulting output voltage. Identification of these non-published parameter values for the piezoelectric cable used in this experimental study was paramount for determining the efficacy of incorporating it into the system described in Section 4.1 and given by (4.9).

Following from the analysis presented in Section 4.1, the equations of motion for the nonlinear portion of the system as a SDOF oscillator can be expressed as

$$m_a\ddot{v} + \left[b_a\frac{v\dot{v}}{v^2+h^2} + k_a(\sqrt{v^2+h^2}-l) - (rk_a)Q\right]\frac{2v}{\sqrt{v^2+h^2}} = F(t) \quad (4.34a)$$

$$R\dot{Q} + (1/C)Q - (rk_a)(\sqrt{v^2+h^2}-l) = 0 \quad (4.34b)$$

where v now describes the absolute displacement of the SDOF harvester, which is directly forced in this case. The electromechanical coupling parameters are realized physically in (4.34) in the stiffness, which now grounds the oscillating mass. The other parameters are the same as described in Section 4.1 for system (3.15). This system will be used to help identify system parameters, as performed in Section 3.2.2.

The experimental apparatus is presented in Fig.4.20. The piezoelectric cable grounds the SDOF oscillating mass via the two upright blue pillars, which provide a rigid boundary. The piezoelectric cable is oriented perpendicular to the direction of oscillation, providing the means for the strong cubic stiffness nonlinearity, as performed in Section 2.3. The piezoelectric cable is coupled to the SDOF oscillating mass via a squeeze clamp, which is connected to a force transducer. This force transducer can be used to approximate the forces experienced within the cable during the response. As described above, the piezoelectric cable was obtained from a past study [25] in which parameter identification wasn't strictly performed. The air-track greatly reduces contact friction, but induces a small linear stiffness component in the dynamics. The piezoelectric cable is fixed such that there is no pretension, minimizing additional linear stiffness components.

Single impulsive forces are applied to the SDOF mass by means of an impact hammer. The nonlinear mechanical parameter values of the experi-

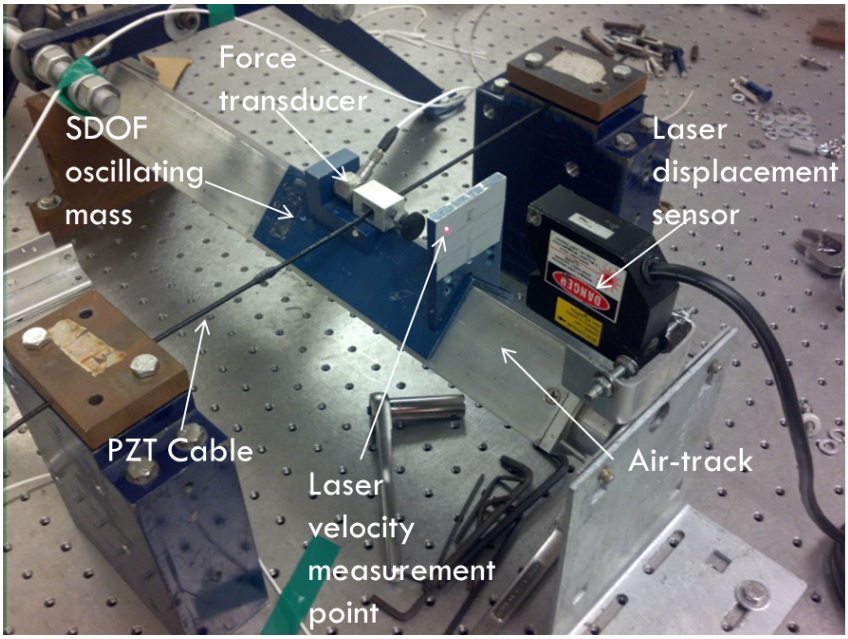

Figure 4.20: Experimental realization of the system (4.34).

Table 4.1: Experimentally identified system parameters for the fixture presented in Fig.4.20.

Parameter	Value
m_a	$0.291kg$
k_a	$270N/m$
h	$0.152m$
b_a	$0.95Ns/m$
C	$1.24nF$
r	$0.08m/C$
R	$507k\Omega$

mental system were identified by utilizing the restoring force surface method [41], as performed in Section 2.3.1. The capacitance of the piezoelectric cable was measured directly using a capacitance meter. The circuit load is free to vary for optimization as discussed above. The only remaining parameter to be determined is the electromechanical coupling parameter r, which is a function of several properties inherent to the piezoelectric material, as outlined in Section 1.1. This parameter was identified by comparing the voltage output from the experimental system to numerical simulations of system (4.34), as performed in Section 3.2.2. An optimized load resistance for the system can then be computed directly from the resulting parameters. The system parameters were identified as shown in Table 4.1. A velocity time series comparison of the experimental system depicted in Fig.4.20 with the numerical system (4.34) and parameters from Table 4.1 for $I_0 = 0.3m/s$ is depicted in Fig.4.21. As seen in the figure, the numerical simulation corresponds strongly to the experimental response, validating the parameter identification.

As stated earlier, for the single impulse excitation a PCB modal hammer was used to apply the excitation to the SDOF oscillator with the system initially at rest. The velocity time series measurement of the SDOF oscillator was obtained using a single Polytec VibraScan laser vibrometer at a sampling frequency of $512Hz$. The displacement time series measurement was also obtained using a MICRO-EPSILON laser scatter displacement sensor. As mentioned previously, a PCB force transducer was placed in series with the piezoelectric cable to approximate the force in the cable. The voltage across the resistive load in the circuit was measured for later computation of output power. The data acquisition was synchronized using the impact hammer as the triggering mechanism, with a small pre-trigger time of $128ms$. The synchronized response of the oscillator system was very important for the accurate computation of the system parameters.

The experimental investigation for this piezoelectric cable element was limited to this SDOF system due to the nano-scale energy harvesting capability of the SDOF oscillator. Due to concerns raised by the identified electromechanical coupling, this piezoelectric coupling element was not incorporated into an experiment representative of system (4.9). The identified system parameters depicted in Table 4.1 correspond to a non-dimensional electromechanical coupling $\beta = r\sqrt{Ck_a} = 4.45 \times 10^{-5}$, which is far below the optimal electromechanical coupling parameter of $\beta = 0.84$ as determined during the

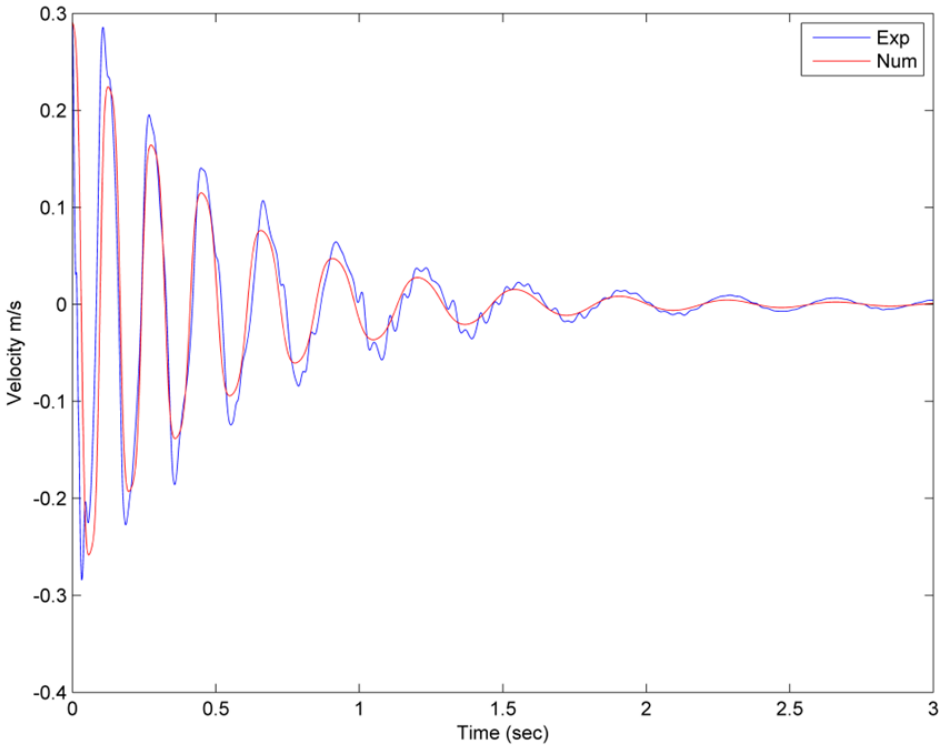

Figure 4.21: Velocity time series comparison of the experimental system from Fig.4.20 with the corresponding numerical simulation of (4.34) for parameter identification validation.

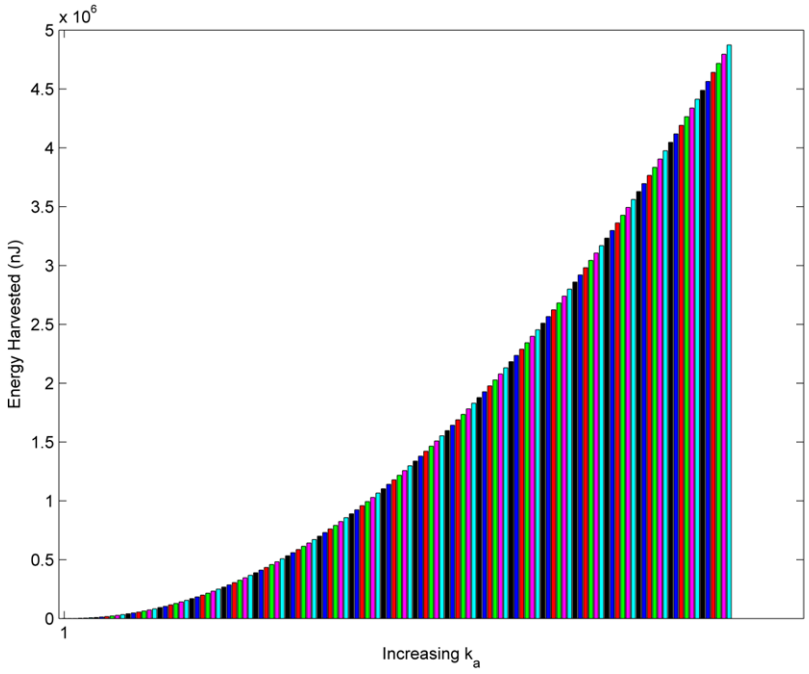

Figure 4.22: Numerical investigation of the effect of varying coupling stiffness k_a on the energy harvesting capability of the system (4.34) for a fixed excitation magnitude.

analysis in Section 4.1. The relatively small piezoelectric strain constants and $nano - Farad$ scale capacitance inherent to these types of piezoelectric cables limits the electromechanical coupling design to the coupling stiffness magnitude.

The effect on electromechanical coupling of varying this coupling stiffness with all other parameters held constant is depicted in Fig.4.22. A range of coupling stiffness coefficients $k_a = [100 - 100000]N/m$ are selected to reflect non-dimensional electromechanical coupling coefficients in the range of $\beta = [1 \times 10^{-5} - 1]$. As expected from the definition of the non-dimensional electromechanical coupling parameter, as the coupling stiffness is increased, the output energy increases. Energy harvesting capability of $milli - Watt$ scale is achievable for large cable stiffness on the order of $O(4)N/m$, which is only physically realizable with additional piezoelectric wires (> 30) placed in parallel. Due to size and damping limitations for the scale of the apparatus and dynamical phenomena required, this coupling restriction is detrimental to this specific apparatus design based on an air-track of this size. This

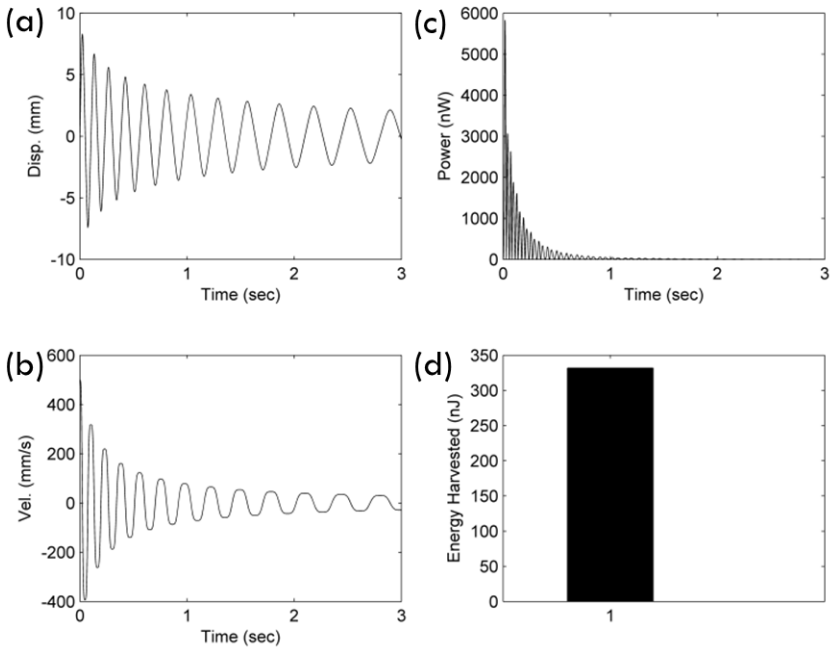

Figure 4.23: Numerical investigation of system (4.34) for coupling stiffness $k_a = 270N/m$ depicting (a) displacement time series of the SDOF mass, (b) velocity time series of the SDOF mass, (c) power output time series, (d) overall energy harvested for the duration of the response for $I_0 = 0.5m/s$.

required stiffness is comparable to that of elastic steel cantilever beam designs, which is an important observation governing the popularity of the cantilevered harvester.

Numerical simulations for the near-minimum and maximum coupling stiffness cases examined in Fig.4.22 can be considered in more detail using the time series responses to realize the effects of the stiffness on the electromechanical coupling. The response depicted in Fig.4.23 represents energy harvesting capability of system (4.34) with the experimentally identified parameters shown in Table 4.1, which represents the near-minimum coupling stiffness case. The displacement time series and velocity time series responses are depicted in Fig.4.23a,b for an excitation magnitude $I_0 = 0.5m/s$. Fig.4.23c indicates the instantaneous power harvested versus time, resulting in a peak power of $6000nW$ and an average power of $\sim 340nW$. Fig.4.23d indicates a maximum energy harvested of $340nJ$.

The response depicted in Fig.4.24 represents energy harvesting capability of system (4.34) with the experimentally identified parameters shown in Table

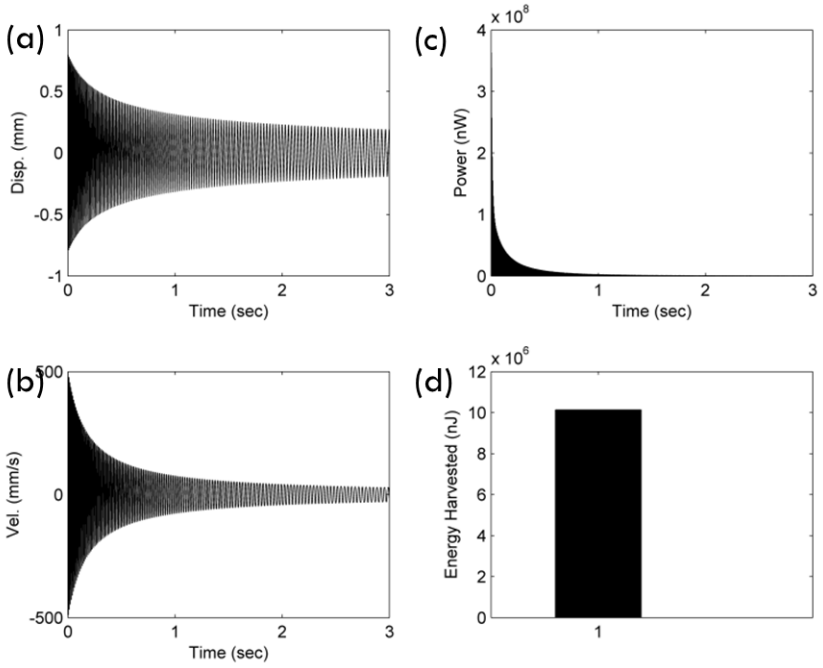

Figure 4.24: Numerical investigation of system (4.34) for coupling stiffness $k_a = 100000N/m$ depicting (a) displacement time series of the SDOF mass, (b) velocity time series of the SDOF mass, (c) power output time series, (d) overall energy harvested for the duration of the response for $I_0 = 0.5m/s$.

4.1 but with the coupling stiffness $k_a = 100000N/m$. This represents the maximum coupling stiffness case presented in Fig.4.22. The displacement time series and velocity time series responses are depicted in Fig.4.24a,b for an excitation magnitude $I_0 = 0.5m/s$. The effect of the increased coupling stiffness has a profound effect on the response of the harvester, as expected, in which the operation frequency is much higher. Fig.4.24c indicates the instantaneous power harvested versus time, resulting in a peak power of $0.3mW$ and an average power of $\sim 0.01mW$. Fig.4.23d indicates a maximum energy harvested of $0.01mJ$.

It is concluded here that piezoelectric electromechanical coupling elements are not suitable for this type and scale of energy harvesting apparatus. The computational analysis provided valuable insight into sustained high-frequency energy harvesting capability and robust system design; however, coupling induced with piezo-cable elements is not suitable for the design requirements.

CHAPTER 5

MAIN FINDINGS OF THIS WORK AND SUGGESTIONS FOR FURTHER RESEARCH

5.1 Research Summary

The research documented in this work presented a computational and experimental study of the impulsive dynamics of a linear oscillator coupled to a lightweight attachment by means of an essentially nonlinear stiffness nonlinearity of the third degree. The term "essential nonlinearity" describes the lack of (or the presence of a small) linear component in the stiffness characteristic. This strong nonlinearity is realized by geometric effects; i.e., by introducing nonlinear effects appearing due to midplane stretching of a linearly elastic wire with negligible or very small internal tension. The presence of essential stiffness nonlinearity leads to negligible (or very small) linearized eigenfrequency of the attachment, in effect removing any preferential resonance frequency in its dynamics. This enables it to engage in nonlinear resonance with the linear oscillator over broad frequency and energy ranges. The resulting broadband dynamics of the strongly nonlinear attachment is manifested in the form of high-frequency dynamical instabilities, whereby the nonlinear attachment reacts to impulsive excitation of the linear oscillator with relatively high-amplitude oscillations of varying frequency content.

These high-frequency oscillations of the attachment are due to continuous resonance scattering of its dynamics on the high-frequency portion of the impulsive orbit manifold IOM of the system, a dynamical phenomenon that is exclusively due to the essential stiffness nonlinearity of the problem and cannot exist in linear or weakly nonlinear settings. As a result, this system represents a good candidate for vibration energy harvesting in situations where a primary system is forced by single or repetitive impulses; lightweight attachments of the type considered in this work can be designed so that the resulting high-frequency dynamical instabilities can be employed for energy

harvesting.

This study then presented a computational and experimental study of the impulsive dynamics of a strongly nonlinear electromechanical energy harvester subjected to various forcing frequencies and magnitudes. Essential cubic stiffness nonlinearities are realized via simple geometric and kinematic effects in the coupling between a primary linear oscillating mass and a lightweight oscillating attachment. Direct impulsive excitation of this primary system with the strong nonlinear coupling gives rise to high-frequency nonlinear transient resonance captures in the damped dynamics of the two oscillators. Low-frequency TRCs are not favorable to the energy harvesting objective, since they lead to low-frequency oscillations of the lightweight harvesting element. On the contrary, high-frequency TRCs occurring in the neighborhood of the IOM of the underlying Hamiltonian system give rise to high-frequency dynamic instability of the harvesting element, which undergoes high-amplitude, high-frequency damped oscillations in the initial, highly energetic regime of the impulsive response of the system. These high-frequency instabilities result in strong energy harvesting through the realization of rapid nonlinear targeted energy transfers from the primary structure to the harvesting element, providing the means for superior energy harvesting.

It was shown that, for an appropriate harvester design incorporating piezoelectrics, this type of high-frequency dynamic instability can be sustained theoretically under repetitive impulsive excitations, resulting in sustained high-efficiency nonlinear energy harvesting. The methodologies developed in this work enable the design of the harvesting system for robust efficiency, which is confirmed by extensive computational studies presented therein. This task was achieved by developing suitable energy harvesting measures for both single and repetitive impulse excitations. In addition, low and high values of these harvesting measures were interpreted by carefully examining the wavelet spectra of the nonlinear transient dynamics of the harvester, superimposed on the frequency-energy plot of the underlying Hamiltonian system. The aforementioned low- and high-energy TRCs become evident in these depictions.

This work showed numerically and experimentally that for proper excitation magnitude and frequency, the high-frequency TRCs can be sustained at steady-state, providing for superior energy harvesting performance relative to

1:1 resonance conditions. This was accomplished with a novel experimental apparatus utilizing electromagnetic harvesting elements. Wavelet spectral analysis was again used to identify the presence of these high-frequency instabilities, which were then compared to energy harvesting rate and average output power.

The experimental apparatus was constructed as a proof-of-concept setup, which was utilized with the repeated impulsive forcing scheme explored in this study. The experimental results discussed in this work indicate an average power output of $\sim 140mW$ under optimal forcing frequencies and an average power output of $\sim 30mW$ under non-optimal forcing frequencies for a single impulse magnitude. A full summary of experimental results is presented in Fig.3.28 and Fig.3.29. Proper optimization of the electrical parameters could further increase energy harvesting performance, which wasn't performed in this study. In addition, proper down-sizing and scaling of the masses can allow this system to operate in the high-frequency regime for lower applied impulse magnitudes.

5.2 Future Research

Extending the high performance region for the steady-state operation of the energy harvesting apparatus presented in Chapter 3 (cf. Fig.3.16f) is of paramount interest for future research. This would allow the system response to engage in sustained high-frequency dynamic instabilities for more excitation frequencies and lower amplitudes, making the system more robust and thus increasing energy harvesting performance. In addition computational exploration of the system subjected to modulated impulsive forcing would help study response robustness. Slightly modulated forcing is realized experimentally for both amplitude and frequency, making this an essential aspect of future work. This is discussed in Chapter 2 for the experimental system, but requires further analysis.

The most immediate alteration to the electromagnetic energy harvesting system presented in Chapter 3 would be to decrease the damping in the coupling. The system identification reported in Table 3.2 indicates a relatively high linear viscous damping in the coupling of $b_2 = 10.0Ns/m$. This relatively large damping is generated due to the interaction of the rod with the

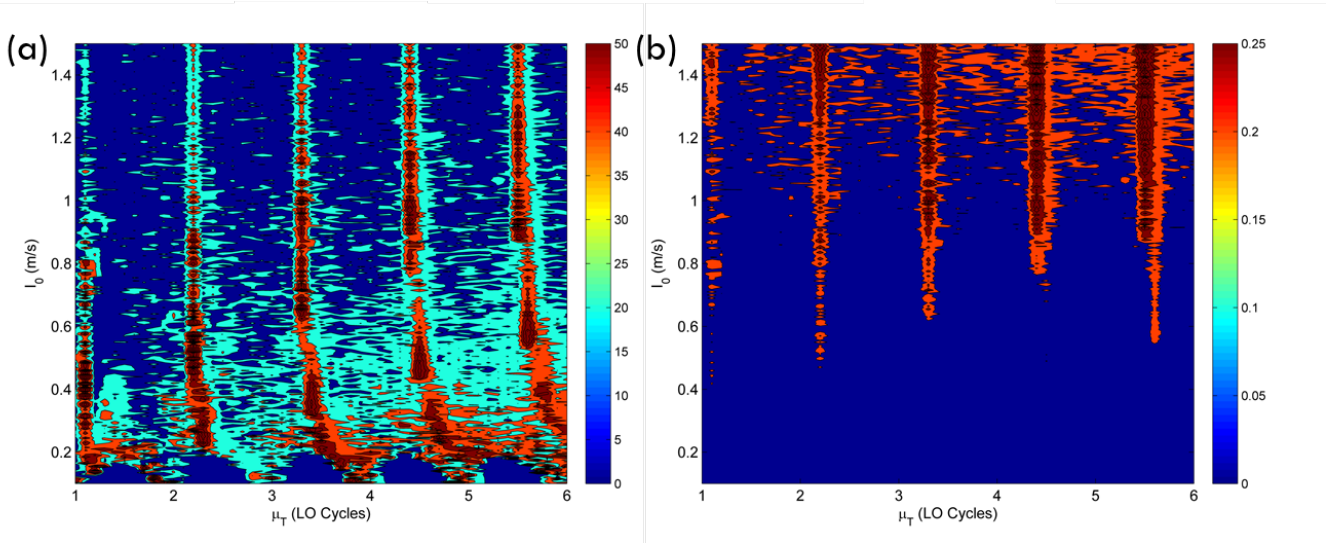

Figure 5.1: Numerical simulation of the 18^{th} impulse for (a) energy harvesting efficiency (3.25) and (b) energy harvesting capability (3.24) for the system (3.15) subject to repeated impulsive excitation with parameters in Table3.2, but with $b_2 = 1.0Ns/m$.

linear bearings in the apparatus depicted in Fig.3.9. Contour plots similar to those presented in Fig.3.15f and Fig.3.16f for the apparatus subject to repeated impulsive excitations were generated for a lower damping value of $b_2 = 1.0Ns/m$, which is depicted in Fig.5.1. As seen in Fig.5.1a, the magnitude of the harvesting efficiency increases greatly, exceeding 50% for various excitation ranges. More importantly, however, is that the high performance ribs are widened to produce better harvesting efficiency for more impulse periods, especially at lower excitation magnitudes. As seen in Fig.5.1b, the energy harvesting capability (3.24) magnitude also increases greatly, exceeding $250mJ$ for various excitation ranges. The reduction in damping extends the high performance ribs slightly downward, resulting in better performance at lower excitation magnitudes, but the effect does not widen the ribs at these lower magnitudes. The damping reduction does, however, widen the high performance ribs for larger impulse magnitudes. Reduction in damping allows for less dissipated energy in the system during each impulse, which in turn provides (i) more energy available to be harvested for each impulse and (ii) more residual energy in the system upon application of the next impulse. As described in Chapter 3, the build up of residual energy in the system allowing for sustained high-frequency instabilities only manifests on the high

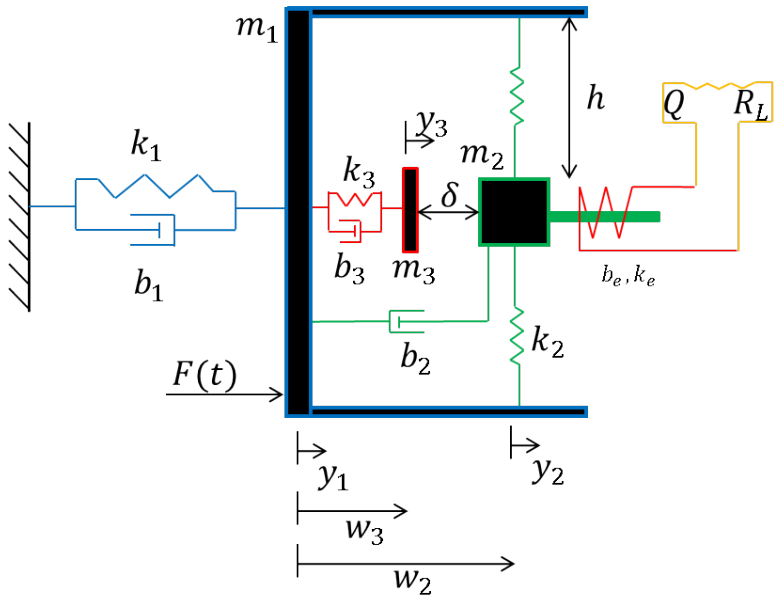

Figure 5.2: Configuration of the system from Chapter 3 with a single-sided vibro-impact element.

performance ribs. The increase in residual energy in the system between application of impulses for lower damping presented here allows the system to engage in these high-frequency dynamics for more forcing frequencies, as indicated by the widening of the ribs in Fig.5.1. Damping should be reduced in the experimental apparatus by incorporating better bearings or a better method of supporting the NES mass.

This alteration does not have enough of an effect for low excitation magnitudes and is more of a "band-aid" fix to boost system performance. High-frequency instabilities need to be induced in the system for lower initial energy states without relying on the build up of energy in the primary system, which currently occurs on the high performance ribs. One method of accomplishing this is with the use of single-sided vibro-impact elements [7]. The system (3.15) discussed in Chapter 3 can be altered such that the NES mass strikes a rigid plate (bumper element), which is connected to the primary system, at a fixed distance δ.

A model for this system is depicted in Fig.5.2, in which a third mass m_3 is coupled to the linear oscillator with linear stiffness k_3 and linear viscous damping b_3 at an initial distance from the NES δ. The equations of motion for this system are thus similar to the system (3.15), but with an extra degree-

of-freedom and some slight alterations. These equations can be expressed as

$$m_1\ddot{y}_1 + b_1\dot{y}_1 + k_1 y_1 - (b_e + b_2)\dot{w}_2 - \frac{k_2}{h^2}w_2^3 - b_3\dot{w}_3 - k_3 w_3 = F(t) \tag{5.1a}$$

$$m_2(\ddot{w}_2 + \ddot{y}_1) + (b_e + b_2)\dot{w}_2 + \frac{k_2}{h^2}w_2^3 = 0 \tag{5.1b}$$

$$m_3(\ddot{w}_3 + \ddot{y}_1) + b_3\dot{w}_3 + k_3 w_3 = 0 \tag{5.1c}$$

$$\dot{Q} - \frac{b_e}{k_e}\dot{w} = 0 \tag{5.1d}$$

where the relative displacement between the NES and primary system is now defined as $w_2 = y_2 - y_1$ and the relative displacement between the bumper and primary system is now defined as $w_3 = y_3 - y_1$.

The bumper is modeled as a separate degree of freedom to provide for freedom in designing its compliance. Additional requirements are imposed on the system, such as a coefficient of restitution for the impacts and the moment at which an impact occurs. An impact occurs between the NES and bumper element when the condition $w_2 - w_3 > -\delta$ is satisfied. With proper optimization of the compliance k_3 and spacing δ, the bumper can induce high-frequency instabilities into the system (5.1) at lower impulse magnitudes, providing the basis needed for the superior energy harvesting capability presented in this document. Continued use of electromagnetic harvesting elements within this system is recommended for the benefits outlined in Chapter 3.

The system (5.1) has not yet been thoroughly investigated, although early simulations for single impulses are encouraging for continued research. This system was inspired by a related model utilizing piezoelectric harvesting elements. A polyvinylidene fluoride dielectric (PVDF) piezo-foam was incorporated as a vibro-impact bumper element similar to the system (5.1), but now without the electromagnetic harvesting elements. Energy is harvested in this system due to deflection of the piezo-bumper when the NES strikes it. This model is depicted in Fig.5.3 with equations of motion expressed as

$$m_1\ddot{y}_1 + b_1\dot{y}_1 + k_1 y_1 - \frac{2b_2}{h^2}w_2^2\dot{w}_2 - \frac{k_2}{h^2}w_2^3 - b_3\dot{w}_3 - k_3 w_3 + k_3 rQ = F(t) \tag{5.2a}$$

$$m_2(\ddot{w}_2 + \ddot{y}_1) + \frac{2b_2}{h^2}w_2^2\dot{w}_2 + \frac{k_2}{h^2}w_2^3 = 0 \tag{5.2b}$$

$$m_3(\ddot{w}_3 + \ddot{y}_1) + b_3\dot{w}_3 + k_3 w_3 - k_3 rQ = 0 \tag{5.2c}$$

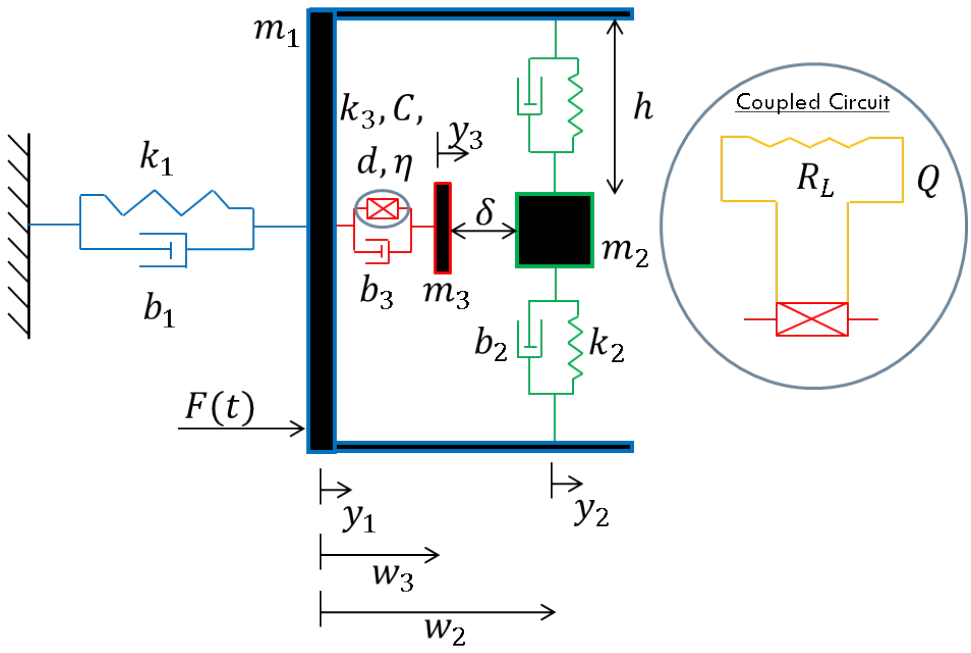

Figure 5.3: Configuration based on the mechanical system from Chapter 2 with a single-sided vibro-impact piezoelectric element.

$$R_L\dot{Q} + \frac{1}{C}Q - k_3 r w_3 = 0 \tag{5.2d}$$

where C describes the capacitance, r describes the electromechanical coupling, and k_3 describes the stiffness of the piezoelectric bumper, which is modeled again an additional degree-of-freedom.

Early simulations of this complex system (5.2) for single and repeated impulse excitation scenarios proved encouraging, which eventually was expanded to an experimental study of the system, which is depicted in Fig.5.4. The experimental harvesting capability of the experimental apparatus suffered the same fate as the system (4.9) presented in Chapter 4, in which the electromechanical coupling was small relative to the optimal value needed for this apparatus and thus resulted in low energy harvesting capability. However, the system (5.2) did provide insight into the effect of using vibro-impact elements to induce high-frequency instabilities within the NES response for low excitation magnitudes, as well as experimental validation of the numerical simulations.

Experimental parameters were identified similar to the processes outlined in Sections 2.3, 3.2.2, and 4.2 and then incorporated into numerical simulations for system (5.2), although some uncertainty existed for the bumper

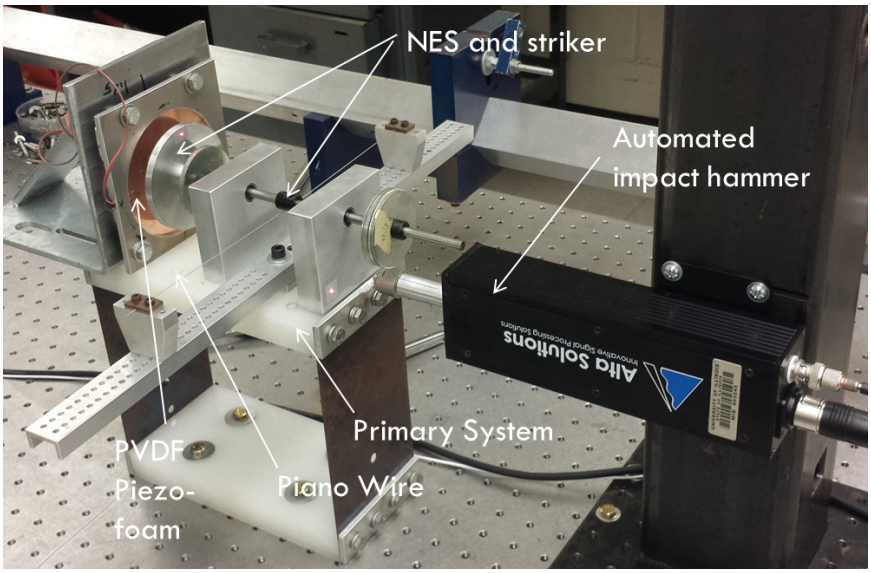

Figure 5.4: Experimental realization of the system (5.2) depicted in Fig.5.3.

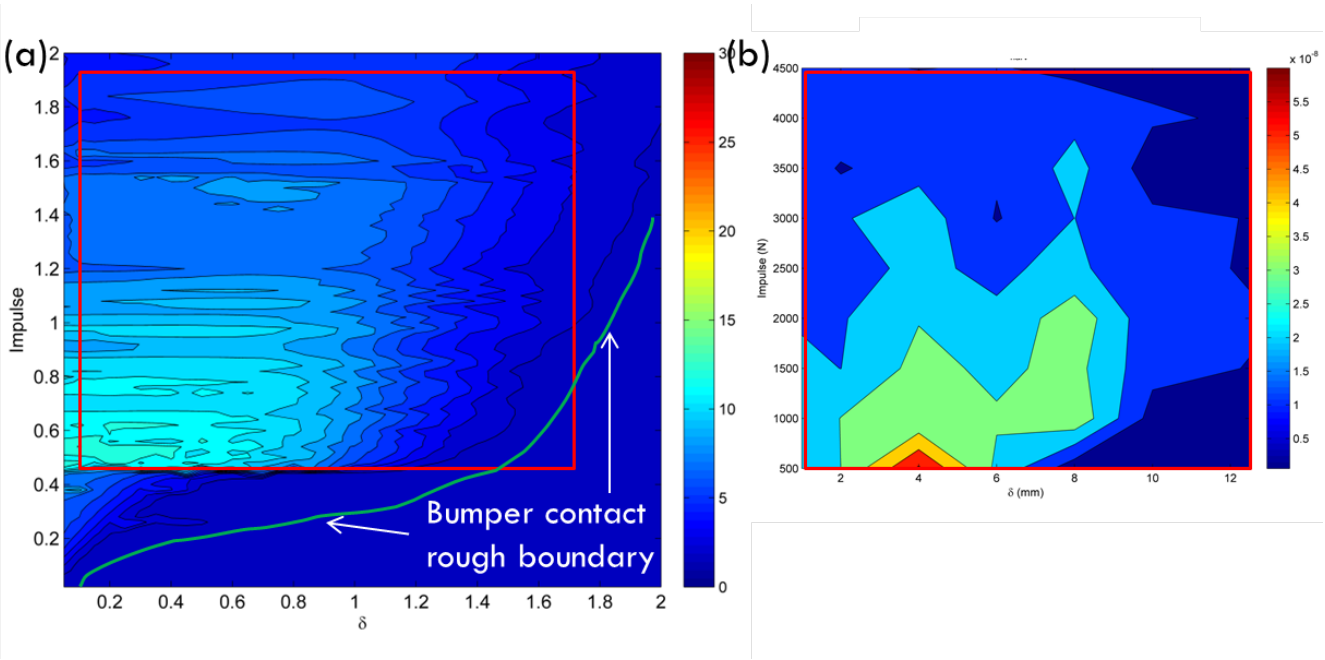

Figure 5.5: Energy harvesting efficiency for (a) numerical simulation of system (5.2) and (b) experimental trails of the apparatus in Fig.5.4 for a range of of impulse magnitudes I_0 and bumper clearances δ.

compliance and coefficient of restitution for the impacts. The single impulse excitation case was considered initially numerically and experimentally for a range of impulse magnitudes I_0 and bumper clearances δ. Contour plots were constructed for energy harvesting efficiency to gage system performance. A series of 63 experimental trails were conducted on the experimental apparatus (cf. Fig.5.4) corresponding to the numerically simulated parameter ranges. A contour plot was also developed for the experimental trials, which are based on the discrete performance measures from the trails with some intermediate interpolation between points. These contour plots are depicted in Fig.5.5, in which the red boundaries denote parameter correspondence between the numerical system (5.2) and experimental apparatus of Fig.5.4.

As seen in Fig.5.5, the numerical simulation and experimental system have strong qualitative correlation, albeit the experimental system performance doesn't match the quantitative performance of the numerically simulated parameters. A rough green line in Fig.5.5a marks the bumper contact boundary for the system. There is no contact between the NES and piezo-bumper for excitation magnitudes and bumper clearances outside of this line, in which the system (5.2) approximates the performance behavior of the mechanical system (2.1) presented in Chapter 2. Contact occurs between the NES and piezo-bumper for excitation magnitudes and bumper clearances inside of this line, in which energy is harvested during the collisions. Regions of high efficiency correspond to scenarios in which the NES impacts the piezo-bumper multiple times with significant magnitude, which can be achieved experimentally with low impulse magnitudes, as indicated in Fig.5.5b. Contact between the NES and piezo-bumper causes high-frequency instabilities in the response of the NES to manifest, which, as seen in Fig.5.5a, can occur for small impulse magnitudes and bumper clearances.

As a brief example, the response of the experimental apparatus for the parameters $I_0 = 500N$ and $\delta = 4mm$ is depicted in Fig.5.6, which corresponds to the highest efficiency experimental trial. As seen in Fig.5.6a,b, the primary system oscillates at its fundamental frequency of $\sim 5Hz$ for the duration of the response, which takes place for $\sim 1.2s$ before the system comes to rest. As seen in the relative displacement wavelet of Fig.5.6d, the response of the NES engages in high-frequency 2:1 resonance capture with the primary system for just about the entire duration of the response. The response drops down to the $S11+$ branch briefly before the system comes to

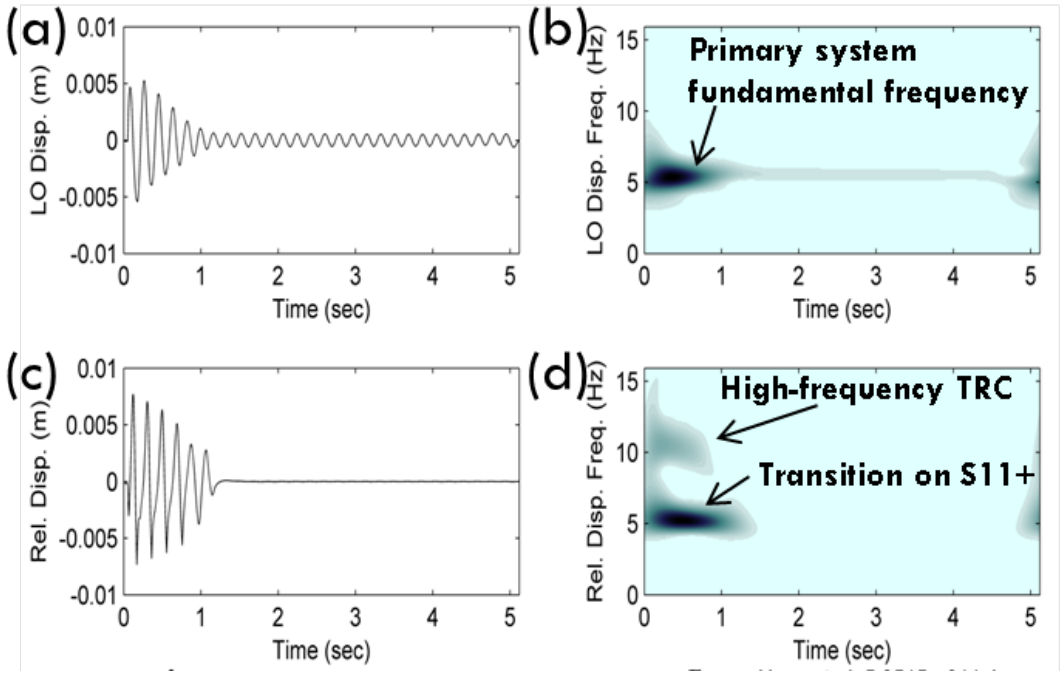

Figure 5.6: (a) primary system displacement time history, (b) primary system displacement wavelet, (c) relative displacement time history, and (d) relative displacement wavelet for the experimental apparatus presented in Fig.5.4 subject to low intensity impulsive excitation of magnitude $I_0 = 500N$ and bumper clearance $\delta = 4mm$.

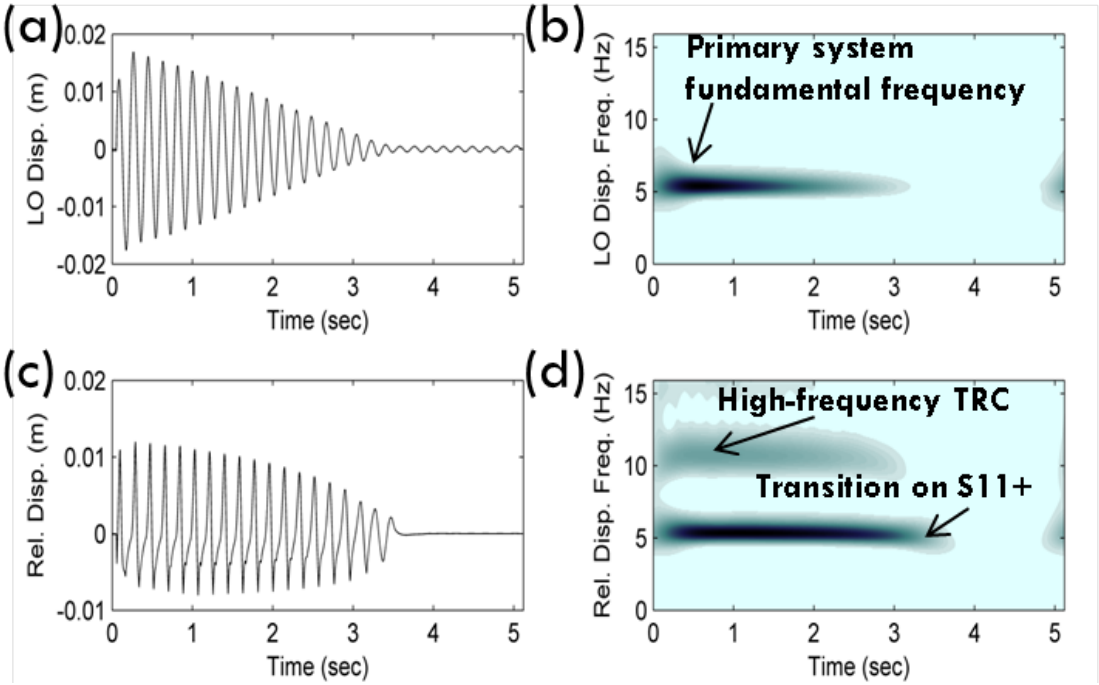

Figure 5.7: (a) primary system displacement time history, (b) primary system displacement wavelet, (c) relative displacement time history, and (d) relative displacement wavelet for the experimental apparatus presented in Fig.5.4 subject to large intensity impulsive excitation of magnitude $I_0 = 4500N$ and bumper clearance $\delta = 4mm$.

rest.

The example is continued for the response of the experimental apparatus for the parameters $I_0 = 4500N$ and $\delta = 4mm$ as depicted in Fig.5.7, which corresponds to a moderate efficiency experimental trial. As seen in Fig.5.7a,b, the primary system oscillates at its fundamental frequency of $\sim 5Hz$ for the duration of the response, which takes place for $\sim 3.5s$ before the system comes to rest. As seen in the relative displacement wavelet of Fig.5.7d, the response of the NES engages again in high-frequency 2:1 resonance capture with the primary system for just about the entire duration of the response. The response drops down to the $S11+$ branch briefly before the system comes to rest.

The responses of Fig.5.6d and Fig.5.7d indicate that high-frequency 2:1 resonance capture can be sustained for the duration of the response as long as the NES is striking the vibro-impact bumper. As indicated in Fig.5.5a, the NES will contact the bumper for low excitation magnitudes and bumper

clearances, which is validated with the experimental study depicted in Fig.5.5b. With the combination of this sustained high-frequency instability at low impulse magnitudes due to the vibro-impact element and the superior energy harvesting capability of electromagnetic elements described in Chapter 3, the system (5.1) presents an encouraging path for increasing robustness and performance of the novel energy harvesting apparatus presented in Chapter 3.

REFERENCES

[1] A. Vakakis, D. McFarland, L. Bergman, L. Manevitch, and O. Gendelman, "Isolated resonance captures and resonance capture cascades leading to single or milti-mode passive energy pumping in damped coupled oscillators," *Journal of Vibration and Acoustics*, vol. 126, pp. 235–244, 2004.

[2] A. Vakakis, O. Gendelman, L. Bergman, D. McFarland, G. Kerschen, and Y. Lee, *Nonlinear Targeted Energy Transfer in Mechanical and Structural Systems.* Springer-Verlag, New York, 2008.

[3] O. Gendelman, A. Vakakis, L. Bergman, and D. McFarland, "Asymptotic analysis of passive nonlinear suppression of aeroelastic instabilities of a rigid wing in subsonic flow," *SIAM Journal of Applied Mathematics*, vol. 70(5), pp. 1655–1677, 2010.

[4] Y. Lee, G. Kerschen, A. Vakakis, P. Panagopoulous, L. Bergman, and D. McFarland, "Complicated dynamics of a linear oscillator with a light, essentially nonlinear attachment," *Physica D*, vol. 204, pp. 41–69, 2005.

[5] G. Kerschen, Y. Lee, A. Vakakis, D. McFarland, and L. Bergman, "Irreversible passive energy transfer in coupled oscillators with essential nonlinearity," *SIAM Journal of Applied Mathematics*, vol. 66(2), pp. 648–679, 2006.

[6] G. Kerschen, O. Gendelman, A. Vakakis, L. Bergman, and D. McFarland, "Impulsive periodic and quasi-periodic orbits of coupled oscillators with essential stiffness nonlinearity," *Communications in Nonlinear Science and Numerical Simulations*, vol. 13, pp. 959–978, 2008.

[7] F. Nucera, A. Vakakis, D. McFarland, L. Bergman, and G. Kerschen, "Targeted energy transfers in vibro-impact oscillators for seismic mitigation," *Nonlinear Dynamics*, vol. 50, pp. 651–677, 2007.

[8] Y. Lee, F. Nucera, A. Vakakis, D. McFarland, and L. Bergman, "Periodic orbits, damped transitions and targeted energy transfers in oscillators with vibro-impact attachments," *Physica D*, vol. 238, pp. 1868–1896, 2009.

[9] A. Itin, A. Neishtadt, and A. Vasiliev, "Captures into resonance and scattering on resonance in dynamics of a charged relativistic particle in magnetic field and electrostatic wave," *Physica D*, vol. 141, pp. 281–296, 2000.

[10] A. Neishtadt, "On the change in the adiabatic invariant on crossing a separatrix in systems with two degrees of freedom," *PMM Journal of Applied Mathematics and Mechanics*, vol. 51(5), pp. 586–592, 1987.

[11] A. Neishtadt, "Scattering by resonances," *Celestial Mechanics and Dynamical Astronomy*, vol. 65(1-2), pp. 1–20, 2006.

[12] A. Neishtadt and A. Vasiliev, "Destruction of adiabatic invariance at resonances in slow-fast hamiltonian systems," *Nuclear Instruments and Methods in Physics Research*, vol. 561, pp. 158–165, 2006.

[13] D. Vainchtein, A. Neishtadt, and I. Mezic, "On passage through resonances in volume-preserving systems," *Chaos*, vol. 16, p. 043123, 2006.

[14] X. Wang, "Construction of frequency-energy plots for nonlinear dynamical systems from time-series data," M.S. thesis, University of Illinois at Urbana-Champaign, 2010.

[15] D. Andersen, A. Vakakis, Y. Starosvetsky, and L. Bergman, "Dynamic instabilities in coupled oscillators induced by geometrically nonlinear damping," *Nonlinear Dynamics*, vol. 67, pp. 807–827, 2012.

[16] Y. Liao and H. Sodano, "Model of a single mode energy harvester and properties for optimal power generation," *Smart Materials and Structures*, vol. 17, p. 065026, 2008.

[17] N. Stephen, "On energy harvesting from ambient vibration," *Journal of Sound and Vibration*, vol. 293, pp. 409–425, 2006.

[18] E. Lefeuvre, A. Badel, C. Richard, and D. Guyomar, "Piezoelectric energy harvesting device optimization by synchronous electric charge extraction," *Journal of Intelligent Material Systems and Structures*, vol. 16, pp. 865–876, 2005.

[19] P. Mitcheson, T. Toh, K. Wong, S. Burrow, and A. Holmes, "Tuning the resonant frequency and damping of an energy harvester using power electronics," *IEEE Transactions on Circuits and Systems*, vol. 58 (Part 2), pp. 792–796, 2011.

[20] G. Szarka, B. Stark, and S. Burrow, "Review of power management for kinetic energy harvesting systems," *IEEE Transactions on Power Electronics*, vol. 27, pp. 803–815, 2012.

[21] G. Szarka, S. Burrow, P. Proynov, and B. Stark, "Maximum power transfer tracking for ultra-low-power electromagnetic energy harvesters," *IEEE transactions on Power Electronics*, vol. 29 (1), pp. 201–212, 2014.

[22] A. Cammarano, S. Burrow, D. Barton, A. Carrella, and L. Clare, "Tuning a resonant energy harvester using a generalized elelectric load," *Smart Materials and Structures*, vol. 19 (5), p. 055003, 2011.

[23] N. duToit and B. Wardle, "Experimental verification of models for microfabricated piezoelectric vibration energy harvesters," *AIAA Journal*, vol. 45 (5), pp. 1126–1137, 2007.

[24] T. Seuaciuc-Osorio and M. Daqaq, "Energy harvesting under excitations of time-varying frequency," *Journal of Sound and Vibration*, vol. 329, pp. 2497–2515, 2010.

[25] D. Quinn, A. Triplett, L. Bergman, and A. Vakakis, "Comparing linear and essentially nonlinear vibration-based energy harvesting," *Journal of Vibration and Acoustics*, vol. 133, pp. 011 001–1, 2011.

[26] B. Mann and N. Sims, "Energy harvesting from the nonlinear oscillations of magnetic levitation," *Journal of Sound and Vibration*, vol. 319, pp. 515–530, 2009.

[27] A. Triplett and D. Quinn, "Experimental investigation of energy harvesting with essential nonlinearities," in *Proceedings of ASME IDETC/CIE*, 2011.

[28] T. Ma and H. Zhang, "Enhancing mechanical energy harvesting with dynamics escaped from potential well," *Applied Physics Letters*, vol. 100, p. 114107, 2012.

[29] T. Ma and H. Zhang, "Reaping the potential of nonlinear energy harvesting with tunable damping and modulation of the forcing functions," *Applied Physics Letters*, vol. 104, p. 214104, 2014.

[30] A. Erturk, J. Hoffmann, and D. Inman, "A piezomagnetoelastic structure for broadband vibration energy harvesting," *Applied Physics Letters*, vol. 94, p. 254102, 2009.

[31] D. Kremer and K. Liu, "A nonlinear energy sink with an energy harvester: transient responses," *Journal of Sound and Vibration*, 2014.

[32] Y. Hu, H. Xue, J. Yang, and Q. Jiang, "Nonlinear behavior of a piezoelectric power harvester near resonance," *IEEE Transactions on Ultrasonics, Ferroelectrics and Frequency Control*, vol. 53 (7), pp. 1387–1391, 2006.

[33] S. Beeby and T. O'Donnel, *Energy Harvesting Technologies*, S. Priya and D. Inman, Eds. Springer, 2009.

[34] C. Cepnik, O. Radler, S. Rosenbaum, T. Stroehla, and U. Wallrabe, "Effective optimization of electromagnetic energy harvesters through direct computation of the electromagnetic coupling," *Sensors and Acutators A: Physical*, vol. 167, pp. 416–421, 2011.

[35] M. Karami and D. Inman, "Equivalent damping and frequency change for linear and nonlinear hybrid vibrational energy harvesting systems," *Journal of Sound and Vibration*, vol. 330, pp. 5583–5597, 2011.

[36] A. Manbachi and R. Cobbold, "Development and application of piezoelectric materials for ultrasound generation and detection," *Ultrasound*, vol. 19(4), pp. 187–196, 2011.

[37] H. Kim, Y. Tadesse, and S. Priya, *Energy Harvesting Technologies*, S. Priya and D. Inman, Eds. Springer, 2009.

[38] K. Mak, M. S., A. Popov, and C. Fox, "Performance of a cantilever piezoelectric energy harvester impacting a bump stop," *Journal of Sound and Vibration*, vol. 330, pp. 6184–6202, 2011.

[39] E. Garcia and A. Wickenheiser, "Broadband vibration-based energy harvesting improvement through frequency up-conversion by magnetic excitation," *Smart Material Structures*, vol. 19, p. 065020, 2010.

[40] D. Andersen, Y. Starosvetsky, M. Mane, S. Hubbard, K. Remick, X. Wang, A. Vakakis, and L. Bergman, "Non-resonant damped transitions resembling continuous resonance scattering in coupled oscillators with essential nonlinearities," *Physica D*, vol. 241, pp. 964–974, 2012.

[41] S. Masri and T. Caughey, "A nonparametric identification technique for nonlinear dynamic problems," *ASME Journal of Applied Mechanics*, vol. 46, pp. 433–447, 1979.

[42] K. Worden, "Data processing and experiment design for the restoring force surface method, part i: Integration and differentiation of measured time data," *Mechanical Systems Signal Processing*, vol. 4(4), pp. 295–319, 1990.

[43] H. Wheeler, "Simple inductance formulas for radio coils," *Proceedings of the Institute of Radio Engineers*, vol. 16, pp. 1398–1400, 1928.

[44] N. Minorsky, "Nonlinear oscillations," *Van Nostrand, Princeton*, 1962.

[45] B. D'Urso, R. Van Handel, B. Odom, D. Hanneke, and G. Gabrielse, "Sinle-particle self-excited oscillator," *Physical Review Letters*, vol. 94, p. 113002, 2005.

[46] A. Badel, D. Guyomar, E. Lefeuvre, and C. Richard, "Efficiency enhancement of a piezoelectric energy harvesting device in pulsed operation by synchronous charge inversion," *Journal of Intelligent Material Systems and Structures*, vol. 16, pp. 889–901, 2005.